technische universität
dortmund

Dissertation
zur Erlangung des Doktorgrades der Naturwissenschaften

Nonequilibrium nuclear spin states in singly charged semiconductor quantum dots

vorgelegt von

Iris Kleinjohann
geboren in Paderborn

August 2022

Fakultät Physik
Technische Universität Dortmund

Erstgutachter:	Prof. Dr. Frithjof B. Anders
Zweitgutachter:	Prof. Dr. Götz S. Uhrig

Abstract

The spin of a localized charge carrier in a semiconductor nanostructure can be coherently controlled by external electromagnetic fields. At cryogenic temperatures, the spin coherence time is limited by the hyperfine interaction with surrounding nuclear spins. The generation of tailored nuclear spin states, however, may drastically increase the electron spin coherence in comparison to the disordered nuclear spin system. By means of a fully quantum mechanical description, we investigate two particular nonequilibrium situations in which a highly ordered nuclear spin state is achieved. First, we focus on the formation of the nuclear-spin polaron state under optical cooling of the nuclear spins. Kinetic rate equations are developed that account for different effective spin temperatures of the charge carrier and the nuclei and provide analytical access to the crossover temperature of the polaron formation. The rate equations are generalized to a Lindblad formalism enabling the numerical investigation of a cooled system with arbitrary anisotropic hyperfine interaction. The second nonequilibrium situation addressed in this thesis is the periodic optical excitation of singly charged quantum dots subject to a transversal magnetic field. Nuclei-induced frequency focusing of the electron spin precession leads to mode-locked spin dynamics. A revival of the electron spin polarization directly before each pump pulse reflects this synchronization of the spin dynamics to the pumping periodicity. In experiments, a magnetic field dependence of the emerging revival amplitude is observed. Our quantum mechanical approach allows for attributing this dependence to the nuclear Zeeman term. Moreover, we discuss various additional influences on the mode-locking effect. We examine the effect of static nuclear-electric quadrupolar interactions, the characteristics of the laser pulses, and the choice of the pulse train.

Zusammenfassung

Der Spin eines lokaliserten Ladungsträgers in einer Halbleiternanostruktur kann mit Hilfe äußerer elektromagnetischer Felder kohärent kontrolliert werden. Die Kohärenzzeit des Spins ist bei kryogenen Temperaturen durch die Hyperfeinwechselwirkung mit umliegenden Kernspins begrenzt. Durch die Erzeugung von maßgeschneiderten Kernspinzuständen kann die Kohärenzzeit im Vergleich zum ungeordneten Kernspinsystem drastisch erhöht werden. Mittels einer vollständig quantenmechanischen Beschreibung untersuchen wir zwei spezielle Nichtgleichgewichtssituationen, in denen ein stark geordneter Kernspinzustand erreicht wird. Zunächst betrachten wir die Entstehung eines Kernspinpolaronenzustands unter optischer Kühlung der Kernspins. Wir entwickeln kinetische Ratengleichungen, die verschiedene effektive Temperaturen des Ladungsträgerspins und der Kernspins berücksichtigen und analytischen Zugang zur Übergangstemperatur für die Polaronenformation gewähren. Die Ratengleichungen werden zu einem Lindblad-Formalismus verallgemeinert, der die numerische Untersuchung eines Systems mit beliebiger Hyperfeinwechselwirkung ermöglichen. Die zweite Nichtgleichgewichtssituation, die in dieser Arbeit untersucht wird, ist die periodische optische Anregung einfach geladener Quantenpunkte in einem transversalen Magnetfeld. Die kernspininduzierte Fokussierung der Elektronenpräzessionsfrequenz führt zu einer Modenkopplung der Spindynamik. Eine Rephasierung der Elektronenspinpolarisation unmittelbar vor den Laserpulsen spiegelt diese Synchronisation der Spindynamik mit der Periodizität der optischen Anregung wider. Im Experiment wird eine Magnetfeldabhängigkeit der entstehenden Polarisationsamplitude des Elektronenspins vor den Laserpulsen beobachtet. Unsere quantenmechanischen Rechnungen führen diese Abhängigkeit auf den Zeeman-Term der Kernspins zurück. Zudem analysieren wir die Auswirkungen verschiedenster Einflüsse auf die Synchronisationseffekte. Wir betrachten unter anderem die quadrupolaren Wechselwirkungen der Kernspins, die Eigenschaften der Laserpulse sowie die Wahl der Pulsfolge.

Publications

Large parts of this thesis are reused and adapted from the author's contributions to the following publications:

- I. Kleinjohann, E. Evers, P. Schering, A. Greilich, G. S. Uhrig, M. Bayer and F. B. Anders
  Magnetic field dependence of the electron spin revival amplitude in periodically pulsed quantum dots
  Phys. Rev. B **98**, 155318 (2018).
- A. Fischer, I. Kleinjohann, F. B. Anders and M. M. Glazov
  Kinetic approach to nuclear-spin polaron formation
  Phys. Rev. B **102**, 165309 (2020).
- I. Kleinjohann, A. Fischer, M. M. Glazov and F. B. Anders
  Nuclear-spin polaron formation: Anisotropy effects and quantum phase transition
  Phys. Rev. B **105**, 195309 (2022).

Further publications with contributions from the author:

- A. Fischer, I. Kleinjohann, N. A. Sinitsyn and F. B. Anders
  Cross-correlation spectra in interacting quantum dot systems
  Phys. Rev. B **105**, 035303 (2022).

Contents

1 Introduction **1**

2 Singly charged quantum dots **5**
2.1 Semiconductor quantum dots 5
2.2 Energy scheme and optical excitation 7
2.3 Readout of electron spin polarization 9
2.4 Central spin model 10
2.5 Hyperfine interaction of electrons and holes 12
2.6 Electron spin relaxation in the frozen Overhauser field approximation 15
2.7 Static nuclear-electric quadrupolar interactions 17

3 Nuclear-spin polaron formation for Ising-type hyperfine interaction **21**
3.1 Two-temperature concept 22
3.2 Mean-field approach 23
3.3 Kinetic rate equation formalism 29
3.3.1 Ising limit of the hyperfine interaction 30
3.3.2 Analytical treatment 32
3.4 Indicators of nuclear-spin polaron formation 34
3.5 Temperature criterion for polaron formation 38
3.6 Effects of the distribution of hyperfine coupling constants 42
3.7 Kinetics of polaron formation 45
3.8 Chapter conclusion 48

4 Nuclear-spin polaron formation for general anisotropic hyperfine interaction **49**
4.1 Lindblad formalism 50
4.1.1 Dynamics of the density operator in matrix representation . 51
4.2 Specified master equations 52
4.2.1 Eigendecomposition of the anisotropic hyperfine Hamiltonian 53
4.2.2 Reduced rate equations 54
4.2.3 Transition rates 56
4.3 Numerical implementation 58
4.4 Nuclear-spin polaron state in the anisotropic system 60

4.5 Crossover temperature for polaron formation 62
4.6 Nuclear distribution functions 65
4.7 Quantum phase transition 70
4.8 Temporal spin fluctuations 72
4.8.1 Autocorrelation function of the charge carrier spin 72
4.8.2 Rotation of the polaron state in the isotropic system 76
4.8.3 Autocorrelation function of the nuclear spin 80
4.9 Chapter conclusion 82

5 Implementation of periodic optical excitation 85
5.1 Pump-probe technique 85
5.2 Modeling optical pulses 88
5.3 Decay of the trion state 91
5.4 Numerical implementation of a repetition period 92
5.5 Ensemble averaging and distribution of the hyperfine coupling constants 98

6 Synchronization effects under periodic optical excitation 103
6.1 Electronic quasistationary steady state 104
6.2 Mode-locking effect and nuclei-induced frequency focusing 108
6.3 Magnetic field dependence of the electron spin revival amplitude . 110
6.4 Excitation with Gaussian shaped pump pulses 114
6.4.1 Trion detuning 117
6.5 Effect of static nuclear-electric quadrupolar interactions 119
6.5.1 Numerical implementation 120
6.5.2 Weakening of the nuclei-induced frequency focusing 123
6.6 Effect of different nuclear isotopes 128
6.7 Chapter conclusion 132

7 Steady-state analysis of the periodically driven spin system 135
7.1 Mapping for a repetition period 135
7.2 Eigenspectrum of the mapping 138
7.2.1 Absolute value of the eigenvalues 139
7.2.2 Complex eigenvalues 143
7.2.3 Overlap with the initial density operator 146
7.3 Truncation scheme 147
7.4 Electron spin revival amplitude in the box model approximation . 150
7.5 Focusing of a single electron spin precession mode 152
7.6 Sweeping of the external magnetic field 154
7.7 Variation of the pulse train 158
7.8 Chapter conclusion 161

8 Conclusion **163**

Bibliography **167**

Chapter 1

Introduction

Quantum information science [1–3] has become a highly popular field of research in the last decades. Innovative technologies [4, 5] and efficient new algorithms [6] have progressed. Nowadays, the first realizations of quantum computers are capable of solving specialized problems [7, 8]. Most recently, the first commercial quantum computers were presented [9]. Moreover, the achievement of quantum supremacy [10], i.e., a quantum computer solving a problem that cannot be solved by any conventional computer in a feasible amount of time, was discussed [11–14]. However, the stage at which quantum computers provide an asset for practical applications remains in the distant future [15].

Historically, the concept of quantum computing [16, 17] dates back to the first proposals by Manin [18] and Feynman [19] in the beginning of the 1980s. Feynman suggested the use of quantum computers for the efficient simulation of quantum mechanical systems. As the Hilbert space dimension of the quantum system grows exponentially with the number of involved particles, the required computational resources rapidly outgrow the capabilities of a conventional computer. Furthermore, Feynman deemed the consistent probabilistic simulation of a quantum mechanical system on a classical computer impossible due to the quantum correlations [19]. As a consequence, he suggested the usage of a quantum computer. Starting from these early suggestions, many further applications for quantum computing have been devised [20–23]. Most prominent are Shor's algorithm [24, 25] for the prime factorization of large numbers in polynomial time and Groover's algorithm [26, 27] for searching databases.

The basic building block for the realization of quantum information processing devices implementing the quantum algorithms is the quantum mechanical analog to a classical bit, the so-called "qubit". While the classical binary bit either has the state '0' or '1', the qubit corresponds to a quantum mechanical two-level system that can be in any superposition of the two states. Examples of such two-level systems include the electron spin or the polarization of a photon. Five requirements for potential physical implementations of qubits have been formulated by DiVincenzo [28]. Among those criteria are the possibility to initialize the qubit in a well defined

state, the manipulation via specific quantum gates, the readout of the qubit state, as well as long decoherence times [29–31]. In addition, the system needs to be scalable with well-characterized qubits. Various candidates fulfilling these demands to a different extent have been proposed [32]. The suggestions range from nuclear spins in molecules that are addressed via nuclear magnetic resonance (NMR) [33, 34] to ions [35, 36] and neutral atoms [37, 38] trapped by electromagnetic fields. Other approaches rely on superconducting qubits [39–41] or nitrogen-vacancy centers in diamond [42, 43]. Moreover, several concepts based on semiconductor quantum dots [44–46] using for instance the localized electron spin or the charge of the dot to store the quantum information have been discussed [47–49].

In this thesis, we address the single localized electron spin in a semiconductor nanostructure [50–53]. For this system, the loss of coherence due to the hyperfine interaction of the electron spin with the surrounding nuclear spins poses a major difficulty [54–61]. Therefore, we focus on nonequilibrium nuclear spin states that promise to significantly increase the electron spin coherence time [62–65]. Two particular scenarios are examined, namely, the nuclear-spin polaron formation [66] under optical cooling of the nuclear spins and the mode-locking effect under periodic optical excitation of quantum dots in a transversal magnetic field [67, 68]. The theoretical foundation for these studies is provided by a fully quantum mechanical description based on the Central Spin Model (CSM). The CSM was first introduced by Gaudin [69] in 1976 and has a star-like topology: The central spin couples to the surrounding nuclear spin bath via hyperfine interaction whereas there is no interaction between the nuclear spins.

For the examination of the nuclear-spin polaron formation, the CSM is extended to account for the optical cooling of the nuclear spin system. In 1998, Merkulov [66] predicted the formation of this highly correlated nuclear spin state characterized by the opposite alignment of the nuclear spins with respect to the electron spin below a critical temperature. A theoretical exploration [70, 71] beyond Merkulov's mean-field approach includes nuclear spin fluctuations and suggests the experimental detection of the polaronic state by spin-noise measurements. However, the polaronic state has not been observed in experiments so far, even though the investigations are ongoing [72, 73]. In this thesis, we provide a fully quantum mechanical description of the electron-nuclear spin system and account for the complete quantum mechanical spin fluctuations. The thermodynamic nonequilibrium situation of two differing effective spin temperatures is captured by kinetic rate equations accounting for the coupling of the electron-nuclear spin system to two external spin reservoirs. This description proves especially useful in the Ising limit of the hyperfine interaction relevant for a localized heavy hole spin. Subsequently, the approach is generalized to a Lindblad formalism enabling the investigation of spin systems with arbitrary anisotropic hyperfine interaction. In particular, the isotropic case relevant for the hyperfine

coupling of a localized electron spin in a quantum dot or bound to a donor is included. We connect the polaronic state to long living spin correlations and provide an estimate for the effective spin temperatures below which the nuclear-spin polaron state forms. While our predictions agree with the mean-field critical temperatures in an intermediate temperature regime, the quantum fluctuations produce an altered behavior for strongly differing effective spin temperatures of the charge carrier and the nuclei.

The second part of this thesis addresses the mode-locking effect emerging in ensembles of singly charged (In,Ga)As quantum dots [67, 68, 74–79]. In pump-probe experiments, the quantum dots are periodically excited with a repetition time $T_R = 13.2\,\mathrm{ns}$ while an external magnetic field is applied perpendicular to the axis of optical excitation. The experiments demonstrate the frequency focusing of the electron spin precession through a reorientation of the surrounding nuclear spins [80, 81]. This nonequilibrium nuclear spin orientation is preserved for tens of minutes in darkness [68, 82]. Theoretical approaches investigating the mode-locking effect are mostly based on a classical or semiclassical description [83–89] due to the large system size of $N \approx 10^5$ nuclear spins in a real quantum dot [53]. A perturbative quantum mechanical approach [90, 91] could include up to $N = 20$ nuclear spins, but was limited to 20000 repetition periods. Here, we focus on the full quantum mechanical spin dynamics during the pulse sequence and limit ourselves to a relatively small system of $N = 6$ nuclear spins. We develop an iterative approach that allows for access to the converged spin dynamics under periodic optical excitation. Thereby, it enables a detailed study of the emerging revival of the electron spin polarization directly before each pump pulse which is governed by the nuclei-induced frequency focusing. Moreover, Uhrig [92] outlined the concept of accessing the quasistationary steady state of the mode-locked system from the eigendecomposition of a mapping comprising the full quantum mechanical spin dynamics during one repetition period and applied it to a system with up to $N = 6$ nuclear spins. In this thesis, we provide a detailed study of the full eigenspectrum of the mapping and extend the approach by a truncation scheme to include up to $N = 500$ nuclear spins in a box model approximation [93]. Aside from periodic optical excitation with repetition time $T_R = 13.2\,\mathrm{ns}$, we address the regime of a reduced pulse separation $T_R = 1\,\mathrm{ns}$ which allows for the focusing of a single electron spin precession mode [94, 95].

This thesis is structured as follows: We provide the basics on singly charged semiconductor quantum dots in Chapter 2. The optical excitation and readout of the electron spin are addressed as well as the CSM for modeling the hyperfine interaction of the localized charge carrier spin. Furthermore, other relevant spin interactions, namely the static nuclear-electric quadrupolar interactions, are discussed. Chapter 3 is devoted to the investigation of the nuclear-spin polaron formation for a spin system in the Ising limit of the hyperfine interaction. Here, we introduce the kinetic rate

equations for the two-temperature situation. In Chapter 4, we focus on the polaron formation in a system with arbitrary anisotropic hyperfine interaction by means of the generalized Lindblad formalism. The foundation for the study of the mode-locking effect in periodically pumped quantum dots is laid in Chapter 5. Experimental basics as well as the related theoretical description are outlined. Chapter 6 presents the results of the iterative calculation of the quantum mechanical spin dynamics during a periodic pulse train. We study the emergence of the electron spin revival and examine the magnetic field dependence of the nuclei-induced frequency focusing. The eigendecomposition of the mapping for one repetition period of the periodic optical excitation is analyzed in Chapter 7. Employing a truncation scheme, we access the dynamics of a large spin system in the box model approximation of the hyperfine coupling constants. Moreover, the quasistationary steady state for repetition times in the range from $T_R = 1\,\mathrm{ns}$ to $T_R = 13.2\,\mathrm{ns}$ is investigated. The conclusion in Chapter 8 sums up the findings and gives a brief outlook.

Chapter 2

Singly charged quantum dots

In this chapter, the basics of singly charged semiconductor quantum dots are discussed to provide a basis for the investigation of the embedded spin system in various nonequilibrium situations. After briefly outlining the specifics of the semiconductor nanostructures employed in the mode-locking experiments [67, 68], the theoretical foundations for the modeling of the related spin dynamics are introduced. We present a scheme for the optical excitation and address the readout of the localized charge carrier spin. Furthermore, we establish the Hamiltonian for the relevant spin interactions in the quantum dots: A central spin model captures the hyperfine interaction of localized electrons and holes with the surrounding nuclear spins as well as the effect of an external magnetic field. Moreover, static nuclear-electric quadrupolar interactions may become important on longer time scales for nuclear spins with spin length $I > 1/2$. Additional weaker effects such as nuclear dipole-dipole interactions [96–98] or potential interactions between the individual electron spins in an ensemble of singly charged quantum dots [99–103] are omitted in this thesis.

The reduced Planck constant is consistently set to $\hbar = 1$ in the following.

2.1 Semiconductor quantum dots

A quantum dot provides a zero-dimensional nanostructure that is typically composed of semiconductor materials and allows for the spatial confinement of a few charge carriers such as electrons or holes [97, 104]. As a result of the confinement, bound states with discrete energy levels form for the charge carriers. Due to the resemblance to the electronic wave functions in atoms, quantum dots occasionally are referred to as ”artificial atoms” [97, 105].

For the fabrication of quantum dots, a variety of techniques have been developed [97] which reach from methods based on colloidal chemistry [106–108] to molecular beam epitaxy [109, 110] or metalorganic chemical vapor deposition [111, 112]. A common technique for the self-assembled growth of quantum dots, which also was

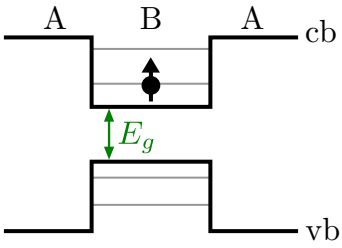

Figure 2.1: Scheme of the energy levels in a semiconductor quantum dot. The material B forming the quantum dot is enclosed by another material A which provides a potential well confining the charge carrier.

employed for the samples utilized in the mode-locking experiments [67, 68], is the molecular beam epitaxy via the Stranski-Krastanow method [104, 113]: Different semiconductor materials are grown in layers on top of each other via vapor deposition. One material A serves as a substrate and another material B is grown in atomic layers on the substrate. As a consequence of the slightly different lattice constants of the materials A and B, strain occurs at the surface between the materials. After growing a few atomic layers of material B, which form a thin film called wetting layer, elevations arise and form small three-dimensional islands. These islands constitute the quantum dots. When the band gap E_g between the conduction band (cb) and the valence band (vb) of the dot material B is smaller than the band gap of the surrounding semiconductor A, charge carriers such as electrons or holes may be confined within the dot, see Fig. 2.1.

The present analysis focuses on singly charged semiconductor quantum dots which mostly are assumed to be charged by an electron. Such a charging of quantum dots is achieved by adding a doping layer in the growth process that provides free charge carriers which tunnel into the dots. The proper adjustment of the donor (or acceptor) density in the doping layer with respect to the dot density enables the charging of the quantum dots with a single charge carrier on average.

The mode-locking experiments [67, 68] inspiring the investigations in Chapters 6 and 7 are conducted on an (In,Ga)As/GaAs quantum dot ensemble in which the self-assembled quantum dots are mostly made up by indium gallium arsenide (InGaAs) and the surrounding layers by gallium arsenide (GaAs). The utilized samples contain multiple layers of quantum dots whose n-type doping is provided by silicon (Si) donor layers in between the quantum dot layers. Within the quantum dot layers, the dot density amounts to $10^{10}\,\mathrm{cm}^{-2}$. The individual dots have a cylindrical shape with roughly 25 nm diameter and 5 nm height and are charged by a single electron spin on average [67, 68]. After production the samples are thermally annealed to shift the ground state emission into experimentally convenient realms around 1.4 eV

[67, 68, 86]. Moreover, the heating of the sample leads to a diffusion of part of the indium (In) out of the dots which homogenizes the quantum dot ensemble and reduces strain within the sample [86, 114, 115].

2.2 Energy scheme and optical excitation

The discrete energy levels in a semiconductor quantum dot provide the basis for versatile optical applications since individual charge carriers can be efficiently photogenerated, manipulated and coherently controlled [116–119]. A detailed discussion of the energy structures in different types of semiconductor quantum dots and the resultant optical addressability may be found, for instance, in Ref. [120]. Here, we restrict ourselves to the relevant aspects with respect to the present studies, i.e., we focus on GaAs-type quantum dots and stick to the optical excitation close to the band gap energy.

The energy bands of a bulk semiconductor transform into discrete energy levels for a quantum dot, see Fig. 2.2. The twofold degenerate conduction band with a total angular momentum $j = 1/2$ turns into two electron states with the projection of the total angular momentum $j^z = \pm 1/2$. The valence bands closest to the band gap have a total angular momentum $j = 3/2$ in a GaAs-type bulk semiconductor whereas the valence band with $j = 1/2$ is split off in energy due to the spin-orbit interaction and, therefore, is disregarded in the following. In a quantum dot, the valence bands with $j = 3/2$ split into two energy levels with twofold degeneracy each. The states with $j^z = \pm 1/2$ correspond to light hole states and the states with $j^z = \pm 3/2$ form the heavy hole states. As a result of the intrinsic strain resulting from the growth process of the sample and the spatial confinement of the charge carriers, the light hole states have lower energy than the heavy hole states in the quantum dot.

Optical excitation with a photon energy exceeding the band gap may induce transitions of an electron in a state with $j = 3/2$ to a state with $j = 1/2$ leaving a hole in the state formerly occupied by the electron. For circularly polarized light, the photons carry an angular momentum ± 1 in the direction of their propagation – set to the z axis here. In the case of σ^+ polarized light, the photon has an angular momentum $+1$ such that according to the conservation of angular momentum an electron with $j^z = -1/2$ and $j = 3/2$ can be exited to the state with $j^z = +1/2$ and $j = 1/2$ leaving behind a light hole. Likewise, the photon can excite an electron from the state with $j^z = -3/2$ and $j = 3/2$ to the state with $j^z = -1/2$ and $j = 1/2$ generating a heavy hole. Here, the latter transition occurs with three times higher probability than the former one. Analogous selection rules apply for the excitation

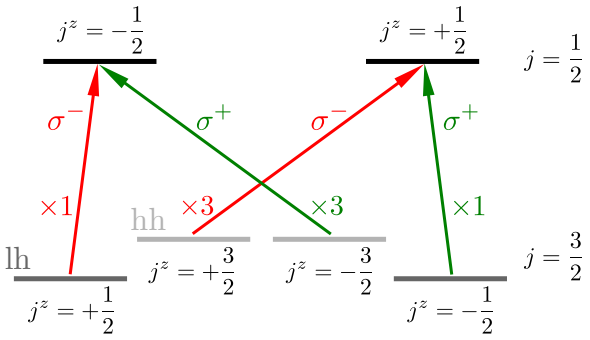

Figure 2.2: Selection rules for optical transitions between the energy levels. The transitions induced by circularly polarized light conserve the angular momentum.

with σ^- polarized light where the photon carries an angular momentum -1, see Fig. 2.2.

For a quantum dot charged by a single electron, the optically excited electron and the resident electron adhere to the Pauli principle, i.e., the optically excited electron spin must have the opposite orientation compared to the resident electron spin. When the excitation energy is adjusted to the gap between the heavy holes states and the electron states with $j = 1/2$, only electrons from the states with $j^z = \pm 3/2$ can be excited. In this case, σ^+ polarized light can only excite the electron from the state with $j^z = -3/2$ and $j = 3/2$ to the state with $j^z = -1/2$ and $j = 1/2$ if the resident electron has an angular momentum $j^z = +1/2$. If the resident electron has an angular momentum $j^z = -1/2$, photogeneration of an electron-hole pair is inhibited due to the Pauli principle. This mechanism enables the experimental manipulation and the readout of the electron spin polarization in quantum dots and is employed in measurements of the electron spin noise [121–125] as well as in pump-probe experiments [67, 68, 126].

After the excitation, the photo-generated electron-hole pair forms a bound state with the resident electron in the singly charged quantum dot. This bound state is called a negatively charged exciton or a trion and has a limited lifetime of several hundred picoseconds [127] due to the rapid recombination of the photo-generated electron-hole pair. A detailed discussion of the exploitation of the trion state excitation in the mode-locking experiments is provided in Chapter 5. Here, we turn towards the optical readout of the electron spin polarization in the quantum dots.

2.3 Readout of electron spin polarization

The optical readout of the electron spin polarization in a quantum dot ensemble can be performed via reflection or transmission setups. While the magneto-optic Kerr effect provides access to the electron spin polarization in a reflection geometry, the Faraday rotation and the Faraday ellipticity signal are obtained from light transmitted through the sample. A magnetization of the sample related to an electron spin polarization in the quantum dots changes the light propagation which is exploited for the optical readout. Employing a linearly polarized laser for probing the quantum dot sample, the laser beam is split into two linearly polarized components after passing the sample. These two components have orthogonal polarizations that are oriented with angle $\pm 45^\circ$ to the incident laser light. The Kerr rotation and the Faraday rotation are then defined by the intensity difference between the two components respectively. The Faraday ellipticity on the other hand is extracted from splitting the transmitted light into two circularly polarized beams and recording their difference in intensity.

As the off-diagonal elements of the dielectric tensor give rise to an anisotropic permittivity of the sample for the magnetized material, the polarization orientation of the transmitted (reflected respectively) light is rotated compared to the linearly polarized incident light beam. The angle of rotation Θ_F (Θ_K) in the respective scenario is expected to be proportional to the magnetization in the sample allowing for measurements of the electron spin polarization along the optical axis.

In transmission, the anisotropic permittivity produces a dependence of the speed of light in the magneto-optic material on the direction of the light polarization. As a consequence, σ^+ and σ^- polarized light cross the sample with slightly different speeds, which is known as circular birefringence. Since the linearly polarized light can be decomposed into the two circularly polarized components with equal amplitudes and the two components acquire a relative phase shift passing the material, a linearly polarized laser beam is subject to the rotation of its polarization axis by the angle Θ_F.

While the Faraday rotation is connected to the real part of the refractive index via the speed of light, the Faraday ellipticity is interrelated with the imaginary part. Passing the sample, the linearly polarized incident light acquires an elliptic component in its polarization which is proportional to the sample magnetization. Assuming the electron spins to be in spin up state ($j^z = 1/2$), the σ^+ polarized light component cannot excite the system, cf. Sec. 2.2, and hence passes the sample. The σ^- polarized component, however, may excite a trion state and thereby partially is absorbed. Consequently, the transmitted light has a stronger proportion of σ^+ than σ^- resulting in an elliptic polarization.

Continuous optical readout of the electron spin polarization by one of the above introduce measures employing a weak linearly polarized probe laser followed by a Fourier transform of the time-dependent signal into the frequency domain is termed spin noise spectroscopy. Since the laser beam has weak intensity only, the spin system is not affected by the readout such that spin noise measurements provide undisturbing access to the spin dynamics.

In more intricate situations, such as an additional optical excitation of the electron spins, the Kerr rotation, the Faraday rotation, and the ellipticity signal may supply complementary information on an ensemble of singly charged quantum dots [128, 129]. As a result of the differing spectral dependencies, a potential detuning between the excitation energy and the probe beam becomes relevant. For the present analysis, however, the assumption that the experimentally measured signal is proportional to the electron spin polarization along the optical axis will be sufficient.

2.4 Central spin model

For a localized charge carrier spin in a semiconductor nanostructure, the predominant interaction is the hyperfine coupling to the surrounding nuclear spins since the spin-orbit interaction based effects relevant in bulk materials are strongly inhibited due to the absence of translational motion. In fact, the hyperfine interaction of the localized charge carrier is enhanced compared to bulk structures as a result of the localized wave function which, e.g., spreads over typically 10^5 lattice sites for an electron contained in a quantum dot [53]. The hyperfine interaction between the charge carrier spin $\mathbf{S}$ and the surrounding nuclear spins $\mathbf{I}_k$ is described by the general Hamiltonian H_{HF},

$$H_{\mathrm{HF}} = \sum_{k=1}^{N} \sum_{\alpha,\beta} A_k^{\alpha,\beta} S^\alpha I_k^\beta, \tag{2.1}$$

where the sum over k includes all nuclear spins within the charge carrier localization volume. The coupling strength to an individual nuclear spin k is given by the matrix $A_k^{\alpha,\beta}$ with α, $\beta \in \{x, y, z\}$ referring to the Cartesian axes. These couplings have different physical origins depending on the respective scenario captured by H_{HF}. We address the specifics of the hyperfine coupling relevant in the case of the localized electron or hole spin in a semiconductor nanostructure in Sec. 2.5.

As an additional component, an external magnetic field may be applied to the spin system which acts on the charge carrier spin as well as on the nuclear spins $\mathbf{I}_k$. The Hamiltonian for the charge carrier spin $\mathbf{S}$ in a magnetic field with magnitude B and

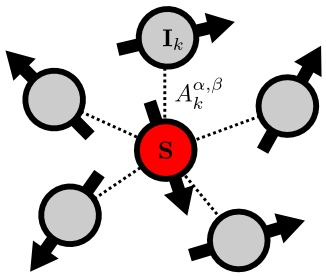

Figure 2.3: Central Spin Model. The central spin **S** couples to the surrounding nuclear spins $\mathbf{I}_k$ via coupling constants $A_k^{\alpha,\beta}$.

orientation $\mathbf{n}_B$ gives rise to a Zeeman splitting,

$$H_{\mathrm{EZ}} = -g_S \mu_B B \mathbf{n}_B \cdot \mathbf{S}, \tag{2.2}$$

governed by the Bohr magneton μ_B and the charge carrier g factor g_S. The g factor of the charge carrier in a semiconductor nanostructure typically differs from that of a free electron, $g_e \approx 2$, due to spin-orbit coupling effects [130–132]. In n doped (In,Ga)As/GaAs quantum dots, for instance, a g factor of $g_e \approx 0.555$ has been found [67, 68]. Furthermore, the g factor of hole spins in self-assembled quantum dots may be anisotropic, i.e., it depends on the orientation of the applied magnetic field [133, 134].

For the nuclear spins, the coupling to the external magnetic field B is roughly three orders of magnitude smaller compared to an electron spin due to the higher mass of the nuclei. Here, the product of the respective nuclear g_k factor and the nuclear magneton μ_N determines the coupling strength in the Zeeman Hamiltonian,

$$H_{\mathrm{NZ}} = -\sum_k g_k \mu_N B \mathbf{n}_B \cdot \mathbf{I}_k. \tag{2.3}$$

For the different isotopes in (In,Ga)As/GaAs quantum dots an average ratio $z = \overline{g_k}\mu_N / g_e \mu_B \approx 1/800$ has been estimated [91, 135].

The general hyperfine Hamiltonian H_{HF} potentially combined with the effect of an external magnetic field, H_{EZ} and H_{NZ}, has the topology of a Central Spin Model (CSM) also called Gaudin model [69, 136]. The central spin **S** couples to all surrounding nuclear spins whereas no interactions within the nuclear spin bath occur, see Fig. 2.3. The CSM is a good approximation when depicting localized charge carriers in a semiconductor since other spin interactions such as static nuclear-electric quadrupolar interactions, see Sec. 2.7, or nuclear dipole-dipole interactions are several orders of magnitude weaker than the hyperfine interaction and therefore contribute on relatively long time scales only. Aside from singly charged quantum dots [57]

and donor-bound charge carriers, the CSM is applied to nitrogen-vacancy centers in diamond [137], triphenylphosphine molecules in a polycrystalline solid [138], electrons in metallic grains [139], atomically thin transition metal dichalcogenides [140], or a ^{13}C nuclear spin qubit coupling to a ^{1}H spin bath [141].

Theoretical studies of the CSM started in 1976 when Gaudin first showed that the isotropic model is exactly solvable by means of a Bethe ansatz [69]. Since then many further studies based on this approach have been conducted [139, 142–146], however, these are either restricted to relatively small systems or require certain specified initial conditions such as a polarized bath. The restrictions could be partially overcome by the combination of the algebraic Bethe ansatz with a stochastic Monte Carlo sampling [147, 148]. For a fully polarized initial state of the nuclear spin system, exact solutions for the central spin dynamics [54, 149] suggest a history-dependent behavior. Perturbative treatments using non-Markovian master equations tailored for fluctuations in the nuclear spin bath [50, 150] and using the Nakajima-Zwanzig or time-convolutionless projection operator technique [151–154] have been developed. These treatments hold for the limit of large spin baths or strong external magnetic fields. Later on, master equations have also been employed in nonperturbative frameworks [155, 156] for various limiting situations and under external control fields [157, 158]. Further numerical approaches to the CSM include Chebyshev expansion techniques [159–161] for spin-noise spectroscopy, time-dependent density matrix renormalization group [162, 163] applicable to the system's short time dynamics as well as cluster expansion techniques for the investigation of the central spin decoherence [164–170]. Persisting quantum correlations in the isotropic CSM have been extracted using a generalized Mazur inequality [171, 172]. The exact quantum mechanical dynamics has been addressed by various sophisticated approaches [173–177] typically restricted to relatively small systems due to the exponential growth of the Hilbert space with the number of bath spins. Alternatively, (semi)classical approaches [55, 162, 178–181] valid for large bath sizes ($N \gg 1$) are employed.

2.5 Hyperfine interaction of electrons and holes

The origin of the hyperfine interaction between the localized charge carrier and the surrounding nuclear spins in a semiconductor nanostructure differs for the cases of a localized electron and hole. While the electron spin couples predominantly via Fermi contact interaction [182] to the nuclear spins, the hyperfine interaction of a hole spin results from the dipole-dipole coupling. Thus, the hyperfine coupling constants $A_k^{\alpha,\beta}$ entering the general hyperfine Hamiltonian H_{HF}, Eq. (2.1), are adapted in the respective scenario.

The Fermi contact interaction was first discussed by Fermi in 1930 [182]. In his theory, Fermi calculated the hyperfine splitting for the spectra of alkaline atoms employing a relativistic treatment of the electron. A nonrelativistic derivation of the hyperfine Hamiltonian was performed later on and includes the Fermi contact contribution as well as the dipole-dipole term relevant for hole spins. The nonrelativistic derivation is based on an approach to the interaction between the charge carrier and the magnetic moment of the nucleus within the framework of the standard quantum mechanical theory of electromagnetism as outlined, for instance, in Refs. [96, 183].

The latter derivation yields the hyperfine Hamiltonian for the interaction of the charge carrier with a single nucleus in first order perturbation theory [183],

$$H_{c-n} = \frac{2\mu_B\mu}{I}\mathbf{I}\cdot\left[\frac{\mathbf{L}}{r^3} - \frac{\mathbf{S}}{r^3} + 3\frac{\mathbf{r}\,(\mathbf{S}\cdot\mathbf{r})}{r^5} + \frac{8\pi}{3}\mathbf{S}\delta(r)\right], \tag{2.4}$$

where the charge carrier has a spin $\mathbf{S}$, an angular momentum $\mathbf{L}$, and the position $\mathbf{r}$ which is measured with respect to the location of the nucleus. For the nuclear magnetic moment, the relation $\boldsymbol{\mu} = \mu\mathbf{I}/I$ was inserted.

The individual contributions in Eq. (2.4) can be interpreted according to their physical origin: The first term accounts for the coupling of the nuclear magnetic moment to the effective magnetic field generated by the orbital motion of the electron with angular momentum $\mathbf{L}$. The combination of the second and the third term yields the dipole-dipole interaction between the charge carrier spin and the nuclear spin. The last contribution constitutes the Fermi contact interaction which is proportional to the probability of the electron being located at the position of the nucleus.

Let us now consider the respective scenario of a conduction electron or a hole in the valence band. Since the conduction band in a GaAs-type semiconductor is mostly made up of the atomic s orbitals of the Ga compound, the conduction electron has zero angular momentum, $l = 0$. Thus, it has a finite nonzero probability to be located at the position of the nucleus. Due to symmetry effects, all other contributions in H_{c-n} except for the Fermi contact term vanish and the Hamiltonian for the hyperfine interaction of a localized electron in a semiconductor is given by

$$H_{\mathrm{FC}} = \frac{16\pi\mu_B}{3}\sum_k \frac{\mu_k}{I_k}\left|\psi(\mathbf{R}_k)\right|^2 \mathbf{S}\cdot\mathbf{I}_k \tag{2.5}$$

including the coupling to numerous nuclei labeled by the index k. The coupling strength is determined by the electron wave function $\psi(\mathbf{R}_k)$ at the position of the k-th nucleus. Here, the nuclear magnetic moment μ_k and the spin length I_k enter as prefactors that differ for the various nuclear isotopes in a semiconductor. The relevant nuclear magnetic moments for (In,Ga)As/GaAs quantum dots can be found

in several tables, for instance, Ref. [135]. The spin length equals $I = 3/2$ for Gallium and Arsenic or $I = 9/2$ for Indium.

Since the Fermi contact interaction is isotropic, it can be cast into the format of the general hyperfine Hamiltonian, Eq. (2.1), with coupling constants $A_k^{\alpha,\beta} = \delta_{\alpha,\beta} A_k$ and

$$A_k = \frac{16\pi\mu_B\mu_k}{3I_k} \left|\psi(\mathbf{R}_k)\right|^2 . \tag{2.6}$$

The electron wave function can be decomposed into a product of the rapidly changing function $u(\mathbf{R}_k)$ respecting the atomic orbitals and a slowly varying envelope function $\phi(\mathbf{R}_k)$ resulting from the electron localization,

$$\psi(\mathbf{R}_k) = u(\mathbf{R}_k)\phi(\mathbf{R}_k). \tag{2.7}$$

Consequently, the hyperfine coupling constants become $A_k \propto \left|u(\mathbf{R}_k)\right|^2 \left|\phi(\mathbf{R}_k)\right|^2$. Assuming identical nuclei and approximating $\left|u(\mathbf{R}_k)\right|^2 = 1$, allows for the derivation of a distribution of the coupling constants A_k that respects the geometry of the localizing potential, e.g., the geometry of the quantum dot, see Ref. [160] and Sec. 3.6 for more details.

The hyperfine interaction between a hole spin and the surrounding nuclei, in contrast, is governed by the dipole-dipole interaction. Since the valence bands are built from the atomic p orbitals, the probability of finding the hole at the position of a nucleus vanishes. Therefore, the Fermi contact interaction does not apply here. The remaining terms in H_{c-n} yield the effective hyperfine Hamiltonian for light and heavy holes respectively and have been evaluated by Testelin et al. [184],

$$H_{\mathrm{HF,lh}} = \Omega \sum_k \frac{C_k}{3} \left|\phi(\mathbf{R}_k)\right|^2 \left[-2\left(S^x I_k^x + S^y I_k^y\right) + S^z I_k^z\right], \tag{2.8}$$

$$H_{\mathrm{HF,hh}} = \Omega \sum_k C_k \left|\phi(\mathbf{R}_k)\right|^2 S^z I_k^z, \tag{2.9}$$

$$C_k = \frac{16\mu_B\mu_k}{5I_k} \left\langle \frac{1}{\rho^3} \right\rangle_k . \tag{2.10}$$

Equations (2.8) and (2.9) make use of the unit cell volume Ω containing two atoms and a sample growth axis aligned in z direction, [001]. The contribution $\left\langle \frac{1}{\rho^3} \right\rangle_k = \int_\Omega d\boldsymbol{\rho} F_x^2(\boldsymbol{\rho})/\rho^3$ for the coupling constants C_k stems from integration of the orbital function of p symmetry, $F_x^2(\boldsymbol{\rho})$, over the unit cell with $\boldsymbol{\rho}$ measured from the position of the k-th nucleus $\mathbf{R}_k$. While the charge carrier spin $\mathbf{S}$ has the length 1/2 for an electron or a light hole, the spin $\mathbf{S}$ associated to the heavy hole is actually a pseudospin with the length 1/2 whose spin states with projection $s^z = \pm 1/2$ correspond the heavy hole states $j^z = \pm 3/2$ [184, 185].

Albeit their fundamentally differing origin, the hyperfine interaction of the electron and hole spins, H_{FC}, $H_{\mathrm{HF,lh}}$ and $H_{\mathrm{HF,hh}}$, can be mapped onto a general Hamiltonian

$$H_{\mathrm{HF}} = \sum_k A_k \left[\lambda \left(S^x I_k^x + S^y I_k^y\right) + S^z I_k^z\right] \tag{2.11}$$

by introducing the anisotropy parameter λ that accounts for the biaxiality of the system. The hyperfine coupling constants A_k in Eq. (2.11) absorb the coupling constants C_k as well as the remaining prefactors in Eqs. (2.8) and (2.9) for the dipole-dipole interaction of a hole spin and adhere to Eq. (2.6) for the electron. The anisotropy parameter λ captures the isotropic case of the conduction electron at $\lambda = 1$, the anisotropic situation of the light hole at $\lambda = -2$ and the Ising limit relevant for the heavy hole at $\lambda = 0$. In real systems, however, typically a mixture of the light and heavy hole state occurs as a result of the valence band mixing due to the spatial distribution of strain in the sample and the anisotropy of the quantum dot shape [53]. Consequently, the effective anisotropy parameter λ may have any value $\lambda \in [-2; 0]$ depending on the specific admixture. Generally, it has been found that the hyperfine interaction of the localized hole spin with $\sum_k A_k \approx 10\,\mu\mathrm{eV}$ [185, 186] is roughly one order of magnitude smaller than the Fermi contact interaction of an electron spin with $\sum_k A_k \approx 100\,\mu\mathrm{eV}$ [55, 57, 187].

2.6 Electron spin relaxation in the frozen Overhauser field approximation

The short time spin dynamics of the electron spin localized in a quantum dot, governed by the Hamiltonian, Eq. (2.11) with $\lambda = 1$, has been calculated by Merkulov et al. [55] within the approximation of frozen nuclear spins. Since the precession frequency of the electron spin in the effective magnetic field generated by all nuclei in the system is much larger than the precession frequency of a nuclear spin in the hyperfine field produced by the electron spin, the approximation that the electron spin sees a frozen random configuration of the nuclear spins is warranted. We introduce the Overhauser field [188],

$$\mathbf{B}_N = \frac{1}{g_e \mu_B} \sum_k A_k \mathbf{I}_k, \tag{2.12}$$

which corresponds to the effective magnetic field produced by the nuclear spin bath acting on the electron spin according to Eqs. (2.11) and (2.2) and consider its quantum mechanical fluctuations $\langle \mathbf{B}_N^2 \rangle$. In the high-temperature limit, the nuclear spin system is in a disordered state with randomly aligned spins producing a three-dimensional Gaussian distribution $p(\mathbf{B}_N)$ of the Overhauser field $\mathbf{B}_N$. The

individual components B_N^α with $\alpha \in \{x, y, z\}$ are uncorrelated and obey a Gaussian distribution respectively,

$$p(B_N^\alpha) = \frac{1}{\sqrt{2\pi\Delta_B^2}} \exp\left(-\frac{(B_N^\alpha)^2}{2\Delta_B^2}\right). \tag{2.13}$$

Its variance Δ_B^2 is given by

$$\Delta_B^2 = \frac{\langle \mathbf{B}_N^2 \rangle}{3} = \frac{1}{3g_e^2\mu_B^2} \sum_k A_k^2 \langle \mathbf{I}_k^2 \rangle, \tag{2.14}$$

where the quantum mechanical expectation value yields $\langle \mathbf{I}_k^2 \rangle = I_k(I_k+1)$ for nuclear spins of an individual length I_k.

The dynamics of an electron spin subject to a fixed magnetic field of strength B and orientation unit vector $\mathbf{n}_B$, Eq. (2.2), is given by the equation of motion,

$$\begin{aligned}\langle \mathbf{S}(t) \rangle = (\mathbf{S}_0 \cdot \mathbf{n}_B)\mathbf{n}_B + [\mathbf{S}_0 - (\mathbf{S}_0 \cdot \mathbf{n}_B)\mathbf{n}_B]\cos(\omega_e t) \\ + \{\mathbf{n}_B \times [\mathbf{S}_0 - (\mathbf{S}_0 \cdot \mathbf{n}_B)\mathbf{n}_B]\}\sin(\omega_e t),\end{aligned} \tag{2.15}$$

where the initial orientation of the electron spin is set to $\langle \mathbf{S}(0) \rangle \equiv \mathbf{S}_0$. The associated Larmor frequency of the electron spin precession in the magnetic field B reads

$$\omega_e = g_e \mu_B B. \tag{2.16}$$

Addressing an ensemble of singly charged quantum dots subject to randomly oriented frozen hyperfine fields and identical $\mathbf{S}_0$, we identify the magnetic field in Eq. (2.15) with the Overhauser field in the respective quantum dot, $B\mathbf{n}_B \equiv -\mathbf{B}_N$ and average Eq. (2.15) over the Overhauser field distribution $p(\mathbf{B}_N)$ of the ensemble. As a result, we obtain the ensemble-averaged electron spin polarization as a function of time,

$$\langle \mathbf{S}(t) \rangle = \frac{\mathbf{S}_0}{3}\left\{1 + 2\left[1 - \frac{4}{3}\left(\frac{t}{T^*}\right)^2\right]\exp\left[-\frac{2}{3}\left(\frac{t}{T^*}\right)^2\right]\right\}. \tag{2.17}$$

The fluctuations of the Overhauser field result in differing precession frequencies and produce a dephasing of the electron spin with the characteristic time

$$T^* = \frac{1}{\sqrt{3g_e^2\mu_B^2\Delta_B^2}} = \frac{1}{\sqrt{\sum_k A_k^2 I_k(I_k+1)}}, \tag{2.18}$$

which we will frequently employ as a reference time scale in the following. Alternatively, Eq. (2.17) can be interpreted in terms of a semiclassical approach to the electron spin dynamics in a single dot, where the quantum mechanical time evolution

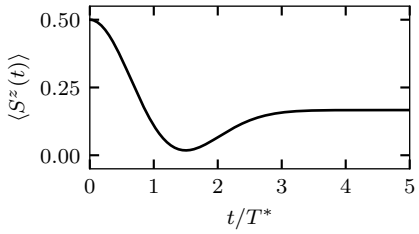

Figure 2.4: Electron spin dephasing in the fluctuations of the frozen Overhauser field according to Eq. (2.17) with initially oriented electron spin, $\mathbf{S}_0 = (0, 0, 0.5)^T$.

of the spin expectation value $\langle \mathbf{S}(t) \rangle$ is approximated by the average over various classical nuclear spin configurations.

The dephasing process of an electron spin according to Eq. (2.17) is displayed in Fig. 2.4 exemplarily for an initial spin orientation in z direction, $\mathbf{S}_0 = (0, 0, 0.5)^T$. The temporal evolution of the spin z component $\langle S^z(t) \rangle$ exhibits a characteristic dip at roughly $t = 3T^*/2$ and subsequently rises to a plateau at a third of the initial electron spin polarization. This plateau is a direct consequence of the conservation of the electron spin component parallel to an applied magnetic field according to the first term in Eq. (2.15). Assuming an isotropic distribution of the axis $\mathbf{n}_B$, the average of this term yields a third of $\mathbf{S}_0$. Taking into account the spin dynamics beyond the frozen Overhauser field approximation, a decay of the plateau on prolonged time scales would be observed due to temporal fluctuations of the Overhauser field produced by the hyperfine feedback of the electron spin onto the nuclear spin bath. Moreover, static nuclear-electric quadrupolar interactions can induce additional dynamics in the nuclear spin bath leading to a speed-up of the decay.

2.7 Static nuclear-electric quadrupolar interactions

As a result of the combination of materials with different lattice constants in the growth process, semiconductor nanostructures, in particular quantum dots, are subject to lattice strain. This strain generates an inhomogeneous electric field within the structures producing electric field gradients that act on the quadrupole moment of a nucleus [189–192]. Since the nuclei do not have an electric dipole moment, they do not couple to a homogeneous electric field. However, nuclei with a spin length $I > 1/2$ have a quadrupole moment resulting from the nonspherical charge distribution, see Fig. 2.5(a). The quadrupole moment interacts with the electric

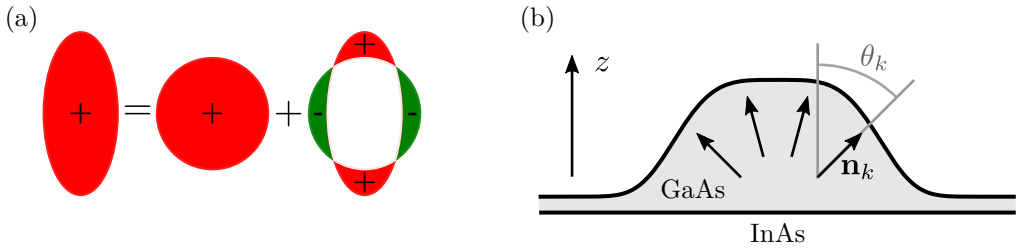

Figure 2.5: (a) Decomposition of the nuclear quadrupole moment. (b) Distribution of the electric field gradients in a quantum dot.

field gradients that arise when the symmetry of the quantum dot is broken due to lattice strain or the interdiffusion of the substrate material into the dot.

For an electric field gradient along the z direction, the quadrupole interaction of a single nuclear spin $\mathbf{I}$ is described by the Hamiltonian [96, 183, 193],

$$H_{f-n} = \frac{eQ_n}{4I(2I-1)} \left\{ \left(V_{xx} - V_{yy}\right) \left[(I^x)^2 - (I^y)^2\right] + V_{zz} \left[3(I^z)^2 - \mathbf{I}^2\right] \right\}. \tag{2.19}$$

Here, e is the elementary charge of the electron, Q_n is the nuclear quadrupole moment and $V_{\alpha\alpha}$ with $\alpha \in \{x, y, z\}$ is the second derivative of the electric potential along the α direction.

For $\mathrm{In}_x\mathrm{Ga}_{1-x}\mathrm{As}$ quantum dots with $0 < x < 1$, it was found that the local field gradients at the positions of the nuclei follow a spatial distribution [194, 195], see Fig. 2.5(b). The Hamiltonian for the quadrupolar interactions of the nuclear spins in a quantum dot,

$$H_{\mathrm{NQ}} = \sum_k q_k \left\{ \frac{\eta_k}{3} \left[(\mathbf{l}_k \cdot \mathbf{I}_k)^2 - (\mathbf{m}_k \cdot \mathbf{I}_k)^2\right] + (\mathbf{n}_k \cdot \mathbf{I}_k)^2 - \frac{I_k(I_k+1)}{3} \right\}, \tag{2.20}$$

includes the local easy axis $\mathbf{n}_k$ at the position of the respective nucleus as well as the coupling strength q_k of the individual spin, $q_k = 3eQ_{n,k}V_{zz,k}/[4I_k(2I_k-1)]$. The anisotropy parameter $\eta_k = (V_{xx,k} - V_{yy,k})/V_{zz,k}$ accounts for the degree of biaxiality of the local field gradients. The unit vectors $\mathbf{l}_k$ and $\mathbf{m}_k$ constitute a Cartesian basis in combination with $\mathbf{n}_k$, whereas the specific orientation of $\mathbf{l}_k$ and $\mathbf{m}_k$ within the plane perpendicular to $\mathbf{n}_k$ is random.

For the determination of the quadrupolar parameter of the quantum dots, we refer to Ref. [122]. The distribution of the local easy axis $\mathbf{n}_k$ found in Ref. [194] is approximated by a uniform distribution of the vector $\mathbf{n}_k$ on the unit sphere restricted to a cone around the growth direction of the sample identified as the z axis here. Accordingly, the angle enclosed by $\mathbf{n}_k$ and the z axis, $\theta_k \in [0, \theta_M]$, is

limited by a maximum angle $\theta_M = 34^\circ$, while the polar angle $\phi_k \in [0, 2\pi]$ within the (xy) plane is uniformly distributed. The set of auxiliary vectors $\mathbf{l}_k$ and $\mathbf{m}_k$ is established randomly in the plane perpendicular to $\mathbf{n}_k$. For the biaxiality, a typical value $\eta_k \equiv \eta = 0.5$ identical for all nuclei is inserted [122, 194].

The nuclear quadrupolar interactions are several orders of magnitude smaller than the hyperfine interaction and therefore become relevant on longer time scales when the CSM approximation is not sufficient anymore. Typical time scales on which nuclear quadrupole effects come into play are in the order of hundreds of nanoseconds [194, 196, 197]. Here, we employ a measure for the strength of the quadrupolar coupling with respect to the hyperfine interaction [160],

$$Q = \frac{\sum_k q_k}{\sum_k A_k}, \tag{2.21}$$

which we establish by adjusting the quadrupolar coupling constants q_k accordingly after drawing them randomly from a uniform distribution in the interval $[0.5; 1]$.

Chapter 3

Nuclear-spin polaron formation for Ising-type hyperfine interaction

The formation of a highly correlated nuclear spin state termed nuclear-spin polaron under optical cooling of the nuclei surrounding a localized electron spin was first predicted by Merkulov [66] in 1998 but has not been observed experimentally yet. However, the experimental efforts of cooling down the electron-nuclear spin system are ongoing [72, 73] as well as the related theoretical investigations [70, 71]. The nuclear-spin polaron state is characterized by a collective alignment of the nuclear spins in relation to the localized charge carrier spin, e.g., the opposite alignment indicated in Fig. 3.1. In this chapter, we introduce the concept of two differing effective spin temperatures for the charge carrier and the nuclei which accounts for the situation of the optical cooling of the nuclear spins. Moreover, we generalize the mean-field treatment employed by Merkulov to the case of a biaxial anisotropy of the hyperfine interaction, Eq. (2.11). Subsequently, we focus on the Ising limit of hyperfine interaction for a first analysis of the temperature dependence of the spin state. Kinetic rate equations for the system's distribution function applying to the two-temperature situation are derived and their steady state is evaluated: An analytic solution allows for the derivation of a temperature criterion for the polaron formation whereas the system with randomly distributed hyperfine coupling constants is addressed by a Monte Carlo simulation. Finally, the kinetics of the polaron formation are examined.

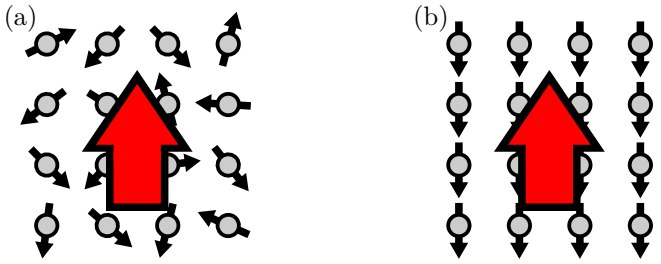

Figure 3.1: (a) Disordered spin state at high temperatures. (b) Nuclear-spin polaron state in the low temperature regime.

Most of the results in this chapter have been published in Refs. [198, 199] and have been obtained in equal parts by Andreas Fischer and the author of this thesis.

3.1 Two-temperature concept

For the theoretical description of the electron-nuclear spin system under the conditions of the optical cooling of the nuclear spins, a two-temperature concept [96, 97, 183] has proven useful [66, 73]. The introduction of an effective temperature of the nuclear spins which differs from the lattice temperature in the semiconductor is justified for a nuclear spin system that couples only weakly to the environment. At the same time, the spin-spin interactions among the nuclei such as dipole-dipole interactions have to be well pronounced. Under these circumstances, the nuclear spins adjust slowly to external influences whereas an equilibrium state within the nuclear spin system is rapidly established. The emerging quasiequilibrium state can be characterized by the occupation of spin states regarding their energy and an effective temperature T_n, i.e., the Boltzmann ratio $\exp(-(\varepsilon_m - \varepsilon_n)/k_B T_n)$ between the probabilities to find the nuclear spin system in the state with energy ε_m or ε_n retrospectively is respected in the quasiequilibrium situation. Here, k_B is the Boltzmann constant converting the effective nuclear spin temperature T_n to energy units. The effective temperature T_n might differ significantly from the lattice temperature: In an optically cooled nuclear spin system, T_n is considerably lower than the lattice temperature T_l [200, 201]. In contrast, the heating of the nuclear spin system is characterized by $T_n > T_l$. Typically, the sign of the effective spin temperature T_n is positive corresponding to a favoring of the states with low energy. Generally, the description by an effective temperature can also be extended to negative values of T_n accounting for a nonequilibrium density operator in which states of high energy are predominantly occupied. For the investigation of the nuclear-spin polaron state, however, the relevant temperature range conforms to positive values with $0 < T_n < T_l$.

In experiments, the cooling of the nuclear spins is achieved by elaborate optical protocols [66, 97]. The electron spin is optically oriented along an externally applied magnetic field. The electron spin polarization then is transmitted to the nuclear spin system via the hyperfine interaction which allows for generating a substantial polarization of the nuclei in direction of the external field under persistent optical excitation. Finally, the external magnetic field is adiabatically switched off such that the effective nuclear spin temperature is efficiently reduced. While the lattice temperature in experiments typically amounts to $T_l \approx 4$ K due to cooling with liquid helium, effective nuclear spin temperatures as low as 0.54 μK have been achieved in a GaAs/(Al,Ga)As quantum [201]. The mean-field critical temperature

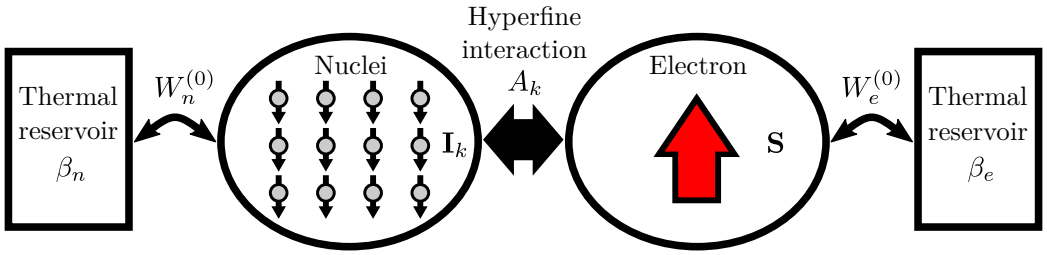

Figure 3.2: Two-temperature concept implemented by distinct thermal reservoirs coupled to the electron spin and the nuclear spin system respectively.

for nuclear-spin polaron formation estimated by Merkulov for a shallow donor in GaAs amounts to roughly 0.1 µK which in principle is deemed to be achievable in experiments [66].

For the theoretical approach via a rate equation formalism, we assume the two effective spin temperatures, $T_e \equiv T_l$ for the electron spin and T_n for the nuclear spins, to be installed via spin-flip coupling of the electron and nuclear spin system to two distinct thermal reservoirs and thereby allow for energy exchange with the environment, see Fig. 3.2. The microscopic origin of the spin interactions within the nuclear system is omitted and the strength of these effects is absorbed in a phenomenological rate W_n^0. Similarly, interactions of the electron spin such as the coupling to the lattice are incorporated in the reservoir-induced spin flips with a rate W_e^0. Due to the strong coupling of the electron spin to the environment, the electron spin flip rate is typically some orders of magnitude larger than the nuclear spin flip rate, $W_e^0 \gg W_n^0$. Since the coupling between the charge carrier spin and the nuclear spin bath is crucial for the polaron formation, the hyperfine interaction is taken into account explicitly in the theoretical description. Before introducing the rate equation formalism incorporating the full quantum fluctuations of the spins, we resort to a simplifying mean-field treatment of the nuclear-spin polaron formation first.

For brevity, we make use of the effective inverse spin temperatures, $\beta_e = 1/k_B T_e$ and $\beta_n = 1/k_B T_n$ in the following.

3.2 Mean-field approach

As a first step towards theoretical examination of the nuclear-spin polaron formation in the cooled electron-nuclear spin system, we explore a mean-field approach for the two-temperature situation. The mean-field treatment was employed in 1998 by

Merkulov when he first predicted the formation of the nuclear-spin polaron state below a critical temperature for the isotropic situation of a donor-bound electron [66]. Here, we generalize the approach to an arbitrary anisotropic hyperfine interaction captured by the Hamiltonian in Eq. (2.11).

The hyperfine interaction of a charge carrier with the surrounding nuclei may be interpreted as the coupling of the charge carrier spin to an effective magnetic field generated by the nuclear spins. The quantum mechanical average of this effective Overhauser field in the case of the anisotropic system, Eq. (2.11), is given by

$$\langle \mathbf{b}_N \rangle = \left(\lambda \sum_k A_k \langle I_k^x \rangle , \lambda \sum_k A_k \langle I_k^y \rangle , \sum_k A_k \langle I_k^z \rangle \right)^T \tag{3.1}$$

employing units of energy for measuring the field. Analogously, we introduce the effective magnetic field generated by the charge carrier spin that acts on the nuclear spin $\mathbf{I}_k$. This field is called the Knight field. Its average measured in energy units reads

$$\left\langle \mathbf{b}_{K,k} \right\rangle = \left(\lambda A_k \langle S^x \rangle , \lambda A_k \langle S^y \rangle , A_k \langle S^z \rangle \right)^T . \tag{3.2}$$

The Knight field includes the scaling of the hyperfine coupling within the (xy) plane by the anisotropy parameter λ, similarly to the definition of the Overhauser field, Eq. (3.1).

In the mean-field approach, the electron spin is subject to the average Overhauser field and a nuclear spin in turn experiences the average Knight field. Potential spin fluctuations are neglected. Assuming the charge carrier spin and the nuclear spins to be in thermal equilibrium at their respective temperatures, the standard quantum mechanical expectation value of a spin subject to an external magnetic field is applied,

$$\langle \mathbf{S} \rangle = -S \frac{\langle \mathbf{b}_N \rangle}{|\langle \mathbf{b}_N \rangle|} \tanh \left(\frac{\beta_e \, |\langle \mathbf{b}_N \rangle|}{2} \right) , \tag{3.3}$$

$$\langle \mathbf{I}_k \rangle = -I_k \frac{\left\langle \mathbf{b}_{K,k} \right\rangle}{\left| \left\langle \mathbf{b}_{K,k} \right\rangle \right|} \tanh \left(\frac{\beta_n \left| \left\langle \mathbf{b}_{K,k} \right\rangle \right|}{2} \right) . \tag{3.4}$$

The insertion of Eq. (3.4) into Eq. (3.3) provides the self-consistency equation for the average electron spin polarization $\langle \mathbf{S} \rangle$,

$$\begin{aligned} \langle \mathbf{S} \rangle = \frac{S}{|\langle \mathbf{b}_N \rangle|} \tanh \left(\frac{\beta_e \, |\langle \mathbf{b}_N \rangle|}{2} \right) \sum_k \frac{A_k^2 I_k}{\left| \left\langle \mathbf{b}_{K,k} \right\rangle \right|} \tanh \left(\frac{\beta_n \left| \left\langle \mathbf{b}_{K,k} \right\rangle \right|}{2} \right) \\ \times \left(\lambda^2 \langle S^x \rangle , \lambda^2 \langle S^y \rangle , \langle S^z \rangle \right)^T . \end{aligned} \tag{3.5}$$

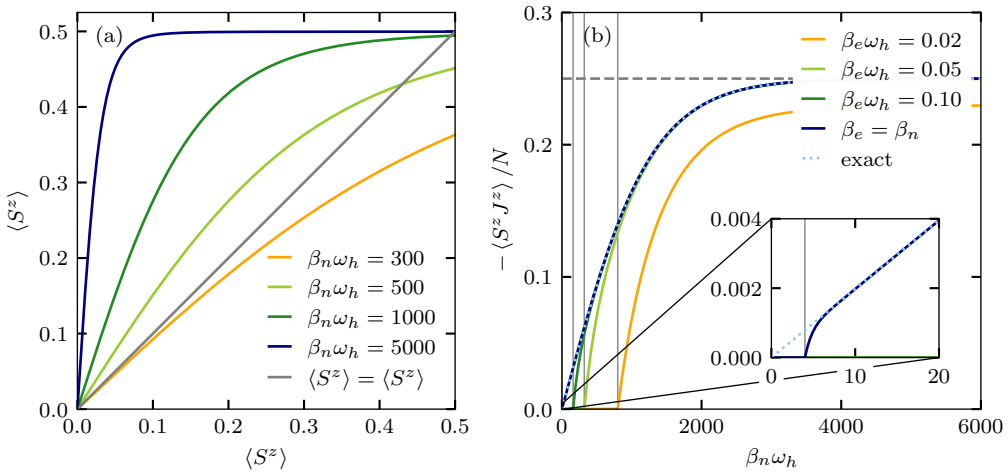

Figure 3.3: Mean-field approach to a system in the Ising limit of the hyperfine interaction, $\lambda = 0$ in Eq. (2.11), with $A_k \equiv A_0$ and $I_k \equiv 1/2$ for $k \in \{1, \ldots, N\}$, $N = 10^5$. (a) Right hand side of the self-consistency equation for $\langle S^z \rangle$, Eq. (3.5). At a fixed inverse electron spin temperature, $\beta_e\omega_h = 0.05$, the inverse nuclear spin temperature β_n determines whether an intersection point of the right hand side with the identity (gray line) exists with $\langle S^z \rangle \neq 0$. (b) Anticorrelation of the electron spin S^z and the total nuclear spin $J^z = \sum_k I_k^z$ as a function of the inverse effective nuclear spin temperature β_n at fixed values of the inverse electron spin temperature β_e. The exact solution in thermal equilibrium, $-\langle S^z J^z \rangle / N = \tanh(\beta A_0/4)/4$ with $\beta_e = \beta_n \equiv \beta$, is added for comparison (light blue dotted line).

Minding the definitions of the Overhauser field and the Knight field, the electron spin enters in $\langle \mathbf{b}_{K,k} \rangle$ and indirectly in $\langle \mathbf{b}_N \rangle$ via Eq. (3.4) as well.

The left hand and right hand side of the self-consistency equation for $\langle S^z \rangle$ in the Ising limit of the hyperfine interaction, $\lambda = 0$ in Eq. (2.11), are illustrated in Fig. 3.3(a) as an example. For high inverse spin temperatures β_e and β_n, a nontrivial solution with $\langle S^z \rangle \neq 0$ is found which we relate to the formation of a polaron state. As a reference scale for measuring the temperatures, we employ the frequency $\omega_h = (\sum_k A_k^2)^{1/2}$ which is proportional to the inverse of the dephasing time T^* of the electron spin in the disordered nuclear spin system assuming a fixed nuclear spin length, $I_k \equiv I$ for all k, cf. Eq. (2.18). In the case of equal hyperfine coupling constants, $A_k \equiv A_0$ for all nuclei, as employed for Fig. 3.3, this reference frequency simplifies to $\omega_h = \sqrt{N A_0^2}$.

As a result of the biaxiality in the general hyperfine Hamiltonian, Eq. (2.11), it is convenient to rewrite the self-consistency equation for $\langle \mathbf{S} \rangle$ in spherical coordinates where the azimuth angle $\theta \in [0; \pi]$ is measured with respect to the z axis. Since

the polar angle within the (xy) plane does not play an important role due to the rotational symmetry of the system, it is disregarded in the following.

To establish the critical temperature for the nuclear-spin polaron formation, we first focus on the absolute value $|\langle \mathbf{S} \rangle|$ and address the orientation of the spin state afterwards. As the right hand side of the self-consistency equation, Eq. (3.5), is a concave function, it is instructive to study its first order derivative to determine if a nontrivial solution with $|\langle \mathbf{S} \rangle| \neq 0$ corresponding to the formation of a polaron state exists. Close to the critical temperature, the spin polarization is very small: $\tanh x \approx x$ for $x \ll 1$. Expanding Eq. (3.5) yields

$$|\langle \mathbf{S} \rangle| = \frac{S\beta_e}{2} \sum_k \frac{A_k^2 I_k \beta_n}{2} \sqrt{\lambda^4 \sin^2\theta + \cos^2\theta}\, |\langle \mathbf{S} \rangle| \,. \tag{3.6}$$

Thus, a state with nonzero electron spin polarization and therefore nonvanishing nuclear spin polarization can form when the condition

$$\beta_e \beta_n > \frac{4}{S \sum_k A_k^2 I_k \sqrt{\lambda^4 \sin^2\theta + \cos^2\theta}} \tag{3.7}$$

is fulfilled. The above criterion indicates that the orientation of the polaron state with respect to the z axis enters the definition of the critical temperatures in combination with the anisotropy parameter λ.

The angle θ of the polaron formation is evaluated by means of its self-consistency equation resulting from Eq. (3.5). To set up the self-consistency equation for θ, we employ the relation $\left(\langle S^x \rangle^2 + \langle S^y \rangle^2\right) / \langle S^z \rangle^2 = \tan^2\theta$ where we insert the spin expectation values $\langle S^\alpha \rangle$ according to the left hand and the right hand side of Eq. (3.5) respectively requesting that the two sides are parallel. The resulting self-consistency equation for θ,

$$\tan^2\theta = \lambda^4 \tan^2\theta, \tag{3.8}$$

is fulfilled by different angles θ depending on the value of the hyperfine anisotropy parameter λ.

For $|\lambda| = 1$, the relation holds for any angle $\theta \in [0; \pi]$. Naturally, in a system with isotropic hyperfine interaction, $\lambda = 1$, the nuclear-spin polaron state forms isotropically, and the charge carrier spin $\langle \mathbf{S} \rangle$ is oriented randomly on the sphere with radius S. The sign of the parameter λ does not affect the value of the hyperfine energy but only defines whether a parallel or antiparallel alignment of the electron spin and the nuclear spins within the (xy) plane is energetically favorable. Hence, a similar situation as for $\lambda = 1$ is realized for $\lambda = -1$. The electron spin is oriented randomly on the S sphere in both cases. However, for $\lambda = 1$, the nuclear spin expectation values $\langle I_k^x \rangle$ and $\langle I_k^y \rangle$ will have the opposite sign of $\langle S^x \rangle$ and $\langle S^y \rangle$

respectively, whereas for $\lambda = -1$ the nuclear spin components will have the same sign as the electron spin.

At $|\lambda| \neq 1$, the self-consistency equation, Eq. (3.8), is consistent with three angles: $\theta = 0$ and $\theta = \pi$ related to the spin orientation along the z axis as well as $\theta = \pi/2$ corresponding to a spin orientation within the (xy) plane. To perform a stability analysis of the three solutions in dependence of the hyperfine anisotropy parameter λ, we rewrite Eq. (3.8),

$$\theta = \arctan\left(\pm\lambda^2 \tan\theta\right) \tag{3.9a}$$

$$\approx \pm\, \lambda^2\theta, \tag{3.9b}$$

where we applied a Taylor expansion for small arguments in the second line of the equation, $\tan x \approx x$ and $\arctan x \approx x$. Accordingly, a small perturbation δ to the point $\theta = 0$ will grow for $\lambda^2 > 1$ indicating an unstable fix point, whereas the fix point is stable for $\lambda^2 < 1$. For examination of the angle $\theta = \pi$, we make use of the relation $\tan(\pi + x) = \tan x$ and thereby obtain the same result as for $\theta = 0$: The fix point $\theta = \pi$ is unstable for $\lambda^2 > 1$ and is stable otherwise. The third angle fulfilling Eq. (3.8), $\theta = \pi/2$, is inspected using an alternate form of the self-consistency equation. Instead of $\tan\theta$ entering Eq. (3.8), we employ the relation $\cot^2\theta = \langle S^z\rangle^2 / \left(\langle S^x\rangle^2 + \langle S^y\rangle^2\right)$ and analogously obtain

$$\cot^2\theta = \lambda^{-4}\cot^2\theta. \tag{3.10}$$

The rewriting of the equation and a subsequent Taylor expansion for $\theta \approx \pi/2$, $\cot(\pi/2 + x) \approx -x$ and $\operatorname{arccot} x \approx \pi/2 - x$ for small x, yield

$$\theta = \operatorname{arccot}\left(\pm\lambda^{-2}\cot\theta\right) \tag{3.11a}$$

$$\approx \frac{\pi}{2} \mp \lambda^{-2}\left(\frac{\pi}{2} - \theta\right). \tag{3.11b}$$

Hence, a small perturbation δ to the fix point $\theta = \pi/2$ produces $\pi/2 + \delta \approx \pi/2 \pm \lambda^{-2}\delta$. Accordingly, the fix point $\theta = \pi/2$ is stable for $\lambda^2 > 1$ and is unstable for $\lambda^2 < 1$.

In summary, the mean-field approach predicts the formation of a nuclear-spin polaron state below a critical temperature in that direction in which the hyperfine interaction, Eq. (2.11), is strongest: For an anisotropy parameter with $|\lambda| < 1$, the hyperfine interaction along the z axis predominates such that the polaron state is oriented along this axis. At $|\lambda| = 1$, the strength of the hyperfine interaction is equal in any direction and the forming polaron state is isotropic. For $|\lambda| > 1$, the transversal hyperfine coupling is enhanced and the nuclear-spin polaron forms isotropically within the (xy) plane. As a consequence, the critical temperature below

which the nuclear-spin polaron state forms depends on the hyperfine anisotropy of the system. The product of the inverse critical temperatures,

$$\beta_{e,c}\beta_{n,c} = \frac{4}{S\sum_k A_k^2 I_k} \times \begin{cases} 1, & |\lambda| \leq 1, \\ \lambda^{-2}, & |\lambda| > 1, \end{cases} \tag{3.12}$$

shifts the temperature regime of the polaron formation to higher spin temperatures for $|\lambda| > 1$.

The mean-field results will be employed as a reference from time to time in Chapters 3 and 4. Here, we exemplarily present the mean-field data for the electron-nuclear spin correlator in a system with Ising-type hyperfine interaction, $\lambda = 0$. Since the related hyperfine Hamiltonian contains only the coupling of the spin z components of the electron and the nuclei, an anticorrelation of the electron spin S^z and the total nuclear spin $J^z = \sum_k I_k^z$ arises at low temperatures (for $A_k > 0$). This anticorrelation is directly connected to the polaron formation. Figure 3.3(b) displays the anticorrelation, $-\langle S^z J^z \rangle / N$ as a function of the effective inverse nuclear spin temperature β_n for fixed values of the inverse electron spin temperature β_e. The critical values $\beta_{n,c}$ of the inverse nuclear spin temperature according to Eq. (3.12), that result for the respective value of the inverse electron spin temperature, are indicated by vertical gray lines. Below the inverse critical temperature, the correlator yields $\langle S^z J^z \rangle = 0$, since no nontrivial solution of Eq. (3.5) with $\langle S^z \rangle \neq 0$ exists. When cooling the nuclear spins, $\beta_n > \beta_{n,c}$, the electron-nuclear spin anticorrelation related to the polaronic state forms with a square-root like behavior in the vicinity of the critical temperature.

For comparison, Fig. 3.3(b) also presents the exact quantum mechanical solution of $-\langle S^z J^z \rangle / N$ in the case of equal temperatures $\beta_e = \beta_n \equiv \beta$ (light blue dotted line). In thermal equilibrium, the density operator obeys the Boltzmann distribution, $\rho = \exp(-\beta H_{\mathrm{HF}})/Z$ with the partition function Z, from which the exact expectation value of the electron-nuclear spin anticorrelation is calculated. The comparison of the mean-field solution for $\beta_e = \beta_n$ (dark blue line) to the exact quantum mechanical solution reveals a significant discrepancy. Where the mean-field approach predicts critical behavior, the spin system actually displays a smooth crossover provided by the exact quantum mechanical result. Clearly, the mean-field treatment fails in this temperature regime calling for a more sophisticated description of the spin system covering the thermal equilibrium situation with equal temperatures as well as the formation of the polaronic state at effective nuclear spin temperatures well below the lattice temperature.

3.3 Kinetic rate equation formalism

A theoretical description of the nuclear-spin polaron formation beyond the mean-field approximation is provided by a kinetic rate equation formalism for the electron-nuclear spin system that includes quantum fluctuations of the electron spin as well as fluctuations in the nuclear spin system. In this formalism, the effective spin temperatures T_e and T_n are established by coupling the electron spin and the nuclear spins to two separate reservoirs inducing the respective temperatures. The rate equations govern the temporal evolution of the diagonal elements of the density operator in the eigenbasis of the hyperfine Hamiltonian and are valid over a broad range of temperatures. The formalism presented in this section proves especially valuable for capturing the system in the Ising limit of the hyperfine interaction relevant for a heavy hole spin since it enables access to all relevant spin observables in this situation. A generalized Lindblad formalism including an arbitrary anisotropic hyperfine interaction is derived in Chapter 4.

For a general introduction to the concept of realizing the two-temperature situation by external reservoirs, we focus on the electron-nuclear spin system with the general hyperfine interaction H_{HF}, Eq. (2.1), and add perturbations for the electron spin and the nuclear spins, respectively. These perturbations stem from randomly fluctuating effective magnetic fields, which are provided by the electron spin-lattice coupling or the nuclear dipole-dipole interactions for example,

$$V_e = B_0 \sum_{\alpha} B^{\alpha} S^{\alpha}, \tag{3.13a}$$

$$V_n = b_0 \sum_{k} \sum_{\alpha} b_k^{\alpha} I_k^{\alpha}. \tag{3.13b}$$

The effective magnetic fields are denoted by dimensionless operators B^{α} (for the electron) and b_k^{α} (for the nuclei) where $\alpha \in \{x, y, z\}$ refers to the Cartesian axis. The coupling strength is controlled by dimensionless constants B_0 and b_0, respectively. We assume that the standard spin relations hold for the operators of the effective fields,

$$\left[b_k^{\alpha}, b_{k'}^{\beta}\right] = i\delta_{k,k'}\epsilon_{\alpha,\beta,\gamma} b_k^{\gamma}, \tag{3.14a}$$

$$\left[B^{\alpha}, B^{\beta}\right] = i\epsilon_{\alpha,\beta,\gamma} B^{\gamma}, \tag{3.14b}$$

$$\left[b_k^{\alpha}, B^{\beta}\right] = 0, \tag{3.14c}$$

where $\delta_{k,k'}$ is the Kronecker delta and $\epsilon_{\alpha,\beta,\gamma}$ the Levy-Civita symbol. Since the fields acting on different spins commute, no interference effects between V_e and V_n occur.

As a next step, we address transitions between the eigenstates of the hyperfine Hamiltonian, Eq. (2.1), induced by the perturbations V_e and V_n. Let us denote the eigenstates by $|\psi_m\rangle$ and the related eigenenergies by ε_m, $H_{\mathrm{HF}}|\psi_m\rangle = \varepsilon_m|\psi_m\rangle$, with $m \in \{1, \ldots, d\}$ in the range of the Hilbert space dimension d. The transition rate between the eigenstates $|\psi_n\rangle$ and $|\psi_m\rangle$ with energy difference $\Delta\varepsilon = \varepsilon_m - \varepsilon_n$ is derived according to Fermi's golden rule under the assumption of weak perturbations,

$$W_{i,mn} = \sum_{R_i,Q_i} \sum_{\Delta\varepsilon=-\Delta E} \frac{2\pi}{Z_i} \exp\left(\beta_i E_{R_i}\right) |\langle Q_i| \langle\psi_m|V_i|\psi_n\rangle |R_i\rangle|^2 \tag{3.15}$$

with $i \in \{e, n\}$ distinguishing between the electron and the nuclear spin system. The reservoir eigenstates $|R_i\rangle$ and $|Q_i\rangle$ have an energy difference $\Delta E = E_{Q_i} - E_{R_i}$ matching $-\Delta\varepsilon$. The partition function of the respective reservoir is Z_i.

The rate equation for a diagonal element of the density operator in the eigenbasis of H_{HF}, $f_m = \langle\psi_m|\rho|\psi_m\rangle$, reads

$$\partial_t f_m = \sum_i \sum_n \left(W_{i,mn} f_n - W_{i,nm} f_m\right), \tag{3.16}$$

taking into account potential transitions between the eigenstate $|\psi_m\rangle$ and any other eigenstate $|\psi_n\rangle$ that are generated by the fluctuations of the electron spin ($i = e$) and the nuclear spins ($i = n$). The ratio of the rates for a specific transition and the related reversed transition,

$$\frac{W_{i,mn}}{W_{i,nm}} = \exp\left(\beta_i \left(\varepsilon_m - \varepsilon_n\right)\right), \tag{3.17}$$

guarantees that the steady-state distribution in the thermodynamic equilibrium $\beta_e = \beta_n \equiv \beta$ is given by $f_m = \exp\left(-\beta\varepsilon_m\right)/Z$ with the system's partition function Z.

3.3.1 Ising limit of the hyperfine interaction

In the Ising limit of the hyperfine interaction, $\lambda = 0$, the hyperfine Hamiltonian, Eq. (2.11), reduces to

$$H_{\mathrm{Is}} = \sum_k A_k S^z I_k^z. \tag{3.18}$$

Since the Ising Hamiltonian commutes with the electron and nuclear spin z component respectively, $[H_{\mathrm{Is}}, S^z] = [H_{\mathrm{Is}}, I_k^z] = 0$, the energy eigenbasis can be expressed by direct product states $|S^z\rangle|\{I_k^z\}\rangle$ with related eigenenergies $\varepsilon(S^z, \{I_k^z\}) = S^z \sum_k A_k I_k^z$. Accordingly, the diagonal elements of the density operator in the eigenbasis are collated into the distribution function $f(S^z, \{I_k^z\})$.

For simplicity, the individual nuclear spins are attributed a spin length $I_k \equiv I \equiv 1/2$ in the following. Then, the rate equations specified for the Ising limit of the hyperfine interaction read

$$\begin{aligned}\partial_t f(S^z, \{I_k^z\}) =& W_e(-S^z, \{I_k^z\}) f(-S^z, \{I_k^z\}) - W_e(S^z, \{I_k^z\}) f(S^z, \{I_k^z\}) \\ &+ \sum_{k'} \left[W_{k'}(S^z, -I_{k'}^z) f(S^z, \{I_1^z, \dots, -I_{k'}^z, \dots, I_N^z\}) \right. \\ &\left. - W_{k'}(S^z, I_{k'}^z) f(S^z, \{I_k^z\}) \right]. \end{aligned} \tag{3.19}$$

The dynamics of the distribution function $f(S^z, \{I_k^z\})$ is governed by individual spin flip rates $W_e(S^z, \{I_k^z\})$ and $W_{k'}(S^z, I_{k'}^z)$ for the electron spin and the nuclear spin due to the coupling to separate reservoirs. The rates for a specific transition in the distribution function are determined by the energy difference between the final and initial state connected by the spin flip as well as the temperature associated with the related reservoir. We introduce the phenomenological flip rate W_e^0 for transitions produced by electron spin flips that reduce the system's energy. In comparison, energetically unfavorable transitions that increase the energy are exponentially suppressed when decreasing the effective electron spin temperature,

$$W_e(S^z, \{I_k^z\}) = W_e^0 \times \begin{cases} 1, & \varepsilon(S^z, \{I_k^z\}) > 0, \\ \exp\left(-\beta_e \left|\sum_k A_k I_k^z\right|\right), & \text{else.} \end{cases} \tag{3.20}$$

For determining, whether the electron spin flip decreases or increases the energy of the system, the sign of the eigenenergy $\varepsilon(S^z, \{I_k^z\})$ of the initial state is decisive since the spin flip changes the sign of the energy but not the absolute value. The energy decreases through the electron spin flip for an initial energy $\varepsilon(S^z, \{I_k^z\}) > 0$. The opposite case, $\varepsilon(S^z, \{I_k^z\}) < 0$, is related to an energy increase. Here, the flip rate is reduced by a factor of the exponential function of the product of the inverse effective spin temperature β_e and the energy difference produced by the flip, $\left|\sum_k A_k I_k^z\right|$.

Analogously, the flip rate for the nuclear spin with index k' due to the coupling to the reservoir with the inverse temperature β_n is established,

$$W_{k'}(S^z, I_{k'}^z) = W_n^0 \times \begin{cases} 1, & A_{k'} S^z I_{k'}^z > 0, \\ \exp\left(-\beta_n \left|A_{k'} S^z\right|\right), & \text{else.} \end{cases} \tag{3.21}$$

For transitions reducing the energy, which are characterized by $A_{k'} S^z I_{k'}^z > 0$, we introduce the phenomenological rate W_n^0. Energetically unfavorable transitions are exponentially suppressed where the inverse nuclear spin temperature β_n and the energy difference generated by the nuclear spin flip enter the exponential function. We note that the rate for flipping the nuclear spin k' is independent of the state of the remaining nuclear spins and depends on the electron spin alone.

3.3.2 Analytical treatment

Analytic access to the steady-state solution of the rate equations, Eq. (3.19), is provided by a simplifying assumption about the hyperfine coupling constants. To this end, we assume the coupling constants A_k to be identical for all nuclear spins, i.e., we set $A_k \equiv A_0$ for all nuclei k. This approach is referred to as the box model approximation [93]. We lift this assumption again in Sec. 3.6 where the effect of a realistic distribution of the hyperfine coupling constants on the polaron formation is discussed. The box model approximation allows for rewriting the hyperfine Hamiltonian in terms of the total nuclear spin $J^z = \sum_k I_k^z$,

$$H_{\mathrm{Is,box}} = A_0 S^z J^z. \tag{3.22}$$

Thus, the energy eigenstates $|S^z\rangle\,|\{I_k^z\}\rangle$ related to the same quantum number J^z are degenerate and it becomes useful to introduce the distribution function $g(S^z, J^z)$ that does not depend on the individual nuclear spins but J^z instead. The kinetic rate equations for $g(S^z, J^z)$ reduce to

$$\begin{aligned}\partial_t g(S^z, J^z) =& W_e(-S^z, J^z) g(-S^z, J^z) - W_e(S^z, J^z) g(S^z, J^z) \\ &+ \sum_{\tau=\pm 1} \left[W_n^\tau(S^z, J^z - \tau) g(S^z, J^z - \tau) - W_n^\tau(S^z, J^z) g(S^z, J^z) \right].\end{aligned} \tag{3.23}$$

The electron spin flip enters analogously to Eq. (3.19), whereas the flips of the individual nuclear spins are replaced by the increase or reduction in the total spin J^z of $\tau = \pm 1$. Correspondingly, the transition rates related to the electron and nuclear spin flips, Eqs. (3.20) and (3.21), are adjusted to the box model eigenstates,

$$W_e(S^z, J^z) = W_e^0 \times \begin{cases} 1, & A_0 S^z J^z > 0, \\ \exp\left(-\beta_e \left|A_0 J^z\right|\right), & \text{else}, \end{cases} \tag{3.24}$$

$$W_n^\tau(S^z, J^z) = W_n^0 N_{-\tau}(J^z) \times \begin{cases} 1, & -\tau A_0 S^z > 0, \\ \exp\left(-\beta_n \left|A_0\right|/2\right), & \text{else}, \end{cases} \tag{3.25}$$

where the index τ distinguishes between a nuclear spin flipping up ($\tau = +1$) and a nuclear spin flipping down ($\tau = -1$). The number $N_{+1}(J^z)$ of nuclear spins in the spin up state or $N_{-1}(J^z) = N - N_{+1}(J^z)$ for the number of nuclear spins in the spin down state that contribute to the respective transition has to be incorporated in the rate $W_n^\tau(S^z, J^z)$.

For further simplification of the rate equations, we make use of the difference in magnitude of the electron and nuclear spin flip rate, $W_e^0 \gg W_n^0$, cf. Sec. 3.1. When the electron spin flips occur at a much faster rate than the spin flips in the nuclear

spin bath, the nuclear spins can be approximated as frozen on the time scale of the electron spin flips. Thus, the occupation of the two electron spin states for a fixed nuclear spin state with the quantum number J^z instantaneously adjusts according to the steady-state distribution with Boltzmann ratio,

$$\frac{g(1/2, J^z)}{g(-1/2, J^z)} = \exp(-\beta_e A_0 J^z). \tag{3.26}$$

Hence, it is useful to introduce the nuclear distribution function,

$$g(J^z) = g(1/2, J^z) + g(-1/2, J^z), \tag{3.27}$$

where the electron spin states have been amalgamated. The kinetic rate equations for the nuclear distribution function $g(J^z)$ result from Eq. (3.23) taking into account the thermal spin flip rates, Eqs. (3.24) and (3.25),

$$\partial_t g(J^z) = \sum_{\tau=\pm 1} \left[\Gamma^\tau(J^z - \tau) g(J^z - \tau) - \Gamma^\tau(J^z) g(J^z) \right]. \tag{3.28}$$

The rate for transitions between states with quantum numbers $J^z - \tau$ and J^z results from the combination of all contributions of a nuclear spin flipping up ($\tau = +1$) or down ($\tau = -1$) according to Eq. (3.23),

$$\Gamma^\tau(J^z) = W_n^0 N_{-\tau}(J^z) \frac{\cosh(\beta_e A_0 J^z/2 + \tau \beta_n A_0/4)}{\cosh(\beta_e A_0 J^z/2) + \exp(\beta_n A_0/4)}. \tag{3.29}$$

The terms for the electron spin flips associated with $g(J^z, 1/2)$ and $g(J^z, -1/2)$ cancel out. As a result, the total transition rate $\Gamma^\tau(J^z)$ above is produced by nuclear spin flip processes only, while the electron spin temperature enters via the Boltzmann ratio of the occupation of the electron spin states at a fixed value of J^z.

Finally, the analytic solution for the steady state, $\partial_t g(J^z) = 0$, can be obtained from the condition of detailed balance between states with neighboring quantum numbers J^z and $J^z + 1$,

$$g(J^z)\Gamma^{(+1)}(J^z) = g(J^z + 1)\Gamma^{(-1)}(J^z), \tag{3.30}$$

which guarantees that the transition from J^z to $J^z + 1$ and the reverse transition are in equilibrium. Rearranging the condition and inserting the transition rate, Eq. (3.29), provides an explicit expression for the occupation ratio of neighboring nuclear spin states,

$$\begin{aligned} \frac{g(J^z + 1)}{g(J^z)} =& \frac{N/2 - J^z}{N^2 + J^z + 1} \times \frac{\cosh(\beta_e A_0 (J^z + 1)/2)}{\cosh(\beta_e A_0 J^z/2)} \\ & \times \frac{\cosh(\beta_n A_0/4 + \beta_e A_0 J^z/2)}{\cosh(\beta_n A_0/4 - \beta_e A_0 (J^z + 1)/2)}. \end{aligned} \tag{3.31}$$

This expression in combination with the normalization,

$$\sum_{J^z=-N/2}^{N/2} g(J^z) = 1, \tag{3.32}$$

allows for direct access to the steady-state nuclear distribution function $g(J^z)$. The probability ratio between the electron spin states results from Eq. (3.26) and the full distribution function $g(S^z, J^z)$ of the electron-nuclear spin system is established. In the following sections, we apply this analytic approach to study the nuclear-spin polaron formation depending on the two effective spin temperatures. Later on, we will also address a realistic distribution of the hyperfine coupling constants by a Monte Carlo method and examine the temporal evolution governed by the rate equations.

3.4 Indicators of nuclear-spin polaron formation

The correlation between the electron spin and the nuclear spins has proven a useful indicator for the formation of the nuclear-spin polaron state, cf. Sec. 3.2. In terms of the previously outlined formalism, the steady-state expectation value of a general spin observable O is calculated by

$$\langle O \rangle = \sum_{S^z} \sum_{\{I_k^z\}} f(S^z, \{I_k^z\}) \langle S^z | \langle \{I_k^z\} | O | \{I_k^z\} \rangle | S^z \rangle , \tag{3.33}$$

where the steady-state distribution function of the kinetic equations, Eq. (3.19), is inserted for $f(S^z, \{I_k^z\})$. Here, we identify $O \equiv S^z J^z$ and exploit that the sum over the nuclear spin states $\{I_k^z\}$ in Eq. (3.33) reduces to a sum over the quantum number J^z for the box model limit. Since the hyperfine coupling constants are positive, the correlator $\langle S^z J^z \rangle$ will be negative at low temperatures such that we address the anticorrelation per nuclear spin, $-\langle S^z J^z \rangle / N$, in the following. The steady-state expectation value of the electron-nuclear anticorrelation as a function of the inverse electron and nuclear spin temperatures, β_e and β_n, is depicted in Fig. 3.4(a). We note that the inverse temperatures are measured with respect to the hyperfine coupling, $\omega_h = (\sum_k A_k^2)^{1/2} \equiv (N A_0)^{1/2}$, as introduced in Sec. 3.2. The system size with $N = 10^5$ nuclear spins is set to a realistic value based on the number of nuclear spins in the electron spin localization volume. The results in Fig. 3.4(a) clearly indicate the formation of the polaron state at low temperatures. In the low temperature regime (large β_e and β_n), the anticorrelation approaches the maximum value of one quarter per nuclear spin (yellow color coding) due to the opposite alignment of the electron spin and the nuclear spins with respective length 1/2.

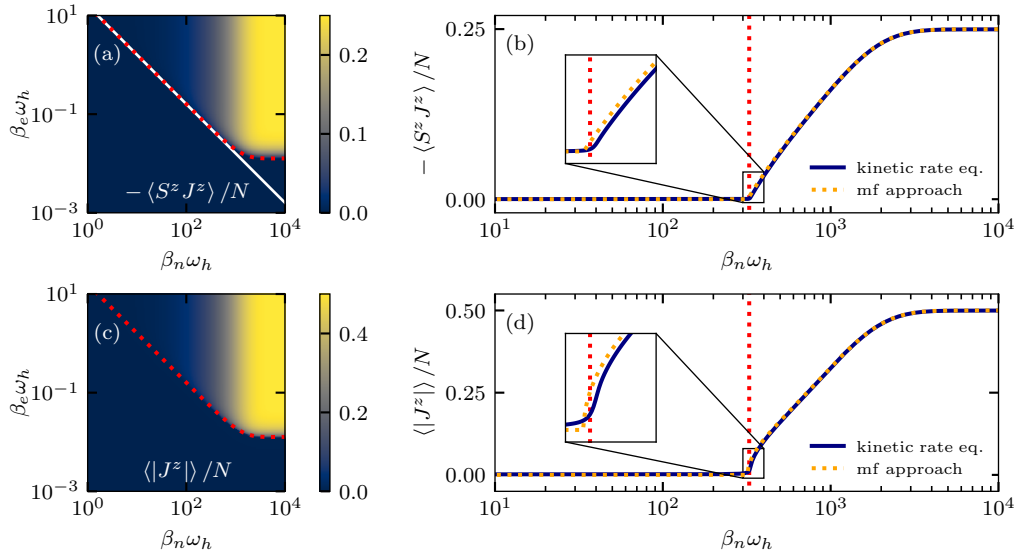

Figure 3.4: Steady-state results of the kinetic rate equations, Eq. (3.23), for a system with $N = 10^5$ nuclear spins depending on the inverse electron and nuclear spin temperatures. (a) Anticorrelation of the electron and nuclear spin z component color-coded in the (β_n, β_e) plane. (b) Electron-nuclear anitcorrelation as a function of β_n at a fixed inverse electron spin temperature, $\beta_e\omega_h = 0.05$. (c) Absolute value of the total nuclear spin z component in the (β_n, β_e) plane. (d) Horizontal cut through panel (c) at $\beta_e\omega_h = 0.05$. The crossover temperature according to Eq. (3.41) is indicated by a red dotted line respectively. Mean-field results are added for comparison in the left hand panels. The mean-field critical temperature is indicated by the white line in panel (a). The figure is taken from Ref. [198].

At high temperatures, the spins are randomly oriented such that $-\langle S^z J^z\rangle/N = 0$ (blue color coding).

The crossover from the disordered high-temperature state to the correlated polaronic state in the cooled system is resolved by the anticorrelation $-\langle S^z J^z\rangle/N$ as a function of the inverse nuclear spin temperature β_n for a fixed value of the inverse electron temperature $\beta_e\omega_h = 0.05$ even more clearly, see Fig. 3.4(b). The steady-state results obtained from the kinetic rate equations display similar behavior as the mean-field data, cf. Fig. 3.3, at the presented temperatures. Close to the mean-field critical temperature, see the inset in Fig. 3.4(b), however, the two approaches slightly differ. The mean-field approach predicts the critical behavior of the system with a sharp transition to the polaron state at the critical temperature,

$$\beta_{e,c}\beta_{n,c} = \frac{16}{NA_0^2}, \tag{3.34}$$

according to Eq. (3.12). At $\beta_e\omega_h = 0.05$, this corresponds to $\beta_{n,c}\omega_h = 320$. In contrast, the kinetic equation formalism yields a smooth crossover as expected for a finite system where a phase transition is naturally absent.

We note that the close agreement of the steady-state results of the kinetic rate equations and the mean-field predictions only holds for the temperature range presented in Fig. 3.4(b): While the results of the approaches resemble each other for differing electron and nuclear spin temperatures, $\beta_e < \beta_n$, they deviate for similar temperatures, $\beta_e \approx \beta_n$. At equal temperatures of the electron and nuclear spins, $\beta_e = \beta_n$, the mean-field treatment indicates critical behavior, cf. Fig. 3.3(b), whereas the kinetic equations reproduce the exact quantum mechanical result providing a smooth increase in the electron-nuclear spin anticorrelation which is a direct consequence of the construction of the flip rates, Eq. (3.17). Moreover, we expect deviations of the two approaches for $\beta_e \ll \beta_n$ as the mean-field treatment neglects the electron spin fluctuations which become relevant at large electron spin temperatures.

A further suitable quantity to indicate the formation of the nuclear-spin polaron state is the expectation value of the absolute value of the total nuclear spin z component. We introduce this expectation value as the sum

$$\langle |J^z| \rangle = \sum_{J^z} g(J^z)\, |J^z| \tag{3.35}$$

with $J^z \in \{-N/2, \ldots, N/2\}$. Alternatively, the expectation value $\langle |J^z| \rangle$ is obtained from the symmetry broken distribution function,

$$g_+(J^z) = [g(J^z) + g(-J^z)]\, \theta(J^z) \tag{3.36}$$

with the Heaviside function $\theta(J^z)$. Inserting the distribution function $g_+(J^z)$ into Eq. (3.33) with $O \equiv J^z$ for the evaluation of the related nuclear spin z polarization, we obtain $\langle |J^z| \rangle = \langle J^z \rangle_+$. In literature [70, 202, 203], the quantity $\langle |J^z| \rangle$ frequently is employed to inspect the polarization in a finite system where a spontaneous symmetry breaking naturally does not arise, i.e., where consistently $\langle J^z \rangle = 0$ without external symmetry breaking field.

The data for the steady-state polarization per nuclear spin, $\langle |J^z| \rangle / N$, as a function of the inverse temperatures β_e and β_n is displayed in Fig. 3.4(c). The results closely resemble those of the electron-nuclear spin anticorrelation in Fig. 3.4(a). In the low temperature range, the maximum value $\langle |J^z| \rangle / N = 1/2$ (yellow color coding) determined by the nuclear spin length forms similarly to the buildup of the electron-nuclear spin anticorrelation. However, the details of the behavior close to the mean-field critical temperature differ for the two quantities. The comparison of $-\langle S^z J^z \rangle / N$ and $\langle |J^z| \rangle / N$ as a function of β_n at the fixed inverse electron spin

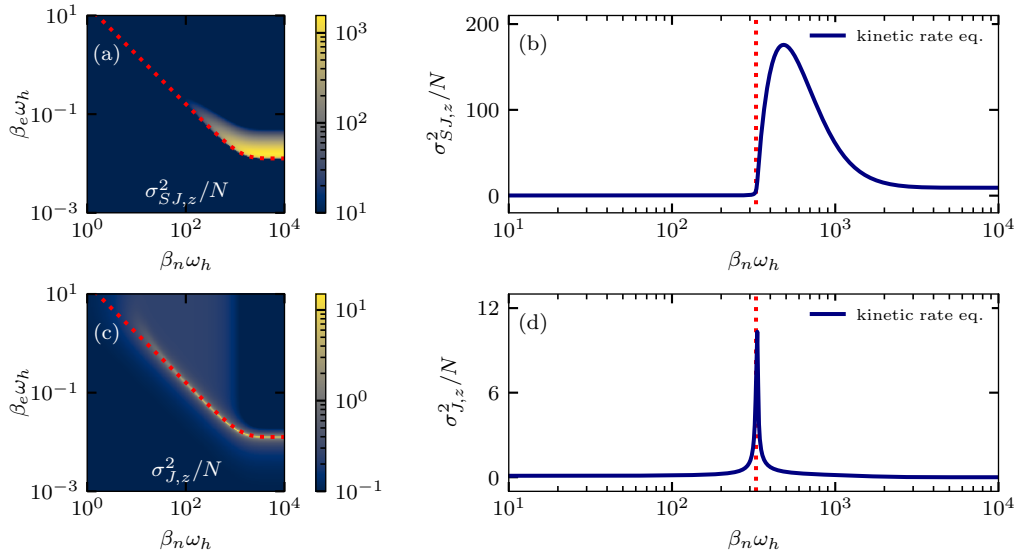

Figure 3.5: Steady-state results for the fluctuations $\sigma^2_{SJ,z}$ [panels (a) and (b)] and $\sigma^2_{J,z}$ [panels (c) and (d)] obtained from the kinetic rate equations, Eq. (3.23), for a system with $N = 10^5$ nuclear spins. (a) and (c): Fluctuations depending on the inverse electron and nuclear spin temperature, β_e and β_n. (b) and (d): Fluctuations as a function of β_n at a fixed inverse electron temperature $\beta_e\omega_h = 0.05$. The crossover temperature according to Eq. (3.41) is indicated by a red dotted line respectively. The figure is taken from Ref. [198].

temperature $\beta_e\omega_h = 0.05$, see Figs. 3.4(b) and 3.4(d) respectively, reveals different dependencies. The electron-nuclear spin anticorrelation exhibits a linear growth when decreasing the nuclear spin temperature starting at the mean-field critical temperature, whereas the absolute value of the nuclear spin polarization obeys a square-root like behavior. These dependencies can be derived from the mean-field results that yield

$$\langle S^z \rangle, \langle J^z \rangle \propto \sqrt{\beta_e\beta_n - \frac{16}{NA_0^2}} \tag{3.37}$$

for the individual spin z components close to the critical temperature and, therefore,

$$\langle S^z J^z \rangle \propto \left(\beta_e\beta_n - \frac{16}{NA_0^2}\right) \tag{3.38}$$

for the electron-nuclear spin correlation.

As an indicator for the crossover temperature, below which the nuclear-spin polaron

state forms, we examine the fluctuations of the two quantities, $\langle S^z J^z \rangle$ and $\langle |J^z| \rangle$,

$$\sigma^2_{SJ,z} = \left\langle (S^z J^z)^2 \right\rangle - \langle S^z J^z \rangle^2 , \tag{3.39}$$

$$\sigma^2_{J,z} = \left\langle (J^z)^2 \right\rangle - \langle |J^z| \rangle^2 . \tag{3.40}$$

The temperature dependence of the steady-state fluctuations obtained from the rate equation formalism for a spin system consisting of $N = 10^5$ nuclear spins is presented in Fig. 3.5. Since the correlator $\left\langle (S^z J^z)^2 \right\rangle$ is proportional to the hyperfine energy of the system, its fluctuations $\sigma^2_{SJ,z}$ correspond to the heat capacity in thermal equilibrium $\beta_e = \beta_n \equiv \beta$ except for a temperature-dependent prefactor. The Landau theory of phase transitions [204] predicts a step-like behavior at the critical temperature for the heat capacity as a function of β, which is reflected by the fluctuations $\sigma^2_{SJ,z}/N$ in the two-temperature situation, see Figs. 3.5(a) and 3.5(b). The fluctuations $\sigma^2_{SJ,z}/N$ rapidly grow, where a nonzero correlation of the electron spin and the nuclear spins emerges, cf. Figs. 3.4(a) and 3.4(b). The fluctuations $\sigma^2_{J,z}/N$ of the absolute value of the total nuclear spin z component presented in Figs. 3.5(c) and 3.5(d) can be interpreted by means of an effective finite-system susceptibility. In case of equal temperatures, $\beta_e = \beta_n \equiv \beta$, the fluctuations of $\langle |J^z| \rangle$ are proportional to the nuclear susceptibility related to the symmetry broken distribution function $g_+(J^z)$. In literature [202, 203], this susceptibility has been introduced since it displays a divergence at the critical temperature even in a finite system and thereby mimics the behavior of the "true" susceptibility proportional to the fluctuations of $\langle J^z \rangle$ in the infinite system [204]. The steady-state results for $\sigma^2_{J,z}/N$ obtained by the kinetic equations reflect this divergence by a relatively sharp peak indicating the temperature below which the nuclear-spin polaron forms. In the (β_n, β_e) plane, the maximum fluctuations $\sigma^2_{J,z}$ provide a temperature line defining the crossover to the polaron regime, see Fig. 3.5(c).

3.5 Temperature criterion for polaron formation

To establish an analytic temperature criterion determining where the nuclear-spin polaron state forms, we examine the nuclear distribution function $g(J^z)$ introduced in Eq. (3.27) in the steady state of the rate equations. Its dependence on the inverse nuclear spin temperature β_n for the system with $N = 10^5$ nuclear spins is displayed in Fig. 3.6(a) at a fixed inverse electron spin temperature of $\beta_e \omega_h = 0.05$. In the high temperature regime, the individual nuclear spins are randomly aligned such that J^z obeys a Gaussian distribution centered around $J^z = 0$, see the orange line in Fig. 3.6(b). At zero effective temperatures, the polaronic state with maximum spin alignment forms, and the weight in the distribution function $g(J^z)$ is split equally

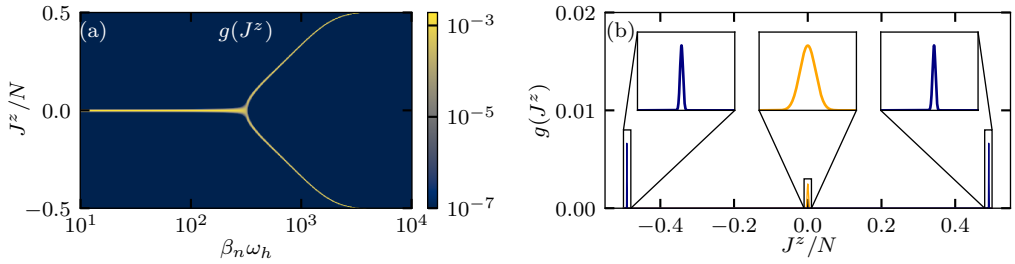

Figure 3.6: Steady-state nuclear distribution function $g(J^z)$ in a system with $N = 10^5$ nuclear spins at a fixed inverse electron spin temperature $\beta_e\omega_h = 0.05$. (a) Formation of the two polaron orientations with increasing β_n. (b) $g(J^z)$ at selected values of the inverse nuclear spin temperature, $\beta_n\omega_h = 10$ (orange) and $\beta_n\omega_h = 3000$ (blue). The figure is taken from Ref. [198].

between $J^z = \pm N/2$ whereas all other values of J^z have zero weight. In between the two limits, the nuclear distribution function $g(J^z)$ exhibits a bifurcation point from the single maximum placed at $J^z = 0$ at high temperatures to two maxima at $J^z \neq 0$ in the cooled system, see the blue line in Fig. 3.6(b). These two peaks of $g(J^z)$ produce the two branches in Fig. 3.6(a) at large β_n and correspond to the two potential orientations of the polaron state along the z axis. In the upper branch, the nuclear spins are preferably in the spin up state and the electron is in the spin down state; for the lower branch, the orientations are reversed. The bifurcation point allows for the derivation of a temperature criterion for the polaron formation. Accordingly, we define the crossover temperature as the temperature at which the maximum of $g(J^z)$ at $J^z = 0$ turns into a minimum with two maxima $J^z \neq 0$ placed symmetrically around it.

As a mathematical criterion for the crossover, we employ the ratio $g(1)/g(0)$ (assuming even N) since $g(1) < g(0)$ in the disordered state and $g(1) \geq g(0)$ when $g(J^z)$ exhibits two maxima. Hence, the crossover temperatures $\beta_{n,p}$ and $\beta_{e,p}$ are defined by

$$1 = \frac{g(1)}{g(0)} = \frac{N}{N+2} \frac{\cosh(\beta_{n,p}A_0/4)\cosh(\beta_{e,p}A_0/2)}{\cosh(\beta_{n,p}A_0/4 - \beta_{e,p}A_0/2)}, \tag{3.41}$$

using the relation for $g(J^z+1)/g(J^z)$ in Eq. (3.31) which was derived for the steady-state distribution function of the kinetic rate equations. This implicit temperature condition determines a temperature line $(\beta_{n,p}, \beta_{e,p})$ which is added in Figs. 3.4(a), 3.4(c), 3.5(a) and 3.5(c) as a red dotted line. The analytic crossover temperature coincides with the step in the fluctuations $\sigma^2_{SJ,z}/N$, cf. Fig. 3.5(a), and the maxima of the fluctuations $\sigma^2_{J,z}/N$, cf. Fig. 3.5(c). The inverse nuclear crossover temperature $\beta_{n,p}\omega_h = 327$ for the given electron temperature $\beta_{e,p}\omega_h = 0.05$ is indicated in Figs. 3.4(b), 3.4(d), 3.5(b) and 3.5(d) by a red dotted vertical line. For $-\langle S^z J^z \rangle / N$

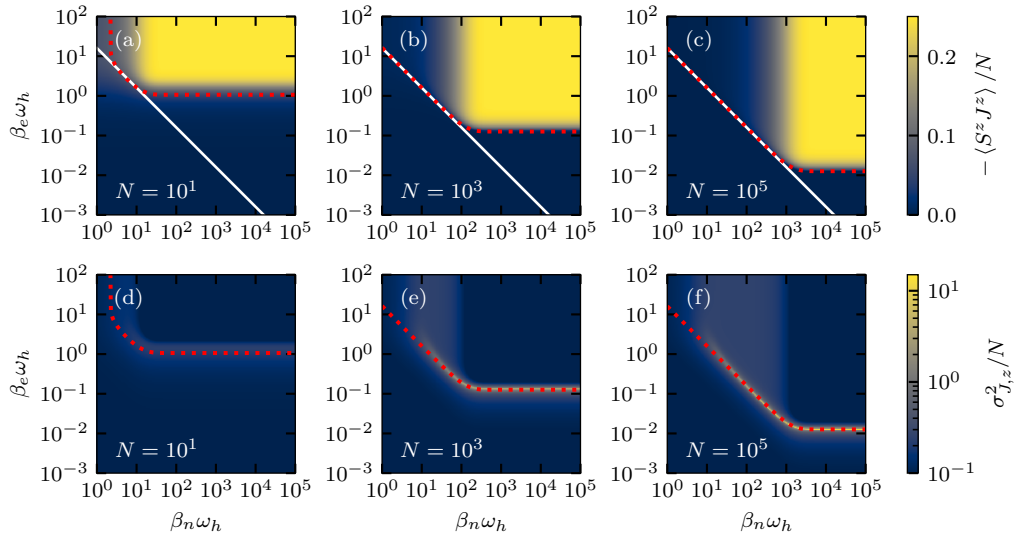

Figure 3.7: Steady-state results of the kinetic rate equations, Eq. (3.23), for different system sizes N. The upper panels display the electron-nuclear spin anti-correlation per nuclear spin $-\langle S^z J^z\rangle/N$; the lower panels present the fluctuations of $|J^z|$ per nuclear spin $\sigma^2_{J,z}/N$. The crossover temperature according to Eq. (3.41) is indicated by a red dotted line. The mean-field critical temperature, Eq. (3.34), is added as a white line in the upper panels.

and $\langle|J^z|\rangle/N$, the nuclear crossover temperature matches the temperature value where the quantities start to significantly increase, cf. Fig. 3.4(b) and 3.4(d). For the fluctuations $\sigma^2_{SJ,z}/N$ and $\sigma^2_{J,z}/N$, $\beta_{n,p}$ indicates the location of the peak, cf. Fig. 3.5(b) and 3.5(d).

The implicit condition for the crossover temperature, Eq. (3.41), can be rewritten into an explicit expression in the limit of large electron spin temperatures assuming $\beta_e A_0 \ll 1$,

$$\beta_{n,p} = \frac{4}{A_0}\,\mathrm{artanh}\left(\frac{4}{(N+2)A_0\beta_{e,p}}\right). \tag{3.42}$$

The explicit relation coincides with the implicit condition within the numerical accuracy for the presented temperature range and the chosen system parameter in Figs. 3.5(b) and 3.5(c). It allows for the interpretation of the temperature dependence of the nuclear-spin polaron formation: Generally, the nuclear spins have to be cooled down to a greater extent at higher electron spin temperatures in order to reach the polaronic state. However, above a certain electron temperature, $\beta_e > 4/(N+2)A_0$, the polaron cannot form even at zero nuclear spin temperature due to the strongly fluctuating electron spin. In the expression, Eq. (3.42), this fact

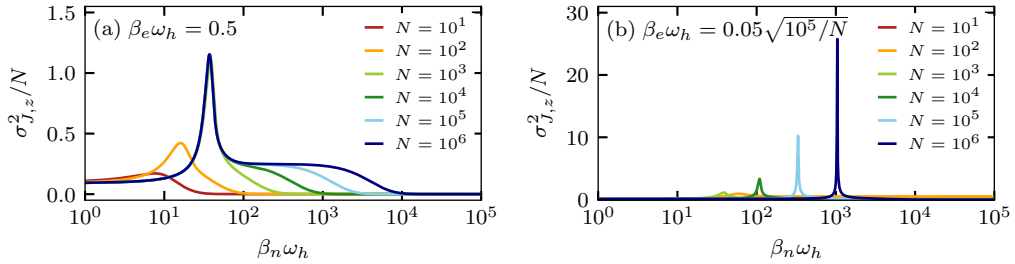

Figure 3.8: Steady-state fluctuations of $|J^z|$ per nuclear spin, $\sigma^2_{J,z}/N$, as a function of the inverse effective nuclear spin temperature β_n for different system sizes N. The inverse electron spin temperature is fixed to (a) $\beta_e\omega_h = 0.5$ and (b) $\beta_e\omega_h = 0.05\sqrt{10^5/N}$ according to the system size.

is indicated by the divergence of artanh(x) at $|x| = 1$ which yields a lower bound of β_e in Eq. (3.42). This bound is shifted to higher electron spin temperatures with growing system size N, see Fig. 3.7. In the mean-field calculations, such a bound of β_e is absent as a result of disregarding the spin fluctuations. Therefore, the mean-field critical temperature (white lines in the upper panes of Fig. 3.7) and the crossover temperature according to Eq. (3.41) (red dotted lines) differ in the range $\beta_e > 4/(N+2)A_0$. For large systems (or low electron spin temperatures), $N \gg (\beta_e A_0)^{-1}$, however, the temperature criterion, Eq. (3.42), converges to the mean-field critical temperature, Eq. (3.34).

The transition from the disordered spin system to the correlated polaron state by decreasing the effective spin temperatures appears to be a crossover phenomenon rather than a phase transition even with increasing the system size $N \to \infty$. This conclusion is based on the scaling of the fluctuations with N. Since the fluctuations $\sigma^2_{J,z}$ are connected to the susceptibility, they are an extensive quantity that is expected to scale with the system size N. Therefore, we displayed $\sigma^2_{J,z}/N$ in the previous figures. Similarly, we address the fluctuations $\sigma_{SJ,z}/N$ related to the heat capacity which is an extensive quantity as well. Examining $\sigma^2_{J,z}/N$ for various system sizes N, we find that the fluctuations per nuclear spin as a function of β_n at a fixed electron spin temperature $\beta_e\omega_h = 0.5$ exhibit a peak of constant height, see Fig. 3.8(a). The selected electron spin temperature does not allow for the polaron formation in small systems, e.g., $N = 10^1$ and $N = 10^2$, such that the peak of $\sigma^2_{J,z}/N$ is rather broad and not much pronounced. For systems with $N \geq 10^3$, the distinct peak coincides in width and amplitude hinting at a crossover behavior rather than an actual phase transition predicted by the mean-field treatment.

For further analysis, we adjust the electron spin temperature to correspond to the value $\beta_e\omega_h = 0.05$ chosen when presenting data for the system of size $N = 10^5$,

i.e., we set $\beta_e\omega_h = 0.05\sqrt{10^5/N}$. By this shift, we follow the lower bound for the polaron formation according to Eq. (3.41) which scales $\propto 1/\sqrt{N}$. The fluctuations $\sigma^2_{J,z}/N$ as a function of the inverse nuclear spin temperature for the adjusted values of the electron spin temperature display a peak that increases in amplitude for larger nuclear spin systems, see Fig. 3.8(b). Simultaneously, the nuclear crossover temperature related to the adjusted values of the electron spin temperature decreases shifting the peak of $\sigma^2_{J,z}/N$ to larger β_n with growing system size N. Thus, the crossover sharpens with growing the system size and increasing the asymmetry of temperatures $\beta_n \gg \beta_e$.

3.6 Effects of the distribution of hyperfine coupling constants

In a semiconductor nanostructure with a localized charge carrier, the hyperfine coupling constants are determined by the wave function of the charge carrier at the position of the respective nucleus as outlined in Sec. 2.5. So far we restricted ourselves to the box model approximation of the hyperfine interaction for the investigation of the nuclear-spin polaron formation exploiting the analytic access to the steady-state distribution function of the rate equations. In the following, we lift the simplification of equal hyperfine coupling constants for all nuclei and include a realistic distribution of the couplings A_k. The relevant distribution $p(A_k)$ is obtained from the introduction of the envelope function of the charge carrier wave function $\psi(\mathbf{r})$,

$$\psi(\mathbf{r}) \propto \exp\left[-r^m/(2L_0^m)\right] \tag{3.43}$$

with a characteristic length scale of localization L_0 such as the quantum dot size. The distribution $p(A_k)$ for this ansatz has been derived in Ref. [181] and reads

$$p(A_k) = \frac{d}{m}\frac{L_0^d}{A_k R^d}\left[\ln\left(\frac{A_{\max}}{A_k}\right)\right]^{d/m-1} \tag{3.44}$$

for a d-dimensional system. For instance, $d = 2$ corresponds to a flat cylindrical quantum dot and $d = 3$ to a spherical dot. The maximum coupling constant $A_{\max}$ and the cutoff radius R determining the smallest coupling constant regularize the distribution $p(A_k)$.

Since analytic access to the steady-state distribution function $g(J^z, S^z)$ is no longer granted for a distribution of the coupling constants A_k, the spin flip processes governed by the rate equations, Eq. (3.19), are implemented in a Monte Carlo simulation. The Monte Carlo simulation starts from initially randomly aligned

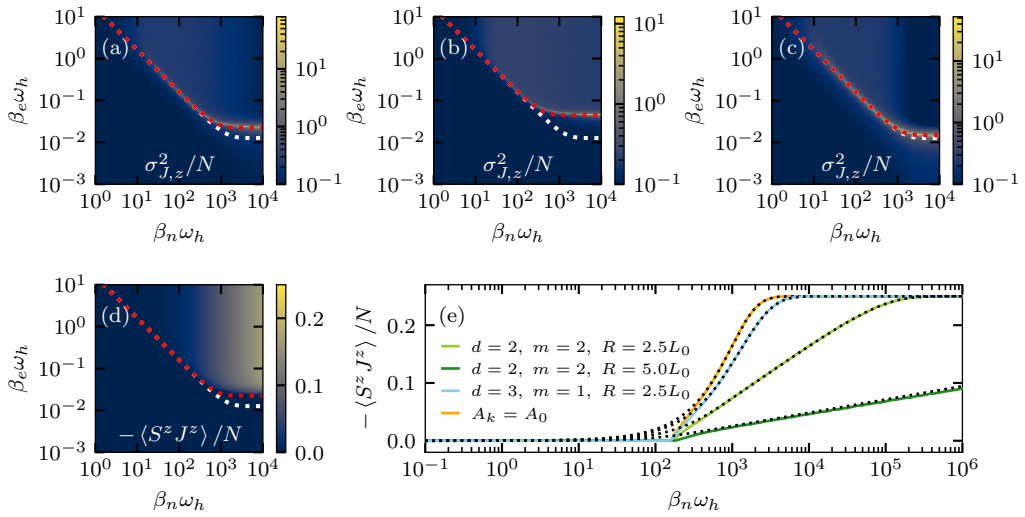

Figure 3.9: Steady-state results of the kinetic rate equations, Eq. (3.19), with $W_e^0/W_n^0 = 10^5$. The hyperfine coupling constants of the $N = 10^5$ nuclear spins following the distribution $p(A_k)$, Eq. (3.44). The upper panels present the fluctuations of $|J^z|$, $\sigma^2_{J,z}/N$, in the (β_n, β_e) plane. The parameters entering $p(A_k)$ differ for the individual panels: (a) $m = 2$, $d = 2$, $R = 2.5L_0$; (b) $m = 2$, $d = 2$, $R = 5.0L_0$; (c) $m = 1$, $d = 2$, $R = 2.5L_0$. The crossover temperature, Eq. (3.41), for the box model approximation is indicated by a white dotted line respectively; the corrected crossover temperature according to Eq. (3.41) with the effective number of nuclear spins N_{eff} is added as a red dotted line. Panel (d) displays the electron-nuclear spin anticorrelation $-\langle S^z J^z\rangle/N$ in the (β_n, β_e) plane; the parameters of $p(A_k)$ are the same as in panel (a). Panel (e) compares the spin anticorrelation $-\langle S^z J^z\rangle/N$ as a function of β_n at a fixed value $\beta_e\omega_h = 0.1$ for the various distributions $p(A_k)$ to the box model data. Parts of the figure are taken from Ref. [198].

spins and subsequently proposes flips of the electron spin or a random nuclear spin respecting the ratio of the electron and nuclear spin flip rate, $W_e^0/W_n^0 = 10^5$. The offered spin flips are accepted with a probability according to Eq. (3.20) for the electron spin and Eq. (3.21) for a nuclear spin respectively. After the equilibration, the spin expectation values are averaged over roughly 10^4 uncorrelated measurements.

The steady-state results for the fluctuation of $|J^z|$ in a system with $N = 10^5$ nuclear spins with hyperfine coupling constants distributed according to Eq. (3.44) are presented in the upper panels of Fig. 3.9 for three relevant parameter sets entering $p(A_k)$. The results indicate a shift of the temperature regime for the polaron formation depending on the specific distribution $p(A_k)$. The original crossover

temperature, Eq. (3.41), derived for the box model approximation (white dotted line) does not match the maximum of the fluctuations $\sigma^2_{J,z}/N$, instead the peak of the fluctuations $\sigma^2_{J,z}$ is shifted to lower temperatures.

For a corrected crossover line, the number of nuclear spins which actually contribute to the polaronic state has to be taken into account. Since the distribution $p(A_k)$ includes coupling constants with a relatively small value for a generic choice of the parameters m, d, and R, the number N_{eff} of nuclear spins effectively relevant for the dynamics can be smaller than N. For the distribution $p(A_k)$, Eq. (3.44), N_{eff} is controlled by the arbitrary cutoff radius R. Modeling a macroscopic system, R has to be sent to infinity while keeping $A_{\max}$ constant such that many nuclear spins irrelevant to the polaronic state would be included. In the box model approximation, in contrast, all nuclear spins contribute equally to the nuclear-spin polaron formation. For quantification of this effect, we focus on the ratio of effectively contributing spins in the system,

$$\frac{N_{\text{eff}}}{N} = \frac{\langle A_k \rangle^2}{\langle A_k^2 \rangle}, \tag{3.45}$$

which is determined by the first two moments of the distribution $p(A_k)$. While the box model yields $N = N_{\text{eff}}$, the effective number N_{eff} is generally smaller $N_{\text{eff}} < N$ for the distribution in Eq. (3.44).

Figure 3.9 presents the steady-state results for three relevant parameter sets of $p(A_K)$. In panels (a) and (d), we adjust $m = 2$, $d = 2$ and $R = 2.5L_0$ for a Gaussian envelope of the electron wave function in a flat quantum dot. For panel (b), the cutoff radius is widened to $R = 5.0L_0$ accommodating smaller values of A_k in the system with size $N = 10^5$ while we keep $m = 2$ and $d = 2$. The data in panel (c) is obtained for a three-dimensional system with an exponential wave function, $m = 1$, $d = 3$ and $R = 2.5L_0$, which captures a donor-bound charge carrier. The resulting number N_{eff} differs in the three scenarios: (a) and (d) $N_{\text{eff}}/N \approx 0.32$, (b) $N_{\text{eff}}/N \approx 0.08$, and (c) $N_{\text{eff}}/N \approx 0.73$. We find that the analytic prediction for the crossover temperature, Eq. (3.41), where we insert N_{eff} instead of N (red dotted lines in Fig. 3.9) coincides with the maximum of the fluctuations $\sigma^z_{J,z}$ obtained by the Monte Carlo simulation. We conclude that the crossover temperature depends primarily on the number of nuclear spins effectively contributing to the dynamics which is defined by the first two moments of $p(A_k)$, whereas the details on the distribution $p(A_k)$ of the hyperfine coupling constants play a minor role.

The formation of the electron-nuclear spin anticorrelation when decreasing the nuclear spin temperature, however, is governed by the individual couplings A_k. Figure 3.9(e) displays the anticorrelation $-\langle S^z J^z \rangle / N$ as a function of β_n at the fixed inverse electron spin temperature $\beta_e \omega_h = 0.1$. The panel compares the spin anticorrelation for the three selected parameter sets for $p(A_k)$ to the box

model result (orange line). Additionally, Fig. 3.9(d) presents $-\langle S^z J^z \rangle / N$ in the temperature plane for an exemplary parameter set. The full anticorrelation of a quarter per nuclear spin is reached at much lower effective nuclear spin temperatures for small ratios N_{eff}/N such that the β_n axis is prolonged up to $\beta_n \omega_h = 10^6$ in Fig. 3.9(e). The slope of the spin anticorrelation as a function of β_n for large inverse temperatures can be understood from the approximation of a frozen electron spin. This approximation holds when the electron spin temperature is low compared to the energy difference produced by an electron spin flip in the strong Overhauser field emerging at low nuclear spin temperatures. Here, the electron spin flip processes are strongly suppressed by the rate, Eq. (3.20), and the electron spin is effectively frozen. For a frozen electron spin, the electron-nuclear spin system factorizes into the subsystems of the individual spins. Accordingly, the electron-nuclear spin correlation results from the sum of the contributions of the individual nuclear spins subject to a fixed Knight field,

$$\langle S^z J^z \rangle \approx -\frac{1}{4} \sum_k \tanh\left(\frac{A_k \beta_n}{4}\right). \tag{3.46}$$

These asymptotics are added in Fig. 3.9(e) as black dotted lines for the selected sets of hyperfine coupling constants $\{A_k\}$. At low nuclear spin temperatures (large β_n), the asymptotics precisely match the data of $-\langle S^z J^z \rangle / N$. In the crossover regime, quantum fluctuations dominate the physics such that the approximation of a frozen electron spin is not valid. For $\beta_n < \beta_{n,p}$, the quantum fluctuations suppress the polaron formation. Thus, the overall slope of the electron-nuclear spin anticorrelation when decreasing the nuclear spin temperature is determined by the individual coupling constants A_k whereas the crossover temperature is governed by the effective number N_{eff} of nuclear spins.

3.7 Kinetics of polaron formation

The kinetic rate equation formalism allows for studying the temporal emergence of the polaronic state. For simplification, we return to the box model approximation after having established that a system with arbitrarily distributed hyperfine couplings can be mapped onto a system with $A_k \equiv A_0$ by an effective system size N_{eff}. To compute the dynamics of the distribution function $g(S^z, J^z)$, the elements of $g(S^z, J^z)$ are collated into a vector $\vec{g}$ that obeys the differential equation $\partial_t \vec{g} = \underline{\underline{W}} \vec{g}$ with the matrix $\underline{\underline{W}}$ defined by the rate equations, Eq. (3.23). Since the numerical evaluation of the solution $\vec{g}(t) = \exp(\underline{\underline{W}} t)\vec{g}(0)$ requires the matrix diagonalization of $\underline{\underline{W}}$ which exceeds the computational resources for the system size $N = 10^5$, we approximate the time evolution by decomposing $\exp(\underline{\underline{W}} t) = (\exp(\underline{\underline{W}} t/N))^N$ and approximate $\exp(\underline{\underline{W}} t/N)$ by a power series of order of four. Thus, we obtain $\vec{g}(t)$ for a given

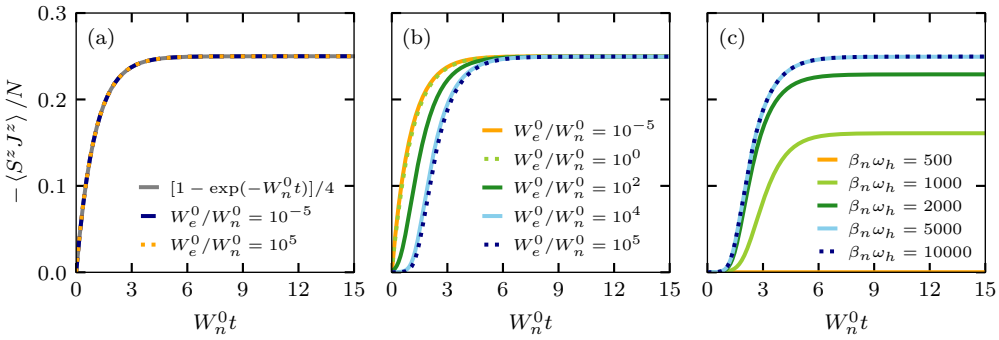

Figure 3.10: Temporal evolution of the electron-nuclear spin anticorrelation governed by the kinetic rate equations, Eq. (3.23), for a system with $N = 10^5$. Different flip rates are compared with the electron spin temperature adjusted (a) deep in the polaronic phase $\beta_e\omega_h = 5$ or (b) close to the crossover regime $\beta_e\omega_h = 0.05$, with $\beta_n\omega_h = 10^4$ in both cases. Panel (c) addresses the effect of the inverse nuclear spin temperature β_n; $\beta_e\omega_h = 0.05$ and $W_e^0/W_n^0 = 10^5$ are fixed. Parts of this figure are taken from Ref. [198].

starting condition $\vec{g}(0)$. For the examination of the emergence of the polaronic state, we start from a disordered system at $t = 0$ and monitor the subsequent temporal evolution at fixed effective spin temperatures. In the disordered initial state with randomly aligned spins, the nuclear distribution function $g(S^z, J^z)$ is determined by the degeneracy of the box-model spin states,

$$g_0(S^z, J^z) = \frac{1}{2^{N+1}} \begin{pmatrix} N \\ N_{+1}(J^z) \end{pmatrix} \tag{3.47}$$

with $N_{+1}(J^z) = N/2 + J^z$ and the binomial coefficient $\binom{a}{b} = a!/(b!(a-b)!)$. For the subsequent time evolution of $\vec{g}(t)$ governed by the rate equations, Eq, (3.23), we fix the temperatures in the polaronic regime and insert finite flip rates W_e^0 and W_n^0. Finally, the time-dependent distribution function is employed to determine the temporal evolution of the electron-nuclear anticorrelation from Eq. (3.33) with $O \equiv S^z J^z$.

At low temperatures deep in the polaronic regime, $\beta_e\omega_h = 5$ and $\beta_n\omega_h = 10^4$, the buildup of the electron-nuclear spin anticorrelation follows a universal behavior controlled by the nuclear spin flip rate W_n^0 alone, whereas the electron spin flip rate W_e^0 does not contribute to the dynamics, see Fig. 3.10(a). Scaling the time with W_n^0, the curves collapse onto the analytic relation

$$-\frac{\langle S^z J^z\rangle}{N} = \frac{1}{4}\left[1 - \exp\left(-W_n^0 t\right)\right] \tag{3.48}$$

independent of the ratio W_e^0/W_n^0. For an explanation, we focus on the energy difference generated by the spin flips. The flip of an individual nuclear spin produces a relatively small change in the system's total energy whereas a flip of the electron spin generates a large energy difference supported by the Overhauser field forming at low temperatures. Consequently, electron spin flip processes are strongly suppressed according to Eq. (3.24) and only nuclear spin flips can occur. Starting from the disordered spin system, the full electron-nuclear spin anticorrelation can be reached by flipping half of the nuclear spins without any flip of the electron spin. Therefore, the formation of spin anticorrelation is solely governed by the nuclear spin flip rate W_n^0.

Closer to the crossover temperature, $\beta_e\omega_h = 0.05$ and $\beta_n\omega_h = 10^4$, the electron spin flip rate W_e^0 starts to play a role, see Fig. 3.10(b). While the maximum anticorrelation is still reached, the buildup process is slowed down and exhibits a more complex behavior than a purely exponential growth. For a fast electron spin flip rate, $W_e^0/W_n^0 > 1$, random electron spin flips counteract the formation of the nuclear polaron state. In the beginning, when the Overhauser field polarization is not very pronounced yet, the electron spin can flip in the energetically unfavorable state with parallel alignment to the nuclear spin polarization and thereby hinder the buildup of the electron-nuclear anticorrelation. Random electron spin flips are only prevented after a sufficiently strong Overhauser field polarization has formed. From this point on, the further temporal evolution is again governed by the nuclear spin flip processes and the related rate W_n^0. The effect of the electron spin flips preventing the polaron formation strengthens with the increase in the rate W_e^0 up to the regime where the electron spin follows the nuclear spins almost instantaneously such that a further increase in W_e^0 has no additional effect on the dynamics anymore (the light and dark blue curves coincide). For electron spin flip rates comparable to the nuclear spin flip rate or smaller, however, the exponential behavior, Eq. (3.48), is recovered.

The nuclear spin temperature has only little effect on the temporal evolution of the anticorrelation $-\langle S^z J^z \rangle / N$ when it is adjusted in the polaron regime, see Fig. 3.10(c). However, β_n determines the maximum anticorrelation reached. For nuclear spin temperatures slightly below the crossover temperature, the electron-nuclear anticorrelation can be very small whereas it approaches the maximum value of a quarter per nuclear spin in the low temperature limit. The overall shape of the approach of $-\langle S^z J^z \rangle / N$ to the respective maximum is similar for the presented nuclear spin temperatures.

3.8 Chapter conclusion

We addressed the formation of a nuclear-spin polaron state characterized by an antiparallel alignment of the localized charge carrier spin and the surrounding nuclear spins by means of a two-temperature concept that accounts for the situation under optical cooling of the nuclear spin system. A kinetic rate equation formalism was developed that captures the dynamics of the distribution function and incorporates the coupling to two external spin reservoirs inducing separate effective spin temperatures for the electron spin and the nuclear spins respectively. The distribution function of the electron-nuclear spin system, which corresponds to the diagonal elements of the density operator in the energy eigenbasis, provides access to all spin observables commuting with the hyperfine Hamiltonian. Therefore, the kinetic rate equation formalism was applied to the spin system with Ising-type hyperfine interaction accounting for a localized heavy hole spin. Here, the dynamics can be addressed in the spin z product basis and the relevant spin observables S^z and J^z yield $[H_{\mathrm{Is}}, S^z] = [H_{\mathrm{Is}}, J^z] = 0$. Furthermore, we employed a box model approximation for the hyperfine coupling constants to gain analytic access to the system in the steady state at given inverse temperatures β_e and β_n. By means of the bifurcation point of the steady-state nuclear distribution function $g(J^z)$ that arises when the nuclear spin temperature is reduced, we derived an analytic temperature criterion for the polaron formation. This analytic prediction matches the maximum line of the spin fluctuations in the (β_n, β_e) plane. Due to $\langle J^z \rangle \equiv 0$ in the fully symmetric system, we had to resort to the fluctuations of $|J^z|$ commonly employed in literature when a spontaneous symmetry breaking is absent. Moreover, the electron-nuclear spin anticorrelation $-\langle S^z J^z \rangle / N$ proved a valuable measure for detecting the polaronic state. A Monte Carlo simulation allowed for the study of the system with a realistic distribution of the hyperfine coupling constants. The results could be mapped onto the box model data by the effective number of nuclear spins relevant to the dynamics. Finally, we examined the temporal transition from randomly aligned spins to the correlated polaronic state which we found mostly governed by the reservoir-induced nuclear spin flips at low temperatures.

Chapter 4

Nuclear-spin polaron formation for general anisotropic hyperfine interaction

The hyperfine interaction of the localized electron spin or light hole spin includes transversal coupling beyond the Ising limit. To account for the polaron formation in these systems, a generalized approach to the nonequilibrium two-temperature situation induced by the optical cooling is required. We develop a Lindblad formalism that includes the results for the Ising-type hyperfine interaction discussed in the previous chapter but extends the theory to a general anisotropic hyperfine Hamiltonian, Eq. (2.1). The differing effective spin temperatures of the electron spin and the nuclear spins are established by the coupling of the spin system to two separate external reservoirs similar as in the rate equations employed in Chapter 3. We apply the Lindblad approach to the relevant physical scenarios of the hyperfine interaction, Eq. (2.11), where the localized charge carrier spin relates to an electron, light hole, or heavy hole respectively. As the nuclear-spin polaron state forms along the direction of strongest hyperfine interaction, the nature of the polaronic state differs significantly for these systems. We examine the polaron formation by means of the electron-nuclear spin correlation for the various scenarios and find that the crossover temperature depends on the hyperfine anisotropy. Furthermore, the distribution functions of the nuclear spin components support the analysis of the characteristics of the polaronic state. Their examination reveals a quantum phase transition of the ground state of the hyperfine Hamiltonian as a function of the hyperfine anisotropy parameter λ. In dependence of λ, the ground state is either N-fold degenerate as for the isotropic system or twofold degenerate when $|\lambda| \neq 1$ and produces the respective orientation of the polaronic state. Moreover, the quantum phase transition transfers to the dynamics in the cooled system. Long living nuclear spin correlations are observed for the polaronic state in the Ising limit of the hyperfine interaction as well as in the isotropic system. For strong in-plane hyperfine interaction, however, the spin correlation is rapidly lost.

This chapter is based on the author's publication [199].

4.1 Lindblad formalism

For the investigation of the nuclear-spin polaron formation in the spin system with arbitrary anisotropic hyperfine interaction, the distinct effective spin temperatures of the electron spin and the nuclear spins are established by separate thermal reservoirs similarly as in the kinetic rate equation formalism. To account for the general hyperfine coupling, we extend the description of the open quantum system to the full density operator ρ rather than relying on the diagonal elements alone. The temporal evolution of ρ is captured by a Lindblad master equation [205, 206] under the assumption of Markovian dynamics,

$$\begin{aligned}\partial_t \rho = \mathcal{L}\rho = -i\left[H_{\mathrm{HF}}, \rho\right] - \sum_{k=0}^{N}\sum_{\alpha}\sum_{m,n}\{&(L_{mn}^{k\alpha})^\dagger L_{mn}^{k\alpha}\rho + \rho(L_{mn}^{k\alpha})^\dagger L_{mn}^{k\alpha} \\ &-2L_{mn}^{k\alpha}\rho(L_{mn}^{k\alpha})^\dagger\}\end{aligned} \tag{4.1}$$

with the Liouvillian $\mathcal{L}$. The Lindblad equation comprises the dynamics governed by the general hyperfine Hamiltonian H_{HF}, Eq. (2.1), as well as the reservoir-induced spin flips mediated by the Lindblad operators $L_{mn}^{k\alpha}$. The Lindblad operators $L_{mn}^{k\alpha}$ are expressed in terms of the eigenstates of H_{HF}, $H_{\mathrm{HF}}\left|\psi_m\right\rangle = \varepsilon_m\left|\psi_m\right\rangle$, such that the sum in the Lindblad equation, Eq. (4.1), incorporates potential transitions between any combination of eigenstates $\left|\psi_m\right\rangle$ and $\left|\psi_n\right\rangle$. The contributions of the individual spins are indicated by the index k: The electron spin flips are included at $k = 0$, and the nuclear spins are labeled $k \in \{1, \ldots, N\}$ in accordance with the Hamiltonian. Furthermore, the spatial component is taken into account by the index $\alpha \in \{x, y, z\}$.

In detail, the Lindblad operators are defined as

$$L_{mn}^{k\alpha} = \sqrt{\Gamma_{mn}^{k\alpha}}\sum_{a,b}\delta_{\varepsilon_a,\varepsilon_m}\delta_{\varepsilon_b,\varepsilon_n}\left\langle\psi_a\right|s_k^\alpha\left|\psi_b\right\rangle\left|\psi_a\right\rangle\left\langle\psi_b\right| \tag{4.2}$$

with the associated hermitian conjugate operators $(L_{mn}^{k\alpha})^\dagger$. The operators generate transitions between any combination of eigenstates $\left|\psi_b\right\rangle$ and $\left|\psi_a\right\rangle$, which have the same energy as the states $\left|\psi_n\right\rangle$ and $\left|\psi_m\right\rangle$ guaranteed by the Kronecker delta $\delta_{\varepsilon_a,\varepsilon_m}$ and $\delta_{\varepsilon_b,\varepsilon_n}$. This construction ensures a free choice of basis states within the subspace of energetically degenerate eigenstates. The transitions between the eigenstates are mediated by the spin operators s_k^α and obey the rate $\Gamma_{mn}^{k\alpha}$. The spin operator corresponds to either the electron spin operator $s_k^\alpha \equiv S^\alpha$ $(k = 0)$ or the operator of an individual nuclear spin $s_k^\alpha \equiv I_k^\alpha$ $(k \in \{1, \ldots, N\})$ with orientation $\alpha \in \{x, y, z\}$. The transition rate comprised by the Lindblad operator,

$$\Gamma_{mn}^{k\alpha} = \frac{W_k^\alpha h_k^\alpha(\Delta_{mn})}{g(\varepsilon_m)g(\varepsilon_n)}, \tag{4.3}$$

is constructed in such a way that the steady-state solution of the Lindblad equation in thermal equilibrium $\beta_e = \beta_n \equiv \beta$ equals the Boltzmann form $\rho = \exp(-\beta H_{\mathrm{HF}})/Z$ with the partition function Z. A phenomenological rate for the specific spin flip process is installed by the factor W_k^α, whereas the degrees of degeneracy of the involved eigenenergies, $g(\varepsilon_m)$ and $g(\varepsilon_n)$, avoid double counting of transitions between energetically degenerate subspaces. The function $h_k^\alpha(\Delta_{mn})$ provides a dimensionless temperature-dependent factor enhancing or attenuating transitions with respect to the energy difference generated by the transition, $\Delta_{mn} = \varepsilon_m - \varepsilon_n$. For a specific transition and the related reverse transition, the detailed balance condition $h_k^\alpha(\Delta_{mn})/h_k^\alpha(\Delta_{nm}) = h_k^\alpha(\Delta_{mn})/h_k^\alpha(-\Delta_{mn}) = \exp(-\Delta_{mn}\beta_k)$ ensures the steady-state Boltzmann density operator in case of equal temperatures $\beta_k \equiv \beta$ for all spins.

4.1.1 Dynamics of the density operator in matrix representation

The rate equations for the individual matrix elements of the density operator are obtained from the Lindblad master equation, Eq. (4.1), after inserting the Lindblad operators, Eq. (4.2),

$$\begin{aligned}\partial_t \rho = -i\,[H_{\mathrm{HF}}, \rho] - \sum_{k,\alpha}\sum_{m,n}\sum_{a,b}\sum_{a',b'} \frac{W_k^\alpha h_k^\alpha(\Delta_{mn})}{g(\varepsilon_m)g(\varepsilon_n)} \delta_{\varepsilon_a,\varepsilon_m}\delta_{\varepsilon_b,\varepsilon_n}\delta_{\varepsilon_{a'},\varepsilon_m}\delta_{\varepsilon_{b'},\varepsilon_n} \\ \times \left\{\delta_{a,a'}(s_k^\alpha)^*_{a'b'}(s_k^\alpha)_{ab}\left(|\psi_{b'}\rangle\langle\psi_b|\,\rho + \rho\,|\psi_{b'}\rangle\langle\psi_b|\right)\right. \\ \left. -2(s_k^\alpha)_{ab}(s_k^\alpha)^*_{a'b'}\,|\psi_a\rangle\langle\psi_b|\rho|\psi_{b'}\rangle\langle\psi_{a'}|\right\}, \end{aligned} \tag{4.4}$$

where we abbreviated $(s_k^\alpha)_{ab} = \langle\psi_a|s_k^\alpha|\psi_b\rangle$ and employed $\langle\psi_a|\psi_{a'}\rangle = \delta_{a,a'}$ for an orthonormal choice of the eigenbasis. Respecting the degree of degeneracy of the energy levels ε_m and ε_n,

$$\sum_{m,n}\delta_{\varepsilon_a,\varepsilon_m}\delta_{\varepsilon_b,\varepsilon_n} = g(\varepsilon_a)g(\varepsilon_b), \tag{4.5}$$

the sum over eigenstates with index m and n is eliminated such that the Lindblad equation simplifies to

$$\begin{aligned}\partial_t \rho = -i\,[H_{\mathrm{HF}}, \rho] - \sum_{k,\alpha}\sum_{a,b}\sum_{a',b'} W_k^\alpha h_k^\alpha(\Delta_{mn})\delta_{\varepsilon_a,\varepsilon_{a'}}\delta_{\varepsilon_b,\varepsilon_{b'}} \\ \times \left\{\delta_{a,a'}(s_k^\alpha)^*_{a'b'}(s_k^\alpha)_{ab}\left(|\psi_{b'}\rangle\langle\psi_b|\,\rho + \rho\,|\psi_{b'}\rangle\langle\psi_b|\right)\right. \\ \left. -2(s_k^\alpha)_{ab}(s_k^\alpha)^*_{a'b'}\,|\psi_a\rangle\langle\psi_b|\rho|\psi_{b'}\rangle\langle\psi_{a'}|\right\}. \end{aligned} \tag{4.6}$$

At this point, the reason for including the degrees of degeneracy, $g(\varepsilon_m)$ and $g(\varepsilon_n)$, as prefactors in the definition of the transition rate, Eq. (4.3), becomes clear. Potential

double counting of transitions between energetically degenerate eigenstates as a result of the sums over eigenstates with index a and b in the definition of the Lindblad operators, Eq. (4.2), is prevented.

The matrix representation of the Lindblad master equation, Eq. (4.1), in the eigenbasis of the Hamiltonian H_{HF} yields a set of coupled differential equations,

$$\begin{aligned}\partial_t \rho_{mn} = -i\Delta_{mn}\rho_{mn} - \sum_{k,\alpha} W_k^\alpha \sum_{a,b} \Big\{ & \delta_{\varepsilon_m,\varepsilon_b} h_k^\alpha (\Delta_{am}) (s_k^\alpha)^*_{am} (s_k^\alpha)_{ab} \rho_{bn} \\ & + \delta_{\varepsilon_n,\varepsilon_b} h_k^\alpha (\Delta_{an}) (s_k^\alpha)^*_{ab} (s_k^\alpha)_{an} \rho_{mb} \\ & - 2\delta_{\varepsilon_m,\varepsilon_n} \delta_{\varepsilon_a,\varepsilon_b} h_k^\alpha (\Delta_{ma}) (s_k^\alpha)_{ma} (s_k^\alpha)^*_{nb} \rho_{ab} \Big\} \end{aligned} \tag{4.7}$$

with the density matrix elements $\rho_{mn} = \langle \psi_m | \rho | \psi_n \rangle$. While the hyperfine interaction produces oscillations of the off-diagonal matrix elements, the exchange with the external spin reservoirs induces transitions between the density matrix elements as well as a decay of the off-diagonal matrix elements.

4.2 Specified master equations

The rate equations derived for the general hyperfine Hamiltonian, Eq. (2.1), are specified for the Hamiltonian, Eq. (2.11), with uniaxial anisotropy of the hyperfine interaction that accounts for the locally bound electron as well as the localized spin of light and heavy hole. For analytic access to the energy eigenstates and eigenenergies of H_{HF}, we resort to the box model approximation, $A_k \equiv A_0$, in the following, recalling that a realistic distribution of the hyperfine coupling constants mostly produces a correction by the effective number of nuclei coupling to the charge carrier spin, cf. Sec. 3.6. The box model approximation allows for the quantum mechanical treatment of relatively large systems with $N \approx 10^3$ nuclear spins. The relevant Hamiltonian,

$$\begin{aligned} H_{\mathrm{HF}} &= A_0 \left[\lambda \left(S^x J^x + S^y J^y \right) + S^z J^z \right] \\ &= A_0 \left[\frac{\lambda}{2} \left(S^+ J^- + S^- J^+ \right) + S^z J^z \right], \end{aligned} \tag{4.8}$$

can be written in terms of the total nuclear spin similar to the box model approximation in the Ising limit, Eq. (3.22). In addition, the Hamiltonian, Eq. (4.8), comprises spin flip terms where the electron spin transfers its z component to the nuclear spins and vice versa. These spin flips are produced by the spin flip operators of the electron spin and the total nuclear spin respectively,

$$S^\pm = S^x \pm i S^y, \tag{4.9}$$

$$J^\pm = J^x \pm i J^y. \tag{4.10}$$

4.2.1 Eigendecomposition of the anisotropic hyperfine Hamiltonian

The analytic diagonalization of the matrix representation of the anisotropic hyperfine Hamiltonian in the box model approximation, Eq. (4.8), is straightforward. For a system consisting of nuclear spins with individual length $I_k \equiv 1/2$, the Hamilton matrix is segmented into (2×2) and (1×1)-dimensional subblocks respectively. The related eigenenergies $\varepsilon^{\pm}_{J,J^z}$ and eigenstates $|\psi^{\pm,\zeta}_{J,J^z,}\rangle$ have been established by Kozloz [207]. From the (2×2)-dimensional subblocks, one obtains

$$\varepsilon^{\pm}_{J,J^z} = -\frac{A_0}{4} \pm \frac{A_0}{2}\sqrt{\left(J^z - \frac{1}{2}\right)^2 + \lambda^2\left[J(J+1) - J^z(J^z-1)\right]}, \tag{4.11a}$$

$$|\psi^{\pm,\zeta}_{J,J^z,}\rangle = c^{\pm}_{J,J^z}\,|\downarrow\rangle\,|J, J^z, \zeta\rangle + d^{\pm}_{J,J^z}\,|\uparrow\rangle\,|J, J^z - 1, \zeta\rangle\,, \tag{4.11b}$$

with $J \in \{0, \ldots, N/2\}$ (assuming an even number N) and $J^z \in \{-J+1, \ldots, J\}$. For the (1×1)-dimensional subblocks, the eigenenergies and eigenstates are directly read off,

$$\varepsilon^{+}_{J,-J} = \frac{A_0 J}{2}, \qquad \varepsilon^{+}_{J,J+1} = \frac{A_0 J}{2}, \tag{4.12a}$$

$$|\psi^{+,\zeta}_{J,-J}\rangle = |\downarrow\rangle\,|J, -J, \zeta\rangle\,, \qquad |\psi^{+,\zeta}_{J,J+1}\rangle = |\uparrow\rangle\,|J, J, \zeta\rangle\,, \tag{4.12b}$$

with $J \in \{0, \ldots, N/2\}$. The eigenstates are expressed in terms of the spin z product basis of the electron and the total nuclear spin where $|\uparrow\rangle$, $|\downarrow\rangle$ label the electron spin state, and $|J, J^z, \zeta\rangle$ refers to the total nuclear spin with the quantum number of the spin length J and the projection on the z axis J^z. The quantum number ζ is introduced to distinguish between energy degenerate subspaces with the same quantum number J arising from the spin addition theorem [207]: The block-diagonal Hamilton matrix can be divided into subblocks with a fixed quantum number J, whereby for each value of J a number of identical blocks occur which are enumerated by $\zeta \in \{1, \ldots, g_N(J)\}$. The degree of degeneracy originating from the number of identical blocks is

$$g_N(J) = \frac{2J+1}{N/2 + J + 1}\binom{N}{N/2 + J} \tag{4.13}$$

for a given number N of nuclear spin and a fixed total nuclear spin length J. The coefficients $c^{\pm}_{J,J^z}$ and $d^{\pm}_{J,J^z}$ in the eigenstates, Eq. (4.11b), result from diagonalization of the (2×2)-dimensional submatrix of the Hamiltonian represented in the basis $|\downarrow\rangle\,|J, J^z, \zeta\rangle$ and $|\uparrow\rangle\,|J, J^z - 1, \zeta\rangle$,

$$H^{2\times 2}_{J,J^z} = \begin{pmatrix} -A_0 J^z/2 & T_{J,J^z} \\ T_{J,J^z} & A_0(J^z-1)/2 \end{pmatrix}, \tag{4.14}$$

with $T_{J,J^z} = \lambda A_0 \sqrt{J(J+1) - J^z(J^z-1)}$. It is noteworthy that the index J^z in the notation of the eigenstates and eigenenergies actually corresponds to the total spin z component $F^z = S^z + J^z$ shifted by $1/2$ such that in Eqs. (4.12a) and (4.12b) the index J^z has a value $J^z = J+1$ which does not comply with the limits of the actual quantum number J^z. However, the labeling allows for a general notation of the eigenstates $|\psi^{\sigma\zeta}_{J,J^z}\rangle$ and eigenenergies $\varepsilon^{\sigma}_{J,J^z}$ with $\sigma \in \{+,-\}$, $J \in \{0,\dots,N/2\}$ and $J^z \in \{-J,\dots,J+1\}$.

4.2.2 Reduced rate equations

By means of the analytically established eigenstates, Eqs. (4.11b) and (4.12b), the general master equation, Eq. (4.7), is customized for the hyperfine Hamiltonian in the box model limit. To this end, the spin operator s^{α}_k is rewritten in terms of the spin flip operators for which we use the notation s^{τ}_k with an index $\tau \in \{-1,0,1\}$,

$$s^{\tau}_k = \begin{cases} s^{-}_k/\sqrt{2}, & \tau = -1, \\ s^{z}_k, & \tau = 0, \\ s^{+}_k/\sqrt{2}, & \tau = 1. \end{cases} \tag{4.15}$$

Insertion of the eigenstates, the eigenenergies and the operator s^{α}_k into Eq. (4.7) yields the specified rate equation,

$$\begin{aligned}
\partial_t \langle \psi^{\sigma_m,\zeta}_{J,J^z_m} | \rho | \psi^{\sigma_n,\zeta}_{J,J^z_n} \rangle = {} & -i\Delta^{\sigma_m,J,J^z_m}_{\sigma_n,J,J^z_n} \langle \psi^{\sigma_m,\zeta}_{J,J^z_m} | \rho | \psi^{\sigma_n,\zeta}_{J,J^z_n} \rangle - \sum_{k,\tau} \sum_{J',\zeta'} \sum_{\sigma,\sigma'} W^{\tau}_k \\
& \times \Big[\delta_{\varepsilon^{\sigma_m}_{J,J^z_m},\varepsilon^{\sigma'}_{J,J^z_m}} h^{\tau}_k(\Delta^{\sigma,J',J^z_m+\tau}_{\sigma_m,J,J^z_m}) \langle \psi^{\sigma',\zeta}_{J,J^z_m} | \rho | \psi^{\sigma_n,\zeta}_{J,J^z_n} \rangle \\
& \quad \times \langle \psi^{\sigma_m,\zeta}_{J,J^z_m} | (s^{\tau}_k)^{\dagger} | \psi^{\sigma,\zeta'}_{J,J^z_m+\tau} \rangle \langle \psi^{\sigma,\zeta'}_{J,J^z_m+\tau} | s^{\tau}_k | \psi^{\sigma',\zeta}_{J,J^z_m} \rangle \\
& + \delta_{\varepsilon^{\sigma_n}_{J,J^z_n},\varepsilon^{\sigma'}_{J,J^z_n}} h^{\tau}_k(\Delta^{\sigma,J',J^z_n\tau}_{\sigma_n,J,J^z_n}) \langle \psi^{\sigma_m,\zeta}_{J,J^z_m} | \rho | \psi^{\sigma',\zeta}_{J,J^z_n} \rangle \\
& \quad \times \langle \psi^{\sigma',\zeta}_{J,J^z_n} | (s^{\tau}_k)^{\dagger} | \psi^{\sigma,\zeta'}_{J',J^z_n\tau} \rangle \langle \psi^{\sigma,\zeta'}_{J',J^z_n+\tau} | s^{\tau}_k | \psi^{\sigma_n,\zeta}_{J,J^z_n} \rangle \\
& - 2\delta_{\varepsilon^{\sigma_m}_{J,J^z_m},\varepsilon^{\sigma_n}_{J,J^z_n}} \delta_{\varepsilon^{\sigma}_{J',J^z_m-\tau},\varepsilon^{\sigma'}_{J',J^z_n-\tau}} h^{\tau}_k(\Delta^{\sigma_m,J,J^z_m}_{\sigma,J',J^z_m-\tau}) \\
& \quad \times \langle \psi^{\sigma,\zeta'}_{J',J^z_m-\tau} | \rho | \psi^{\sigma',\zeta'}_{J',J^z_n-\tau} \rangle \\
& \quad \times \langle \psi^{\sigma_m,\zeta}_{J,J^z_m} | s^{\tau}_k | \psi^{\sigma,\zeta'}_{J',J^z_m-\tau} \rangle \langle \psi^{\sigma',\zeta'}_{J',J^z_n-\tau} | (s^{\tau}_k)^{\dagger} | \psi^{\sigma_n,\zeta}_{J,J^z_n} \rangle \Big] .
\end{aligned} \tag{4.16}$$

Each sum over the full set of eigenstates in the original equation, Eq. (4.7), initially is replaced by sums over the box model quantum numbers J, J^z, σ, and ζ respectively. In Eq. (4.16), we eliminated some of these sums already. First, we made use of the fact that the matrix elements of type $\langle \psi^{\sigma_m,\zeta}_{J,J^z_m} | s^{\tau}_k | \psi^{\sigma_n,\zeta'}_{J',J^z_n} \rangle$ only provide a nonzero

contribution when $J_m^z = J_n^z + \tau$ for the electron spin flips as well as the nuclear spin flips. Thus, any sums over the box model index J^z cancel out of the master equation. Furthermore, we assume that the density operator is diagonal in the quantum numbers J and ζ in accordance with the Hamiltonian, Eq. (4.8). As a consequence, part of the sums over these quantum numbers are omitted such that only one sum over J' and one sum over ζ' is left. The energy difference produced by a transition between the box model eigenstates is abbreviated $\Delta^{\sigma,J,J^z}_{\sigma',J',J^{z\prime}} = \varepsilon^{\sigma}_{J,J^z} - \varepsilon^{\sigma'}_{J',J^{z\prime}}$.

For further reduction of the rate equations, we introduce matrix elements of the type $p^J_{J^z_m,\sigma_m;J^z_n,\sigma_n}$ that comprise all elements of the density operator for a given combination of the quantum numbers J, J^z and σ by summing up the contributions for varying the index ζ,

$$\begin{aligned} p^J_{J^z_m,\sigma_m;J^z_n,\sigma_n} &= \sum_{\zeta} \langle \psi^{\sigma_m,\zeta}_{J,J^z_m} | \rho | \psi^{\sigma_n,\zeta}_{J,J^z_n} \rangle \\ &= g_N(J) \, \langle \psi^{\sigma_m,\zeta}_{J,J^z_m} | \rho | \psi^{\sigma_n,\zeta}_{J,J^z_n} \rangle \, . \end{aligned} \tag{4.17}$$

As the spin dynamics does not depend on ζ, we additionally make the assumption that all density elements $\langle \psi^{\sigma_m,\zeta}_{J,J^z_m} | \rho | \psi^{\sigma_n,\zeta}_{J,J^z_n} \rangle$ that solely differ in the index ζ are equally occupied. This is justified since the energy differences enter in the transition rates only and allows us to write $p^J_{J^z_m,\sigma_m;J^z_n,\sigma_n}$ in terms of the degree of degeneracy $g_N(J)$ in the second line of the above equation with some representative element $\langle \psi^{\sigma_m,\zeta}_{J,J^z_m} | \rho | \psi^{\sigma_n,\zeta}_{J,J^z_n} \rangle$ with arbitrary index ζ. The rate equations for the elements $p^J_{J^z_m,\sigma_m;J^z_n,\sigma_n}$ are established from Eq. (4.16) by summing over ζ,

$$\begin{aligned} \partial_t p^J_{J^z_m,\sigma_m;J^z_n,\sigma_n} = & -i\Delta^{\sigma_m,J,J^z_m}_{\sigma_n,J,J^z_n} p^J_{J^z_m,\sigma_m;J^z_n,\sigma_n} \\ & - \Big\{ \sum_{\tau} \sum_{J',\sigma'} \Big[\Gamma^{\tau}_{J',J}(J^z_m + \tau, J^z_m + \tau; \sigma', \sigma', \sigma_m, \sigma_m) \\ & + \Gamma^{\tau}_{J',J}(J^z_n + \tau, J^z_n + \tau; \sigma', \sigma', \sigma_n, \sigma_n) \Big] \Big\} p^J_{J^z_m,\sigma_m;J^z_n,\sigma_n} \\ & + \sum_{\tau} \sum_{J',\sigma,\sigma'} 2\Gamma^{\tau}_{J,J'}(J^z_m, J^z_n; \sigma_m, \sigma_n, \sigma, \sigma') p^J_{J^z_m-\tau,\sigma;J^z_n-\tau,\sigma'}, \end{aligned} \tag{4.18}$$

where we collate the transition rates into the rather complicated expression

$$\begin{aligned} \Gamma^{\tau}_{J,J'}(J^z_a, J^z_b; \sigma_a, \sigma_b, \sigma_c, \sigma_d) = & \, \delta_{\varepsilon^{\sigma_a}_{J,J^z_a},\varepsilon^{\sigma_b}_{J,J^z_b}} \delta_{\varepsilon^{\sigma_c}_{J',J^z_a+\tau},\varepsilon^{\sigma_d}_{J',J^z_b+\tau}} \sum_k \frac{W^{\tau}_k}{g_N(J')} h^{\tau}_k(\Delta^{\sigma_a,J,J^z_a}_{\sigma_c,J',J^z_a-\tau}) \\ & \times \sum_{\zeta,\zeta'} \langle \psi^{\sigma_a,\zeta}_{J,J^z_a} | s^{\tau}_k | \psi^{\sigma_c,\zeta'}_{J',J^z_a-\tau} \rangle \, \langle \psi^{\sigma_d,\zeta'}_{J',J^z_b-\tau} | (s^{\tau}_k)^{\dagger} | \psi^{\sigma_b,\zeta}_{J,J^z_b} \rangle \, , \end{aligned} \tag{4.19}$$

which will be evaluated in the following subsection.

4.2.3 Transition rates

To determine the value of the transition rate, Eq. (4.19), we address the electron and nuclear spin flips separately. The contribution induced by electron spin flips with $s_0^\tau \equiv S^\tau$ contains matrix elements of the type $\langle \psi^{\sigma,\zeta}_{J,J^z} | S^\tau | \psi^{\sigma',\zeta'}_{J',J^z-\tau} \rangle$. For their evaluation, we insert the eigenstates, Eqs. (4.11b) and (4.12b), and exploit the orthonormality of the nuclear spin states,

$$\langle \psi^{\sigma,\zeta}_{J,J^z} | S^\tau | \psi^{\sigma',\zeta'}_{J',J^z-\tau} \rangle = \delta_{J,J'}\delta_{\zeta,\zeta'} \times \begin{cases} c^\sigma_{J,J^z} d^{\sigma'}_{J',J^z-\tau}/\sqrt{2}, & \tau = -1, \\ \left(d^\sigma_{J,J^z} d^{\sigma'}_{J',J^z-\tau} - c^\sigma_{J,J^z} c^{\sigma'}_{J',J^z-\tau} \right)/2, & \tau = 0, \\ d^\sigma_{J,J^z} c^{\sigma'}_{J',J^z-\tau}/\sqrt{2}, & \tau = 1. \end{cases} \tag{4.20}$$

Thus, the sums over ζ and ζ' in the transition rate, Eq. (4.19), reduce to a factor of $g_N(J)$ which cancels out with the term $g_N(J')$ in the definition of the rate.

For transitions related to a nuclear spin flip, the matrix elements occurring in the transition rate can be decomposed into

$$\begin{aligned} \langle \psi^{\sigma,\zeta}_{J,J^z} | I^\tau_k | \psi^{\sigma',\zeta'}_{J',J^z-\tau} \rangle = {} & c^\sigma_{J,J^z} c^{\sigma'}_{J',J^z-\tau} \langle J, J^z, \zeta | I^\tau_k | J', J^z - \tau, \zeta' \rangle \\ & + d^\sigma_{J,J^z} d^{\sigma'}_{J',J^z-\tau} \langle J, J^z - 1, \zeta | I^\tau_k | J', J^z - 1 - \tau, \zeta' \rangle , \end{aligned} \tag{4.21}$$

by rewriting the box model eigenstates into the spin z basis via Eqs. (4.11b) and (4.12b) and applying the orthonormality of the electron spin states. Subsequently, the arising matrix elements in the nuclear spin z basis can be evaluated by means of Clebsch-Gordan coefficients. For this purpose, the nuclear spin bath consisting of N spins with individual length $1/2$ is separated into the selected spin k and the spin bath of size $N-1$ comprising the remaining nuclear spins. Accordingly, a nuclear spin state $|J, J^z, j, \zeta_j, 1/2\rangle$ is characterized by the total nuclear spin J, its projection onto the axis of quantization J^z, the total nuclear spin j in the reduced nuclear spin bath excluding spin k, the index ζ_j accounting for the degeneracy of j (in analogy to ζ in the full spin bath) and the spin length $I_k \equiv 1/2$. Here, j, ζ_j, and I_k were previously amalgamated in the quantum number ζ. For brevity, the degeneracy index ζ_j is omitted in the following. Employing the Clebsch-Gordan coefficients, the state $|J, J^z, j, 1/2\rangle$ can be disassembled into states of the format $|j, j^z; 1/2, I^z_k\rangle$ with the spin z projection j^z in the reduced spin bath and the spin z component I^z_k of spin k,

$$\begin{aligned} \left| J, J^z, j = J \pm \frac{1}{2}, \frac{1}{2} \right\rangle = {} & \mp \sqrt{\frac{1}{2}\left(1 \mp \frac{J^z}{j+1/2}\right)} \left| j, J^z - \frac{1}{2}; \frac{1}{2}, \frac{1}{2} \right\rangle \\ & + \sqrt{\frac{1}{2}\left(1 \pm \frac{J^z}{j+1/2}\right)} \left| j, J^z + \frac{1}{2}; \frac{1}{2}, -\frac{1}{2} \right\rangle , \end{aligned} \tag{4.22}$$

where either $I_k^z = 1/2$ or $I_k^z = -1/2$ and $j^z = J^z - I_k^z$ respectively. This format finally allows for the application of the spin operator I_k^τ which results in

$$I_k^{-1}\left|J, J^z, j = J \pm \frac{1}{2}, \frac{1}{2}\right\rangle = \mp\frac{1}{2}\sqrt{1 \mp \frac{J^z}{j+1/2}}\left|j, J^z - \frac{1}{2}; \frac{1}{2}, -\frac{1}{2}\right\rangle , \tag{4.23a}$$

$$\begin{aligned} I_k^{0}\left|J, J^z, j = J \pm \frac{1}{2}, \frac{1}{2}\right\rangle = &\mp\sqrt{\frac{1}{8}\left(1 \mp \frac{J^z}{j+1/2}\right)}\left|j, J^z - \frac{1}{2}; \frac{1}{2}, \frac{1}{2}\right\rangle \\ &- \sqrt{\frac{1}{8}\left(1 \pm \frac{J^z}{j+1/2}\right)}\left|j, J^z + \frac{1}{2}; \frac{1}{2}, -\frac{1}{2}\right\rangle , \end{aligned} \tag{4.23b}$$

$$I_k^{+1}\left|J, J^z, j = J \pm \frac{1}{2}, \frac{1}{2}\right\rangle = \frac{1}{2}\sqrt{1 \pm \frac{J^z}{j+1/2}}\left|j, J^z + \frac{1}{2}; \frac{1}{2}, \frac{1}{2}\right\rangle . \tag{4.23c}$$

As a next step, the matrix elements in the nuclear spin z basis are evaluated,

$$\begin{aligned} &\left\langle J', J^z + \tau, j' = J' \pm \frac{1}{2}, \frac{1}{2}\right| I_k^\tau \left|J, J^z, j = J \pm \frac{1}{2}, \frac{1}{2}\right\rangle \\ &\quad = \delta_{j,j'} \times \begin{cases} (J-j)\sqrt{\frac{1}{2}\left(1 + 2\frac{(J'-j)(J^z-1)}{j+1/2}\right)\left(1 + 2\frac{(j-J)J^z}{j+1/2}\right)}, & \tau = -1, \\ (J'-j)(J-j)\sqrt{\left(1 + 2\frac{(J'-j)J^z}{j+1/2}\right)\left(1 + 2\frac{(J-j)J^z}{j+1/2}\right)} & \\ \quad -\frac{1}{4}\sqrt{\left(1 + 2\frac{(j-J')J^z}{j+1/2}\right)\left(1 + 2\frac{(j-J)J^z}{j+1/2}\right)}, & \tau = 0, \\ (J'-j)\sqrt{\frac{1}{2}\left(1 + 2\frac{(J'-j)(J^z+1)}{j+1/2}\right)\left(1 + 2\frac{(j-J)J^z}{j+1/2}\right)}, & \tau = +1. \end{cases} \end{aligned} \tag{4.24}$$

These expressions have to be inserted in Eq. (4.21) for the transformation of the matrix element into the eigenbasis of H_{HF}.

Since the nuclear spins in the box model limit are all equal, we introduce an isotropic transition rate $W_k^\tau = W_n^0$ for $\tau \in \{-1, 0, 1\}$, which is identical for all nuclear spins $k \in \{1, \ldots, N\}$. Accordingly, we set $h_k^\tau = h_n$ for $\tau \in \{-1, 0, 1\}$ and $k \in \{1, \ldots, N\}$. Analogously, the isotropic electron spin flip rate $W_0^\tau = W_e^0$ is employed. Under the assumption of the equivalence of all nuclear spins, the above evaluation of the matrix element, Eq. (4.21), applies to any individual nuclear spin and the sum over k in Eq. (4.19) only produces a prefactor of N for the nuclear share. The sum over ζ (ζ' respectively) in Eq. (4.19) splits into a sum over $j = J \pm 1/2$ ($j' = J' \pm 1/2$) and ζ_j ($\zeta_{j'}$) for the transition induced by a nuclear spin. When the system is diagonal in the quantum number ζ and therefore ζ_j, the sums over ζ_j and $\zeta_{j'}$ reduce to a single sum with $\zeta_j = \zeta_{j'}$, which simplifies to the prefactor of $g_{N-1}(j')$ for the nuclear

contributions. Finally, the transition rate, Eq. (4.19), can be specified by

$$\begin{aligned}\Gamma^{\tau}_{J,J'}(J^z_a,J^z_b;\sigma_a,\sigma_b,\sigma_c,\sigma_d) = \delta_{\varepsilon^{\sigma_a}_{J,J^z_a},\varepsilon^{\sigma_b}_{J,J^z_b}}\delta_{\varepsilon^{\sigma_c}_{J',J^z_a-\tau},\varepsilon^{\sigma_d}_{J',J^z_b-\tau}}\Big[&W^0_e h_e(\Delta^{\sigma_a,J,J^z_a}_{\sigma_c,J',J^z_a-\tau})\\ &\times\langle\psi^{\sigma_a,\zeta}_{J,J^z_a}|S^{\tau}|\psi^{\sigma_c,\zeta'}_{J',J^z_a-\tau}\rangle\,\langle\psi^{\sigma_b,\zeta'}_{J',J^z_b-\tau}|(S^{\tau})^{\dagger}|\psi^{\sigma_b,\zeta}_{J,J^z_b}\rangle\\ &+NW^0_n\sum_{j,j'}\frac{g_{N-1}(j')}{g_N(J')}h_n(\Delta^{\sigma_a,J,J^z_a}_{\sigma_c,J',J^z_a-\tau})\\ &\times\langle\psi^{\sigma_a,\zeta}_{J,J^z_a}|I^{\tau}_k|\psi^{\sigma_c,\zeta'}_{J',J^z_a-\tau}\rangle\,\langle\psi^{\sigma_d,\zeta'}_{J',J^z_b-\tau}|(I^{\tau}_k)^{\dagger}|\psi^{\sigma_b,\zeta}_{J,J^z_b}\rangle\Big]\end{aligned} \tag{4.25}$$

where the matrix elements of type $\langle\psi^{\sigma_a,\zeta}_{J,J^z_a}|s^{\tau}_k|\psi^{\sigma_c,\zeta'}_{J',J^z_a-\tau}\rangle$ are evaluated according to Eq. (4.20) (electron) and Eq. (4.21) (nuclei).

The dimensionless functions mediating the inverse electron and nuclear spin temperature, β_e and β_n respectively, are set to

$$h_e(\varepsilon)=\begin{cases}e^{-\beta_e\varepsilon}, & \varepsilon>0,\\ 1, & \varepsilon\le 0,\end{cases}\qquad\qquad h_n(\varepsilon)=\begin{cases}e^{-\beta_n\varepsilon}, & \varepsilon>0,\\ 1, & \varepsilon\le 0,\end{cases} \tag{4.26}$$

in compliance with the transition rates employed in the Ising limit, Eq. (3.20) and Eq. (3.21). Transitions decreasing the energy of the system, $\varepsilon\le 0$, occur with maximum rate, whereas transitions increasing the hyperfine energy, $\varepsilon>0$ are exponentially suppressed at low temperatures. This choice of the rates obeys the detailed balance relation $h_i(\varepsilon)/h_i(-\varepsilon)=\exp(-\beta_i\varepsilon)$ with $i\in\{e,n\}$ and, therefore, guarantees the correct Boltzmann form of the density operator in the steady state at equal temperatures, $\beta_e=\beta_n$.

4.3 Numerical implementation

As the Lindblad formalism, Eq. (4.18), couples the dynamics of specific matrix elements of the density operator, it is useful to identify groups of coupled elements $p^{J}_{J^z_m,\sigma_m;J^z_n,\sigma_n}$ and address the dynamics within the subspaces separately. Due to the structure of the spin flip matrix elements in the box model approximation, we find two decoupled groups of density matrix elements: one group contains the diagonal matrix elements and the other group comprises the off-diagonal elements. Furthermore, the group of the off-diagonal elements can be decomposed into several decoupled subgroups some of which contain a single matrix element only. The matrix elements of a respective subspace are collated into the vector $\vec{f}$ whose dynamics is governed by a differential equation of the format $\partial_t\vec{f}=\underline{\underline{W}}\vec{f}$ where the transition

matrix $\underline{\underline{W}}$ is set up according to Eq. (4.18). The specific value of the matrix elements of $\underline{\underline{W}}$ is obtained from the previously outlined evaluation of the transition rate, Eq. (4.19). Accordingly, the steady-state density elements of $\vec{f}$ result from the right eigenvector of the nonsymmetric matrix $\underline{\underline{W}}$ related to the eigenvalue zero. We extract the relevant eigenvectors in the respective subspaces by means of an Arnoldi method [208, 209]. To this end, the identity matrix normalized to a trace of one is employed as a starting condition for the density operator ρ. After the evaluation in the individual subspaces, the full steady-state density operator ρ_0 is composed from the steady-state matrix elements of all subspaces.

A unique steady state of the system is guaranteed at finite nonzero temperatures. Here, the off-diagonal density matrix elements eventually decay to zero according to the master equations, Eq. (4.18). The rates between the diagonal elements can be rewritten in terms of a stochastic matrix $\underline{\underline{M}} = \underline{\underline{1}} + \delta\underline{\underline{W}}$ with $0 < \delta \ll 1$ such that the eigenvectors of $\underline{\underline{W}}$ remain eigenvectors of $\underline{\underline{M}}$ and the eigenvalues $\Lambda_{M,i}$ of $\underline{\underline{M}}$ relate to the eigenvalues $\Lambda_{W,i}$ of $\underline{\underline{W}}$ via $\Lambda_{M,i} = 1 + \delta\Lambda_{W,i}$. Accordingly, the steady-state solution of the rate equation matches the eigenvector of $\underline{\underline{M}}$ related to the eigenvalue one. When $\underline{\underline{M}}$ allows for (indirect) transitions between any elements [210], i.e., $\underline{\underline{M}}$ is an irreducible matrix [211], the eigenvalue one is ensured to be nondegenerate by the Perron-Frobenius theorem [212, 213] producing a unique steady state. This condition on $\underline{\underline{M}}$ is fulfilled at finite nonzero temperatures due to the structure of the master equations, Eq. (4.18), which produce transitions between the neighboring values of J^z while simultaneously changing the quantum number J by ± 1 or 0. At zero temperatures, however, the above argumentation cannot be directly applied since a large number of transitions is prohibited according to Eq. (4.26) as they are related to an energy increase of the system.

The time evolution governed by the Lindblad equation is obtained from the diagonalization of the matrices $\underline{\underline{W}}$ for the individual subspaces of coupled matrix elements. The Arnoldi method with an appropriate number of iterations N_{it} is applied for the calculation of N_{it} Ritz eigenvalues approximating the eigenspectrum of $\underline{\underline{W}}$ for a given initial state. The temporal evolution of the system $\vec{f}(t) = \exp(\underline{\underline{W}}t)$ is approximated in the Krylov space spanned by the Ritz eigenvectors whose overlap with the initial state determines the contribution of the related Ritz eigenvalue to the dynamics. This procedure is applied in Sec. 4.8 where we address the temporal dynamics of the spin autocorrelation functions.

4.4 Nuclear-spin polaron state in the anisotropic system

The extended Lindblad formalism offers the chance to study the formation of the nuclear-spin polaron state in the system with arbitrary biaxiality of the hyperfine interaction, Eq. (4.8). Initially, we focus on the steady-state spin expectation values to gain a profound understanding of the emerging polaronic state in the anisotropic system. Since the formation of the nuclear-spin polaron state is accompanied by the emergence of an anticorrelation of the electron spin and the nuclear spins for positive hyperfine coupling constants and a positive anisotropy parameter, $A_0 > 0$ and $\lambda > 0$, it is instructive to investigate the spin anticorrelation $-\langle S^\alpha J^\alpha \rangle / N$ with $\alpha \in \{x, y, z\}$. The electron-nuclear spin anticorrelation reveals the orientation of the polaronic state originating from the minimization of the hyperfine energy, Eq. (4.8), by the opposite alignment of the electron spin and the nuclear spins at low temperatures. For negative values of the hyperfine coupling constants, in contrast, a parallel alignment of the electron and nuclear spins is expected. The following investigations however are restricted to positive values of A_0 and λ, since their sign only determines the sign of the electron-nuclear spin correlation but does not affect the fundamental physics.

The steady-state anticorrelation $-\langle S^\alpha J^\alpha \rangle / N$ is obtained from the steady-state density operator ρ_0, $\partial_t \rho_0 = 0$ according to the master equations, Eq. (4.18), which is inserted into the relation $\langle O \rangle = \mathrm{Tr}\left[O\rho_0\right]$ for the expectation value of a general observable O, here $O \equiv S^z J^z$. The rate equations allow for convenient treatment of a quantum mechanical system with $N = 10^3$ nuclear spins in the box model limit, whose steady-state density operator is obtained numerically as outlined in the previous section. For the transition rates, we use $W_e^0 = 10^{-3}\omega_h$ and $W_n^0 = 10^{-6}\omega_h$ to ensure that electron spin flips occur with three orders of magnitude faster rate than the nuclear spin flips. These rates provide a rough estimate: The main energy scale of the system ω_h is provided by the hyperfine coupling and corresponds to a time scale of 1 ns. We expect the electron spin to relax on a time scale of 1 µs [214] via spin-lattice coupling whereas the nuclear spin flip rates are governed by the nuclear dipole-dipole interactions which occur on a time scale of 1 ms. The choice of the system size and the flip rates is kept for the following sections unless stated otherwise. As a reference scale for measuring time and energy, we utilize $\omega_h = (\sum_k A_k^2)^{1/2} \equiv (N A_0^2)^{1/2}$ as in the examination of the Ising system in Chapter 3.

The dependence of the nuclear-spin polaron formation on the hyperfine anisotropy is examined by three physically relevant scenarios: (a) the Ising limit $\lambda = 0$ applicable to heavy hole spins, which was previously studied in Chapter 3, (b) the isotropic system $\lambda = 1$ arising for the electron spin, and (c) an anisotropic system with

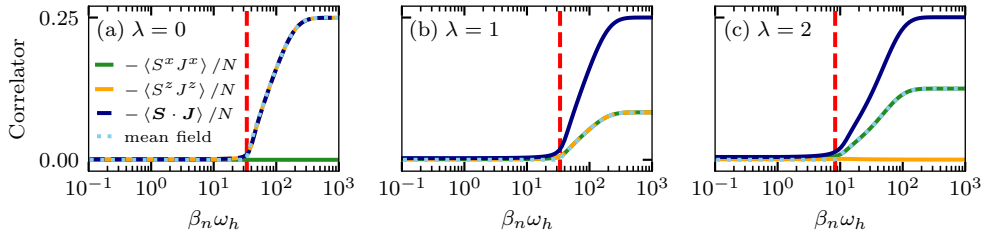

Figure 4.1: Anticorrelation of the electron spin and the total nuclear spin. The individual components as well as the total anticorrelation are presented for three different values of the hyperfine anisotropy parameter λ in (a), (b), and (c). The legend in panel (a) applies to the entire figure. The spin anticorrelation is displayed as a function of the inverse nuclear spin temperature β_n whereas the inverse electron spin temperature is fixed to $\beta_e\omega_h = 0.5$. The figure is taken from Ref. [199].

$\lambda = 2$ capturing the light hole spin. We find that while the total anticorrelation, $-\langle \mathbf{S}\cdot\mathbf{J}\rangle/N$, matches in the three cases, the individual contributions $-\langle S^\alpha J^\alpha\rangle/N$ are clearly governed by the hyperfine anisotropy, see Fig. 4.1. At an electron spin temperature fixed in the intermediate regime, $\beta_e\omega_h = 0.5$, the total spin anticorrelation (blue line) as a function of the inverse nuclear spin temperature β_n starts at zero for high temperatures and approaches the maximum value of a quarter per nuclear spin $-\langle \mathbf{S}\cdot\mathbf{J}\rangle/N = 1/4$ when decreasing the nuclear spin temperature. For the spatial components, we display $-\langle S^x J^x\rangle/N$ (green line) which equals $-\langle S^y J^y\rangle/N$ due to the axial rotation symmetry of the Hamiltonian (4.8) as well as $-\langle S^z J^z\rangle/N$ (orange line).

In the Ising limit, $\lambda = 0$, the electron-nuclear spin correlation is solely made up by the z component whereas the transversal components $\langle S^x J^x\rangle = \langle S^y J^y\rangle = 0$ remain zero even at low temperatures, see Fig. 4.1(a). Since only the spin z components enter the hyperfine energy at $\lambda = 0$ and the spin flip terms are absent, the polaron state is oriented along the z axis. It is noteworthy that similar behavior is observed for any system with $\lambda \in [0, 1)$, where the hyperfine interaction along the z axis dominates the transversal contributions. The results for $\lambda \in [0, 1)$ would fully coincide with those in Fig. 4.1(a) and therefore are not presented here.

The spin anticorrelation in the isotropic system, $\lambda = 1$, is equally distributed between the individual components, $\langle S^x J^x\rangle = \langle S^y J^y\rangle = \langle S^z J^z\rangle$, such that at low temperatures each component contributes with $-\langle S^\alpha J^\alpha\rangle/N = 1/12$ per nuclear spin, see Fig. 4.1(b). As a result of a lack of spatial preference in the hyperfine Hamiltonian, the forming nuclear-spin polaron state is completely isotropic.

In an anisotropic system with $|\lambda| > 1$, the hyperfine interaction within the (xy) plane

predominates. Consequently, the electron-nuclear spin anticorrelation forms in the components $-\langle S^x J^x \rangle / N$ and $-\langle S^y J^y \rangle / N$ whereas the z component remains zero. For a light hole in a quantum dot, the anisotropy parameter $\lambda = -2$ is realized [184]. Since the sign of λ only determines whether a parallel or antiparallel orientation of the electron spin and the nuclear spins in the (xy) plane forms, we restrict ourselves to positive values of λ and exemplarily present the data for a system with $\lambda = 2$, see Fig. 4.1(c). At a vanishing z contribution of the spin correlation, the anticorrelation is split equally between the x and y component such that $\langle S^x J^x \rangle$ constitutes half of the full correlator $\langle \mathbf{S} \cdot \mathbf{J} \rangle$ and reaches $-\langle S^x J^x \rangle / N = 1/8$ at low temperatures. In the system with $|\lambda| > 1$, the temperature at which the polaron formation starts is shifted to higher values. This effect will be addressed in the subsequent section.

4.5 Crossover temperature for polaron formation

Since the crossover temperature for the nuclear-spin polaron formation depends on the anisotropy of the hyperfine interaction, we derive a temperature criterion for the polaron formation with respect to the anisotropy parameter λ. The mean-field calculations in Sec. 3.2 provide the critical temperatures,

$$\beta_{e,c}\beta_{n,c} = \frac{16}{N a_0^2}. \tag{4.27}$$

Here, we rewrote Eq. (3.12) in terms of a rescaled hyperfine coupling constant a_0. The coupling constant a_0 covers the complete prefactor in the electron-nuclear spin interaction along the axis of polaron formation in the respective realization of the hyperfine Hamiltonian,

$$a_0 = \begin{cases} A_0, & |\lambda| \leq 1, \\ \lambda A_0, & |\lambda| > 1. \end{cases} \tag{4.28}$$

The original coupling constant A_0 is multiplied by the parameter λ for the polaron formation within the (xy) plane and applies unaltered when the polaron state is oriented along the z axis.

In accordance with the findings of the mean-field treatment, we apply the analytically derived criterion, Eq. (3.42), for the polaron formation in the Ising limit of the hyperfine interaction and insert the adjusted hyperfine coupling constant a_0,

$$\beta_{n,p} = \frac{4}{a_0} \operatorname{artanh}\left(\frac{4}{(N+2) a_0 \beta_{e,p}} \right). \tag{4.29}$$

Aiming at the temperature line in the (β_n, β_e) plane for the onset of polaron formation, we study the spin fluctuations as a function of the two inverse temperatures.

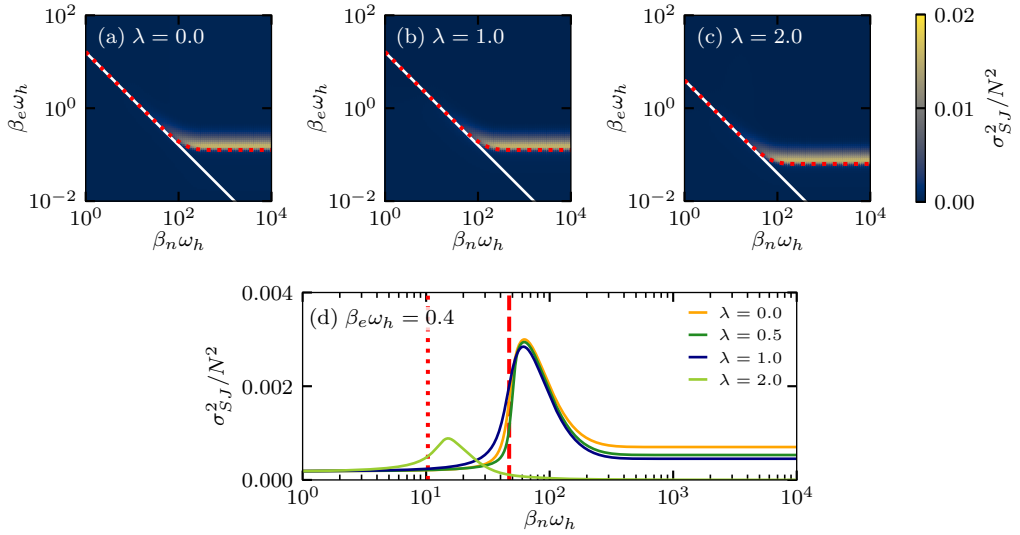

Figure 4.2: Fluctuations σ^2_{SJ}/N of the electron-nuclear spin correlation as a function of the inverse electron and nuclear spin temperatures for three select values of the hyperfine anisotropy parameter (a), (b), and (c). The color coding in the three upper panels is the same (see the legend on the right). Panel (d) displays the fluctuations σ^2_{SJ} at a fixed electron spin temperature, $\beta_e\omega_h = 0.4$. The nuclear crossover temperature according to Eq. (4.29) is indicated by the dashed ($\beta_{n,p}\omega_h = 41.3$ for $|\lambda| \leq 1$) or dotted ($\beta_{n,p}\omega_h = 10.1$ for $|\lambda| = 2$) red vertical line. The figure is taken from Ref. [199].

Since the total electron-nuclear spin correlation $\langle \mathbf{S} \cdot \mathbf{J} \rangle$ has proven to unambiguously indicate the polaron formation independent of the hyperfine anisotropy, we focus on the associated fluctuations,

$$\sigma^2_{SJ} = \langle (\mathbf{S} \cdot \mathbf{J})^2 \rangle - \langle \mathbf{S} \cdot \mathbf{J} \rangle^2 \,, \tag{4.30}$$

which we expect to exhibit a peak at those temperatures at which the electron-nuclear spin anticorrelation starts to rise. Figure 4.2 displays the fluctuations σ^2_{SJ}/N as a function of the inverse temperatures β_n and β_e for three selected values of the hyperfine anisotropy parameter, (a) $\lambda = 0$, (b) $\lambda = 1$, and (c) $\lambda = 2$, for a system comprising $N = 10^3$ nuclear spins. The maximum line of σ^2_{SJ}/N (yellow color coding) matches the analytic criterion, Eq. (4.29), (red dotted line) in all three cases. For comparison, the mean-field critical temperature, Eq. (4.27), in the anisotropic system is added (white line). A horizontal cut through the upper panels of Fig. 4.2 located at the inverse electron spin temperature of $\beta_e\omega_h = 0.4$, see Fig. 4.2(d), reveals that the inverse nuclear crossover temperature $\beta_{n,p}$ is positioned at the rising flank of the fluctuations σ^2_{SJ}/N respectively. For $|\lambda| \leq 1$ the nuclear-spin polaron

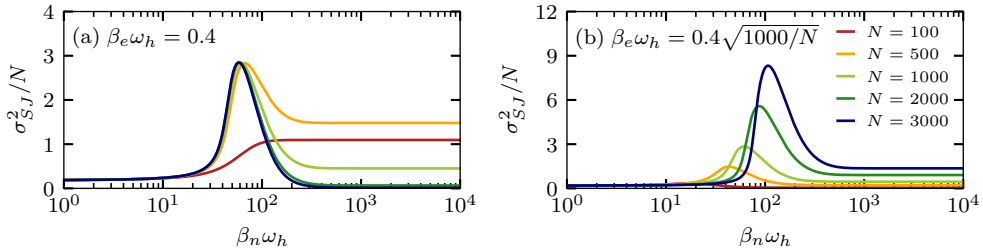

Figure 4.3: Fluctuations σ^2_{SJ}/N of the electron-nuclear spin correlation in the isotropic system as a function of the inverse nuclear spin temperature. The inverse electron spin temperature is fixed at (a) $\beta_e\omega_h = 0.4$ and (b) $\beta_e\omega_h = 0.4\sqrt{10^3/N}$. The legend indicating the system size N in panel (b) applies to both panels. The figure is taken from Ref. [199].

forms below the same crossover temperature, whereas for $|\lambda| > 1$ the crossover regime is shifted to higher temperatures.

Similarly to the spin system with Ising-type hyperfine interaction for which we presented the analysis of the fluctuations $\sigma^2_{SJ,z}/N$ of the electron-nuclear spin z correlation, cf. Fig. 3.5, the fluctuations σ^2_{SJ}/N can be interpreted by means of the heat capacity of the system in thermal equilibrium $\beta_e = \beta_n$. At low temperatures, the correlator $\langle \mathbf{S} \cdot \mathbf{J} \rangle$ is proportional to the hyperfine energy under the assumption that the spins align either completely within the (xy) plane or along the z axis with the respective scenario determined by the parameter λ. The fluctuations σ^2_{SJ}/N are proportional to the heat capacity for $\beta_e = \beta_n$ which would exhibit a discontinuity at the critical temperature according to Landau theory of phase transitions [204]. Naturally, the finite system of size $N = 10^3$ does not exhibit an actual phase transition but rather a crossover that sharpens with increasing N.

For a detailed analysis of the scaling with the system size N, we examine the extensive quantity σ^2_{SJ} per nuclear spin (as discussed in the previous chapter for the Ising-type hyperfine interaction). Figure 4.3(a) presents the fluctuations σ^2_{SJ}/N as a function of β_n for various sizes of the isotropic system (see legend in panel (b)) at a fixed inverse electron spin temperature $\beta_e\omega_h = 0.4$. Similarly as the fluctuations $\sigma^2_{J,z}/N$ of the absolute value of the total nuclear spin z component examined for the Ising-type hyperfine coupling, cf. Fig. 3.8, the fluctuations σ^2_{SJ}/N of the electron-nuclear spin correlation per nuclear spin exhibit a peak whose height is independent of the system size. Here, we present σ^2_{SJ}/N in the system with isotropic hyperfine interaction exemplarily; the results for any other value of the anisotropy parameter λ resemble these data. The findings for σ^2_{SJ}/N support the assumption that nuclear-spin polaron formation is a crossover phenomenon rather

than an actual phase transition.

Following the shift of the polaron formation to higher electron spin temperatures with increasing N, we scale the value of the electron spin temperature by $1/\sqrt{N}$ in accordance with Eq. (4.29) in order to correspond to $\beta_e\omega_h = 0.4$ for the system size $N = 10^3$. The electron-nuclear spin fluctuations, displayed as a function of β_n in Fig. 4.3(b), illustrate the sharpening of the crossover with increasing system size N. For larger values of N, the peak of σ^2_{SJ}/N grows in amplitude while moving to lower nuclear spin temperatures. As a result of including the full density operator in the Lindblad formalism for the isotropic system, the investigation for $\lambda = 1$ is limited to system sizes of several thousand nuclei and cannot reach realistic system sizes of $N = 10^5$.

4.6 Nuclear distribution functions

A detailed analysis of the nuclear spin reorientation at decreasing temperatures is facilitated by the distribution functions of the quantum numbers of the total nuclear spin. We define the distribution function $g(J^z)$ of the nuclear spin quantum number J^z based on the diagonal elements $p^J_{J^z,\sigma;J^z,\sigma}$ of the steady-state density operator obtained from the master equation, Eq. (4.18). The diagonal elements are transformed from the energy eigenbasis into the spin z basis according to Eqs. (4.11b) and (4.12b). Subsequently, all contributions to a fixed value of the spin projection J^z are added up,

$$g(J^z) = \sum_{J=-N/2}^{N/2} \sum_{\sigma=\pm} \left[(c^\sigma_{J,J^z})^2 p^J_{J^z,\sigma;J^z,\sigma} + (d^\sigma_{J,J^z+1})^2 p^J_{J^z+1,\sigma;J^z+1,\sigma} \right]. \tag{4.31}$$

Accordingly, the definition, Eq. (4.31), comprises sums over the box model quantum numbers J and σ respectively. Respecting the axial rotation symmetry of the hyperfine interaction, we introduce the perpendicular component of the total nuclear spin,

$$J^{p2} = J(J+1) - J^{z2}, \tag{4.32}$$

as an additional observable that allows for the study of the transversal spin orientation. The transversal spin component J^{p2} is deduced from the quantum numbers of the total nuclear spin J and the spin projection J^z, and according to Eq. (4.32) is limited to values $J^{p2} \in \{0, \ldots, N/2(N/2+1)\}$. The distribution function of the transversal component J^{p2} is implemented analogously to the distribution function

of the quantum number J^z,

$$g(J^{p2}) = \sum_{J=-N/2}^{N/2} \sum_{J^z=-J}^{J+1} \sum_{\sigma=\pm} \Big[(c^{\sigma}_{J,J^z})^2 p^J_{J^z,\sigma;J^z,\sigma} + (d^{\sigma}_{J,J^z+1})^2 p^J_{J^z+1,\sigma;J^z+1,\sigma} \Big] \delta_{J^{p2},J(J+1)-J^{z2}}, \tag{4.33}$$

where all contributions to a fixed value of J^{p2} from various combinations of the box model quantum numbers J, J^z, and σ are accumulated. As a result of the nonequidistant values of J^{p2}, the data for the distribution function $g(J^{p2})$ is processed as a histogram. The histogram typically consists of 200 bins in the range $J^{p2} \in \{0, \ldots, 250500\}$ for $N = 10^3$. Figure 4.4 displays the continuous change of the distribution functions $g(J^z)$ and $g(J^{p2})$ when increasing the inverse nuclear spin temperature β_n at a fixed inverse electron spin temperature of $\beta_e \omega_h = 0.5$. The nuclear distribution functions at exemplary values of the nuclear spin temperature are provided in Fig. 4.5. Both figures present the results for the three relevant cases of hyperfine anisotropy, $\lambda = 0$, $\lambda = 1$, and $\lambda = 2$.

The resulting distribution function at high temperatures is universal and does not depend on the details of the hyperfine interaction: When the thermal energy exceeds the energy scale of the system, the spins are randomly oriented forming a fully isotropic spin state. In the distribution function of the nuclear spin projection onto an arbitrary axis, e.g., the z axis, this state translates to the Gaussian distribution, $g(J^z) \propto \exp(-2J^{z2}/N)$, see left panels of Fig. 4.5 (red lines). The transversal spin component J^{p2} reflects the disordered nuclear spin state at high temperatures by a distribution function $g(J^{p2}) \propto \exp(-2J^{p2}/N)$, see right panels of Fig. 4.5 (red lines). However, the distribution functions at lower temperatures are governed by the hyperfine anisotropy.

For an Ising-type hyperfine interaction, $\lambda = 0$, the distribution function $g(J^z)$ has already proven to be a valuable indicator for the polaron formation, cf. Sec. 3.5. The distribution function, Eq. (4.31), defined for the results obtained by the Lindblad formalism exactly coincides with the definition, Eq. (3.27), introduced for the rate equations. In the Ising limit of hyperfine interaction, the Lindblad formalism with appropriately adjusted parameters, such as the functions $h_e(\varepsilon)$ and $h_n(\varepsilon)$ as well as the transition rates W^0_e and W^0_n, reproduces the steady-state results of the rate equations as a special case. Accordingly, the distribution function $g(J^z)$ in Fig. 4.4(a) matches the results in Fig. 3.6. We note however that the system size differs for the two approaches. At high temperatures, the nuclear spins are randomly aligned producing the Gaussian shape of $g(J^z)$ with the maximum at $J^z = 0$. Cooling the nuclear spins, $g(J^z)$ exhibits two maxima at $J^z \neq 0$ which reflect the polaron orientation along the positive and negative z direction. Figure 4.5(a) presents $g(J^z)$

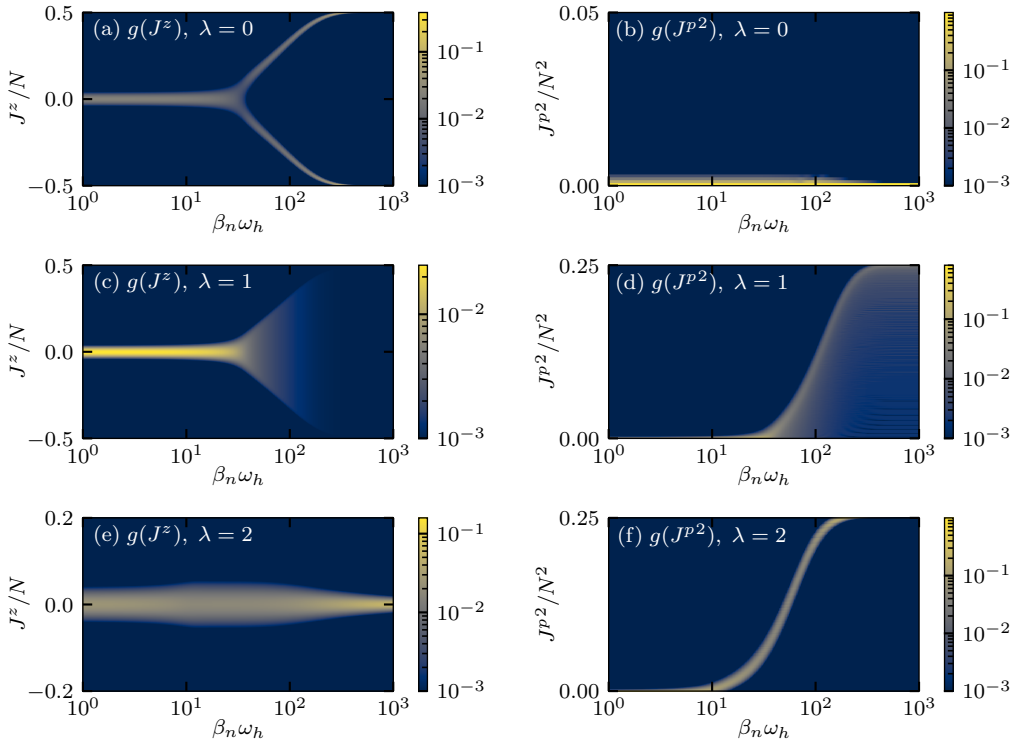

Figure 4.4: Nuclear distribution functions of the quantum numbers J^z (left panels) and J^{p2} (right panels) for different hyperfine anisotropy parameters: $\lambda = 0$ (upper panels), $\lambda = 1$ (middle panels), and $\lambda = 2$ (lower panels). The distributions are displayed as a function of the effective inverse nuclear spin temperature β_n for a fixed value of the inverse electron spin temperature $\beta_e\omega_h = 0.5$. The figure is taken from Ref. [199].

at three selected nuclear spin temperatures, i.e., it provides vertical cuts through Fig. 4.4(a). We recall that the bifurcation point, at which the single peak of $g(J^z)$ splits into two maxima, served as a basis for the derivation of the temperature criterion for polaron formation, Eq. (4.29). The orientation of the nuclear spin along positive or negative z direction for Ising-type hyperfine interaction is accompanied by the reduction of the transversal component J^{p2}. Figure 4.4(b) displays the focusing of $g(J^{p2})$ around $J^{p2} = 0$, which cannot be resolved in Fig. 4.5(b), where the distribution functions $g(J^{p2})$ at the three selected nuclear spin temperatures coincide as a result of the limited values of J^{p2} for $N = 10^3$.

For the spin system with isotropic hyperfine interaction, $\lambda = 1$, the polaron state is isotropic such that the behavior of the spin components J^x, J^y, and J^z is identical, see Fig. 4.4(c) for $g(J^z)$. Starting from the crossover temperature, $\beta_{n,p}\omega_h = 32.6$ for

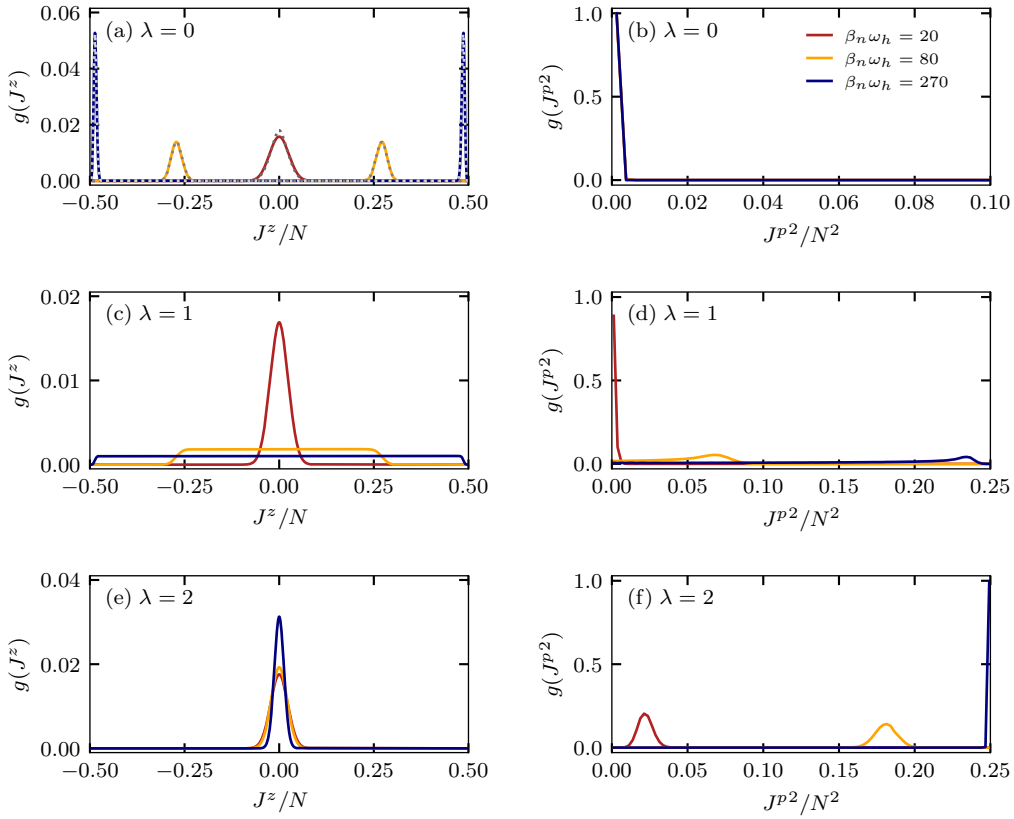

Figure 4.5: Nuclear distribution functions $g(J^z)$ (left panels) and $g(J^{p2})$ (right panels) at fixed electron and nuclear spin temperatures. The inverse electron temperature is set to $\beta_e\omega_h = 0.5$. The inverse nuclear spin temperature is indicated by the legend in panel (b). In panel (a), we added the results for $\lambda = 0.5$ as gray dotted lines for comparison. The figure is taken from Ref. [199].

$\beta_{e,p}\omega_h = 0.5$, the Gaussian distribution fans out to a uniform distribution which covers a range approaching the maximum range $J^z \in \{-N/2, \ldots, N/2\}$ with increasing β_n. Figure 4.5(c) presents $g(J^z)$ at exemplary nuclear spin temperatures. Here, the emerging uniform distribution is resolved even more clearly. The distribution function of the transversal component approaches $g(J^{p2}) = (N/2(N/2+1) - J^{p2})^{-1/2}$ at zero temperatures, see Figs. 4.4(d) and 4.5(d).

The nuclear distribution functions in the case of anisotropic hyperfine interaction with $|\lambda| > 1$ show the formation of a nuclear-spin polaron state within the (xy) plane. Here, we exemplarily study the system with an anisotropy parameter $\lambda = 2$. Since the perpendicular spin component J^{p2} reaches a maximum in the polaronic

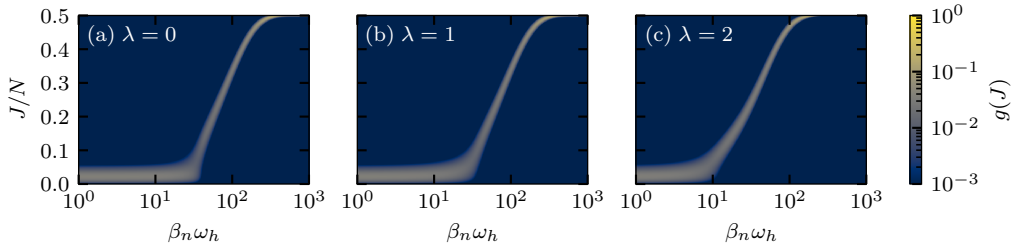

Figure 4.6: Distribution function of the total nuclear spin J depending on the inverse nuclear spin temperature β_n for a fixed electron spin temperature $\beta_e\omega_h = 0.5$.

state, see Fig. 4.4(f), the axial component J^z minimizes, see Fig. 4.4(e). The maximum of the distribution function $g(J^{p2})$ moves from small values of J^{p2} at high temperatures to the limit $J^{p2} = N/2(N/2+1)$, i.e, $J^{p2}/N^2 \approx 1/4$ for large N, when lowering the nuclear spin temperature, see Fig. 4.5(f). Concurrently, the Gaussian high-temperature distribution of J^z sharpens around $J^z = 0$ to allow for the transversal spin alignment, see Fig. 4.5(e).

Albeit the spatial orientation of the nuclear-spin polaron state is determined by the hyperfine anisotropy and transmits to the distribution functions of J^z and J^{p2}, the behavior of the quantum number of total nuclear spin J agrees for the various values of the anisotropy parameter λ. The distribution function of J is defined in accordance with $g(J^z)$ and $g(J^{p2})$,

$$g(J) = \sum_{J^z=-J}^{J+1} \sum_{\sigma=\pm} \left[(c^{\sigma}_{J,J^z})^2 p^J_{J^z,\sigma;J^z,\sigma} + (d^{\sigma}_{J,J^z+1})^2 p^J_{J^z+1,\sigma;J^z+1,\sigma} \right]. \tag{4.34}$$

Figure 4.6 displays $g(J)$ as a function of the inverse nuclear spin temperature β_n for a fixed value of the electron spin temperature, $\beta_e\omega_h = 0.5$. At high temperatures, small values of J outweigh the larger ones whereas with lowering the temperature the maximum weight in $g(J)$ approaches the maximum total nuclear spin $J = N/2$. This process starts at the inverse nuclear crossover temperature $\beta_{n,p}\omega_h = 32.6$. We note that for $\lambda = 2$ the polaron formation is shifted to higher temperatures, $\beta_{n,p}\omega_h = 8.0$, such that $g(J)$ in Fig. 4.6(c) differs from the results in Figs. 4.6(a) and 4.6(b) obtained for $\lambda = 0$ and $\lambda = 1$ respectively.

4.7 Quantum phase transition

The change of the nuclear-spin polaron state as a function of the anisotropy parameter λ can be directly connected to the transformation of the ground state of H_{HF}. The minimum eigenenergy of the Hamiltonian, Eq. (4.8), is invariably given by ε^{-}_{J,J^z} according to Eq. (4.11a), since the remaining eigenenergies, $\varepsilon^{+}_{J,-J}$ and $\varepsilon^{+}_{J,J+1}$ defined in Eq. (4.12a) as well as ε^{+}_{J,J^z} according to Eq. (4.11a), are unambiguously larger in magnitude. For the determination of the quantum numbers J and J^z minimizing ε^{-}_{J,J^z}, we rewrite Eq. (4.11a) into

$$\varepsilon^{-}_{J,J^z} = -\frac{A_0}{4} - \frac{A_0}{2}\sqrt{\frac{1}{4} + \lambda^2 J(J+1) + (1-\lambda^2)J^z(J^z-1)} \tag{4.35}$$

and find that the quantum number of total nuclear spin J has to be consistently maximized: $J = N/2$ holds in the ground state for any value of λ which fully complies with Fig. 4.6. Clearly, the sign of λ has no effect. Furthermore, the quantum number J^z that minimizes the energy depends on the absolute value of the anisotropy parameter. For $|\lambda| < 1$, the hyperfine energy is minimized for the box model quantum numbers $J^z = -N/2+1$ and $J^z = N/2$. The twofold degenerate ground state is given by $|\uparrow\rangle\,|J = N/2, J^z = -N/2\rangle$ and $|\downarrow\rangle\,|J = N/2, J^z = N/2\rangle$. For $|\lambda| = 1$, the quantum number J^z does not enter Eq. (4.35) and the ground state is N-fold degenerate, $J^z \in \{-N/2+1, \ldots, N/2\}$. For $|\lambda| > 1$, the product $J^z(J^z-1)$ in Eq. (4.35) has to be minimized such that the twofold degenerate ground state is provided by the box model eigenstates with index $J^z = 0$ and $J^z = 1$.[1] The resulting ground state energy ε_0 for the three cases is given by

$$\varepsilon_0 = -\frac{A_0}{4} - \begin{cases} \frac{A_0}{2}\sqrt{\frac{1}{4} + \frac{N}{2}(\frac{N}{2}-1) + \lambda^2 N}, & |\lambda| < 1, \\ \frac{A_0}{2}\sqrt{\frac{1}{4} + \frac{N}{2}(\frac{N}{2}+1)}, & |\lambda| = 1, \\ \frac{A_0}{2}\sqrt{\frac{1}{4} + \lambda^2\frac{N}{2}(\frac{N}{2}+1)}, & |\lambda| > 1. \end{cases} \tag{4.36}$$

The change of the ground state degeneracy as a function of the hyperfine anisotropy parameter λ translates to a quantum phase transition at $|\lambda_c| \equiv 1$.

We draw attention to the profound difference between the twofold degenerate ground states at $|\lambda| < 1$ and $|\lambda| > 1$ respectively. For $|\lambda| < 1$, no transition between the two ground states can occur at zero temperatures as a result of the vanishing transition rate, Eq. (4.25), between the respective ground state and the neighboring spin states that can be reached by a single spin flip. Any transition between the

[1] Here, we assume an even number N. We note that for odd N the ground state for $|\lambda| > 1$ would be nondegenerate.

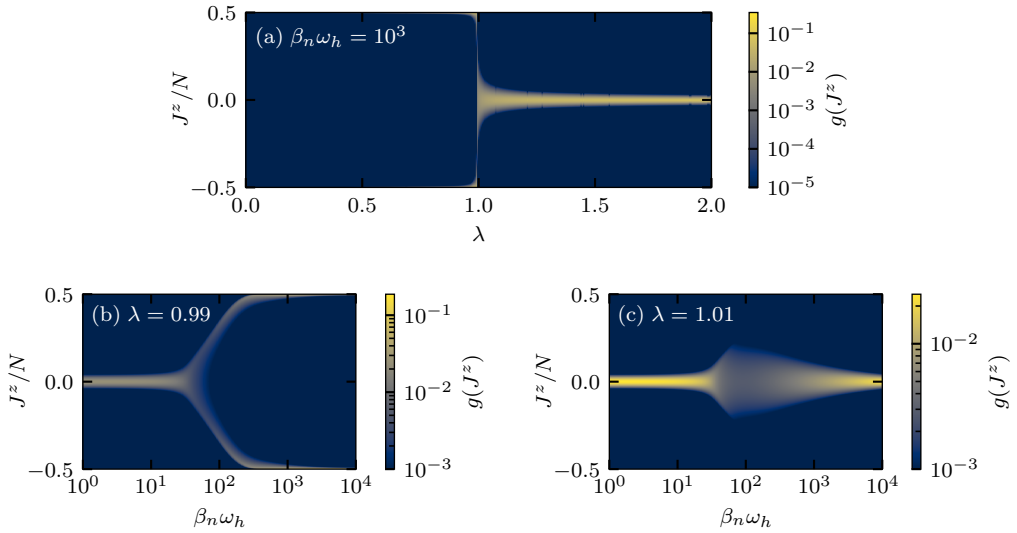

Figure 4.7: Nuclear distribution function $g(J^z)$ at the inverse electron spin temperature of $\beta_e\omega_h = 0.5$. (a) $g(J^z)$ depending on the hyperfine anisotropy parameter λ at the fixed inverse nuclear spin temperature $\beta_n\omega_h = 10^3$. (b) $g(J^z)$ depending on β_n for $\lambda = 0.99 < \lambda_c$. (c) $g(J^z)$ depending on β_n for $\lambda = 1.01 > \lambda_c$. The figure is taken from Ref. [199].

eigenstates of H_{HF} that is related to a single spin flip process would connect the ground state to another spin state of higher energy. However, at $T_e = T_n = 0$ we evaluate $h_e(\varepsilon) = h_n(\varepsilon) = 0$ for $\varepsilon > 0$ according to Eq. (4.26), and hence the total transition rate vanishes. Thus, the two ground states for $|\lambda| < 1$ are disconnected at low temperatures. The two ground states for $|\lambda| > 1$, in contrast, are directly connected by a single spin flip. Since no energy change is required for this transition, it can take place even at zero temperatures. This difference in the nature of the ground state is reflected in the mean-field approach, cf. Sec. 3.2, by two separate polaron states oriented along the z axis for $|\lambda| < 1$ and continuously connected polaron states within the (xy) plane for $|\lambda| > 1$.

The distribution function of the total nuclear spin z component illustrates the change of the ground states. We display $g(J^z)$ as a function of the anisotropy parameter λ for fixed inverse temperatures, $\beta_e\omega_h = 0.5$ and $\beta_n\omega_h = 10^3$, such that we expect the formation of a polaron in the system comprising $N = 10^3$ nuclear spin, see Fig. 4.7(a). The change of quantum numbers J^z constituting the nuclear polaron state as a function of the parameter λ becomes clearly visible: For $\lambda < 0$, $g(J^z)$ displays contributions at $J^z/N = \pm 1/2$ corresponding to the twofold degenerate ground state. As these peaks of $g(J^z)$ are relatively sharp, they are hard to detect in the figure. At $\lambda = 1$, the distribution function spreads uniformly from $J^z/N = -0.5$

to $J^z/N = 0.5$ reflecting the N-fold degeneracy of the ground state. For $\lambda > 1$, the distribution of J^z narrows around $J^z = 0$ with a remaining width that originates from the nonzero temperatures in the calculations.

The temperature-dependent nuclear distribution reveals the convergence towards the respective ground state with increasing β_n. As an example for an almost isotropic system with an anisotropy parameter slightly below or above the value $\lambda_c = 1$, we consider $\lambda = 0.99 < \lambda_c$, see Fig. 4.7(b), and $\lambda = 1.01 > \lambda_c$, see Fig. 4.7(c). For $\lambda = 0.99$, the two branches related to the nuclear-spin polaron state oriented along the z axis form similar to the Ising limit, cf. Fig. 4.4(a). For $\lambda = 1.01$, the weight of the distribution function $g(J^z)$ focuses around $J^z = 0$ for low nuclear spin temperatures and indicates the spin orientation within the (xy) plane. Compared to the results for a larger anisotropy parameter, $\lambda = 2$, cf. Fig. 4.4(e), the distribution function $g(J^z)$ for $\lambda = 1.01$ exhibits a somewhat blurred behavior close to the crossover temperature. Decreasing the nuclear spin temperature below the crossover temperature, $g(J^z)$ first spreads to a broader range of J^z before it eventually focuses around zero.

4.8 Temporal spin fluctuations

The nuclear polaron is a strongly correlated spin state and significantly differs from the randomly aligned nuclear spins in the high temperature limit. As a consequence, the overall spin dynamics in the system are massively affected by the formation of the polaronic state. For the analysis of the temporal evolution of the system, we examine the autocorrelation functions of the charge carrier spin and the total nuclear spin respectively in the subsequent sections and reveal profound differences in the temporal spin fluctuations depending on the selected temperature regime. In particular, the autocorrelation functions at low temperatures exhibit long living spin correlations for a hyperfine interaction with anisotropy parameter $|\lambda| \leq 1$.

4.8.1 Autocorrelation function of the charge carrier spin

The autocorrelation function of the localized electron or hole spin is directly accessible by spin noise measurements with optical techniques [121, 123, 125, 215–217]. These noninvasive measurements allow for an undisturbed study of the temporal evolution of the optically responsive charge carrier spin [218]. In the framework of the Lindblad formalism, Eq. (4.1), the autocorrelation function $C_S^\alpha(t)$ of the charge carrier spin $\mathbf{S}$ with $\alpha \in \{x, y, z\}$ is given by

$$C_S^\alpha(t) = \langle S^\alpha(0) S^\alpha(t) \rangle = \mathrm{Tr}[\rho_0 S^\alpha S^\alpha(t)] = \mathrm{Tr}[S^\alpha \mathcal{L}(S^\alpha \rho_0)], \tag{4.37}$$

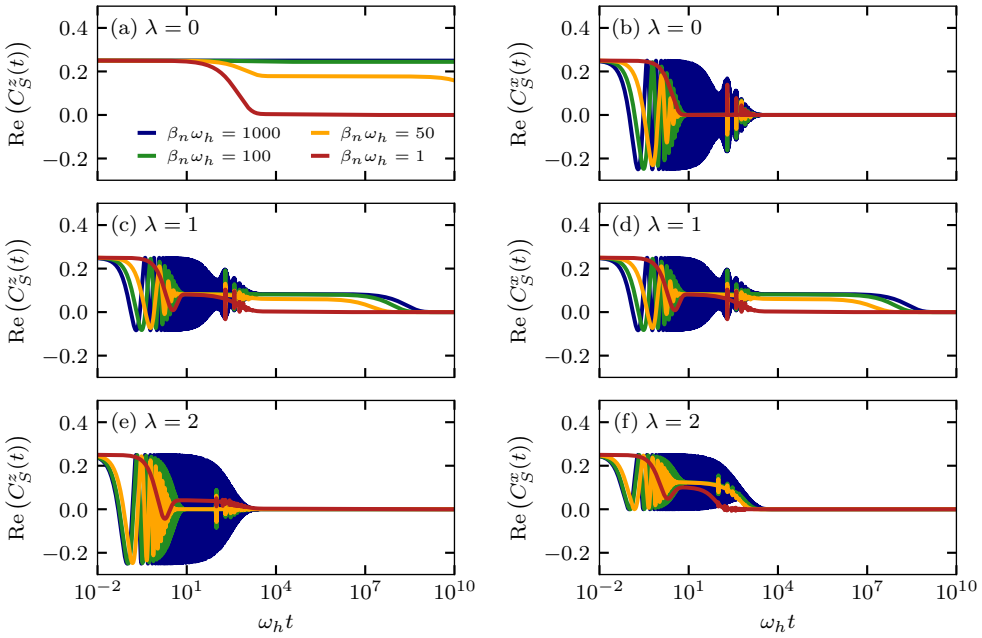

Figure 4.8: Real part of the autocorrelation function of the charge carrier spin coupled to $N = 10^3$ nuclear spins. The flip rates are set to $W_e^0 = 10^{-3}\omega_h$ and $W_n^0 = 10^{-6}\omega_h$ respectively. The left panels present the spin z autocorrelation, and the right panels relate to the in-plane spin component x. Results for three different values of the hyperfine anisotropy parameter are presented: $\lambda = 0$ (upper panels), $\lambda = 1$ (middle panels), and $\lambda = 2$ (lower panels). The inverse electron spin temperature is consistently fixed at $\beta_e\omega_h = 0.5$ whereas the inverse nuclear spin temperature is varied. The legend in panel (a) applies to the entire figure. The figure is taken from Ref. [199].

where the Liouville operator $\mathcal{L}$ governs the time evolution of the system. While the superoperator $\mathcal{L}$ is applied to the density operator ρ in Eq. (4.1), it acts on the operator product $S^\alpha\rho_0$ in the definition above [219]. Since we are interested in an observable whose measurement provides a real value, we examine the real part of the correlation function $C_S^\alpha(t)$ in the following which corresponds to the symmetrized spin autocorrelation,

$$\mathrm{Re}(C_S^\alpha(t)) = \frac{1}{2}\left[\langle S^\alpha(0)S^\alpha(t)\rangle + \langle S^\alpha(t)S^\alpha(0)\rangle\right]. \tag{4.38}$$

Figure 4.8 presents the data for $\mathrm{Re}(C_S^z(t))$ as well as $\mathrm{Re}(C_S^x(t))$ in the spin system with size $N = 10^3$ for three cases of the hyperfine anisotropy, $\lambda = 0$, $\lambda = 1$, and $\lambda = 2$. For the charge carrier spin with the length $1/2$, the initial value

unambiguously yields $\mathrm{Re}(C_S^\alpha(0)) = 1/4$. However, the subsequent evolution of the spin autocorrelation depends strongly on the respective hyperfine scenario and the installed temperatures.

In the system with Ising-type hyperfine interaction, $\lambda = 0$, the electron spin z component decays at high temperatures on a timescale given by the electron spin flip rate W_e^0, here $W_e^0 = 10^{-3}\omega_h$, see Fig. 4.8(a) (red line). Decreasing the nuclear spin temperature, the autocorrelation function does not decay completely to zero anymore within the presented time range of up to $t\omega_h = 10^{10}$ but to a plateau (orange line). This plateau lifts when reducing the nuclear spin temperature until no decay is visible in the presented time range anymore (blue line). At finite nonzero temperatures, however, we expect an eventual decay to zero on a prolonged time scale, $\mathrm{Re}(C_S^z(t)) = 0$ for $t \to \infty$. This ultimate decay is a result of the exponentially suppressed spin flips according to Eq. (4.26) which occur with a small but nonvanishing rate at nonzero temperatures.

The autocorrelation function of the charge carrier spin x component for the Ising limit of the hyperfine interaction approaches zero relatively fast in contrast to $\mathrm{Re}(C_S^z(t))$, see Fig. 4.8(b). At high temperatures (red line), the decay takes place on the time scale determined by the hyperfine fluctuations, $1/\omega_h$, as the spin $\mathbf{S}$ precesses around the randomly fluctuating z component of the Overhauser field. At lower nuclear spin temperatures, an oscillatory component to $\mathrm{Re}(C_S^x(t))$ emerges in the system with $\lambda = 0$ (orange line). When the nuclear spins start to align along the z direction forming the nuclear-spin polaron state, the spin $\mathbf{S}$ precesses in the (xy) plane. Lowering the temperature, the z component of the Overhauser field becomes stronger such that the electron precession frequency increases (green line). Simultaneously, the reduced fluctuations of the Overhauser field produce a prolonged envelope function of the oscillatory component. While the dephasing time results from the hyperfine fluctuations with the rate ω_h at high temperatures, the envelope of $\mathrm{Re}(C_S^x(t))$ is governed by the rate W_e^0 in the low temperature regime (blue line).

We note that the equidistant spikes in the electron spin autocorrelation function $\mathrm{Re}(C_S^x(t))$ for $\lambda = 0$ are an artifact of the box model approximation here. For equal hyperfine coupling constants in the finite system ($A_k \equiv A_0$), the Overhauser field acting on the electron spin is quantized and the individual components are an integer multiple of a_0. As a consequence, all electron spin precession frequencies are commensurate producing a rephasing at times $T_n = 2\pi n/a_0$ with an integer n, i.e., at $T_n\omega_h = 2\pi n\sqrt{N}$ for $|\lambda| \leq 1$ which yields $T_1\omega_h \approx 200$ for $N = 10^3$. This effect becomes visible in the autocorrelation functions for $\lambda = 1$ and $\lambda = 2$ as well.

The autocorrelation functions in the isotropic system with $\lambda = 1$ exhibit similar oscillatory behavior as $\mathrm{Re}(C_S^x(t))$ for $\lambda = 0$. Naturally, for $\lambda = 1$ the autocorrelation

functions of the various spin components coincide, i.e., $\mathrm{Re}(C_S^x(t)) = \mathrm{Re}(C_S^y(t)) = \mathrm{Re}(C_S^z(t))$, see Fig. 4.8(c) and Fig. 4.8(d) respectively. At high temperatures, the electron spin autocorrelation functions (red lines) conform to the analytic prediction, Eq. (2.17), derived by Merkulov et al. [55] for times $t\omega_h \leq 10^2$. As the prediction was performed for the closed isotropic system in the frozen Overhauser field approximation, deviations from Eq. (2.17) are found on longer time scales exceeding $t\omega_h = 10^2$. Here, the dynamics in the nuclear spin bath and the reservoir-induced spin flips are no longer negligible. According to the prediction by Merkulov et al., the spin autocorrelation reaches a plateau at a third of the starting value $\mathrm{Re}(C_S^\alpha(0))/3 = 1/12$ after roughly $t\omega_h = 10$. At times $t\omega_h \approx 10^3$, however, the plateau decays governed by the rate W_e^0 for the coupling to the thermal reservoir. A decrease in the nuclear spin temperature yields again an oscillatory component similar to $\mathrm{Re}(C_S^x(t))$ for $\lambda = 0$. In the system with $\lambda = 1$, the autocorrelation functions oscillate around the value 1/12 as a result of the isotropic polaron formation: The emerging Overhauser field is isotropically oriented and therefore the component parallel to the α axis protects part of the autocorrelation function $\mathrm{Re}(C_S^\alpha(t))$ from decay. The perpendicular Overhauser field components, in contrast, produce the oscillations which again become faster with strengthening Overhauser field while their dephasing to the plateau of 1/12 is prolonged from $1/\omega_h$ to $1/W_e^0$ when increasing β_n.

At low temperatures, the plateau persists for times up to $t\omega_h \approx 10^9 > \omega_h/W_e^0$ which is longer than dictated by the electron spin flip rate W_e^0. Eventually, the plateau decays to zero even at minimum temperatures. The specific rate of the decay depends on the effective spin temperatures as well as the spin flip rates W_e^0 and W_n^0. The reason for the decay is the rotation of the nuclear-spin polaron state in the isotropic system. For instance, the polaron state, where the electron spin is initially oriented along z direction, may rotate on the Bloch sphere to a state pointing in any other direction producing a loss of temporal spin correlation without a change of the energy. For the rate of polaron rotation at low temperatures, we obtain

$$W_r = \frac{W_e^0}{N^2} + \frac{W_n^0}{N} \tag{4.39}$$

from considering the diffusion process on the diagonal of the operator $S^z\rho_0$ which enters $C_S^\alpha(t)$ via the definition, Eq. (4.37). For a detailed derivation of the rotation rate, Eq. (4.39), we refer to the next section. The evaluation for the applied parameters ($W_e^0 = 10^{-3}\omega_h$, $W_n^0 = 10^{-6}\omega_h$ and $N = 10^3$) yields $W_r = 2 \times 10^{-9}\omega_h$ which matches the data in Figs. 4.8(c) and 4.8(d) (blue lines respectively).

In the spin system with anisotropic hyperfine interaction with $\lambda = 2$, the hyperfine interaction along the x and y direction is a factor of two stronger than along the z axis. The autocorrelation functions $\mathrm{Re}(C_S^x(t))$ and $\mathrm{Re}(C_S^z(t))$ for this system, see

Fig. 4.8(e) and Fig. 4.8(f) respectively, resemble the data for the isotropic case with slight modifications. The high-temperature autocorrelation functions (red lines) for shorter time scales match the analytically predicted behavior, Eq. (2.17), with small deviations produced by the amplification of the hyperfine interaction in the (xy) plane: The dip in $\mathrm{Re}(C_S^x(t))$ and $\mathrm{Re}(C_S^z(t))$ is shifted to earlier times and the plateau is lowered (z component) or lifted (x component). For the low temperature results, the electron precession about the emerging Overhauser field shows again. The autocorrelation function $\mathrm{Re}(C_S^z(t))$ oscillates around zero as the Overhauser field forms within the (xy) plane for $|\lambda| > 1$. When decreasing the temperature, the oscillations become faster, and the envelope function passes from a dephasing with the rate ω_h in the disordered nuclear spin system to a prolonged envelope function with a dephasing rate governed by reservoir-induced spin flips. We note that the precession frequency of the electron spin at the same temperatures is faster for $\lambda = 2$ than for $\lambda = 1$ due to the enhancement of the in-plane Overhauser field components by a factor of two. The oscillatory behavior of the correlation function $\mathrm{Re}(C_S^x(t))$ at lower temperatures is similar for $\lambda = 1$ and $\lambda = 2$. However, the spin x fluctuations oscillate around half of the initial spin correlation $\mathrm{Re}(C_S^x(0))/2 = 1/8$ for $\lambda = 2$, since the Overhauser field polarization related to the polaron state forms isotropically within the (xy) plane. Interestingly, the plateau of 1/8 decays on the time scale $t\omega_h \approx 10^3$ for $\lambda = 2$ even at low temperatures (blue line) which is relatively fast compared to the isotropic system. The profound difference in the long time behavior of the correlation function at low temperatures originates from the differing nature of the polaronic ground state as demonstrated in Sec. 4.7. This effect is discussed in more detail in the next section.

4.8.2 Rotation of the polaron state in the isotropic system

The long living electron spin correlations in the polaronic phase of the isotropic system and their ultimate decay to zero on prolonged time scales raise the question about the mechanism behind the loss of correlation. Previously, we phenomenologically attributed the final decay of $\mathrm{Re}(C_S^\alpha(t))$ to the rotation of the isotropic nuclear-spin polaron state and stated the related rotation rate W_r, Eq. (4.39). Here, we extend the discussion employing the relevant rate equations and present a comprehensive derivation of the rate W_r.

To this end, we focus on the temporal evolution of the operator product $O\rho_0$. The product with $O \equiv S^z$ enters the evaluation of the electron spin autocorrelation function $C_S^z(t)$ according to Eq. (4.37), however, the following analysis can also be extended to $O \equiv J^z$, which we address later. Previously, we aggregated the elements of the density operator ρ into the elements $p^J_{J^z_m,\sigma_m;J^z_n,\sigma_n}$ which combine different

degeneracy indices ζ, cf. Eq. (4.17). In conformity with this procedure, we introduce the elements $\chi^J_{J^z_m,\sigma_m;J^z_n,\sigma_n}$ of the product $O\rho_0$,

$$\begin{aligned}\chi^J_{J^z_m,\sigma_m;J^z_n,\sigma_n} &= \sum_\zeta \langle \psi^{\sigma_m,\zeta}_{J,J^z_m} | O\rho_0 | \psi^{\sigma_n,\zeta}_{J,J^z_n} \rangle \\ &= p^J_{J^z_n,\sigma_n;J^z_n,\sigma_n} \, \langle \psi^{\sigma_m,\zeta}_{J,J^z_m} | O | \psi^{\sigma_n,\zeta}_{J,J^z_n} \rangle \, .\end{aligned} \tag{4.40}$$

Since the steady-state density operator ρ_0 is diagonal in the energy eigenbasis, it allows for the replacement by the associated diagonal elements $p^J_{J^z_n,\sigma_n;J^z_n,\sigma_n}$ in the second line of Eq. (4.40). We note that the degeneracy index ζ that occurs on the right hand side of the definition can take an arbitrary exemplary value $\zeta \in \{1, \dots, g_N(J)\}$ as the related elements all have the same value. The temporal evolution of $O\rho_0$, which enters the spin autocorrelation function according to Eq. (4.37), is governed by the Liouvillian $\mathcal{L}$ that was originally introduced in the context of the time evolution of the density operator, cf. Eq. (4.1). Accordingly, the differential equations for the matrix elements $\chi^J_{J^z_m,\sigma_m;J^z_n,\sigma_n}$ comply with the rate equations for $p^J_{J^z_m,\sigma_m;J^z_n,\sigma_n}$, see Eq. (4.18).

Aiming at the low temperature dynamics, we set $T_e = T_n = 0$ in the following analysis for simplicity. As a consequence, the density operator only has nonzero entries in the elements $p^{N/2}_{J^z,-;J^z,-}$ which are related to the ground state of the hyperfine Hamiltonian characterized by $J = N/2$ and $\sigma_m = \sigma_n = -$, cf. Sec. 4.7. Moreover, the operator O obeys the relations $[O, \mathbf{J}^2] = [O, J^z + S^z] = 0$ for $O \equiv S^z$ (or $O \equiv J^z$). Hence, O does not produce any transitions in the density operator to subspaces with $J < N/2$ nor a change of the box model index J^z, which as we recall actually corresponds to the shifted total spin component $S^z + J^z + 1/2$. Thus, it is sufficient to focus on matrix elements of the type $\chi^{N/2}_{J^z,\sigma;J^z,-}$ since the remaining elements of $O\rho_0$ vanish at zero temperatures.

The rate equations of these elements differ for diagonal and off-diagonal contributions, $\chi^{N/2}_{J^z,-;J^z,-}$ and $\chi^{N/2}_{J^z,+;J^z,-}$ respectively. For the off-diagonal elements, we obtain the temporal evolution according to

$$\begin{aligned}\partial_t \chi^{N/2}_{J^z,+;J^z,-} = -\Bigg\{ & i\Delta^{+,J,J^z}_{-,J,J^z} + \sum_{\tau=-1}^{1} \sum_{J',\sigma'} \Big[\Gamma^\tau_{J',J}(J^z+\tau, J^z+\tau; \sigma', \sigma', +, +) \\ & + \Gamma^\tau_{J',J}(J^z+\tau, J^z+\tau; \sigma', \sigma', -, -) \Big] \Bigg\} \chi^{N/2}_{J^z,+;J^z,-}\end{aligned} \tag{4.41}$$

from adjusting Eq. (4.18) appropriately. Here, the coupling to other matrix elements provided by the last line of Eq. (4.18) drops out, since the related rate $\Gamma^\tau_{J,J'}(J^z, J^z; +, -, \sigma, \sigma')$ is zero due to the energy mismatch in the first Kronecker

delta in definition, Eq. (4.25). The rate equations for the off-diagonal elements $\chi^{N/2}_{J^z,+;J^z,-}$ produces damped oscillations with frequency $\Delta^{+,J,J^z}_{-,J,J^z} = A_0(J+1/2)$ whose decay rate is determined by the summed contributions in Eq. (4.41). The decay rate is assumed to be roughly proportional to $W_e^0 + NW_n^0$ based on Eq. (4.25) from approximating the matrix elements $\langle\psi^{\sigma_a,\zeta}_{J,a^z}|s^\tau_k|\psi^{\sigma_c,\zeta'}_{J',J^z_a-\tau}\rangle$ by a constant, exploiting $g_N(N/2) = g_{N-1}((N-1)/2) = 1$ and minding that the function $h_k(\varepsilon)$ according to Eq. (4.26) corresponds to the Heaviside function $\Theta(-\varepsilon)$ for $T_e = T_n = 0$. The prefactor for the proportionality to $W_e^0 + NW_n^0$ can be predicted by evaluating $\langle\psi^{\sigma_a,\zeta}_{J,a^z}|s^z_k|\psi^{\sigma_c,\zeta'}_{J',J^z_a-\tau}\rangle \approx 1/2$ and $\langle\psi^{\sigma_a,\zeta}_{J,a^z}|s^{\pm1}_k|\psi^{\sigma_c,\zeta'}_{J',J^z_a-\tau}\rangle \approx 1/\sqrt{8}$ according to Eq. (4.15) such that the sum of their squares produces one half as a constant of proportionality. In the low temperature result for $C^z_S(t)$ (blue line in Fig. 4.8(c)), these findings are reflected by the fast oscillatory component dephasing on the time scale $1/(W_e^0 + NW_n^0) = 500/\omega_h$ for the given choice of parameters, where the prefactor of a half is canceled out by the prefactors resulting from the definition of the Lindblad equation, Eq. (4.1).

The rate equation for the diagonal elements $\chi^{N/2}_{J^z,-;J^z,-}$ is obtained analogously from Eq. (4.18) minding that $J' = N/2$ and $\sigma = \sigma' = -$ in the ground state,

$$\begin{aligned}\partial_t \chi^{N/2}_{J^z,-;J^z,-} = 2\sum_{\tau=-1}^{1}\Big\{&-\Gamma^\tau_{N/2,N/2}(J^z+\tau, J^z+\tau;-,-,-,-)\chi^{N/2}_{J^z,-;J^z,-}\\ &+\Gamma^\tau_{N/2,N/2}(J^z, J^z;-,-,-,-)\chi^{N/2}_{J^z-\tau,-;J^z-\tau,-}\Big\}. \end{aligned} \tag{4.42}$$

In the above equation, the contribution for $\tau = 0$ is canceled out since the two terms in the brace equal one another except for the sign. Consequently, we restrict our further analysis to $\tau = \pm 1$ and obtain the corresponding rate according to Eq. (4.25) where we insert $g_N(N/2) = g_{N-1}((N-1)/2) = 1$ and $h_k(\varepsilon) = \Theta(-\varepsilon)$ due to $T_e = T_n = 0$,

$$\begin{aligned}&\Gamma^\tau_{N/2,N/2}(J^z, J^z;-,-,-,-) =\\ &\quad W_e^0\,\langle\psi^{-,\zeta}_{N/2,J^z}|S^\tau|\psi^{-,\zeta'}_{N/2,J^z-\tau}\rangle\,\langle\psi^{-,\zeta'}_{N/2,J^z-\tau}|(S^\tau)^\dagger|\psi^{-,\zeta}_{N/2,J^z}\rangle\\ &\quad + NW_n^0\,\langle\psi^{-,\zeta}_{N/2,J^z}|I^\tau_k|\psi^{-,\zeta'}_{N/2,J^z-\tau}\rangle\,\langle\psi^{-,\zeta'}_{N/2,J^z-\tau}|(I^\tau_k)^\dagger|\psi^{-,\zeta}_{N/2,J^z}\rangle\,. \end{aligned} \tag{4.43}$$

For the first rate occurring in Eq. (4.42), J^z in the above expression has to be replaced by $J^z + \tau$.

For further simplification of the rate equation, Eq. (4.42), we again approximate the matrix elements $\langle\psi^{-,\zeta}_{N/2,J^z}|s^\tau_k|\psi^{-,\zeta'}_{N/2,J^z-\tau}\rangle \approx 1/\sqrt{8}$ by a constant respecting definition, Eq. (4.15). When the resulting rate $\Gamma^\tau_{N/2,N/2}(J^z, J^z;-,-,-,-) = (W_e^0 + NW_n^0)/8$

is inserted into the Eq. (4.42), the simplified rate equation becomes

$$\partial_t \chi^{N/2}_{J^z,-;J^z,-} = \frac{W_e^0 + NW_n^0}{4} \left(\chi^{N/2}_{J^z-1,-;J^z-1,-} - 2\chi^{N/2}_{J^z,-;J^z,-} + \chi^{N/2}_{J^z+1,-;J^z+1,-} \right). \tag{4.44}$$

Due to the coupling to one neighboring matrix element only, the rate equations for the outer elements $\chi^{N/2}_{J^z,-;J^z,-}$ with $J^z = -J+1$ or $J^z = J$ are obviously modified to

$$\partial_t \chi^{N/2}_{-J+1,-;-J+1,-} = \frac{W_e^0 + NW_n^0}{4} \left(-\chi^{N/2}_{-J+1,-;-J+1,-} + \chi^{N/2}_{-J+2,-;-J+2,-} \right), \tag{4.45a}$$

$$\partial_t \chi^{N/2}_{J,-;J,-} = \frac{W_e^0 + NW_n^0}{4} \left(\chi^{N/2}_{J-1,-;J,-} - \chi^{N/2}_{J,-;J,-} \right). \tag{4.45b}$$

In a next step, we employ the continuum limit of J^z realized for $N \to \infty$ and replace the matrix elements $\chi^{N/2}_{J^z,-;J^z,-}(t)$ by a continuous function $\chi(J^z,t)$. The above rate equation in the continuum limit is given by the differential equation

$$\partial_t \chi(J^z,t) = D\partial^2_{J^z} \chi(J^z,t) \tag{4.46}$$

with the diffusion constant $D = (W_e^0 + NW_n^0)/4$. This one-dimensional diffusion equation has the fundamental solution

$$\chi(J^z,t) = \frac{1}{\sqrt{4\pi Dt}} \exp\left(-\frac{J^{z2}}{4Dt} \right). \tag{4.47}$$

The characteristic time scale of the diffusion process on the diagonal elements $\chi(J^z,t)$ that governs the rotation of the isotropic polaron state results from the temporal evolution of the variance $\sigma^2_\chi(t) = 2Dt$ of the Gaussian distribution of J^z controlled by Eq. (4.47). Demanding that the distribution of J^z has the standard deviation of half of the maximum range $J^z \in \{-N/2, \ldots, N/2\}$, i.e., $\sigma^2_\chi(t_r) = (N/2)^2$ after a characteristic time t_r, yields the relation $2Dt_r = (N/2)^2$. The related rotation rate is identified as the inverse of t_r adjusted by a factor two originating from the prefactors entering the Lindblad master equation, Eq. (4.1), such that $W_r = 1/(2t_r)$. Consequently, we obtain $W_r = D/(N/2)^2$ which eventually results in the rotation rate of the isotropic polaronic state stated in Eq. (4.39).

Interestingly, the isotropic polaron state causes a loss of the spin coherence on the prolonged time scale t_r even at zero effective spin temperatures. This provides a sharp contrast to the anisotropic system with $|\lambda| < 1$ where we expect nondecaying spin autocorrelation functions for $T_e = T_n = 0$. For $|\lambda| < 1$, the twofold degenerate ground states are disconnected at zero temperatures since any flip rates $\Gamma^\tau_{J,J'}(\ldots)$ vanish either as a result of the associated energy increase or the inaccessibility of the related eigenstates by a single spin flip mediated by the operator s^τ_k.

For the analysis of the anisotropic system with $|\lambda| > 1$, we follow the above analysis up to the rate equation, Eq. (4.42), and the simplifications of the related transition rate, Eq. (4.43). However, the ground state at $|\lambda| > 1$ is restricted to $J^z = 0$ and $J^z = 1$ such that the coupled differential equations for the relevant diagonal elements $\chi^{N/2}_{0,-;0,-}$ and $\chi^{N/2}_{1,-;1,-}$ read

$$\partial_t \chi^{N/2}_{0,-;0,-} = \frac{W_e^0 + NW_n^0}{4} \left(-\chi^{N/2}_{0,-;0,-} + \chi^{N/2}_{1,-;1,-} \right), \tag{4.48a}$$

$$\partial_t \chi^{N/2}_{1,-;1,-} = \frac{W_e^0 + NW_n^0}{4} \left(\chi^{N/2}_{0,-;0,-} - \chi^{N/2}_{1,-;1,-} \right). \tag{4.48b}$$

A single spin flip between the two ground states at $|\lambda| > 1$ produces a complete loss of spin correlation, whereas the correlation at $\lambda = 1$ is gradually lost by successive spin flips. Thus, the autocorrelation function $\mathrm{Re}(C_S^z(t))$ for $|\lambda| > 1$ decays with the rate $(W_e^0 + NW_n^0)/2$, which is by a factor of N^2 faster than in the isotropic case. Accordingly, the spin autocorrelation function $C_S^z(t)$ for $\lambda = 2$ (blue line in Fig. 4.8(e)) dephases on the time scale $1/(W_e^0 + NW_n^0) = 500/\omega_h$ at the selected flip rates.

4.8.3 Autocorrelation function of the nuclear spin

As the formation of the nuclear-spin polaron state implies a profound reorientation of the nuclear spins, the question about the robustness of the nuclear spin state arises. Albeit the nuclear spin autocorrelation function is not directly accessible by optical techniques in experiments, it provides a valuable theoretical tool for the investigation of the nuclear spin fluctuations [220, 221]. Analogously to $C_S^\alpha(t)$ for the charge carrier spin, we introduce the autocorrelation function $C_J^\alpha(t)$ of the total nuclear spin,

$$C_J^\alpha(t) = \langle J^\alpha(0) J^\alpha(t) \rangle = \mathrm{Tr}[\rho_0 J^\alpha J^\alpha(t)] = \mathrm{Tr}[J^\alpha \mathcal{L}(J^\alpha \rho_0)], \tag{4.49}$$

with $\alpha \in \{x, y, z\}$.

Figure 4.9 presents the results of $\mathrm{Re}(C_J^z(t))$ for the three physically most relevant hyperfine scenarios, (a) $\lambda = 0$, (b) $\lambda = 1$, and (c) $\lambda = 2$. The fast oscillations observed in the electron spin autocorrelation functions are absent here, and we find a plain decay process at rather long time scales. This decay depends on the hyperfine anisotropy as well as on the spin temperatures and the reservoir-related spin flip rates. Since we expect an ultimate decay of $\mathrm{Re}(C_J^z(t)) \to 0$ for $t \to \infty$ at nonzero temperatures for any value of the hyperfine anisotropy parameter, we introduce the decay time τ_d as that time at which the nuclear spin autocorrelation function has decreased to the fraction of $1/e$ of its initial value, i.e., $\mathrm{Re}(C_J^z(\tau_d)) = \mathrm{Re}(C_J^z(0))/e$.

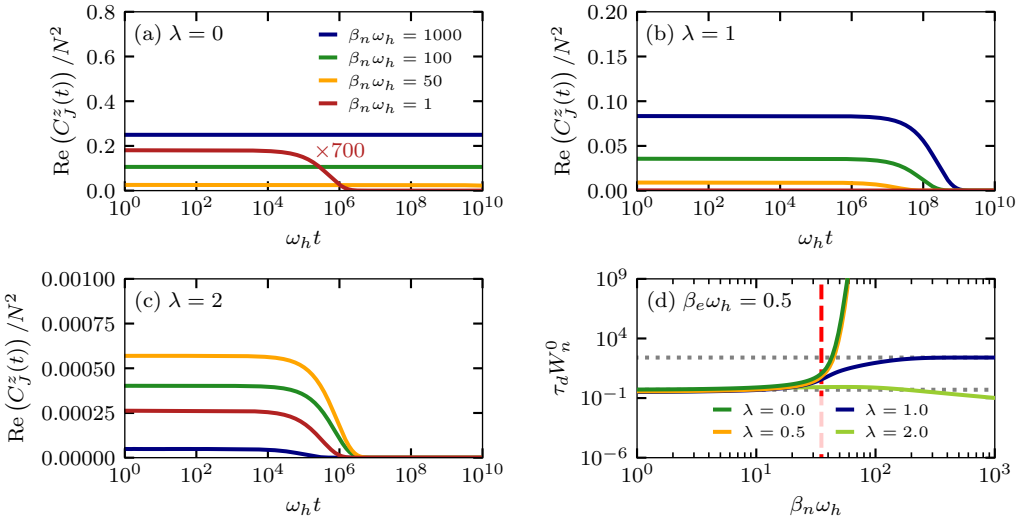

Figure 4.9: Autocorrelation function of the total nuclear spin z component for three different values of the hyperfine anisotropy parameter, (a) $\lambda = 0$, (b) $\lambda = 1$, and (c) $\lambda = 2$ with $N = 10^3$ respectively. The flip rates are set to $W_e^0 = 10^{-3}\omega_h$ and $W_n^0 = 10^{-6}\omega_h$. The inverse electron spin temperature is fixed at $\beta_e\omega_h = 0.5$. The inverse nuclear spin temperature β_n is varied; the legend in panel (a) applies to panels (b) and (c) as well. Panel (d) displays the decay time τ_d as a function of β_n for the different values of λ. The inverse nuclear crossover temperature $\beta_{n,p} = 327$ for $|\lambda| \leq 1$ is indicated by the red dashed vertical line. The figure is taken from Ref. [199].

The decay time τ_d as a function of the inverse nuclear spin temperature displays strongly diverging behavior for the various values of λ, see Fig. 4.9(d) for which $\beta_e\omega_h = 0.5$. While the decay time is consistently governed by the nuclear spin flip rate W_n^0 (here $W_n^0 = 10^{-6}\omega_h$) at high temperatures independent of the parameter λ, the behavior of τ_d when increasing β_n differs depending on λ. The high temperature limit $\tau_d \approx 1/(2W_n^0)$ is indicated by the lower dotted gray horizontal line in Fig. 4.9(d). For $|\lambda| < 1$, the decay time τ_d strongly increases above the inverse crossover temperature for polaron formation $\beta_{n,p} = 327$, see Fig. 4.9(d) (dark green line for $\lambda = 0$, orange line for $\lambda = 0.5$). Similarly to the electron spin autocorrelation function $\mathrm{Re}(C_S^z(t))$ depicted in Fig. 4.8(a), the nuclear spin fluctuations $\mathrm{Re}(C_J^z(t))$ for the Ising-type hyperfine interaction do not decay visibly in the presented time frame in Fig. 4.9(a). Due to the twofold degenerate polaronic ground state maximizing J as well as J^z, the relevant elements of $J^z\rho_0$ can be mixed only by several consecutive spin flips, each exponentially suppressed by the temperature-dependent flip rates. Consequently, τ_d increases exponentially below the crossover temperature for $|\lambda| <$

1.

For the isotropic hyperfine interaction, $\lambda = 1$, the decay time τ_d (blue line in Fig. 4.9(d)) at low temperatures is bound to an upper limit provided by the rate W_r of the rotation of the polaron state, Eq. (4.39), which yields $W_r = 2 \times 10^{-9}\omega_h$. The related decay time $1/(2W_r) = 0.25 \times 10^9 \omega_h$ is indicated by the upper dotted gray horizontal line in Fig. 4.9(d) and matches the upper bound of τ_d. We note that the derivation of the rotation rate of the polaronic state in the isotropic system presented in the previous subsection can also be conducted for $O \equiv J^z$ in Eq. (4.40). This analysis directly provides W_r as the characteristic rate for the diffusion process of the diagonal elements of $J^z\rho_0$ which governs the loss of the autocorrelation $C_J^z(t)$.

In the anisotropic system with $\lambda = 2$, the decay of the correlation function $C_J^z(t)$ is regulated by the coupled rate equations for the twofold degenerate ground state with box-model quantum numbers $J^z = 0$ and $J^z = 1$, Eqs. (4.48a) and (4.48b). Here, $\chi^J_{J^z,\sigma;J^z,\sigma}$ is introduced from $O \equiv J^z$ in Eq. (4.40). Accordingly, $\mathrm{Re}(C_J^z(t))$ decays on the time scale $1/(W_e^0 + NW_n^0) = 500/\omega_h$ similarly as $\mathrm{Re}(C_S^z(t))$. The twofold degenerate ground state does not protect the spin system from a loss of coherence, contrary to the Ising limit of the hyperfine interaction, since the two ground state elements $\chi^{N/2}_{J^z,-;J^z,-}$ with $J^z = 0$ and $J^z = 1$ are directly connected by a single spin flip.

4.9 Chapter conclusion

In this chapter, we extended the investigation of the polaron formation under optical cooling of the nuclear spins to the case of a general anisotropic hyperfine interaction. The situation of differing effective spin temperatures for the localized charge carrier spin and the surrounding nuclear spins was established by a Lindblad formalism which incorporates the coupling to two separate temperature-inducing reservoirs. The Lindblad master equation allows to access the dynamics of the full density operator ρ in contrast to the rate equations employed in the previous chapter which were limited to the diagonal elements of ρ in the eigenbasis of the hyperfine Hamiltonian H_{HF}. In the special case of the hyperfine interaction in the Ising limit, the Lindblad formalism exactly reproduces the steady-state results of the rate equations. Furthermore, the Lindblad equation enables the examination of the polaron formation in the physically relevant cases of an isotropic system and strong in-plane hyperfine interaction, e.g., $\lambda = 2$. These cases capture the localized electron or light hole spin respectively. The distribution of the hyperfine coupling constants only enters as an effective number of nuclear spins in the dynamics and does not change the overall temperature-dependent behavior. Therefore, we applied the box

model approximation of the hyperfine coupling constants which provides numerical access to a system with $N = 10^3$ nuclear spins. The anticorrelation of the charge carrier spin and the nuclear spins in this system indicates the orientation of the polaronic state along the axis of the strongest hyperfine interaction. Moreover, the temperature criterion for the polaron formation derived from the rate equations was generalized to arbitrary anisotropic hyperfine interaction. The distribution functions of the total nuclear spin, $g(J^z)$ and $g(J^{p2})$, reveal a quantum phase transition which the system undergoes for a change of the hyperfine anisotropy parameter λ. At the value, $\lambda_c \equiv 1$, the degeneracy of the ground state of H_{HF} changes from a twofold degenerate ground state for $\lambda < \lambda_c$ to an N-fold degenerate ground state at λ_c back to a twofold degenerate ground state for $\lambda > \lambda_c$. Finally, the autocorrelation functions of the charge carrier spin and the nuclear spin respectively were examined with regard to the polaron formation. Long living nuclear spin correlations were found for $\lambda \leq 1$, whereas the correlation of the polaronic state is rapidly lost for $\lambda > 1$ as a result of the respective nature of the ground states.

Chapter 5

Implementation of periodic optical excitation

The second part of this thesis focuses on the mode-locking effect [67, 68] that emerges under periodic optical excitation of the localized electron spin in a quantum dot. This chapter provides the fundamental basics of the realization of the mode-locking effect in optical pump-probe experiments [67, 68, 74–79]. Moreover, we outline the theoretical modeling of periodic pulse trains acting on the electron-nuclear spin system. In the quantum mechanical description, the implementation of the pulse sequence consists of two components, namely the optical pump pulses and the time evolution between the pulses. The pump pulse excites the resident electron spin to the bound trion state, and the subsequent temporal evolution comprises the trion decay as well as the additional spin dynamics related to the hyperfine interaction and the precession about the external magnetic field. We address these two parts separately in the following and develop an efficient procedure for their numerical implementation. In particular, the dynamics between pulses are tackled since the straightforward approach would require the handling of nonhermitian square matrices which have a row number of the squared Hilbert space dimension. We present a procedure that circumvents this computationally expensive task and allows for the calculation of the full quantum mechanical time evolution of a system with $N = 6$ nuclear spins over millions of repetition periods. Such a long simulation time is required for the convergence of the spin dynamics to a quasistationary steady state under the periodic optical excitation and enables the study of the mode-locking effect. Finally, we introduce a configuration average to make up for the relatively small system size and discuss the evaluation of the numerical results.

5.1 Pump-probe technique

Time-resolved optical measurements with pump-probe technique provide a valuable tool for the experimental investigation of ultra fast spin dynamics. Pulsed lasers periodically excite the spin system by pump pulses and record the resulting spin dynamics via temporally delayed probe pulses. Typically, the pump and probe beam originate from the same laser whose beam is split into a high intensity pump

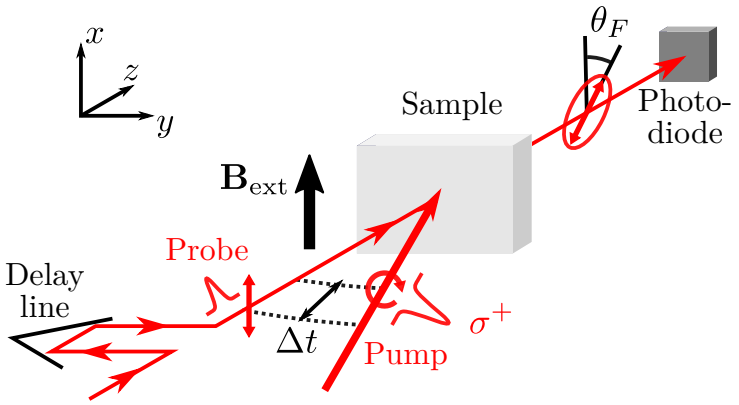

Figure 5.1: Scheme of a typical pump-probe experiment.

share and a much weaker probe proportion. Hence, pump and probe pulses have the same repetition time T_R respectively. The temporal delay T_R between consecutive pump pulses commonly is in the order of several nanoseconds. After separation from the pump beam, the probe beam is directed through a mechanical delay line to adjust the temporal displacement Δt between excitation and readout, see Fig. 5.1. Circularly polarized pump pulses are applied to the quantum dot ensemble for the excitation of the trion state as discussed in Sec. 2.2. Thereby, an electron spin polarization along the optical axis is generated. The probe beam in contrast is linearly polarized in order to read out the electron spin polarization in the quantum dots via Faraday rotation or ellipticity of the transmitted light, cf. Sec. 2.3. Since the probe pulse is much weaker than the pump pulse, it is assumed to allow for a nonperturbing measurement. Varying the temporal delay Δt and averaging the signal over several repetition periods T_R, a time-resolved signal proportional to the electron spin polarization is obtained. For the mode-locking experiments, additionally, an external magnetic field is applied to the sample perpendicular to the optical axis.

Exemplary traces for the Faraday ellipticity of self-assembled (In,Ga)As/GaAs quantum dots are presented in Fig. 5.2(a). Here, the optical axis coincides with the growth direction of the semiconductor heterostructure. The laser repetition time is $T_R = 13.2\,\text{ns}$, and the delay of $t = 0\,\text{ns}$ equals the incidence time of the pump pulse. The individual traces were recorded for different external magnetic field strengths and are vertically shifted for clarity. As a result of the transversal magnetic field, the electron spin polarization initially oriented along the optical axis starts to precess which is reflected by the oscillations of the ellipticity signal that become faster with increasing magnetic field strength. The envelope function of the oscillations indicates a dephasing of the electron spin precession due to the fluctuating hyperfine fields on

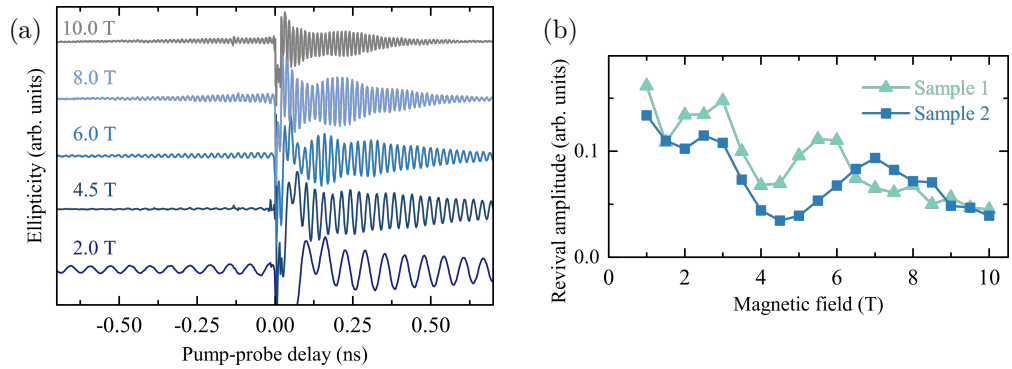

Figure 5.2: (a) Time-resolved ellipticity signal (in arbitrary units) measured for periodically pulsed (In,Ga)As/GaAs quantum dots (Sample 2) at a temperature of 4.7 K. The curves recorded at different magnetic field strengths are shifted vertically for clearness. (b) Amplitude of the revival before the pump pulse as a function of the external magnetic field for two different samples. Both panels are taken from Ref. [86].

the timescale of roughly a nanosecond. Furthermore, a shortening of the dephasing with increasing the external magnetic field strength is observed which is explained by the variation of the electron g factor in the quantum dot ensemble. As the laser pulses have a finite spectral width, they excite a subset of the inhomogeneous quantum dots whose trion excitation energies match the laser spectrum. Due to the linear dependence of the electron g factor on the trion excitation energy [77, 101, 128, 222], the excited quantum dot subensemble is subject to a spread of the electron spin precession frequencies which increases linearly with the applied magnetic field. Additional modulations of the dephasing envelope originate from oscillations of the trion hole spin [127] and vanish after the trion recombination time of roughly 400 ps [127].

Interestingly, the ellipticity signal exhibits a revival directly before the incidence of the pump pulse at negative pump-probe delay hinting at the synchronization of the spin dynamics with the periodic excitation. Indeed, the periodic pump pulses give rise to the mode-locking effect. As the nuclear spins in the quantum dot couple to the optically driven electron spin via the hyperfine interaction, the periodicity of the pump pulses is imprinted on the nuclear spin system. The nuclear spin orientation adjusts in such a way that the electron spin performs a certain number of rotations for the precession about the sum of the external magnetic field and the nuclear Overhauser field during the repetition time T_R. This effect is called nuclei-induced frequency focusing [68].

Since the data in Fig. 5.2(a) indicates a dependence of the electron spin revival

amplitude on the external magnetic field, the revival amplitudes are extracted from the time-resolved measurements systematically by fitting the data with a cosine with Gaussian envelope function [86]. The fitted amplitudes are displayed as a function of the applied magnetic field in Fig. 5.2(b). Results for two different samples with an ensemble of self-assembled (In,Ga)As/GaAs quantum dots are provided for which the In concentration in the dots differs due to the thermal annealing after production [86]. For both samples, the electron spin revival amplitude exhibits a clearly nonmonotonic dependence on the applied magnetic field. Overall, the amplitude decreases with increasing magnetic field strength. The increase is superimposed by additional modulations that differ for the two samples. We attribute these differences to the differing In and Ga content in the dots, see Sec. 6.6. However, the samples have a profound minimum of the revival amplitude at roughly 4 T in common.

5.2 Modeling optical pulses

The mode-locking experiments [67, 68] employ circularly polarized pump pulses for the periodic optical excitation of the electron spins in the singly charged quantum dots. For the theoretical description of this excitation, we recollect the optical selection rules presented in Sec. 2.2 and focus on σ^+ polarized light as an example. The description of σ^- polarized pulses would be fully analogous. For simplicity, however, we restrict ourselves to σ^+ polarization in this thesis. The σ^+ polarized laser with appropriately adjusted photon frequency can excite an electron at the conduction level with spin state $|\uparrow\rangle$ to a trion state $|\uparrow\downarrow\Uparrow\rangle$ by photo-generation of an electron-hole pair, whereas the electron spin state $|\downarrow\rangle$ is left unaffected by the pulse. We introduce $|T\rangle \equiv |\uparrow\downarrow\Uparrow\rangle$ for the trion state and address the laser excitation by the Hamiltonian for light-matter interaction assuming a classical light field,

$$H_L(t) = \left[f(t)\exp(i\varepsilon_P t) + f^*(t)\exp(-i\varepsilon_P t)\right]\left(|T\rangle\langle\uparrow| + |\uparrow\rangle\langle T|\right). \tag{5.1}$$

The envelope function of the pulse is determined by $f(t)$ and its complex conjugate $f^*(t)$; ε_P specifies the pump frequency. Furthermore, we account for the energy gap ε_T between the electron state $|\uparrow\rangle$ and the trion state $|T\rangle$ by the Hamiltonian

$$H_T = \varepsilon_T |T\rangle\langle T|. \tag{5.2}$$

The transformation of the combination $H_P(t) = H_L(t) + H_T$ into the rotating frame of the trion resonance via the unitary operator $U_T(t) = |\uparrow\rangle\langle\uparrow| + |\downarrow\rangle\langle\downarrow| + \exp(i\varepsilon_T t)|T\rangle\langle T|$ provides an adjusted time-dependent Hamiltonian for the optical excitation,

$$\begin{aligned}\tilde{H}_P(t) = &\left[f^*(t)\exp(-i[\varepsilon_P + \varepsilon_T]t) + f(t)\exp(i[\varepsilon_P - \varepsilon_T]t)\right]|\uparrow\rangle\langle T| \\ &+ \left[f^*(t)\exp(-i[\varepsilon_P - \varepsilon_T]t) + f(t)\exp(i[\varepsilon_P + \varepsilon_T]t)\right]|T\rangle\langle\uparrow|.\end{aligned} \tag{5.3}$$

Based on the rotating-wave approximation, fast oscillating contributions with frequency $(\varepsilon_P + \varepsilon_T)$ are omitted as they quickly average out. The remaining terms with frequency $\pm(\varepsilon_P - \varepsilon_T)$ are transformed back out of the rotating frame by the operator $U_T^\dagger(t)$. Finally, the Hamiltonian for the optical excitation by a pump pulse reads

$$H_P(t) = f(t)\exp(i\varepsilon_P t)\left|\uparrow\right\rangle\left\langle T\right| + f^*(t)\exp(-i\varepsilon_P t)\left|T\right\rangle\left\langle\uparrow\right| + \varepsilon_T\left|T\right\rangle\left\langle T\right|. \tag{5.4}$$

The full dynamics during a pulse are governed by the complete Hamiltonian $H(t)$ which comprises the pulse effect $H_P(t)$ as well as the additional spin dynamics in the system,

$$H(t) = H_{\mathrm{HF}} + H_{\mathrm{EZ}} + H_{\mathrm{NZ}} + H_P(t). \tag{5.5}$$

Further effects included in the Hamiltonian are the hyperfine interaction H_{HF} according to Eq. (2.11) with $\lambda = 1$ as well as the effect of the external magnetic field on the electron spin H_{EZ} and the nuclear spins H_{NZ}, Eqs. (2.2) and (2.3) respectively. The radiative decay of the trion state, see Sec. 5.3, is disregarded on the timescale of the pulse as the pulse duration amounts to a few picoseconds and therefore is relatively short compared to the recombination time of the photo-generated electron-hole pair which is of the order of several hundreds of picoseconds.

To capture the pulse effect onto the spin system, we address the transformation of the density operator ρ in the d-dimensional Hilbert space. The laser pulse incorporated in $H_P(t)$ acts on the electron spin only such that it could be described within the three-dimensional Hilbert space spanned by states, $|\uparrow\rangle$, $|\downarrow\rangle$ and $|T\rangle$. However, the hyperfine interaction couples the electron spin to the nuclear spins during the pulse such that the dynamics are extended to the full electron-nuclear spin Hilbert space with the dimension $d = 3\prod_k(2I_k+1)$. For the numerical implementation of the pump pulse, the full Hamiltonian $H(t)$ is transformed into the rotating frame of the laser frequency via the unitary transformation $U_P(t) = \left|\uparrow\right\rangle\left\langle\uparrow\right| + \left|\downarrow\right\rangle\left\langle\downarrow\right| + \exp(i\varepsilon_P t)\left|T\right\rangle\left\langle T\right|$. In the transformed Hamiltonian,

$$\tilde{H}(t) = H_{\mathrm{HF}} + H_{\mathrm{EZ}} + H_{\mathrm{NZ}} + f(t)\left|\uparrow\right\rangle\left\langle T\right| + f^*(t)\left|T\right\rangle\left\langle\uparrow\right| - \delta_T\left|T\right\rangle\left\langle T\right|, \tag{5.6}$$

any fast oscillations with the laser frequency ε_P vanish. Above we introduce the detuning of the laser energy with respect to the trion resonance, $\delta_T = \varepsilon_P - \varepsilon_T$.

The Hamiltonian $\tilde{H}(t)$ varies only slowly with time through the pulse envelope function $f(t)$ and allows for discretization in small time steps on which it can be approximated as constant. Accordingly, the time evolution operator for the laser pulse is approximated by a series of unitary operators,

$$U_P'(t_n) = \exp(-i\tilde{H}(t_n)\Delta_t) \tag{5.7}$$

with $\Delta_t = t_n - t_{n-1}$. For a sufficiently small step width Δ_t, the Trotter error becomes negligible and the effect of the pump pulse is approximated by the product

$$\begin{aligned} U_P &= \exp(-i\varepsilon_P T_P \left|T\right\rangle \left\langle T\right|) \prod_n U'_P(t_n) \\ &= \exp(-i\varepsilon_P T_P \left|T\right\rangle \left\langle T\right|) U'_P(T_P) \ldots U'_P(t_1), \end{aligned} \tag{5.8}$$

where we introduced the pulse duration T_P and the front exponential function originates from transforming out of the rotating frame of the laser frequency. The above approximation becomes exact for $\Delta_t \to 0$ at a finite pulse duration T_P.

Applying the operator U_P to the density operator ρ, the evolution from the time $t = t_0$ directly before the pulse to the time $t = t_0 + T_P$ after the pulse is given by

$$\rho(t_0 + T_P) = U_P \rho(t_0) U_p^\dagger. \tag{5.9}$$

From a numerical point of view, this transformation requires two matrix multiplications where the matrix representation of U_P is set up for the chosen pulse shape, pump energy, and pulse duration once at the beginning of the calculation. Afterward, the transformation in Eq. (5.9) is repetitively applied for the evaluation of a periodic pulse train.

As an alternative to Eq. (5.8), the laser pulses can be approximated as instantaneous assuming a short pulse duration and relatively slow spin dynamics in comparison. Here, the pulse shape becomes irrelevant and the pulse effect is determined by the effective pulse area,

$$F = 2 \int_{-\infty}^{\infty} f(t) dt, \tag{5.10}$$

and the energy detuning δ_T alone. Under the assumption of an instantaneous pump pulse, $T_P = 0$, the density operator is transformed according to

$$\rho(t_0^+) = U_P \rho(t_0^-) U_P^\dagger, \tag{5.11}$$

where t_0^- marks the time directly before the incidence of the pulse and t_0^+ denotes the time directly after the pulse. Focusing on resonant π pulses, i.e., $F = \pi$, the unitary pulse operator is given by

$$U_P = \left|T\right\rangle \left\langle\uparrow\right| - \left|\uparrow\right\rangle \left\langle T\right| + \left|\downarrow\right\rangle \left\langle\downarrow\right|. \tag{5.12}$$

The approximation of instantaneous pulses is often well justified and, therefore, is applied for a large number of numerical calculations in this thesis. However, for instance, a strong external magnetic field induces rapid spin dynamics acting on the time scale of the pulse duration [78]. At an exemplary magnetic field of 8 T, the electron spin precession period of roughly 16 ps (assuming $g_e = 0.555$) becomes comparable to the pulse duration such that the related spin dynamics during the pulse has a relevant effect on the pulse efficiency, see Sec. 6.4.

5.3 Decay of the trion state

After the optical excitation, the trion state decays rapidly by the recombination of the photo-generated electron-hole pair. A trion lifetime of 400 ps [127] was extracted for the self-assembled (In,Ga)As/GaAs quantum dots employed in the mode-locking experiments [67, 68]. To account for the decay of the trion state population, the spin system is treated as an open quantum system, and the radiative trion decay is incorporated in a Lindblad master equation [205, 206],

$$\partial_t \rho = \mathcal{L}\rho = -i[H, \rho] - \gamma(s^\dagger s\rho + \rho s^\dagger s - 2s\rho s^\dagger). \tag{5.13}$$

The dynamics of the density operator ρ in the d-dimensional Hilbert space is regulated by the Liouvillian super operator $\mathcal{L}$ that comprises the effect of the total Hamiltonian H as well as an additional term proportional to the rate γ which governs the trion decay via the operators $s = |\uparrow\rangle\langle T|$ and $s^\dagger = |T\rangle\langle\uparrow|$.

The Hamiltonian H enters in the von Neumann part of the Lindblad equation and includes the hyperfine interaction according to Eq. (2.11), the effect of the external magnetic field introduced in Eqs. (2.2) and (2.3) as well as the trion state contribution given in Eq. (5.2),

$$H = H_{\mathrm{HF}} + H_{\mathrm{EZ}} + H_{\mathrm{NZ}} + H_T. \tag{5.14}$$

Furthermore, it can be extended by additional spin interactions such as the nuclear quadrupolar interactions established in Eq. (2.20). The effect of the pump pulse controlled by the envelope function $f(t)$ is not included in H, since $f(t)$ fully vanishes at the times in between the pump pulses at which the Lindblad equation is applied.

The trion decay in the Lindlad equation, Eq. (5.13), is mediated by the operator $s = |\uparrow\rangle\langle T|$ and its hermitian conjugate $s^\dagger = |T\rangle\langle\uparrow|$ which map the trion state to the spin up state along the optical axis and vice versa. Accordingly, the term $s^\dagger s$ in the above master equation equals the projection onto the trion state, $s^\dagger s = |T\rangle\langle T|$. Based on the experimental estimate, we consistently set the decay rate of the trion state to $\gamma = 10\,\mathrm{ns}^{-1}$ in the following [127].

The Lindblad equation, Eq. (5.13), applies for the time range between consecutive pump pulses, i.e., it is employed to obtain the time evolution of the density operator from the time t_0 after a pulse to the time $t_0 + T_L$ directly before the next pump pulse. The duration $T_L = T_R - T_P$ is determined from the difference between the repetition time T_R of the periodic optical excitation and the pulse duration T_P. According to the above Lindblad equation, Eq. (5.13), the temporal evolution between the pump pulses is given by the analytic solution

$$\rho(t_0 + t) = \exp(\mathcal{L}t)\rho(t_0), \tag{5.15}$$

where $\rho(t_0)$ is the density operator after the pulse and $t \leq T_L$. However, the matrix representation of the super operator $\mathcal{L}$ has the dimension $D \times D$ with $D = d^2$ for a Hilbert space dimension d. Assuming nuclei of identical spin length, $I_k \equiv I$ for all k, the Hilbert space dimension $d = 3(2I+1)^N$ grows exponentially with the number N of nuclear spins. As a result, the evaluation of Eq. (5.15) would require the diagonalization of a matrix with the dimension $(9(2I+1)^{2N}) \times (9(2I+1)^{2N})$. This task straightly performed becomes quickly unmanageable with increasing N, see also Chapter 7 for more details. Therefore, we outline an alternative approach in the following that relies on the handling of matrices with the dimension $d \times d$ only.

5.4 Numerical implementation of a repetition period

For the quantum mechanical simulation of a pulse train, the Hamiltonian H comprising the spin interactions in the quantum dots is specified and the relevant physical parameters are adjusted according to the mode-locking experiments [67, 68]. We refer to singly negatively charged quantum dots such that the hyperfine Hamiltonian H_{HF} is isotropic, i.e., $\lambda = 1$ in Eq. (2.11). The hyperfine coupling constants A_k are set to produce a dephasing of the electron spin on the characteristic time scale of $T^* = 1\,\mathrm{ns}$, cf. Eq. (2.18), which is estimated from Fig. 5.2(a). In the electron Zeeman term H_{EZ}, the electron g factor $g_e = 0.555$ extracted for the self-assembled (In,Ga)As/GaAs quantum dots [68, 77, 127] enters the Eq. (2.2). The nuclear g factor g_k in the Hamiltonian H_{NZ}, Eq. (2.3), is assumed to be equal for all nuclear spins for simplicity, i.e., $g_k \equiv g_N$ for all nuclei k, and we fix g_N to the average ratio $z = g_N\mu_N/(\mu_B g_e) = 1/800$ for the isotopes in the (In,Ga)As/GaAs quantum dots [91]. The effect of nuclear quadrupolar interactions is neglected for the time being due to the much weaker energy scale but will be addressed in Sec. 6.5. As a result, the complete Hamiltonian for the spin dynamics specified from Eq. (5.14) reads

$$H = \sum_k A_k \mathbf{S} \cdot \mathbf{I}_k - \omega_e S^x - \omega_n \sum_k I_k^x + \varepsilon_T |T\rangle \langle T| \,. \tag{5.16}$$

Here, the external magnetic field B is applied in the x direction, perpendicular to the optical axis along the z direction. The strength of B amounts to up to 10 T. The electron and nuclear Larmor frequency, $\omega_e = g_e\mu_B B$ and $\omega_n = g_N\mu_N B$, include the respective g factor. For an exemplary magnetic field strength of $B = 2\,\mathrm{T}$, this produces a precession period of $T_e = 2\pi/\omega_e = 2\pi/(g_e\mu_B B) \approx 64\,\mathrm{ps}$ for the electron spin and the much longer time $T_n = 2\pi/\omega_n = 2\pi/(g_N\mu_N B) \approx 51\,\mathrm{ns}$ for the nuclear spins with a field independent ratio $z = T_e/T_n$.

As indicated in Sec. 5.3, the numerical evaluation of the time evolution between the pump pulses poses a computationally challenging task since it has to be repeated several million times and the matrix dimensions grow exponentially with the number of nuclear spins included in the dynamics. Therefore, we developed an efficient scheme that limits the dimensions of the handled matrices to the Hilbert space dimension d rather than the dimension $D = d^2$ related to the Liouvillian super operator $\mathcal{L}$. We start with the elimination of the nuclear Larmor precession during the decay of the trion state. To this end, we transform into the frame, in which all spins rotate with the frequency ω_n, by the application of the unitary operator $U_n = \exp(-i\omega_n F^x t)$ that acts on the total spin x component $F^x = S^x + \sum_k I_k^x$. Due to $[H, F^x] = [H_{\mathrm{HF}}, F^x] = 0$, the transformed Hamiltonian $\tilde{H} = U_n(H + \omega_n F^x)U_n^\dagger$ does not acquire any time dependency,

$$\tilde{H} = \sum_k A_k \mathbf{S} \cdot \mathbf{I}_k - (\omega_e - \omega_n) S^x + \varepsilon_T |T\rangle \langle T| . \tag{5.17}$$

Analogously, we transform the density operator, $\tilde{\rho} = U_n \rho U_n^\dagger$, and the operator s introduced for the Lindblad equation, Eq. (5.13), $\tilde{s} = U_n s U_n^\dagger$. The latter yields

$$\tilde{s} = \frac{1}{\sqrt{2}} \left\{ \exp\left(\frac{i\omega_n t}{2}\right) |\uparrow\rangle_x \langle T| + \exp\left(-\frac{i\omega_n t}{2}\right) |\downarrow\rangle_x \langle T| \right\} \tag{5.18}$$

with the hermitian conjugate $\tilde{s}^\dagger$ resulting accordingly. Here, we employed the electron spin x basis along the magnetic field orientation,

$$\begin{aligned} |\uparrow\rangle_x &= (|\uparrow\rangle + |\downarrow\rangle)/\sqrt{2}, \\ |\downarrow\rangle_x &= (|\uparrow\rangle - |\downarrow\rangle)/\sqrt{2}, \end{aligned} \tag{5.19}$$

for the direct evaluation of the time evolution induced by U_n.

After transformation into the rotating frame, the Lindblad master equation encompasses the new operators denoted by "$\tilde{...}$",

$$\begin{aligned} \partial_t \tilde{\rho} &= -i \left[\tilde{H}, \tilde{\rho}\right] - \gamma \left(\tilde{s}^\dagger \tilde{s} \tilde{\rho} + \tilde{\rho} \tilde{s}^\dagger \tilde{s} - 2\tilde{s} \tilde{\rho} \tilde{s}^\dagger\right) \\ &= -i \left[\tilde{H}, \tilde{\rho}\right] - \gamma \left(|T\rangle \langle T| \rho + \rho |T\rangle \langle T|\right) + \langle T|\tilde{\rho}|T\rangle \left(|\uparrow\rangle_x \langle\uparrow|_x \right. \\ &\quad \left. + e^{i\omega_n t} |\uparrow\rangle_x \langle\downarrow|_x + e^{-i\omega_n t} |\downarrow\rangle_x \langle\uparrow|_x + |\downarrow\rangle_x \langle\downarrow|_x \right). \end{aligned} \tag{5.20}$$

For the second line of the above equation, the operators $\tilde{s}$ and $\tilde{s}^\dagger$ according to Eq. (5.18) have been inserted. The Lindblad equation in the rotating frame enables direct analytic access to the decay of the trion state population. For brevity, we introduce $\tilde{\rho}_{TT} \equiv \langle T|\tilde{\rho}|T\rangle$ which corresponds to the suboperator of the density operator where the electron spin state is fixed to the trion state $|T\rangle$ and solely the

nuclear spin degrees of freedom remain. Thus, the matrix representation of $\tilde{\rho}_{TT}$ has dimension $d_n \times d_n$ with $d_n = (2I+1)^N$. From the above Lindblad equation, we obtain the differential equation regulating the temporal evolution of the suboperator $\tilde{\rho}_{TT}$,

$$\partial_t \tilde{\rho}_{TT} = -2\gamma \tilde{\rho}_{TT}. \tag{5.21}$$

The dynamics of $\tilde{\rho}_{TT}$ decouples from the remaining parts of the density operator and is analytically solved by

$$\tilde{\rho}_{TT}(t_0 + t) = e^{-2\gamma t} \tilde{\rho}_{TT}(t_0), \tag{5.22a}$$
$$\rho_{TT}(t_0 + t) = e^{-2\gamma t} e^{-iH_{\mathrm{NZ}}t} \rho_{TT}(t_0) e^{iH_{\mathrm{NZ}}t}, \tag{5.22b}$$

where $\tilde{\rho}_{TT}(t_0) = \rho_{TT}(t_0)$ denotes the suboperator directly after the pump pulse. The matrix elements in the sector $\tilde{\rho}_{TT}$ of the full density operator $\tilde{\rho}$ decay exponentially with a rate 2γ without any further dynamics as a result of the transformation into the rotating frame. When the system is transformed back into the original frame, i.e., we leave the rotating frame, the dynamics of the suboperator ρ_{TT} is extended to the precession of the nuclear spins about the external magnetic field, see Eq. (5.22b).

Similarly as for $\tilde{\rho}_{TT}$, we extract the dynamics of the eight remaining suboperators $\langle e|\tilde{\rho}|e'\rangle$ with $|e\rangle$, $|e'\rangle \in \{|\uparrow\rangle_x, |\downarrow\rangle_x, |T\rangle\}$ from the Lindblad master equation, Eq. (5.20). As a first step, we focus on the trion spin coherence suboperators, i.e., those suboperators for which either $|e\rangle$ or $|e'\rangle$ corresponds to the trion state $|T\rangle$. The differential equations of these four suboperators are coupled via the von Neuman term in the Lindblad equation but do not relate to the dynamics of those suboperators restricted to a combination of the resident electron spin states for which $|e\rangle$, $|e'\rangle \in \{|\uparrow\rangle_x, |\downarrow\rangle_x\}$. Due to the first two terms within the parentheses in Eq. (5.20), the matrix elements of the trion coherence suboperators decay exponentially with the rate γ. Since $\gamma T_R \gg 1$ for repetition times of several nanoseconds, the matrix elements of the four trion coherence suboperators have fully vanished within the numerical precision at the incidence time of the consecutive pump pulse. Consequently, they do not enter the dynamics of the next repetition period and consistently are omitted in the numerical calculations.

Finally, we are left with the determination of the dynamics of the four suboperators $\langle e|\tilde{\rho}|e'\rangle$ with $|e\rangle$, $|e'\rangle \in \{|\uparrow\rangle_x, |\downarrow\rangle_x\}$ which we comprise in a combined density operator $\tilde{\rho}_S$. The density operator $\tilde{\rho}_S$ incorporates the spin up and down state of the resident electron as well as the nuclear spin degrees of freedom. Therefore, its matrix representation has the dimension $d' \times d'$ with $d' = 2(2I+1)^N$. We substitute the temporal evolution of the suboperator $\tilde{\rho}_{TT}$, Eq. (5.22a), into the Lindblad equation, Eq. (5.20), and omit terms acting on the trion state. As a result, we obtain the

differential equation of the suboperator $\tilde{\rho}_S$,

$$\begin{aligned}\partial_t\tilde{\rho}_S + i\left[\tilde{H}_S, \tilde{\rho}_S\right] = \gamma e^{-2\gamma t}\tilde{\rho}_{TT}(t_0)\left(|\uparrow\rangle\langle\uparrow| + e^{i\omega_n t}|\uparrow\rangle\langle\downarrow|\right.\\ \left.+e^{-i\omega_n t}|\downarrow\rangle\langle\uparrow| + |\downarrow\rangle\langle\downarrow|\right), \qquad (5.23)\end{aligned}$$

$$\tilde{H}_S = \sum_k A_k \mathbf{S}\cdot\mathbf{I}_k - (\omega_e - \omega_n)S^x, \qquad (5.24)$$

where the Hamiltonian $\tilde{H}_S$ is the projection of $\tilde{H}$ onto the Hilbert space of reduced dimension d' excluding the trion state.

Equation (5.23) is a nonhomogeneous differential equation with a homogeneous part on the left hand side and a source term on the right hand side of the equation. Accordingly, the temporal evolution of $\tilde{\rho}_S$ results from the combination of the solution $\tilde{\rho}_{S,h}(t_0+t)$ for the homogeneous part and a particular solution $\tilde{\rho}_{S,p}(t+t_0)$ which respects the full equation, Eq. (5.23), including the source term,

$$\tilde{\rho}_S(t_0+t) = \tilde{\rho}_{S,h}(t_0+t) + \tilde{\rho}_{S,p}(t_0+t). \qquad (5.25)$$

For the homogeneous part corresponding to a von Neumann type equation, the solution is established utilizing the unitary time evolution operator,

$$\tilde{\rho}_{S,h}(t_0+t) = \exp\left(-i\tilde{H}_S t\right)\tilde{\rho}_{S,h}(t_0)\exp\left(i\tilde{H}_S t\right). \qquad (5.26)$$

As an ansatz for the particular solution of the full Eq. (5.23), we choose

$$\tilde{\rho}_{S,p}(t_0+t) = \sum_\tau \tilde{\rho}^{(\tau)}_{S,p}(t_0)e^{(-2\gamma+i\tau\omega_n)t} \qquad (5.27)$$

with $\tau \in \{-1, 0, 1\}$ taking into account the exponential functions in the source term on the right hand side of Eq. (5.23). From the insertion of the ansatz into the differential equation and a subsequent comparison of the prefactors for the exponential functions, we obtain the initial conditions at the time t_0 for the respective values of τ,

$$(-2\gamma + i\tau\omega_n)\tilde{\rho}^{(\tau)}_{S,p}(t_0) + i\left[\tilde{H}_S, \tilde{\rho}^{(\tau)}_{S,p}(t_0)\right] = \gamma\tilde{\rho}_{TT}(t_0)S^{(\tau)}, \qquad (5.28)$$

where the associated operators for the electron spin,

$$S^{(\tau)} = \begin{cases}|\downarrow\rangle_x\langle\uparrow|_x, & \tau = -1,\\ |\uparrow\rangle_x\langle\uparrow|_x + |\downarrow\rangle_x\langle\downarrow|_x, & \tau = 0,\\ |\uparrow\rangle_x\langle\downarrow|_x, & \tau = +1,\end{cases} \qquad (5.29)$$

are introduced. Based on the initial conditions, the matrix elements of $\tilde{\rho}^{(\tau)}_{S,p}(t_0)$ for the particular solution can be established from the trion state population $\tilde{\rho}_{TT}(t_0)$ at the

time t_0. To this end, the eigenbasis of the Hamiltonian $\tilde{H}_S$, $\tilde{H}_S\,|\tilde{\psi}_{S,a}\rangle = \tilde{\varepsilon}_{S,a}\,|\tilde{\psi}_{S,a}\rangle$ with eigenstates $|\tilde{\psi}_{S,a}\rangle$ and eigenenergies $\tilde{\varepsilon}_{S,a}$, serves as a basis. Accordingly, the matrix elements for the particular solution read

$$\langle\tilde{\psi}_{S,a}|\tilde{\rho}^{(\tau)}_{S,p}(t_0)|\tilde{\psi}_{S,b}\rangle = \tilde{G}^{(\tau)}_{a,b}\,\langle\tilde{\psi}_{S,a}|\tilde{\rho}_{TT}(t_0)S^{(\tau)}|\tilde{\psi}_{S,b}\rangle \tag{5.30a}$$

with the coefficients

$$\tilde{G}^{(\tau)}_{a,b} = \frac{\gamma}{-2\gamma + i\omega_n\tau + i(\tilde{\varepsilon}_{S,a} - \tilde{\varepsilon}_{S,b})}. \tag{5.30b}$$

Since the ansatz, Eq. (5.27), vanishes after the time T_L due to the decaying exponential functions, the contribution $\tilde{\rho}_{S,p}(t_0 + T_L)$ can be omitted in the evaluation of the full time evolution, Eq. (5.25), at time $t_0 + T_L$. As a consequence, the main effect of the particular solution onto the temporal evolution, Eq. (5.25), consists of an adjustment of the initial density operator $\tilde{\rho}_{S,h}(t_0)$ entering the unitary time evolution, Eq. (5.26). Thus, the evolution of the density suboperator $\tilde{\rho}_S$ for a full repetition period is determined from Eq. (5.26) with $\tilde{\rho}_{S,h}(t_0)$ resulting from the starting condition $\tilde{\rho}_S(t_0) = \tilde{\rho}_{S,h}(t_0) + \tilde{\rho}_{S,p}(t_0)$,

$$\begin{aligned}\tilde{\rho}_S(t_0 + T_L) &= \exp\left(-i\tilde{H}_S T_L\right)\tilde{\rho}_{S,h}(t_0)\exp\left(i\tilde{H}_S T_L\right)\\ \text{with}\qquad \tilde{\rho}_{S,h}(t_0) &= \tilde{\rho}_S(t_0) - \sum_\tau \tilde{\rho}^{(\tau)}_{S,p}(t_0).\end{aligned} \tag{5.31}$$

As a last step, the dynamics has to be transformed back out of the frame rotating with the nuclear Larmor frequency ω_n via $\rho_S(t_0 + T_L) = U_n^\dagger\tilde{\rho}_S(t_0 + T_L)U_n$. Finally, we obtain the complete dynamics in the reduced Hilbert space denoted by S,

$$\rho_S(t_0 + T_L) = e^{-iH_S T_L}\left\{\rho_S(t_0) - \sum_\tau \rho^{(\tau)}_{S,p}(t_0)\right\}e^{iH_S T_L}, \tag{5.32}$$

where we inserted the relation, $\exp\left(i\omega_n F^x T_L\right)\exp\left(-i\tilde{H}_S T_L\right) = \exp\left(-iH_S T_L\right)$, that holds due to $[\tilde{H}_S, F^x] = 0$. Furthermore, we exploited the fact that the operators $\rho_S(t_0)$ and $\rho^{(\tau)}_{S,p}(t_0)$ at the time t_0 coincide to the associated operators in the rotating frame denoted by "$\tilde{\ldots}$".

The time evolution, Eq. (5.32), can also be expressed conveniently in terms of the eigenbasis of the Hamiltonian H_S,

$$H_S = U_n^\dagger\tilde{H}_S U_n = \sum_k A_k\mathbf{S}\cdot\mathbf{I}_k - \omega_e S^x - \omega_n\sum_k I^x_k. \tag{5.33}$$

We denote the related eigenstates and eigenenergies by $|\psi_{S,a}\rangle$ and $\varepsilon_{S,a}$ respectively with $H_S\,|\psi_{S,a}\rangle = \varepsilon_{S,a}\,|\psi_{S,a}\rangle$, and address the dynamics of the associated matrix

elements of the density operator ρ_S. Abbreviating the individual matrix elements by $\rho_{a,b} = \langle\psi_{S,a}|\rho_S|\psi_{S,b}\rangle$, the evolution from time t_0 to time T_L is given by

$$\begin{aligned}\rho_{a,b}(t_0+T_L) &= e^{-i(\varepsilon_{S,a}-\varepsilon_{S,b})T_L}\left\{\rho_{a,b}(t_0)-\sum_\tau \langle\psi_{S,a}|\rho^{(\tau)}_{S,p}(t_0)|\psi_{S,b}\rangle\right\}\\ &= e^{-i(\varepsilon_{S,a}-\varepsilon_{S,b})T_L}\left\{\rho_{a,b}(t_0)-\sum_\tau G^{(\tau)}_{a,b}\,\langle\psi_{S,a}|\rho_{TT}(t_0)S^{(\tau)}|\psi_{S,b}\rangle\right\}.\end{aligned} \tag{5.34}$$

The coefficients $G^{(\tau)}_{a,b}$ are rewritten in terms of the eigenenergies $\varepsilon_{S,a}$ of H_S which replace the eigenenergies $\tilde{\varepsilon}_{S,a}$ of $\tilde{H}_S$ in the original definition, Eq. (5.30a),

$$G^{(\tau)}_{a,b} = \frac{\gamma}{-2\gamma + i\omega_n\{\tau + (F^x_a - F^x_b)\} + i(\varepsilon_{S,a}-\varepsilon_{S,b})}. \tag{5.35}$$

Here, we employed the relation $H_S = \tilde{H}_S + \omega_n F^x$ in combination with the commutator $[H_S, F^x] = [\tilde{H}_S, F^x] = [H_S, \tilde{H}_S] = 0$, which provides $\varepsilon_{S,a} = \tilde{\varepsilon}_{S,a} - \omega_n F^x_a$ as a result of fixing $|\psi_{S,a}\rangle$ as the common eigenbasis of the three operators,

$$H_S\,|\psi_{S,a}\rangle = \varepsilon_{S,a}\,|\psi_{S,a}\rangle\,, \quad \tilde{H}_S\,|\psi_{S,a}\rangle = \tilde{\varepsilon}_{S,a}\,|\psi_{S,a}\rangle \quad \text{and} \quad F^x\,|\psi_{S,a}\rangle = F^x_a\,|\psi_{S,a}\rangle\,. \tag{5.36}$$

For the investigation of a periodic train of pump pulses, the combination of the unitary transformation capturing the effect of a pump pulse as outlined in Sec. 5.2 and the temporal evolution for the duration $T_L = T_R - T_P$ according to the Lindblad equation, Eq. (5.13), has to be iterated for a large number of repetition periods. The starting operators $\rho_S(t_0)$ and $\rho_{TT}(t_0)$ of the solution, Eq. (5.32), of the Lindblad equation are constructed from the density operator resulting after the pulse, Eq. (5.9) or Eq. (5.11). In the numerical implementation, the combination of the pump pulse and the subsequent time evolution comprises roughly eight matrix multiplications of $(d \times d)$-dimensional matrices and has to be iterated for up to 20 million times to approach the quasistationary steady-state relevant in mode-locking experiments. As a result of including the full quantum mechanical dynamics over this long period of time, the numerical calculations are limited to six to eight nuclear spins with an individual length $I = 1/2$.

Other theoretical approaches aiming at the study of the nuclei-induced frequency focusing of the electron spin precession under periodic optical excitation are often based on (semi)classical approaches [80, 81, 84, 85, 87–89, 223, 224] or dynamical mean-field theory [225] treating relatively large nuclear spin baths at the expense of disregarding inherent quantum effects [83]. Moreover, a quantum mechanical approach based on perturbation theory for the number of electron-nuclear spin flips

during T_R has been developed in Refs. [90, 91] and allows for incorporating $N = 20$ nuclear spins. However, due to CPU runtime limitations, this approach was restricted to roughly 10^4 repetition periods and did not reach the quasistationary steady state. Recently, the full quantum mechanical time evolution between consecutive pump pulses has been embedded into a linear mapping for the density operator by Ref. [92], see also Chapter 7. The diagonalization of this mapping allows for direct access to the quasistationary steady-state but is still limited to $N = 6$ nuclear spins in Ref. [92].

5.5 Ensemble averaging and distribution of the hyperfine coupling constants

In order to compensate for the relatively small size of the nuclear spin bath in the quantum mechanical treatment, we employ an ensemble average that bridges the gap to real singly charged quantum dots where the hyperfine interaction mediates the coupling of the electron spin to roughly 10^5 nuclear spins. As it was shown that the spin dynamics in the system with a reduced nuclear bath size adequately captures the generic features of a larger system [160], we introduce an additional averaging over slightly different realizations of the spin system representing individual quantum dots in the ensemble. These realizations differ in their hyperfine coupling constants $\{A_{1,l}, \ldots, A_{N,l}\}$ where we introduce an index l distinguishing the various realizations, $l \in \{1, \ldots, N_C\}$. Typically, we choose $N_C \approx 100$ for the number of averaged realizations. The individual realizations are treated separately during the whole pulse sequence as described in the previous section and the results are merged only at the end of a numerical simulation.

For the distribution $p(A_{k,l})$ of the hyperfine coupling constants, we employ a uniform distribution since it was found [84] that the details of the distribution have a negligible effect on the quasistationary steady state of a periodic pulse sequence. To exclude nuclear spins, which have only a weak impact on the electron spin in the already small system, we draw the hyperfine coupling constants randomly in the range $[0.2; 1]$ and subsequently scale them to produce a dephasing of the electron spin on the experimentally observed time scale of a nanosecond. Referring to Eq. (2.18), we introduce the ensemble-averaged dephasing time of the electron spin in the disordered nuclear spin system,

$$T^* = \left(\frac{1}{N_C} \sum_{l=1}^{N_C} \sum_{k=1}^{N} A_{k,l}^2 \left\langle \mathbf{I}_{k,l}^2 \right\rangle \right)^{-1/2}, \tag{5.37}$$

which we employ for scaling the hyperfine coupling constants to $T^* = 1\,\mathrm{ns}$ consistently throughout the following chapters.

The ensemble-averaged electron spin polarization $\langle S^\alpha(t)\rangle$ with $\alpha \in \{x, y, z\}$ is defined by the average over the quantum mechanical expectation values of the individual realizations,

$$\langle S^\alpha(t)\rangle = \frac{1}{N_C}\sum_{l=1}^{N_C}\langle S_l^\alpha(t)\rangle = \frac{1}{N_C}\sum_{l=1}^{N_C}\mathrm{Tr}[S^\alpha\rho_j(t)]. \tag{5.38}$$

For illustration of the electron spin dephasing in the disordered nuclear spin system, we plot the temporal evolution of $\langle S^z(t)\rangle$ in Fig. 5.3(a). Initially, the electron spins are polarized in the z direction, i.e, the electron spins in the individual realizations are in the $|\uparrow\rangle$ state at $t = 0$. We comprise $N = 6$ nuclear spins with individual length $I_{k,l} \equiv I \equiv 1/2$ in each realization ($N_C = 100$) and choose the normalized identity operator as a starting condition for the nuclear spin sector of the density operator respectively. During the time evolution, the electron spins are subject to an external magnetic field $\mathbf{B} = B\mathbf{n}_x$ with $B = 0.49\,\mathrm{T}$ producing oscillations in the spin z component. Moreover, the random nuclear Overhauser field governs the dephasing with the envelope function

$$\langle S^z(t)\rangle_{\mathrm{env}} = S_0 \exp\left(-\frac{t^2}{6T^{*2}}\right). \tag{5.39}$$

The analytically predicted Gaussian envelope function, which is indicated by the gray dashed line in Fig. 5.3(a), matches the dephasing observed in the ensemble-averaged $\langle S^z(t)\rangle$ except for minor deviations which originate from the relatively small number of nuclear spins included in the numerical calculation.

As a result of the setup of the hyperfine coupling constants, the dephasing time T_l^* in the individual realizations slightly differs. Since we fix the ensemble-averaged dephasing time to $T^* = 1\,\mathrm{ns}$ via Eq. (5.37), the individual sets of coupling constants $\{A_{k,l}\}$ produce a variation of the dephasing time T_l^* in the respective realizations labeled by the index l. We introduce the ratio T_l^*/T^* according to

$$\left(\frac{T^*}{T_l^*}\right)^2 = \sum_{k=1}^{N}(T^*A_{k,l})^2\left\langle \mathbf{I}_{k,l}^2\right\rangle \tag{5.40}$$

and study the associated probability distribution $p(T_l^*/T^*)$ in Fig. 5.3(b). To obtain a smooth distribution, we randomly generated the set $\{A_{k,l}\}$ of N coupling constants for $N_C = 100$ realizations fulfilling $T^* = 1\,\mathrm{ns}$ and repeated this process 1000 times to process all resulting dephasing times into a histogram. The comparison of the distribution $p(T_l^*/T^*)$ for different system sizes N indicates a self-averaging with increasing the number of nuclei in the system, i.e., the weight focuses around $T_l^* = T^*$

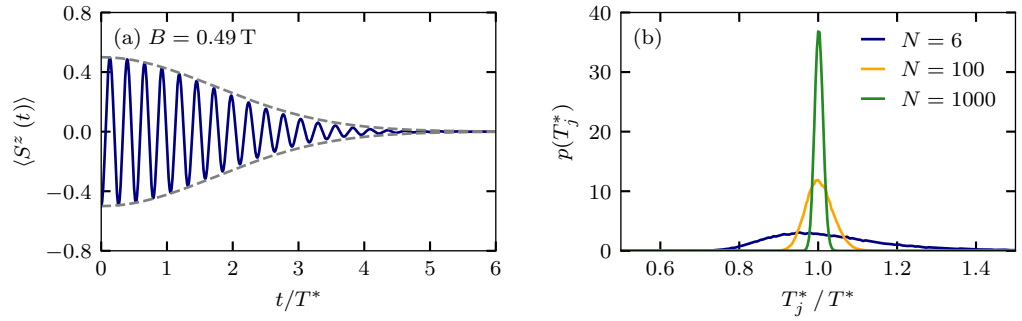

Figure 5.3: Dephasing time T^* of the electron spin in the disordered nuclear spin bath ($I = 1/2$). (a) Dephasing of the initially oriented electron spin, $\langle S^z(0)\rangle = 0.5$, with an externally applied magnetic field, $\mathbf{B} = B\mathbf{n}_x$. The width of the Gaussian envelope function (gray dashed line) is determined by T^*, see Eq. (5.39). The results were averaged over 100 realizations with differing sets of hyperfine coupling constants ($N = 6$). (b) Distribution of the dephasing time T_l in the individual realizations l. To obtain a smooth curve, we processed the dephasing time T_l of 1000 realizations, which each contain 100 sets of $\{A_{k,l}\}$ scaled to $T^* = 1\,\mathrm{ns}$, into a histogram. The figure is taken from Ref. [86].

for $N \to \infty$ employing normalized coupling constants $a_{k,l} = T^* A_{k,l}$ in Eq. (5.40). Mimicking a quantum dot ensemble by incorporating a large number of nuclear spins in the simulation, the coupling constants $a_{k,l}$ had to be replaced by $\tilde{a}_{k,l} = T_l^* A_{k,l}$ with dephasing times T_l^* of the individual quantum dots that are generated from the experimentally relevant distribution $p(T_l^*)$.

As the effect of the periodic optical excitation of the electron spin is expected to imprint on the nuclear spin system leading to the mode-locking effect via nuclei-induced frequency focusing of the electron spin precession, we require a suitable quantity reflecting the nuclear spin state. To this end, we examine the probability distribution of the Overhauser field component B_N^x along the orientation of the external magnetic field [83, 84, 90, 91]. The ensemble-averaged Overhauser field in accordance with Eq. (2.12) reads

$$\begin{aligned} \langle B_N^x \rangle &= \frac{1}{N_C} \sum_{l=1}^{N_C} \left\langle B_{N,l}^x \right\rangle = \frac{1}{N_C} \sum_{l=1}^{N_C} \mathrm{Tr}[B_{N,l}^x \rho_l] \\ &= \frac{1}{N_C} \sum_{l=1}^{N_C} \sum_{e,K} \langle e, K|\rho_l|e, K\rangle \langle K|B_{N,l}^x|K\rangle \,, \end{aligned} \tag{5.41}$$

where we employed the spin x product basis with the electron spin degree of freedom e and the nuclear spin state K such that the operator $B_{N,l}^x$ is diagonal. The last

line of the above equation allows for the interpretation in terms of the average over a probability distribution, where the Overhauser field of value

$$B^x_{K,l} = \langle K|B^x_{N,l}|K\rangle \tag{5.42}$$

occurs with the probability

$$p_{K,l} = \sum_e \frac{\langle e,K|\rho_l|e,K\rangle}{N_C}. \tag{5.43}$$

Exploiting that the spectrum of $B^x_{N,l}$ is dense, we introduce a continuous probability distribution [90],

$$p(B^x_N) = \frac{1}{N_C}\sum_{l=1}^{N_C}\sum_{e,K}\langle e,K|\rho_l|e,K\rangle\,\delta(B^x_N - B^x_{K,l}), \tag{5.44}$$

employing the delta distribution $\delta(x)$. The distribution $p(B^x_N)$ is normalized by construction [83] and is obtained as a histogram [90] with appropriate bin size for the finite system here.

For brevity, the configuration index l is omitted in the following unless we explicitly address individual realizations of the spin system.

Chapter 6

Synchronization effects under periodic optical excitation

The full quantum mechanical approach outlined in the previous chapter is applied for the investigation of the spin dynamics in singly charged quantum dots subject to a periodic pulse train. In particular, we target an in-depth analysis of the mode-locking effect [67, 68] emerging under the periodic optical excitation. A mode-locked state characterized by the synchronization of the electron spin precession with the driving periodicity provides the starting point for further studies. The electron spin adapts to the periodic excitation within a couple of repetition periods while the nuclear spins remain unaffected on this time scale. As a next step, we address the mode-locking effect mediated by the nuclei-induced frequency focusing of the electron spin precession that was realized in the pump-probe experiments performed by Greilich et al. [67, 68]. This effect requires the application of several million pump pulses in the quantum mechanical simulations since the synchronization with the periodic optical excitation has to be transmitted to the nuclear spin bath via the hyperfine interaction. The reorganization of the Overhauser field distribution produces favored precession modes of the electron spin which govern the revival of the electron spin polarization directly before the pump pulse. In pump-probe experiments, the magnitude of the revival amplitude was found to be dependent on the external magnetic field [86], cf. Sec. 5.1. We relate this dependence to the nuclear Zeeman term H_{NZ} which imposes a resonance condition for the nuclear Larmor precession [91]. Moreover, we attribute the overall decrease in the revival amplitude when increasing the external magnetic field to the finite nonzero duration of the optical pulses. Finally, the quantum mechanical implementation is extended to incorporate additional effects in the nuclear spin system. We include the static nuclear-electric quadrupolar interactions and find that they significantly weaken the nuclei-induced frequency focusing. Furthermore, the extended approach allows for taking into account differing nuclear g factors. In the (In,Ga)As/GaAs quantum dots, the g factors of the various nuclear isotopes are expected to produce contrasting resonance conditions according to the respective Zeeman terms such that additional modulations arise for the electron spin revival amplitude as a function of the external magnetic field.

Large parts of this chapter have been published in Ref. [86].

6.1 Electronic quasistationary steady state

At the beginning of a periodic pulse sequence, the electron spin starts to synchronize with the driving periodicity whereas the nuclear spins are mostly left unaffected on the timescale of a few repetition periods. We focus on this purely electronic quasistationary steady state reached after roughly ten repetition periods before addressing the imprint of the periodic pumping onto the nuclear spins in the later sections. Figure 6.1(a) displays the electron spin dynamics after the first few pump pulses. We approximate the pump pulses by instantaneous resonant π pulses in the first instance and employ Eqs. (5.11) and (5.12). At the beginning of the pulse train, the nuclear spins are in a completely disordered state resulting from the high-temperature limit which is valid at typical experimental temperatures of 4 K. Here, the thermal energy of roughly 0.3 meV exceeds the relevant energy scale of the hyperfine interaction since $\sum_k A_k$ is in the order of 10 µeV [48, 187, 226]. During the first repetition periods, the nuclear spins retain the disordered state. As a result, the electron spin polarization generated by the optical pulses along the negative z direction dephases with an envelope function that is governed by the ensemble dephasing time T^*, cf. Eq. (5.37). In Fig. 6.1(a), the incidence of the pump pulses at times $N_P T_R$ corresponds to $t = 0$ ns, and the number N_P of preceding pump pulses is indicated in the legend. The oscillation of the electron spin z component in the external magnetic field $B = 1.95$ T applied in x direction cannot be resolved on the timescale of the repetition time $T_R = 13.2$ ns in Fig. 6.1(a), as the Larmor precession period amounts to 66 ps for the electron g factor $g_e = 0.555$. Therefore, we provide an inset with the zoomed electron spin dynamics directly before the next pump pulse.

Starting from the second pump pulse (orange line), a revival of the electron spin polarization before the incidence of the next pump pulse emerges which gains in amplitude up to the tenth pulse (green line). The rephasing of the electron spin precession before a pump pulse clearly indicates the synchronization of the electron spin dynamics with the pumping periodicity. As the electron spin which is oriented in negative z direction after the pump pulse precesses in the (yz) plane perpendicular to the external field, the electron spin polarization after the time T_R may be aligned with any angle within the (yz) plane. Thus, we define the electron spin revival amplitude directly before a pump pulse as

$$S^{\perp}(N_P) = \sqrt{\left\langle S^y(N_P T_R^-)\right\rangle^2 + \left\langle S^z(N_P T_R^-)\right\rangle^2}. \tag{6.1}$$

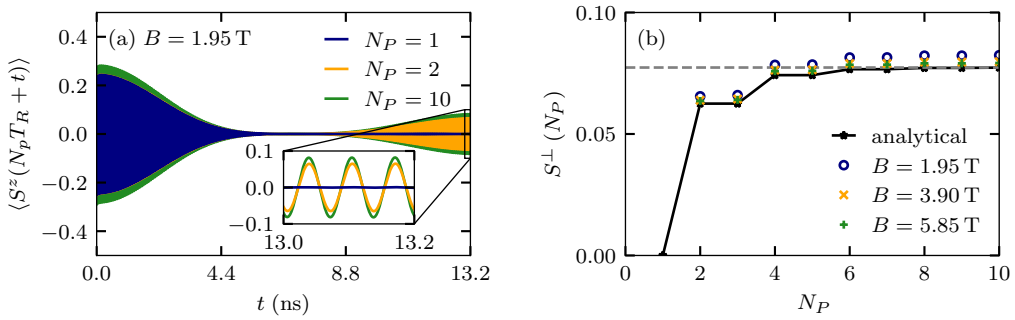

Figure 6.1: Emergence of the electronic quasistationary steady state in the disordered nuclear spin bath ($N = 6$, $I = 1/2$, $N_C = 100$). (a) Temporal evolution of the electron spin component $\langle S^z\rangle$ between consecutive pump pulses with repetition time $T_R = 13.2\,\mathrm{ns}$. The evolution after different numbers N_P of preceding instantaneous resonant π pulses is displayed, where $t = 0\,\mathrm{ns}$ corresponds to the incidence time of the N_P-th pump pulse. The external magnetic field, $B = 1.95\,\mathrm{T}$, entails rapid oscillations which are resolved in the inset only. (b) Amplitude $S^\perp(N_P)$ of the electron spin polarization directly before a pump pulse as a function of the number N_P of preceding pump pulses. Data for various external magnetic fields is presented alongside the analytical prediction, Eq. (6.7). The figure is taken from Ref. [86].

To inspect the emergence of the electron spin synchronization, the revival amplitude $S^\perp(N_P)$ is displayed in Fig. 6.1(b) as a function of the number N_P of preceding pump pulses. We find that the revival amplitude exhibits a rapid increase with the second pump pulse and subsequently increases in steps of two pump pulses approaching a plateau. This behavior is mostly independent of the strength of the applied magnetic field.

For a better understanding of the emergence of the revival, we employ a simplifying analytical treatment of the electron spin dynamics during the repetition period. According to Eqs. (5.11) and (5.12), the pump pulse induces an electron spin polarization along the optical axis,

$$\langle S^z(N_P T_R^+)\rangle = \frac{1}{2}\left(\langle S^z(N_P T_R^-)\rangle - \frac{1}{2}\right), \tag{6.2}$$

where $\langle S^z(N_P T_R^-)\rangle$ and $\langle S^z(N_P T_R^+)\rangle$ denote the electron spin polarization before and after the incidence of the pump pulse, respectively. The spin components $\langle S^x(N_P T_R^+)\rangle$ and $\langle S^y(N_P T_R^+)\rangle$ however are set to zero by the pulse. To obtain the electron spin dynamics between the pump pulses, we assume the nuclear spins to be frozen, cf. Sec. 2.6, since the repetition time T_R is short compared to the time scale of the nuclear spin dynamics. Furthermore, a strong external magnetic

field along the x direction suppresses the effect of the transversal Overhauser field components B_N^y and B_N^z, $|-\mathbf{B}+\mathbf{B}_N| \approx -B + B_N^x$ employing a Taylor expansion for $|\mathbf{B}_N|/|\mathbf{B}| \ll 1$. Accordingly, we focus on the electron spin precession about the constant total magnetic field $B + B_N^x$ aligned in x direction for the analytic approach. As a consequence, the electron spin dynamics between the pump pulses for a fixed nuclear spin configuration K simplifies to

$$\langle S^z((N_P+1)T_R^-)\rangle_K = \langle S^z(N_P T_R^+)\rangle_K \cos((\omega_e - \omega_K)T_R), \tag{6.3}$$

where we neglect the trion decay due to $\gamma \ll \omega_e$ for simplicity. The electron spin precession frequency $\omega_e - \omega_K$ is the combination of the Larmor frequency ω_e in the external field introduced in Eq. (2.16) and the frequency ω_K for the precession about the Overhauser field of the nuclear configuration K,

$$\omega_K = g_e \mu_B B_K^x = \sum_k A_k \langle K|I_k^x|K\rangle . \tag{6.4}$$

The revival amplitude at a fixed nuclear configuration K after N_P pump pulses, i.e., directly before the (N_P+1)-th pump pulse, results from the iteration of the pulse effect and the time evolution. Repetitive insertion of Eq. (6.2) into Eq. (6.3) and vice versa yields

$$\langle S^z(N_P T_R^-)\rangle_K = -\sum_{n=1}^{N_P} \frac{1}{2^{n+1}} [\cos((\omega_e - \omega_K)T_R)]^n. \tag{6.5}$$

We note that the instantaneous pump pulses do not act on the nuclear spin state such that Eq. (6.2) holds for each nuclear configuration K separately.

The total electron spin polarization is obtained from averaging the result of the individual nuclear configurations K over the occurring precession frequencies ω_K weighted by their probability distribution $p(\omega_K)$,

$$\langle S^z(N_P T_R^-)\rangle = \int_{-\infty}^{\infty} d\omega_K p(\omega_K) \langle S^z(N_P T_R^-)\rangle_K , \tag{6.6}$$

where $p(\omega_K)$ is approximated as a continuous Gaussian distribution with standard deviation $1/\sqrt{3}T^*$ and zero mean in the high-temperature limit according to Eq. (2.13). Since $\langle S^z(N_P T_R^-)\rangle_K$ is periodic in ω_K with the repetition period T_R, it oscillates faster than the Gaussian distribution $p(\omega_K)$ whose width is governed by $T^* = 1\,\mathrm{ns}$. Consequently, we approximate $p(\omega_K)$ as constant during one period of $\langle S^z(N_P T_R^-)\rangle_K$, and obtain the average $\langle S^z(N_P T_R^-)\rangle$ by integration of $\langle S^z(N_P T_R^-)\rangle_K$

over one period,

$$\begin{aligned}\langle S^z(N_P T_R^-)\rangle &= \frac{T_R}{2\pi}\int_0^{2\pi/T_R} d\omega_K \langle S^z(N_P T_R^-)\rangle_K \\ &= -\frac{T_R}{2\pi}\sum_{n=1}^{N_P}\frac{1}{2^{n+1}}\int_0^{2\pi/T_R} d\omega_K \left[\cos((\omega_e-\omega_K)T_R)\right]^n \\ &= -\sum_{n=1}^{\lfloor N_P/2\rfloor}\frac{(2n)!}{2^{4n+1}(n!)^2} \end{aligned} \tag{6.7}$$

due to $\int_{-\infty}^{\infty} d\omega_K p(\omega_K) = 1$. For the second line, we inserted the definition of $\langle S^z(N_P T_R^-)\rangle_K$ in Eq. (6.5). The third line is obtained by exploiting the periodicity of the cosine where we replaced the index n in the second line by $n/2$ as the contributions for odd n vanish due to the antisymmetric integrand. Thus, $\langle S^z(N_P T_R^-)\rangle$ is predicted to increase in steps of two pulses as observed in Fig. 6.1(b). The analytic prediction (black circles) matches the numerical results independently of the applied magnetic field whose effect cancels out in Eq. (6.7) due to integration over a full period of the cosine.

The electron spin y component directly before the pump pulse results from replacing the cosine originating from the final repetition period by a sine in Eq. (6.5),

$$\langle S^y(N_P T_R^-)\rangle_K = \sum_{n=1}^{N_P}\frac{1}{2^{n+1}}[\cos((\omega_e-\omega_K)T_R)]^{n-1}\sin((\omega_e-\omega_K)T_R). \tag{6.8}$$

The average over the electron spin precession frequency ω_K produces $\langle S^y(N_P T_R^-)\rangle = 0$ for the evaluation analogous to $\langle S^z(N_P T_R^-)\rangle$. Therefore, the electron spin revival amplitude is determined by the electron spin z component alone in the analytic approach, $S^\perp(N_P) = |\langle S^z(N_P T_R^-)\rangle|$.

Increasing the number of pump pulses to infinity in Eq. (6.7), $N_P \to \infty$, the revival amplitude of the electronic quasistationary steady state approaches the value $S^\perp_{\mathrm{ess}}$,

$$S^\perp_{\mathrm{ess}} = \left|\frac{1}{2} - \frac{1}{\sqrt{3}}\right| \approx 0.077, \tag{6.9}$$

indicated by the dashed gray horizontal line in Fig. 6.1(b). However, on a prolonged time scale exceeding ten repetition periods, the full hyperfine interaction becomes relevant such that the approximation of frozen nuclear spins does not hold anymore. Here, the synchronization of the electron spin with the driving periodicity transfers to the nuclear spin bath. Accordingly, the electron spin revival amplitude under continued optical excitation may differ significantly from $S^\perp_{\mathrm{ess}}$.

6.2 Mode-locking effect and nuclei-induced frequency focusing

In mode-locking experiments, the periodic optical excitation is typically applied over several minutes [68] to enable the reorientation of the nuclear spins in the quantum dot ensemble and thereby allow for nuclei-induced frequency focusing of the electron spin precession. For the numerical simulations, we find further synchronization of the coupled electron-nuclear spin dynamics beyond the previously discussed purely electronic quasistationary steady state under a pulse train comprising thousands of pump pulses. The numerical data indicates the progression of synchronization to the nuclear spin system, for instance, by the electron spin revival amplitude evolving further from the value $S^{\perp}_{\mathrm{ess}} = 0.077$. Here, we focus on the mode-locking effect at an exemplary external magnetic field of $B = 1.95\,\mathrm{T}$ to provide a general understanding of the synchronization effects. We extend the analysis to a broader range of external magnetic field strengths in the following section.

Under continuous pumping with instantaneous resonant π pulses, the revival amplitude $S^{\perp}(N_P)$ grows, starting from the initial electronic steady-state value $S^{\perp}_{\mathrm{ess}}$ reached after ten pump pulses, see Figs. 6.2(a) and 6.2(b). This increase in the revival amplitude is attributed to the realignment of the Overhauser field acting on the electron spin [80, 81, 84, 87, 88, 90, 91]. The approximately Gaussian initial distribution of the Overhauser field component B^x_N along the axis of the external magnetic field, see Fig. 6.2(c), transforms into a peaked distribution $p(B^x_N)$ with Gaussian envelope function as a consequence of the periodic excitation, see Fig. 6.2(d). At the external magnetic field of $B = 1.95\,\mathrm{T}$, the Overhauser field adjusts preferably in such a way that the electron spin performs an integer number m of revolutions between consecutive pump pulses,

$$T_R = m\frac{2\pi}{g_e\mu_B(B - B^x_N)}. \tag{6.10}$$

In the following, the external magnetic field is consistently set to a value

$$B = m'\frac{2\pi}{g_e\mu_B T_R} \tag{6.11}$$

with an integer number m' respecting this finding. In the above definition, m' corresponds to the number of electron spin revolutions during the repetition time T_R at zero Overhauser field, e.g., $m' = 200$ produces $B \approx 1.95\,\mathrm{T}$. The resonant values of the Overhauser field B^x_N, at which the number of electron spin revolutions m in the combination of the external magnetic field and the Overhauser field equals an integer number, are indicated by black dotted vertical lines in Fig. 6.2(d) and subsequent

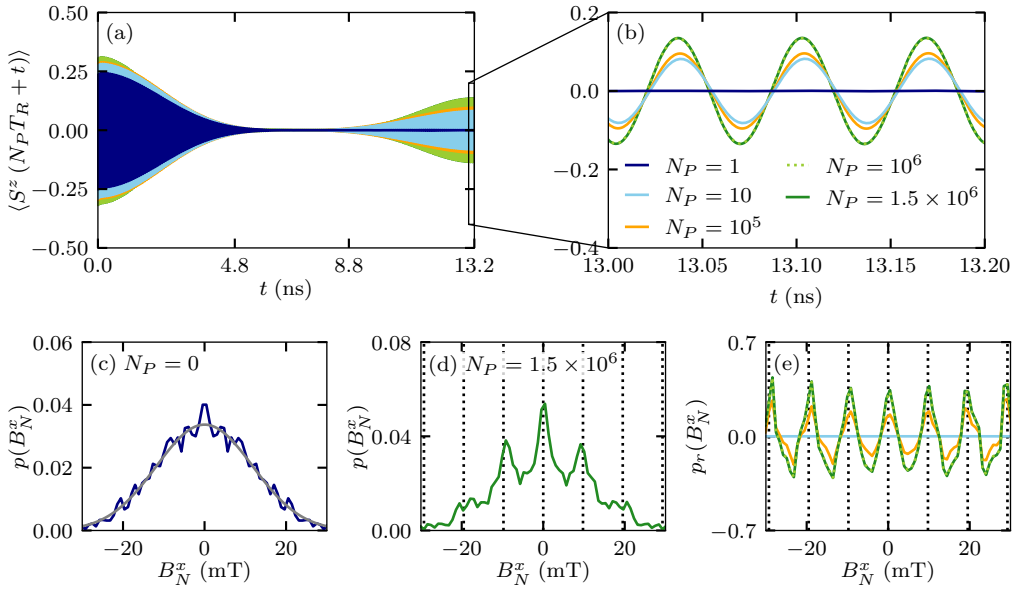

Figure 6.2: Mode-locking effect in the spin system ($N = 6$, $I = 1/2$, $N_C = 100$) under periodic optical excitation with instantaneous resonant π pulses. The external magnetic field is fixed to $B = 1.95\,\mathrm{T}$. (a) Temporal evolution of the electron spin component $\langle S^z(N_P T_R + t)\rangle$ between two pump pulses. The incidence time of the N_P-th pump pulse corresponds to $t = 0\,\mathrm{ns}$ respectively. The number of preceding pump pulses is color coded according to the legend in panel (b). (b) Zoomed electron spin dynamics directly before the next pump pulse. (c) Initial Overhauser field distribution $p(B_N^x)$. The analytic Gaussian prediction, Eq. (2.13), is indicated by a gray line. (d) Overhauser field distribution $p(B_N^x)$ after periodic excitation with $N_P = 1.5 \times 10^6$ pump pulses. (e) Relative Overhauser field distribution $p_r(B_N^x)$ after various numbers of pump pulses. The color coding complies with the legend in panel (b). The figure is taken from Ref. [86].

figures of the Overhauser field distribution. After a train of $N_P = 1.5 \times 10^6$ periodic pump pulses, the distribution $p(B_N^x)$ clearly favors these resonances and exhibits peaks at the indicated positions.

To extract the nuclei-induced frequency focusing more clearly, we introduce the relative Overhauser field distribution $p_r(B_N^x)$ as the relative deviation of the probability distribution $p(B_N^x)$ after a periodic pulse train from the initial probability distribution $p_0(B_N^x)$ with approximately Gaussian shape [90],

$$p_r(B_N^x) = \frac{p(B_N^x) - p_0(B_N^x)}{p_0(B_N^x)}. \tag{6.12}$$

The relative Overhauser field distribution allows for detecting small changes in

the orientation of the nuclear spins and therefore resolves the redistribution of the Overhauser field component B_N^x at an earlier stage during the pulse train. The numerical results of $p_r(B_N^x)$ after different numbers N_P of pump pulses are presented in Fig. 6.2(e). During the pulse train, the peaks at the resonant Overhauser field values emerge, and a steady-state distribution is approached after roughly one million pulses. After ten pump pulses (light blue line), no notable reorientation of the nuclear spins is visible yet. Continuing the periodic excitation up to $N_P = 10^5$ pump pulses (orange line), peaks at the resonant modes emerge which increase further under the prolonged pulse train. Finally, the distributions for $N_P = 10^6$ (light green line) and $N_P = 1.5 \times 10^6$ (dark green line) fully coincide hinting at the convergence to a quasistationary steady state under the periodic driving. The quasistationary steady state is reflected by the matching revival of the electron spin polarization in Fig. 6.2(b) as well.

6.3 Magnetic field dependence of the electron spin revival amplitude

The mode-locking experiments indicate a nonmonotonic behavior of the electron spin revival amplitude as a function of the applied magnetic field. Based on these findings, we target the magnetic field dependence of the mode-locking effect by quantum mechanical simulations. Figure 6.3(a) displays the emergence of the electron spin revival amplitude $S^\perp(N_P)$ under the periodic pulse train at distinct strengths of the external magnetic field. At some magnetic field strengths (such as $B = 1.95\,\mathrm{T}$), the revival amplitude increases starting from the initial value of $S^\perp_{\mathrm{ess}} = 0.077$ under continued optical excitation whereas the revival amplitude decreases below $S^\perp_{\mathrm{ess}}$ at other magnetic field strengths. In both scenarios, the revival amplitude $S^\perp(N_P)$ as a function of the number N_P of pump pulses approaches a steady-state value. This value is reached after roughly one million pump pulses for relatively weak external magnetic fields, whereas longer pulse trains are required for stronger external magnetic fields, e.g., at $B = 9.75\,\mathrm{T}$ we applied 20 million consecutive pump pulses. The converged revival amplitude $S^\perp$ as a function of the external magnetic field B in the range up to 10 T is presented in Fig. 6.3(b) (blue markers). The revival amplitude clearly demonstrates a nonmonotonic dependence on B. Similar to the experiments, cf. Fig. 5.2(b), we find a profound minimum of $S^\perp$ around 4 T. Furthermore, the revival amplitude exhibits a second minimum around 8 T as well as two equally pronounced maxima at 2 T and 6 T respectively. Overall, the numerical results indicate an oscillatory behavior of $S^\perp$ in the range of up to 10 T, whereas the experimental measurements provide an overall decrease in the revival amplitude with increasing magnetic field strength which is superimposed

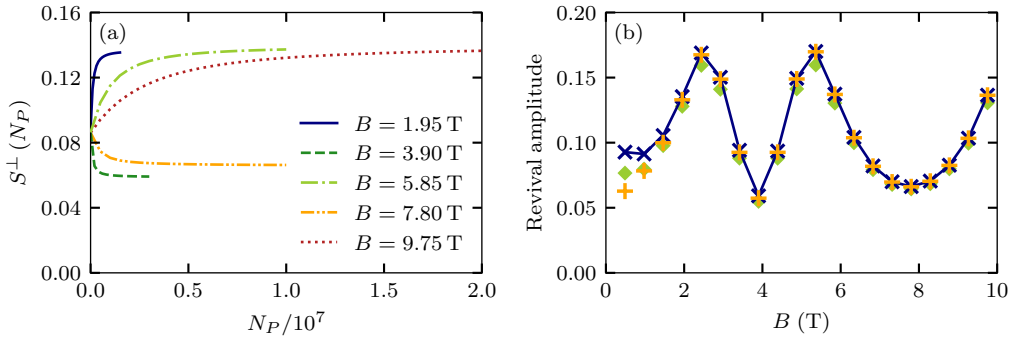

Figure 6.3: Magnetic field dependence of the electron spin revival amplitude in the spin system ($I = 1/2$, $N = 6$, $N_C = 100$) driven by periodic instantaneous resonant π pulses. (a) Evolution of the revival amplitude $S^{\perp}(N_P)$ during the pulse train for various external magnetic fields. (b) Revival amplitude $S^{\perp}$ in the quasistationary steady state as a function of the external magnetic field (blue markers, the line is provided as a guide to the eye). Additionally, we display the converged absolute value $|\langle S_c^z \rangle|$ of the electron spin polarization along the optical axis directly before the pump pulse (orange crosses) and the revival amplitude $S^{\perp}$ calculated according to Eq. (6.15) from the associated Overhauser field distributions (green diamonds). The figure is taken from Ref. [86].

by additional modulations. This mismatch is a result of the theoretical modeling missing relevant effects such as the duration of the pump pulses as well as the differing g factors of the nuclear isotopes in the quantum dots. We will address these additional effects one by one in Sec. 6.4 and Sec. 6.6 respectively. Here, we aim at a general understanding of the magnetic field dependence of the revival amplitude first.

The emergence of either an enhanced or attenuated revival amplitude under the prolonged pulse sequence originates from the nuclei-induced frequency focusing effect. Hence, it is instructive to examine the reorientation of the nuclear spins depending on the magnetic field strength. Jäschke et al. [84] derived two distinct types of modes for the electron spin precession from the condition that the average Knight field acting on the nuclear spins between consecutive pump pulses vanishes. At these modes, the Overhauser field adjusts in such a way that the electron spin performs either an integer or half-integer number m of revolutions during T_R. For the external magnetic field of $B = 1.95\,\mathrm{T}$, we found already that the former resonances are favored by the Overhauser field, cf. Fig. 6.2(d) and Fig. 6.2(e). In Ref. [91], a resonance condition for the nuclear Larmor precession was proposed based on the effect of the Hamiltonian H_{NZ} which determines whether integer or half-integer

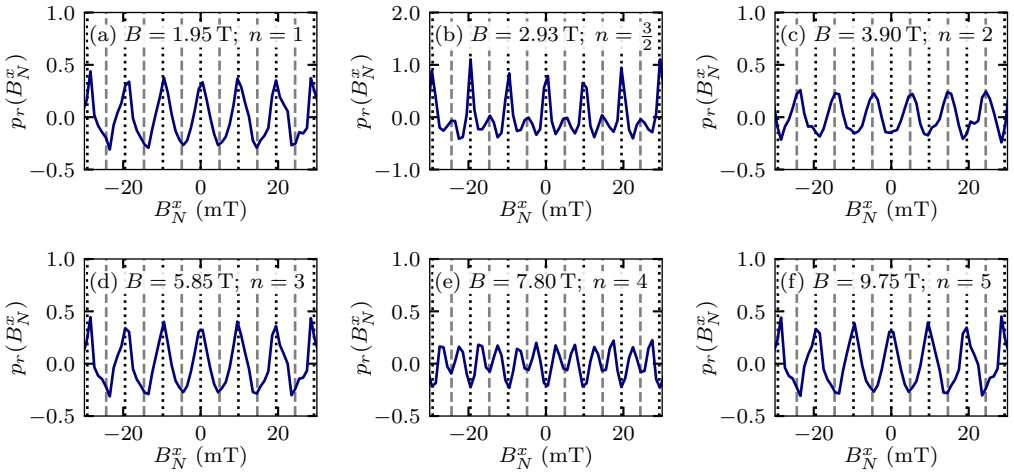

Figure 6.4: Relative Overhauser field distribution $p_r(B_N^x)$ in the quasistationary steady state for different strengths of the external magnetic field B. The number of instantaneous pump pulses applied to the spin system ($N = 6$, $I = 1/2$, $N_C = 100$) is in the range $1.5 \times 10^6 \leq N_P \leq 2 \times 10^7$. Overhauser fields that produce an integer (half-integer respectively) number of electron spin revolutions between consecutive pump pulses are indicated by black dotted (gray dashed) vertical lines. The figure is taken from Ref. [86].

numbers m are favored. When the external magnetic field fulfills

$$B = n \times \frac{\pi}{2T_R g_N \mu_N} \approx n \times 1.95\,\mathrm{T} \tag{6.13}$$

with an odd number n, the nuclear spins are predicted to form an Overhauser field B_N^x which produces an integer number m of electron spin revolutions during T_R. An even number n in the above condition, however, indicates that half-integer numbers m are favored. Here, n corresponds to the number of quarter revolutions of the nuclear spins between consecutive pump pulses. Figure 6.4 presents the converged relative Overhauser field distribution $p_r(B_N^x)$ after several million pump pulses for selected values of B. For the magnetic field strengths $B = 1.95\,\mathrm{T}$ ($n = 1$), $B = 5.85\,\mathrm{T}$ ($n = 3$) and $B = 9.75\,\mathrm{T}$ ($n = 5$), the Overhauser field distribution exhibits peaks at the integer resonances of the electron spin precession indicated by the black dotted vertical lines, see Figs. 6.4(a), 6.4(d) and 6.4(f) respectively. At an external magnetic field of $B = 3.90\,\mathrm{T}$ ($n = 2$), the peak positions in $p_r(B_N^x)$ correspond to the half-integer resonances of the electron spin precession marked by the gray dashed vertical lines, see Fig. 6.4(c). For $B = 7.80\,\mathrm{T}$ ($n = 4$), which exceeds the magnetic field range considered in Ref. [91], the prediction according to Eq. (6.13) does not hold anymore. While we would expect the favoring of the half-integer

precession modes, the distribution $p_r(B_N^x)$ in Fig. 6.4(e) displays peaks in between the integer and half-integer resonances. When the external magnetic field does not comply with Eq. (6.13) with an integer n, the Overhauser field distribution may form peaks corresponding to both mode types. Figure 6.4(b) shows the distribution for $B = 2.93\,\mathrm{T}$ ($n = 3/2$) as an example.

To connect the results for the Overhauser field distribution to the extracted revival amplitudes, we perform an analytical analysis of $\langle S^z(N_P T_R^-)\rangle$ employing the frozen Overhauser field approximation. Focusing on a fixed nuclear spin configuration K, we obtain the quasistationary steady state under the periodic pumping from the requirement that the electron spin revival has converged, $\langle S^z(N_P T_R^-)\rangle = \langle S^z((N_P+1)T_R^-)\rangle$. The insertion of Eq. (6.2) for the pulse effect into Eq. (6.3) for the temporal evolution between the pulses and the subsequent application of the steady-state criterion yields the electron spin z polarization before a pump pulse for the nuclear spin configuration K,

$$\langle S^z(N_P T_R^-)\rangle_K = -\frac{\cos((\omega_e - \omega_K)T_R)}{2[2 - \cos((\omega_e - \omega_K)T_R)]}. \tag{6.14}$$

The total electron spin revival amplitude is given by the sum over all contributions $\langle S^z(N_P T_R^-)\rangle_{K,l}$ of the individual nuclear spin configurations K according to their weight $p_{K,l}$ defined in Eq. (5.43),

$$\langle S^z(N_P T_R^-)\rangle = \sum_{K,l} p_{K,l}\, \langle S^z(N_P T_R^-)\rangle_{K,l}\,. \tag{6.15}$$

Here, we reintroduced the index l distinguishing the various realizations of the spin system differing by the set of hyperfine coupling constants. The relation, Eq. (6.15), allows for connecting the Overhauser field distribution obtained from the numerical calculations directly to the electron spin revival amplitude. The revival amplitude $S_{\mathrm{ess}}^{\perp}$ of the electronic steady state, Eq. (6.9), which is related to the Gaussian distribution of B_N^x in the disordered nuclear spin system, can be extracted directly from the above equation. We added $|\,\langle S^z(N_P T_R^-)\rangle\,|$ calculated from the numerical data for $p_{K,l}$ according to the analytic relation, Eq. (6.15), in Fig. 6.1(b) as green diamonds. The results fully match the revival amplitude $S^{\perp}$ extracted straight from the full quantum mechanical treatment for external magnetic fields $B > 1\,\mathrm{T}$. For weaker magnetic fields, the approximation of a fast electron Larmor precession compared to the trion decay, $\gamma \ll \omega_e$, does not hold, and therefore the temporal evolution between the pulses is more intricate than Eq. (6.3). Moreover, the approximation of a frozen Overhauser field becomes less justified for small external magnetic fields.

The agreement for $B > 1\,\mathrm{T}$ demonstrates that the revival amplitude of the electron spin polarization in the mode-locked system is fully determined by the alignment of the nuclear spins along the direction of the external magnetic field. Thus, the magnetic field dependence of the revival amplitude can be directly connected to the resonance condition, Eq. (6.13), arising from the nuclear Zeeman term. For odd values of n, the integer modes of the electron spin precession are favored producing an enhanced revival amplitude. For even values of n, however, the half-integer modes of the electron spin precession attenuate the revival effect. Assuming δ peaks in the Overhauser field distribution at either the integer or half-integer modes, the extreme values of the electron spin z component [84] result from Eq. (6.15): $\langle S^z(N_P T_R^-)\rangle = -1/2$ for the integer modes where $[\omega_e - \omega_K]T_R = 2a\pi$ and $\langle S^z(N_P T_R^-)\rangle = 1/6$ for the half-integer modes where $[\omega_e - \omega_K]T_R = (2a+1)\pi$ with $a \in \mathbb{Z}$ respectively.[1] Accordingly, the revival amplitude starting from the initial value $S^\perp_{\mathrm{ess}}$ either increases (integer modes) or decreases (half-integer modes) under continued optical excitation. As the converged Overhauser field distributions in Fig. 6.4 exhibit peaks of finite width, we observe a superposition of the contributions of the two mode types which produces the evolution of the revival amplitude presented in Fig. 6.3(a).

6.4 Excitation with Gaussian shaped pump pulses

For a realistic description of the pump pulses, we replace the modeling with instantaneous resonant π pulses by Gaussian shaped laser pulses of finite nonzero duration. We employ the pulse Hamiltonian, Eq. (5.4), with a real Gaussian envelope function, $f(t) = f^*(t)$, whose iterated area equals π. The full width at half maximum of $f(t)$ is chosen to be 6 ps which is slightly longer than the laser pulses in experiments but illustrates the relevant physical effects more clearly [78]. We capture the pump pulse up to the time where the envelope function $f(t)$ has decayed to a hundredth of its maximum value and therefore set the pulse duration to $T_P = 22\,\mathrm{ps}$. The temporal evolution during the pulse is discretized according to Eq. (5.8) into 10^3 equally spaced time steps. The spin dynamics for the subsequent period of duration $T_L = T_R - T_P$ up to the next pump pulse is calculated in accordance to Eq. (5.13) by means of the procedure presented in Sec. 5.4.

As a first step, we address the periodic excitation with resonant Gaussian pump pulses for which $\epsilon_P = \epsilon_T$, i.e., the detuning yields $\delta_T = 0\,\mathrm{meV}$. The repetition time $T_R = 13.2\,\mathrm{ns}$ as well as other physical parameters are kept from the previous section for comparability. Figure 6.5(a) displays the emergence of the electron spin revival amplitude $S^\perp(N_P)$ under a pulse train consisting of resonant Gaussian pump pulses.

[1] The weight $p_{K,l}$ for the population of the individual modes does not enter here.

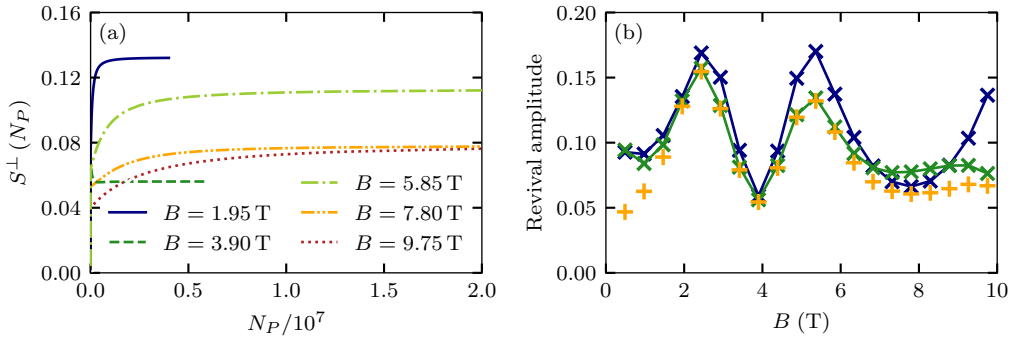

Figure 6.5: Revival amplitude of the electron spin polarization under periodic excitation with Gaussian shaped pump pulses with 6 ps width ($N = 6$, $I = 1/2$, $N_C = 100$). (a) Emergence of the revival amplitude $S^\perp(N_P)$ during the pulse train for different external magnetic fields. (b) Revival amplitude $S^\perp$ in the quasistationary steady state as a function of the external magnetic field (green markers – the line is provided as a guide to the eye). Additionally, the converged absolute value $|\langle S_c^z \rangle|$ (orange crosses) as well as the converged revival amplitude $S^\perp$ for instantaneous pump pulses (blue markers) are displayed. The latter is taken from Fig. 6.3(b). The figure is taken from Ref. [86].

For accurately extracting the maximum revival amplitude, we now measure $S^\perp(N_P)$ in the middle of the pulse at times $N_P T_R + T_P/2$ where the envelope function $f(t)$ of the pulse has its maximum respectively. In comparison to the instantaneous pump pulses, cf. Fig. 6.3(a), the stationary revival amplitude at a select external magnetic field emerges after a larger number N_P of pump pulses for the Gaussian shaped pulses as a consequence of the slower rate of change. In particular, at high magnetic fields, the generation of electron spin polarization by the Gaussian pump pulses of a finite duration becomes inefficient due to the notable electron spin precession during the pulse. Hence, for $B = 9.75\,\mathrm{T}$, the spin system has not fully reached the nonequilibrium steady state after the maximum simulation time of 20 million pump pulses (red dotted line).

The weakening polarization effect of the Gaussian pump pulses when increasing the external magnetic field is reflected by the converged electron spin revival amplitudes $S^\perp$ presented in Fig. 6.5(b). The overall periodic behavior of $S^\perp$ as a function of B in the range of up to 10 T is similar to the results for the excitation with instantaneous pulses. While the revival amplitude obtained for Gaussian pump pulses (green markers) roughly matches the data for the instantaneous pulses (blue markers) up to a magnetic field strength of 4 T, stronger deviations arise for larger magnetic fields, $B > 4\,\mathrm{T}$. The second maximum of the revival at 6 T is significantly less pronounced in the case of the excitation with Gaussian pump pulses. This

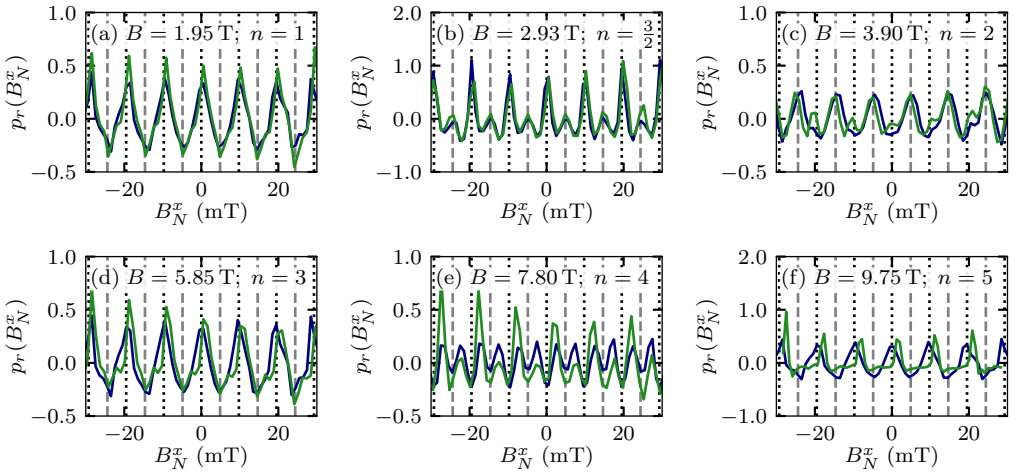

Figure 6.6: Relative Overhauser field distribution $p_r(B_N^x)$ of the spin system ($N = 6$, $I = 1/2$, $N_C = 100$) in the quasistationary steady state for different strengths of the external magnetic field B. The data (green lines) is obtained after periodic application of Gaussian shaped pump pulses with a width of 6 ps, $2.5 \times 10^6 \leq N_P \leq 2 \times 10^7$. For comparison, the distributions $p_r(B_N^x)$ obtained for instantaneous pump pulses taken from Fig. 6.4 are added as well (blue lines). An even (odd respectively) number of electron spin revolutions between consecutive pump pulses is indicated by black dotted (gray dashed) vertical lines. The figure is taken from Ref. [86].

observation corresponds to the experimental findings of an overall decrease in the revival amplitude for a strengthening magnetic field. We note that the minimum at 8 T in Fig. 6.5(b) seems less pronounced as the results for magnetic fields larger than 9 T have not fully converged, cf. Fig. 6.3(a). The converged absolute value of the electron spin polarization along the optical axis measured at the maximum of the pump pulse, $|\langle S_c^z\rangle| \equiv |\langle S^z(N_P T_R + T_P/2)\rangle|$, reveals that the revival amplitude for the Gaussian pump pulses is mostly made up by the electron spin z component in the magnetic field range $1\,\mathrm{T} < B < 7\,\mathrm{T}$, see orange crosses in Fig. 6.5(b). Here, the electron spin component $|\langle S_c^y\rangle| \equiv |\langle S^y(N_P T_R + T_P/2)\rangle|$ vanishes. Differences between $S^\perp$ and $|\langle S_c^z\rangle|$ are detected for small magnetic fields similarly as for the instantaneous pulses. Furthermore, additional deviations occur for the Gaussian shaped pulses at large magnetic fields for which the pumping becomes inefficient.

To extract the effect of the Gaussian shaped pump pulses on the nuclei-induced frequency focusing, we inspect the relative Overhauser field distribution of the spin system in the nonequilibrium steady state. Figure 6.6 displays $p_r(B_N^x)$ for the same external magnetic fields as for the instantaneous pump pulses in Fig. 6.4. Alongside the distribution $p_r(B_N^x)$ resulting after periodic excitation with the Gaussian pulses

(green lines), the data for the instantaneous pulses is added (blue lines) for comparison. Up to $B \lesssim 3\,\mathrm{T}$ where the electron spin precession during the pulses is negligible, the distributions $p_r(B_N^x)$ for the two pulse types match. For larger external magnetic fields $B > 3\,\mathrm{T}$, modifications of the electron spin precession modes arise due to the Gaussian pulse shape: At $B = 3.90\,\mathrm{T}$ ($n = 2$), where the half-integer modes (gray dashed vertical lines) were favored exclusively for the instantaneous pulses, the Overhauser field distribution exhibits tiny peaks corresponding to the integer modes for the Gaussian pump pulses as well. At the odd resonance $B = 5.85\,\mathrm{T}$ ($n = 3$), the peaks of $p_r(B_N^x)$ are slightly shifted to larger Overhauser fields with respect to the positions of the integer modes similarly as at $B = 9.75\,\mathrm{T}$ ($n = 5$). At the magnetic field of $B = 7.80\,\mathrm{T}$ ($n = 4$), the peaks in between the resonant modes of the electron spin precession are more pronounced on the right hand side of the integer modes than on the left hand side. Thus, the deviations of the electron spin revival amplitude in Fig. 6.5(b) from the results for instantaneous pump pulses in Fig. 6.3(b) at large values of B can be directly connected to deviations of $p_r(B_N^x)$ from the prediction according to Eq. (6.13) arising for strong external magnetic fields.

6.4.1 Trion detuning

Now, we take into account a detuning of the optical pulses from the trion excitation energy. We employ the modeling of Gaussian pump pulses with the same parameter as before and add a finite nonzero energy detuning δ_T. The magnitude of the detuning is adjusted to the order of the spectral pulse width which amounts to a standard deviation of 0.26 meV at the full width at half maximum of 6 ps in the time domain. For the detuned excitation, the electron spin obtains a component along the direction of the external magnetic field by the pump pulses, i.e., $\langle S^x \rangle$ no longer remains zero during the pulse sequence. The converged electron spin polarization $\langle S_c^x \rangle \equiv \langle S^x(N_P T_R + T_P/2) \rangle$ under the periodic optical excitation with detuned pump pulses with $\delta_T = 0.1\,\mathrm{meV}$ is shown in Fig. 6.7(a) as a function of the external magnetic field (blue crosses). The steady-state electron spin polarization along the external magnetic field axis increases with the magnetic field strength B. Via the hyperfine interaction, the electron spin polarization can be transmitted to the nuclear spins. Figure 6.7(b) reflects the nuclear polarization by a shift of the envelope function of the Overhauser field distribution $p(B_N^x)$ to the right at $B = 1.95\,\mathrm{T}$. The favoring of the integer precession modes of the electron spin according to the resonance condition, Eq. (6.13) with $n = 1$, however, is left unaffected. When increasing the magnetic field strength, the polarization of the nuclear spin system reduces, see the relative Overhauser field distributions $p_r(B_N^x)$ in Fig. 6.7(c). At $B = 3.90\,\mathrm{T}$ and $B = 5.85\,\mathrm{T}$ respectively, the peaks of the distribution $p_r(B_N^x)$ at

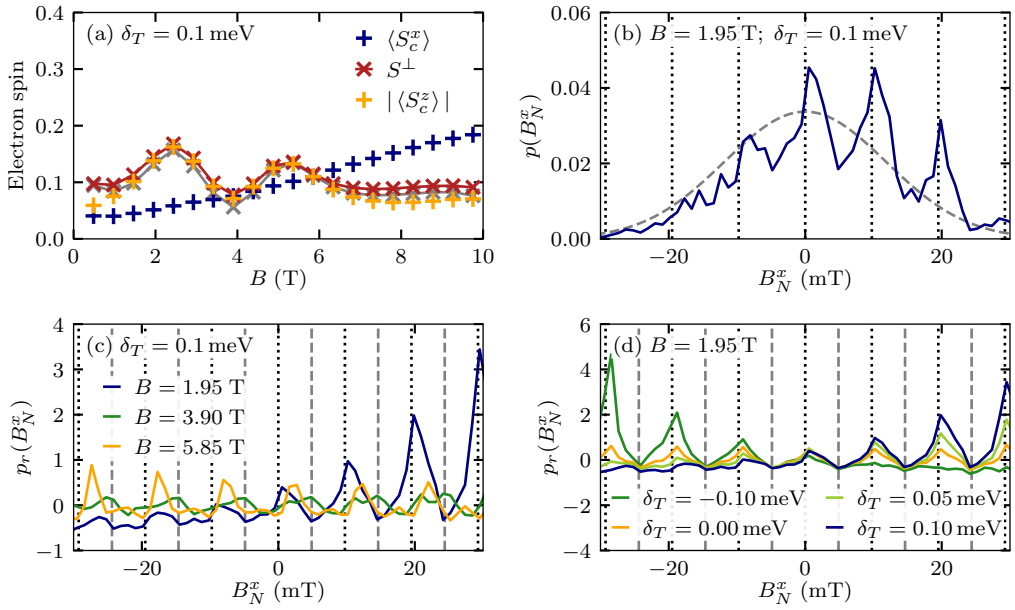

Figure 6.7: Effect of the energy detuning δ_T of the Gaussian shaped pump pulses ($N = 6$, $I = 1/2$, $N_C = 100$). (a) Converged electron spin revival amplitude $S^\perp$ for a periodic train of Gaussian pump pulses with detuning $\delta_T = 0.1\,\text{meV}$; the related spin component $|\langle S_c^z \rangle|$ and the polarization $\langle S_c^x \rangle$ are displayed as well. For comparison, we add the revival amplitude $S^\perp$ for resonant Gaussian pump pulses (gray markers) taken from Fig. 6.5(b). (b) Overhauser field distribution $p(B_N^x)$ after $N_P = 4 \times 10^6$ detuned Gaussian pump pulses ($\delta_T = 0.1\,\text{meV}$) at an external magnetic field of $B = 1.95\,\text{T}$. (c) Relative Overhauser field distribution $p_r(B_N^x)$ in the nonequilibrium steady-state for detuned Gaussian pump pulses ($\delta_T = 0.1\,\text{meV}$) and different magnetic field strengths. (d) Relative Overhauser field distributions $p_r(B_N^x)$ after $N_P = 4 \times 10^6$ Gaussian pump pulses with different detuning δ_T for an external magnetic field of $B = 1.95\,\text{T}$.

the resonant electron spin precession modes are roughly equally pronounced in the full range of B_N^x in contrast to the distribution at $B = 1.95\,\text{T}$. We attribute this decrease in the nuclear polarization to the suppression of the spin flip terms of the hyperfine interaction by a large external magnetic field. Accordingly, the electron spin cannot transfer its polarization to the nuclear spin bath efficiently.

The electron spin revival amplitude, however, remains unaffected by a potential polarization of the spin system along the magnetic field direction. Figure 6.7(a) displays the steady-state revival amplitude $S^\perp$ as a function of the external magnetic field. The comparison of the results for Gaussian pump pulses with and without energy detuning δ_T (red and gray markers respectively) reveals almost no differences.

While a nuclear spin x polarization may be induced by the detuning δ_T, the Overhauser field distribution still favors the same type of electron spin precession modes as for resonant excitation such that the weight of $p(B_N^x)$ is solely redistributed between modes of the same type which produce the same electron spin revival amplitude according to Eqs. (6.14) and (6.15).

Finally, we note that the sign of the spin polarization along the magnetic field axis is determined by the sign of the energy detuning of the pump pulses, see Fig. 6.7(d). As the detuning affects the orientation of the electron spin after the pump pulses and, in particular, determines the electron spin x component, it governs the polarization of the spin system. At a fixed external magnetic field of $B = 1.95\,\mathrm{T}$, the polarization induced in the nuclear spin system is oriented in positive x direction for a positive detuning $\delta_T > 0\,\mathrm{meV}$ whereas the polarization becomes negative for $\delta_T < 0\,\mathrm{meV}$. Furthermore, a stronger detuning produces a more pronounced shift of the Overhauser field distribution in the presented energy range of δ_T. These findings comply with experimental data [227] that hints at a broadening of the distribution of the electron spin precession frequencies produced by the nuclei-induced frequency focusing. As the experiment focuses on a quantum dot ensemble, we expect the measurements to comprise contributions from quantum dots with positive and negatively detuning with respect to the laser frequency. Therefore, the electron spin precession frequencies in the quantum dot ensemble cover a broader range with nuclei-induced frequency focusing than without.

6.5 Effect of static nuclear-electric quadrupolar interactions

Since the emergence of the quasistationary steady state under the periodic pulse train requires up to 20 million repetition periods which correspond to a duration of roughly 0.3 s, the question about the effect of additional weaker spin interactions arises. The nuclear quadrupolar interactions introduced in Sec. 2.7 have been found to become relevant for times in the order of several hundred nanoseconds [194, 196, 197]. We address their effect by extending the quantum mechanical approach to incorporate the additional spin dynamics induced by the quadrupolar interactions for the temporal evolution between the pump pulses. For modeling the pump pulses, we return to instantaneous resonant π pulses captured by Eqs. (5.11) and (5.12) for simplicity. The repetition period remains $T_R = 13.2\,\mathrm{ns}$. As the full quantum mechanical treatment is limited to small system sizes due to the exponentially growing Hilbert space dimension $d = 3(2I+1)^N$, we focus on a system with $N = 3$ nuclear spins of the individual length $I = 3/2$ which applies for Ga

and As. The resulting Hilbert space dimension $d = 192$ equals the dimension of the previously treated system comprising $N = 6$ nuclear spins with $I = 1/2$. In view of this limitation, we aim at a general understanding of the impact that the nuclear quadrupolar interactions impose on the mode-locking effect rather than a quantitative description of the real quantum dot ensemble.

6.5.1 Numerical implementation

To incorporate the quadrupolar interactions in the implementation of the spin dynamics, the procedure outlined in Sec. 5.4 has to be adjusted. First, the Hamiltonian H, Eq. (5.16), is complemented by the static nuclear-electric quadrupolar interactions H_{NQ} introduced in Eq. (2.20),

$$\begin{aligned} H &= H_T + H_{\mathrm{HF}} + H_{\mathrm{EZ}} + H_{\mathrm{NZ}} + H_{\mathrm{NQ}} \\ &= \epsilon_T |T\rangle \langle T| + \sum_k A_k \mathbf{S} \cdot \mathbf{I}_k - \omega_e S^x - \omega_n I_k^x \\ &\quad + \sum_k q_k \left\{ \frac{\eta}{3} \left[(\mathbf{l}_k \cdot \mathbf{I}_k)^2 - (\mathbf{m}_k \cdot \mathbf{I}_k)^2 \right] + (\mathbf{n}_k \cdot \mathbf{I}_k)^2 - \frac{I(I+1)}{3} \right\}. \end{aligned} \tag{6.16}$$

The extended Hamiltonian H enters the Lindblad master equation, Eq. (5.13), governing the temporal evolution of the density operator ρ between consecutive pulses. It is convenient to transform the Lindblad equation into the frame of the Hamiltonian $H_0 = -\omega_n F^x + H_{\mathrm{NQ}}$ comprising the relatively slow nuclear spin dynamics as well as the additional electron contribution $\omega_n S^x$ as shown in Sec. 5.4. Employing the redefined unitary operator $U_n = \exp(iH_0 t)$, we obtain the Lindblad master equation for the transformed operators $\tilde{\rho} = U_n \rho U_n^\dagger$ and $\tilde{s} = U_n s U_n^\dagger$,

$$\partial_t \tilde{\rho} = -i \left[\tilde{H}, \tilde{\rho} \right] - \gamma \left(\tilde{s}^\dagger \tilde{s} \tilde{\rho} + \tilde{\rho} \tilde{s}^\dagger \tilde{s} - 2 \tilde{s} \tilde{\rho} \tilde{s}^\dagger \right). \tag{6.17}$$

Here, the operator $\tilde{s}$ retains the form stated in Eq. (5.18). However, the transformed Hamiltonian $\tilde{H}(t)$,

$$\tilde{H}(t) = e^{i(-\omega_n F^x + H_{\mathrm{NQ}})t} \left(H_{\mathrm{HF}} - (\omega_e - \omega_n) S^x + H_T \right) e^{-i(-\omega_n F^x + H_{\mathrm{NQ}})t}, \tag{6.18}$$

becomes time dependent since generally $\left[F^x, H_{\mathrm{NQ}} \right] \neq 0$.

We continue along the same lines as in Sec. 5.4 and separate the temporal evolution of the density suboperator $\tilde{\rho}_{TT}$ for the trion population from the dynamics of the remaining parts of the density operator. The master equation for $\tilde{\rho}_{TT}$ complies with Eq. (5.21) but with redefined operators $\tilde{O}$. Thus, the time evolution of $\tilde{\rho}_{TT}$ is given by Eq. (5.22a) but is supplemented by H_{NQ} in the original frame,

$$\rho_{TT}(t_0 + t) = e^{-2\gamma t} e^{-i(H_{\mathrm{NZ}} + H_{\mathrm{NQ}})t} \rho_{TT}(t_0) e^{i(H_{\mathrm{NZ}} + H_{\mathrm{NQ}})t}. \tag{6.19}$$

The master equation for the remaining sector of the density operator $\tilde{\rho}_S$ related to a reduced matrix dimension $d' \times d'$, which comprises the electron spin states $|\uparrow\rangle$ and $|\downarrow\rangle$, reads

$$\begin{aligned}\partial_t \tilde{\rho}_S + i\left[\tilde{H}_S(t), \tilde{\rho}_S\right] = \gamma e^{-2\gamma t}\tilde{\rho}_{TT}(t_0)\,(|\uparrow\rangle\langle\uparrow| + e^{i\omega_n t}\,|\uparrow\rangle\langle\downarrow| \\ + e^{-i\omega_n t}\,|\downarrow\rangle\langle\uparrow| + |\downarrow\rangle\langle\downarrow|)\,. \end{aligned} \tag{6.20a}$$

This equation is similar to Eq. (5.23), but the Hamiltonian $\tilde{H}_S(t)$ is time dependent,

$$\tilde{H}_S(t) = e^{i(-\omega_n F^x + H_{\mathrm{NQ}})t}\,(H_{\mathrm{HF}} - (\omega_e - \omega_n)S^x)\,e^{-i(-\omega_n F^x + H_{\mathrm{NQ}})t}. \tag{6.20b}$$

We note that for vanishing quadrupolar interactions, i.e., $q_k = 0$ for all k, the Hamiltonian $\tilde{H}_S(t)$ simplifies to $\tilde{H}_S = H_{\mathrm{HF}} - (\omega_e - \omega_n)S^x$ as in Eq. (5.24).

In the case of nonvanishing quadrupolar interactions, we tackle the time dependence of $\tilde{H}_S(t)$ by exploiting the fact that the dynamics governed by H_0 is slow compared to the time evolution resulting from $H_{\mathrm{HF}} - (\omega_e - \omega_n)S^x$. We define small intervals of time with duration Δ_t. In these intervals, we approximate $\tilde{H}_S$ as constant in time and employ a midpoint rule. For the individual steps of discretization, we proceed as outlined in Sec. 5.4 and compose the time evolution of ρ_S from a unitary part solving the homogeneous part of Eq. (6.20a) and a particular solution of the full nonhomogeneous equation, Eq. (6.20a).

The error $\epsilon(\Delta_t)$ arising from the midpoint rule is determined by the second order derivative of $\tilde{H}_S(t)$ in time,

$$\epsilon(\Delta_t) \leq \frac{\Delta_t^3}{24}\,|[H_0, [H_0, H_{\mathrm{HF}} - (\omega_e - \omega_n)S^x]]| = \frac{\Delta_t^3}{24}\,\left|\left[H_0, \left[H_{\mathrm{NQ}}, H_{\mathrm{HF}}\right]\right]\right|. \tag{6.21}$$

Aiming at an upper bound of the error, we address the worst case scenario for $\epsilon(\Delta_t)$ and estimate the commutator analytically by four times the product of the maximum eigenvalues of H_0, H_{NQ} and H_{HF}. The maximum eigenvalues are approximated by $\omega_n/2 + NI\omega_n + N\bar{q}_k I^2 - I(I+1)/3$ for H_0, $N\bar{q}_k I^2 - I(I+1)/3$ for H_{NQ}, and $N\bar{A}_k I$ for H_{HF} respectively, where $\bar{A}_k$ and $\bar{q}_k$ denote the average hyperfine and quadrupolar coupling constant respectively. The product of these estimates yields that the step width has to be smaller than 0.9 ns for $Q = 0.01$ and $B = 2\,\mathrm{T}$ in accordance with Eq. (6.21). The numerical evaluation of the commutator for various sets of randomly distributed coupling constants generated as outlined in Sec. 2.7 and Sec. 5.5 produces the requirement of time steps that are smaller than 1.7 ns for the same parameters as before.

For the practical application of the approach, a step width of $\Delta_t = 0.6\,\mathrm{ns}$ has proven reasonable. Figure 6.8 presents a comparison of the data obtained with different

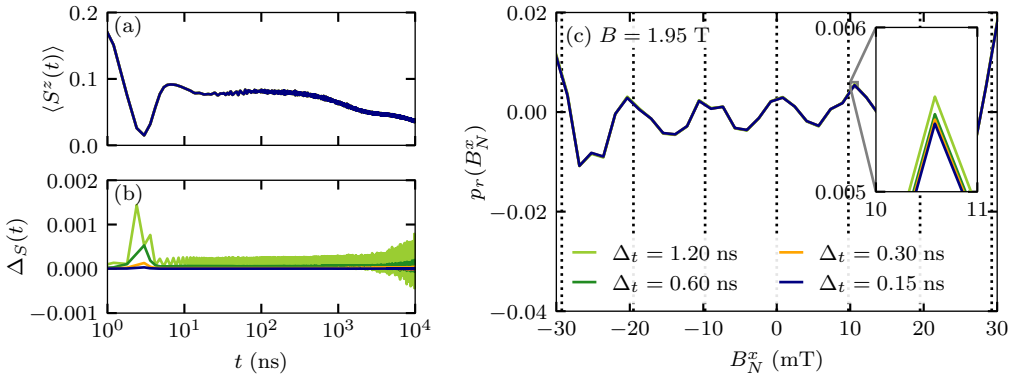

Figure 6.8: Discretization error arising from the numerical treatment including the nuclear quadrupolar interactions ($Q = 0.01$, $\eta = 0.5$, $\theta_M = 34°$) in the spin system ($N = 3$, $I = 3/2$, $N_C = 800$). (a) Time evolution of the electron spin $\langle S^z(t)\rangle$ for the system in equilibrium. (b) Relative deviation Δ_S due to the discretization from the exact unitary time evolution extracted from the results in (a). (c) Relative Overhauser field distribution $p_r(B_N^x)$ in the mode-locked system ($B = 1.95\,\mathrm{T}$, $N_P = 10^5$). The legend indicating the step width Δ_t of the discretization in panel (c) applies to the whole figure.

step widths Δ_t at the quadrupolar strength $Q = 0.01$ with biaxiality $\eta = 0.5$ and maximum angle $\theta_M = 34°$. As a first step, we focus on the spin dynamics in equilibrium, i.e., the external magnetic field and the periodic optical excitation are absent, so that an exact unitary time evolution can serve as a reference, see Figs. 6.8(a) and 6.8(b). In the beginning, $t = 0$, the electron spin polarization is set to $\langle S^z(0)\rangle = 0.5$ while the high-temperature limit is applied to nuclear spins, cf. Sec. 2.6. The exact time evolution of $\langle S^z(t)\rangle$ (black line – not visible) and the approximated data for different step widths of discretization presented in Fig. 6.8(a) fully coincide on the time scale of 10^4 ns such that they cannot be distinguished in the figure. Therefore, we provide the relative deviation Δ_S of the discretized calculation from the exact unitary evolution in Fig. 6.8(b). Minor deviations occur especially for the step width $\Delta_t = 1.2$ ns. Since these deviations recede rapidly when decreasing Δ_t, the choice $\Delta_t = 0.6$ ns proves a good balance between numerical accuracy and computational effort.

The examination of the periodically driven spin system supports this choice. The relative Overhauser field distributions $p_r(B_N^x)$ of the mode-locked system at an exemplary external magnetic field of $B = 1.95\,\mathrm{T}$ match almost perfectly for the presented step widths Δ_t in Fig. 6.8(c). In the case of the periodic optical excitation, it is advantageous to exploit the rapidly decaying trion state, i.e., the fact that the trion occupation is in the range of computational accuracy roughly 1.2 ns after the

instantaneous pump pulse for the rate $\gamma = 10\,\mathrm{ns}^{-1}$. Thus, we only need to employ two steps of discretization for the period directly after a pump pulse. The remaining time between two consecutive pump pulses, $T_R - 2\Delta_t$, is covered by an exact unitary time evolution disregarding the trion state.

6.5.2 Weakening of the nuclei-induced frequency focusing

To analyze the effect of the nuclear-electric quadrupolar interactions on the nuclei-induced frequency focusing, we initially focus on a fixed exemplary external magnetic field of $B = 1.95\,\mathrm{T}$. The parameters of the quadrupolar interactions, namely the biaxiality η and the easy axes $\mathbf{n}_k$, are adjusted as discussed in Sec. 2.7. We employ the extended quantum mechanical approach and iteratively compute the periodic pulse train. Figure 6.9(a) displays the emergence of the electron spin revival amplitude $S^{\perp}(N_P)$ for various strengths of the quadrupolar interactions measured by Q defined in Eq. (2.21). At the selected external magnetic field of $B = 1.95\,\mathrm{T}$ corresponding to $n = 1$ in the resonance condition, Eq. (6.13), we observe an increase in the revival amplitude starting from the value $S^{\perp}_{\mathrm{ess}} = 0.077$ without the quadrupolar interactions which is indicated by black markers for comparison. Incorporating the quadrupolar interactions, the emerging revival amplitude clearly decreases with strengthening Q. This decrease indicates that the quadrupolar interactions counteract the synchronization of the spin system with the periodic optical excitation. Similar observations have been made in Ref. [225] employing a dynamical mean-field approach for a larger system in the box model limit of the hyperfine interaction.

Since the increasing revival amplitude at the external magnetic field of $B = 1.95\,\mathrm{T}$ is connected to the nuclei-induced frequency focusing, we inspect the relative Overhauser field distributions $p_r(B_N^x)$ of the mode-locked system after ten million pump pulses which are related to the steady-state revival amplitudes in Fig. 6.9(a), see Fig. 6.9(b). The peaks in the Overhauser field distribution corresponding to the integer modes of the electron spin precession become less pronounced when increasing the strength of the quadrupolar interactions. We attribute this finding to the additional disorder induced by the quadrupolar Hamiltonian H_{NQ} in the nuclear spin bath. At the quadrupolar strength of $Q = 0.01$, we still find minor peaks of $p_r(B_N^x)$ (dark green line, mostly covered by the orange curve) which produce an electron spin revival amplitude that does not exceed the electronic steady-state value $S^{\perp}_{\mathrm{ess}}$ by much. Quadrupolar interactions with strength $Q = 0.1$ (orange line), however, completely prohibit the emergence of nuclei-induced frequency focusing. Accordingly, the related revival amplitude does not reach the value $S^{\perp}_{\mathrm{ess}}$ at all. Indeed, quadrupolar interactions of this strength have been found to produce a feedback effect onto the electron spin via the hyperfine coupling that leads to an

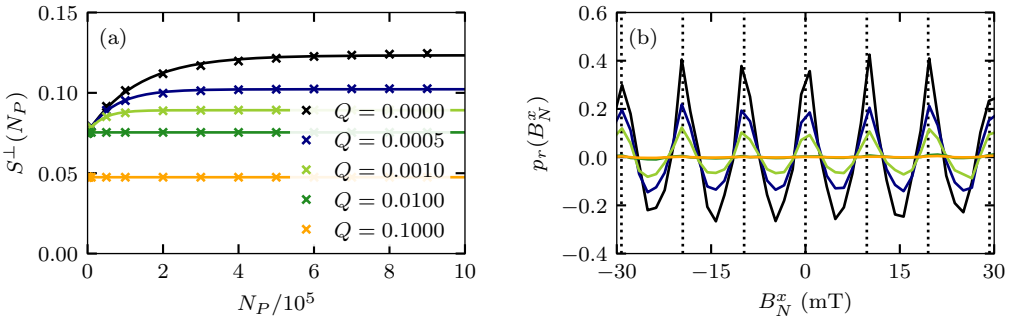

Figure 6.9: Mode locking in the spin system ($N = 3$, $I = 3/2$, $N_C = 800$) with quadrupolar interactions of varying strength Q. The external magnetic field is adjusted to $B = 1.95\,\mathrm{T}$. The quadrupolar easy axes are randomly distributed in a cone with opening angle $\theta_M = 34^\circ$ around the z axis; the anisotropy is $\eta = 0.5$. (a) Emergence of the electron spin revival amplitude $S^{\perp}(N_P)$ with increasing the number N_P of pump pulses. (b) Relative Overhauser field distribution $p_r(B_N^x)$ after $N_P = 10^6$ pump pulses at varying values of Q [color coded according to the legend in panel (a)]. The dark green line is mostly covered by the orange line.

electron spin dephasing on the time scale of roughly 100 ns. This dephasing time is comparable to the time scale $N_P T_R = 10 \times 13.2\,\mathrm{ns}$ on which the electronic steady state emerges, cf. Sec. 6.1, such that two effects become competitive.

For a more detailed analysis of the quadrupolar effects, we fit the electron spin revival amplitude $S^{\perp}(N_P)$ as a function of the number of preceding pump pulses by the function

$$S^{\perp}(N_P) = S^{\perp}_{\infty} - S^{\perp}_{\Delta} e^{-N_P/N_R}. \tag{6.22}$$

We use the revival amplitude $S^{\perp}_{\infty}$ in the nonequilibrium steady state, the increment $S^{\perp}_{\Delta}$ during the pulse train, and a characteristic number N_R of pump pulses required to approach the steady-state revival amplitude as fit parameters. Exemplary fit functions for the respective quadrupolar parameter are added in Fig. 6.9(a) as solid lines. Figures 6.10(a) and 6.10(b) present the resulting fit parameter $S^{\perp}_{\infty}$ and N_R as a function of the quadrupolar coupling strength Q. We provide the fit parameter obtained for quadrupolar easy axes $\mathbf{n}_k$ distributed in a cone with opening angle $\theta_M = 34^\circ$ around the optical axis (blue markers) as well as for easy axes fixed either along the external magnetic field direction (orange triangles) or the optical axis (green squares), i.e., $\mathbf{n}_k \equiv \mathbf{e}_x$ or $\mathbf{n}_k \equiv \mathbf{e}_z$ for all nuclear spins respectively. The quadrupolar anisotropy is consistently set to $\eta = 0$ in the three scenarios.

The converged electron spin revival amplitude $S^{\perp}_{\infty}$ in the system with the quadrupolar easy axes fixed along the z direction decreases when increasing the quadrupolar coupling strength Q and quickly approaches a plateau at $S^{\perp}_{\mathrm{ess}} \approx 0.077$ (gray dotted

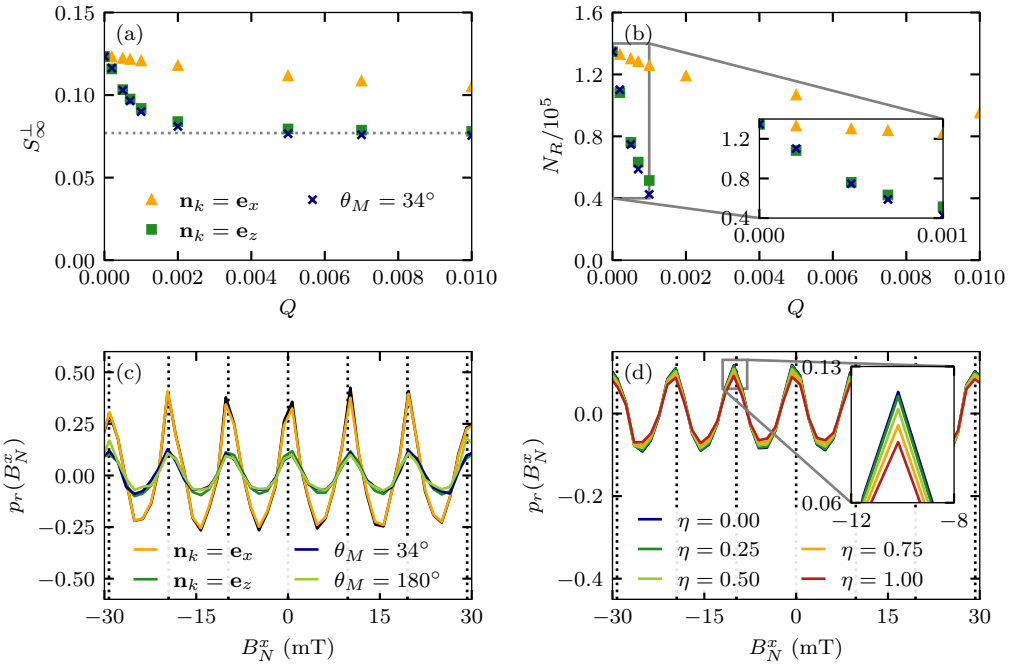

Figure 6.10: Effect of the quadrupolar interactions on the mode-locking effect in the electron-nuclear spin system ($N = 3$, $I = 3/2$, $N_C = 800$) at the external magnetic field of $B = 1.95\,\mathrm{T}$. (a) Steady-state revival amplitude $S^{\perp}_{\infty}$ fitted according to Eq. (6.22) as a function of the quadrupolar interaction strength Q. Data for several scenarios for the quadrupolar easy axes $\mathbf{n}_k$ are presented; $\eta = 0$. (b) Characteristic pulse number N_R for the buildup of the revival amplitude fitted according to Eq. (6.22). The quadrupolar parameters equal those in panel (a). (c) Relative Overhauser field distribution $p_r(B^x_N)$ after $N_P = 10^6$ pump pulses for different orientations of the quadrupolar easy axes; $Q = 0.001$ and $\eta = 0$. For comparison, the distribution for $Q = 0$ is added in black (mostly covered by the orange line). (d) Relative Overhauser field distribution $p_r(B^x_N)$ after $N_P = 10^6$ pump pulses for different values of the quadrupolar anisotropy parameter η; $Q = 0.001$ and $\mathbf{n}_k \equiv \mathbf{e}_z$.

horizontal line) which is preserved in the range up to $Q = 0.01$. This behavior does not change much when the quadrupolar easy axes are distributed in a cone with opening angle $\theta_M = 34°$ around the z axis. For easy axes fixed along the direction of the external magnetic field, however, the attenuation of the revival effect is much weaker and $S^{\perp}_{\infty}$ remains significantly larger than $S^{\perp}_{\mathrm{ess}}$ over the full range up to $Q = 0.01$. For an explanation, we start with the case $\mathbf{n}_k \equiv \mathbf{e}_x$. Here, the quadrupolar interactions H_{NQ} produce an additional effective magnetic field in x direction for the individual nuclear spins. Accordingly, the individual spin

components I_k^x along the external magnetic field direction remain mostly conserved when omitting the Knight field which we assume to average to zero as a result of the fast electron spin precession. Quadrupolar contributions with a nonzero projection of the easy axes onto the (yz) plane however lift the spin conservation of I_k^x and therefore induce a disorder counteracting the nuclei-induced frequency focusing. Thus, the quadrupolar contributions along the magnetic field direction affect the nuclei-induced frequency focusing significantly less than the transversal components. The quadrupolar contributions in x direction produce slightly differing strengths of the total effective magnetic fields $B + q_k I_k^z$ acting on the individual nuclear spins. Consequently, the nuclear spins obtain differing precession frequencies, and the resonance condition, Eq. (6.13), disperses leading to a reduction of the electron spin revival amplitude.

The characteristic number of repetition periods N_R required to approach the non-equilibrium steady state under the periodic optical excitation decreases alongside the converged revival amplitude, see Fig. 6.10(b). The increased electron spin revival amplitude at the fixed magnetic field $B = 1.95\,\mathrm{T}$ originates from pronounced peaks in the Overhauser field distribution at the integer precession modes whose emergence originates from a profound reorientation of the nuclear spins. Hence, the more pronounced nuclei-induced frequency focusing at small values of Q requires a stronger reorientation of the nuclear spins evolving on a longer time frame. In other words, the additional perturbations due to the quadrupolar interactions produce a faster convergence to a less ordered nuclear spin configuration in the quasistationary steady state. The relative Overhauser field distributions $p_r(B_N^x)$ of the mode-locked system in Fig. 6.10(c) provide further insight. For quadrupolar easy axes aligned along the external magnetic field (orange line), the peaks at the integer modes of the electron spin precession are almost as pronounced at a quadrupolar coupling strength of $Q = 0.001$ as without quadrupolar interactions (black line). Quadrupolar easy axes deviating from the magnetic field direction inherently result in less distinct peaks of $p_r(B_N^x)$. All peaks are equally reduced to less than half of the original amplitude for $\mathbf{n}_k \equiv \mathbf{e}_z$ (dark green line) as well as for the uniform distribution in the cone with arbitrary opening angle Θ_M from the z axis (blue and light green line respectively).

Similar observations are made when focusing on the dependence of the nuclei-induced frequency focusing on the quadrupolar biaxiality parameter η. The relative Overhauser field distributions $p_r(B_N^x)$ for various choices of η (which previously was set to zero) nearly coincide for $Q = 0.001$ and $\mathbf{n}_k \equiv \mathbf{e}_z$, see Fig. 6.10(d). Minor deviations of $p_r(B_N^x)$ are only resolved in the inset and hint at a slightly less pronounced nuclei-induced frequency focusing when increasing η. As the quadrupolar easy axes are fixed perpendicular to the magnetic field direction, we impose a maximum counter-effect to the reorganization of the Overhauser field by

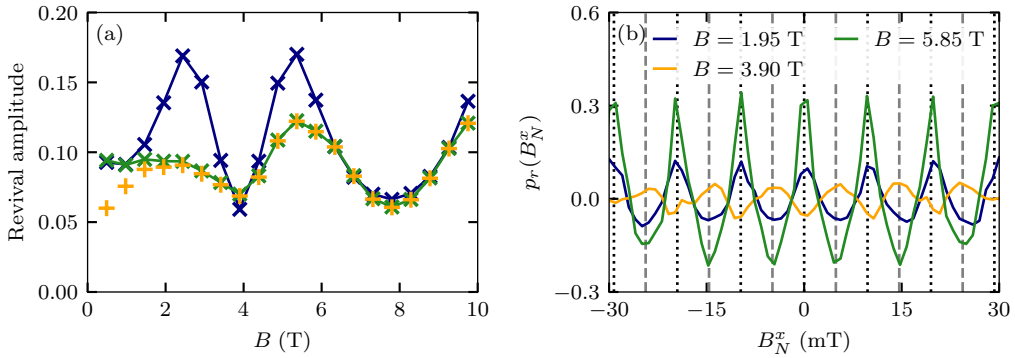

Figure 6.11: Magnetic field dependence of the mode-locking effect in the spin system ($N = 3$, $I = 3/2$, $N_C = 800$) with quadrupolar interactions; $Q = 0.001$, $\eta = 0.5$ and $\theta_M = 34°$. (a) Converged electron spin revival amplitude $S^\perp$ (green markers) and the related electron spin component $|\langle S_c^z \rangle|$ (orange crosses) as a function of the magnetic field strength B. For comparison, the converged amplitude $S^\perp$ of the system without quadrupolar interactions – taken from Fig. 6.3(b) – is added (blue markers). (b) Relative Overhauser field distribution $p_r(B_N^x)$ after $2 \times 10^6 \leq N_P \leq 2 \times 10^7$ pump pulses for different external magnetic fields.

this choice already and the mode-locking effect is not suppressed much further due to the increasing biaxiality.

Finally, we extend the examination of the mode-locked spin system with nuclear quadrupolar interactions to the dependence on the external magnetic field. To this end, the quadrupolar parameters are adjusted as initially introduced in Sec. 2.7, $Q = 0.001$, $\eta = 0.5$, and $\theta_M = 34°$. The converged electron spin revival amplitude $S^\perp$ after up to 20 million pump pulses as a function of the magnetic field B is presented in Fig. 6.11(a) (green markers). The revival amplitude retains the nonmonotonic behavior originating from the resonance condition, Eq. (6.13), with maxima at roughly 2 T and 6 T respectively and minima in between, i.e., at 4 T and 8 T. However, the maximum revival amplitudes are reduced compared to the data for the spin system without quadrupolar interactions (blue markers). In particular, the maximum revival amplitude at 2 T is affected. While the two maxima at 2 T and 6 T have equal amplitude for $Q = 0$, the maximum at 2 T is considerably less pronounced than the maximum at 6 T for $Q = 0.001$. Accordingly, the relative Overhauser field distribution $p_r(B_N^x)$ in the system with quadrupolar interactions exhibits peaks of smaller amplitude at $B = 1.95$ T compared to the distribution at $B = 5.85$ T, see Fig. 6.11(b). For $Q = 0$, in contrast, the peak amplitudes were similar at these magnetic fields, cf. Fig. 6.4. Thus, the quadrupolar interactions have a stronger effect at small external magnetic fields. We ascribe this behavior to the suppression of the quadrupolar couplings by the nuclear Zeeman term at strong

external magnetic fields as discussed in Ref. [228].

We conclude by noting that the quadrupolar interaction strength measured with respect to the hyperfine coupling via the measure Q introduced in Eq. (2.21) is relatively weak at the value $Q = 0.001$ compared to Ref. [122]. Since the small system size in the quantum mechanical investigations does not allow for a detailed portraying of the distribution of the quadrupole parameter [194] in real quantum dots comprising up to 10^6 nuclear spins, the present analysis is aiming towards a basic understanding of the interplay of the mode-locking effect and the quadrupolar interactions rather than a quantitative analysis. The quadrupole parameter for the individual isotopes in the (In,Ga)As/GaAs quantum dot ensemble differ significantly. Furthermore, the strain-induced electric field gradients vary in the sample as well as within the individual quantum dots. These interrelations potentially induce a correlation between the hyperfine coupling constants A_k and the quadrupolar couplings q_k of the individual nuclear spins. The modeling of this intricate situation is beyond the scope of this thesis and is left as a task for future research.

6.6 Effect of different nuclear isotopes

The nonmonotonic dependence of the electron spin revival amplitude on the external magnetic field measured in pump-probe experiments is superimposed by various modulations, cf. Fig. 5.2(b), rather than displaying the straight periodic behavior observed in the theoretical investigation, cf. Fig. 6.1(b). We tackle the question about the additional modulations in the experimental data by addressing the individual nuclear isotopes in the (In,Ga)As/GaAs quantum dots separately where we previously employed a nuclear spin of average type. The five relevant isotopes in the (In,Ga)As/GaAs quantum dots differ in the spin length I, the magnetic moment μ, and thereby the nuclear g factor $g_N = \mu/(\mu_N I)$, see Tab. 6.1. Hence, the Eq. (6.13) at a fixed external magnetic field implies different values of n for the nuclear Zeeman terms of the individual isotopes. Accordingly, the favoring of different types of electron spin precession modes is predicted for the respective nuclear isotopes. For comparison, we added a column in Tab. 6.1 with the external magnetic field B_2 corresponding to $n = 2$ in Eq. (6.13) for the different nuclear isotopes. At these magnetic fields B_2, we would expect a minimum of the electron spin revival amplitude due to the favoring of the integer precession modes taking into account the respective nuclear isotope alone. For the composite system of (In,Ga)As quantum dots, the interplay of these resonances becomes relevant. Previously, this question has been addressed in Ref. [91] by a perturbative quantum mechanical treatment that does not reach the quasistationary steady state, and by a classical

Isotope	N. A.	I	μ/μ_N	g_N	$g_N\mu_N$ (MHz/T)	B_2 (T)
^{69}Ga	0.601	3/2	2.02	1.34	10.25	3.70
^{71}Ga	0.399	3/2	2.56	1.71	13.02	2.91
^{75}As	1.000	3/2	1.44	0.96	7.32	5.18
^{113}In	0.043	9/2	5.53	1.23	9.37	4.04
^{115}In	0.957	9/2	5.54	1.23	9.39	4.04

Table 6.1: Stable nuclear isotopes in the self-assembled (In,Ga)As/GaAs quantum dots and their properties. Listed are natural abundance (N. A.), spin length, magnetic moment, g factor, coupling strength to the magnetic field, and the external magnetic field at which the minimum electron spin revival amplitude is expected according to Eq. (6.13) with $n = 2$. The data for I and μ/μ_N are taken from Ref. [135].

approach for the box model approximation of the hyperfine coupling constants in Ref. [89].

For the investigation of the electron-nuclear spin system comprising nuclear spins with different g factors, we employ the extended quantum mechanical approach outlined for including the nuclear quadrupolar interactions, cf. Sec. 6.5.1. Here, we substitute the Hamiltonian, Eq. (6.16), by

$$H = H_T + H_{\mathrm{HF}} + H_{\mathrm{EZ}} + H_{\mathrm{NZ}} \tag{6.23a}$$

with

$$\begin{aligned} H_{\mathrm{NZ}} &= -\sum_k g_k \mu_N B I_k^x \\ &= -\overline{\omega}_n \sum_k I_k^x - \sum_k \Delta_k I_k^x = H_{\overline{\mathrm{NZ}}} + H_{\mathrm{NZ},\Delta} \end{aligned} \tag{6.23b}$$

such that each nuclear spin enters with its individual g factor g_k. Furthermore, we introduce the average Larmor frequency $\overline{\omega}_n = \overline{g}_k \mu_N B$ based on the mean g factor $\overline{g}_k$ as well as the g factor deviations $\Delta_k = (g_k - \overline{g}_k)\mu_N B$ for the individual nuclear spins. In the case of varying nuclear precession frequencies, it proves useful to transform into the rotating frame of the redefined Hamiltonian $H_0 = -\overline{\omega}_n F^x + H_{\mathrm{NZ},\Delta}$. Subsequently, we proceed analogously as in Sec. 6.5.1 with $\overline{\omega}_n$ replacing ω_n as well as $H_{\mathrm{NZ},\Delta}$ replacing H_{NQ}. The time-dependent Hamiltonian in the rotating frame analogous to Eq. (6.20b) reads

$$\tilde{H}_S(t) = e^{i(-\overline{\omega}_n F^x + H_{\mathrm{NZ},\Delta})t} \left(H_{\mathrm{HF}} - (\omega_e - \overline{\omega}_n) S^x\right) e^{-i(-\overline{\omega}_n F^x + H_{\mathrm{NZ},\Delta})t}. \tag{6.24}$$

Hence, the time dependence of the Hamiltonian $\tilde{H}_S(t)$ would be lifted again when returning to identical g factors for all nuclear spins due to $H_{\mathrm{NZ},\Delta} = 0$.

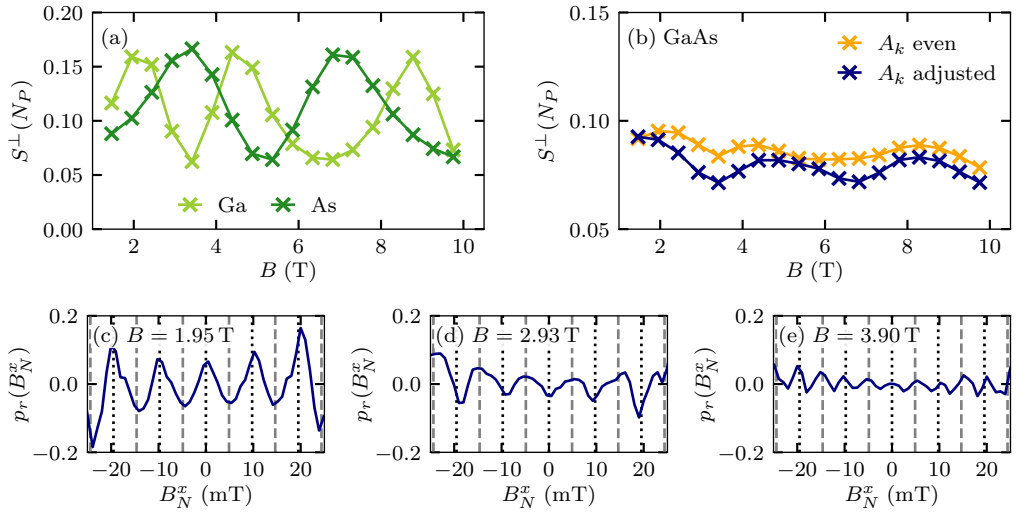

Figure 6.12: Magnetic field dependence of the mode-locked system ($N = 6$, $I = 1/2$, $N_C = 100$, $N_P = 10^7$) comprising different nuclear species. (a) Electron spin revival amplitude $S^\perp$ as a function of the external magnetic field considering the nuclear species separately. (b) Electron spin revival amplitude $S^\perp$ in the system containing three nuclear spins of Ga type and As type respectively. (c),(d) and (e) Relative Overhauser field distribution $p_r(B_N^x)$ at different external magnetic fields examining the composite GaAs system with adjusted hyperfine coupling constants of the two components.

For differing nuclear g factors, the time dependence of $\tilde{H}_S(t)$ is treated similarly as for the nuclear quadrupolar interactions. The time evolution during the trion decay, i.e., 1.2 ns after the pump pulse, is discretized in small time steps on which $\tilde{H}_S(t)$ is approximated as constant employing a midpoint rule such that the treatment outlined in Sec. 5.4 can be applied to each individual step in time. The remaining time evolution after the trion decay with duration 12.0 ns is covered by the exact unitary evolution capturing the full dynamics of the Hamiltonian H, Eq. (6.23a).

As the full quantum mechanical treatment is limited to $N = 6$ nuclear spins of individual length $I = 1/2$, we focus on the spin system comprising three nuclear spins with the g factor of As indicated in Tab. 6.1 and three nuclear spins with the nuclear g factor corresponding to the average of the two Ga isotopes weighted by their natural abundance, i.e., $g_{N,\overline{\mathrm{Ga}}}\mu_N = 11.35\,\mathrm{MHz/T}$ with $B_{2,\overline{\mathrm{Ga}}} = 3.34\,\mathrm{T}$. For simplicity, the nuclear quadrupolar interactions are omitted in this analysis. We start by presenting the magnetic field dependence of the converged electron spin revival amplitude $S^\perp$ that is obtained when considering the two exemplary nuclear species separately in Fig. 6.12(a). In the system consisting of six nuclear spins, the

nuclear g factor is chosen equally for all nuclear spins. Its value is either fixed to the value of As (dark green markers) or the average value of the Ga isotopes (light green markers). The data for the two scenarios clearly differs and the maxima and minima of the nonmonotonic functions are placed at strongly differing external magnetic fields as expected from the prediction by Eq. (6.13).

As a next step, we examine the interplay of the two exemplary nuclear g factors. The converged revival amplitude $S^{\perp}$ for the spin system comprising three spins of each of the two nuclear species is displayed in Fig. 6.12(b) (orange markers). Since half of the nuclear spins have the average g factor of Ga and the g factor of As is assigned to the other half of the nuclear spins, the nuclei-induced frequency focusing is subject to two mostly counteracting components. Where the data for Ga exhibits a peak of the revival amplitude, the nuclear spins of As type induce a minimum, cf. Fig. 6.12(a). As a consequence, the maxima and minima of $S^{\perp}$ in the composite system are significantly less pronounced in Fig. 6.12(b).

We recall that the hyperfine coupling of the localized electron spin to the surrounding nuclear spins results from the Fermi contact interaction. The hyperfine coupling constants in the relevant Hamiltonian H_{FC}, Eq. (2.5), scale with μ_k/I_k, i.e., $g_k\mu_N$. Accordingly, it is intuitive to multiply the hyperfine coupling constants by the respective value of g_k after drawing random values from a uniform distribution as outlined in Sec. 5.5. Finally, the coupling constants are adjusted to produce the collective dephasing time $T^* = 1\,\mathrm{ns}$ of the electron spin. The converged electron spin revival amplitude $S^{\perp}$ of the composite GaAs system with properly adjusted hyperfine coupling constants of the two compounds is added in Fig. 6.12(b) (blue markers). Since the g factor of the Ga isotopes is stronger than that of As, we find that the revival amplitude for the adjusted hyperfine coupling constants favors the behavior of Ga, cf. the light green markers in Fig. 6.12(a). The minima of $S^{\perp}$ as a function of the magnetic field at roughly $B_{2,\overline{\mathrm{Ga}}} = 3.34\,\mathrm{T}$ and $2B_{2,\overline{\mathrm{Ga}}} = 6.68\,\mathrm{T}$ are more pronounced compared to the data for evenly weighted hyperfine coupling constants of the two nuclear species.

For the examination of the nuclei-induced frequency focusing, we address the relative Overhauser field distributions $p_r(B_N^x)$ in the composite system with properly adjusted hyperfine coupling constants. Figures 6.12(c), 6.12(d) and 6.12(e) present the converged distributions for exemplary external magnetic field strengths. At $B = 1.95\,\mathrm{T}$, the external magnetic field is close to the case $n = 1$ in Eq. (6.13) for the Ga-type g factor which favors the integer modes of the electron spin precession in Fig. 6.12(c). Due to the strong g factor of Ga, the distribution $p_r(B_N^x)$ is dominated by these Ga-induced precession modes whereas the effect of the As compound with weaker hyperfine coupling is suppressed. Similarly, the Overhauser field distribution at $B = 2.93\,\mathrm{T}$ in Fig. 6.12(d) exhibits peaks corresponding to the half-integer modes

of the electron spin precession, since this magnetic field strength is close to $B_{2,\overline{\mathrm{Ga}}}$ for the average Ga g factor. The integer modes predicted by Eq. (6.13) for the g factor of As however are vacated. When the external magnetic field fulfills Eq. (6.13) with an integer n for neither of the nuclear species, the behavior of $p_r(B_N^x)$ is not as clear. At $B = 3.90\,\mathrm{T}$ for example, the nuclei-induced frequency focusing favors the integer modes as well as the half-integer modes, see Fig. 6.12(e).

6.7 Chapter conclusion

We employed the quantum mechanical approach developed in the previous chapter to simulate the effect of a periodic pulse train on the spin dynamics in the singly charged quantum dots. The quantum mechanical approach is based on the iterative calculation of consecutive repetition periods and requires up to 20 million pump pulses to reach the quasistationary steady state of the electron-nuclear spin system. Due to the exponential growth of the Hilbert space dimension and the long pulse trains, we restrict the present analysis to systems comprising $N = 6$ nuclear spins of individual length $I = 1/2$ or equivalently $N = 3$ spins with $I = 3/2$.

By means of the full quantum mechanical calculations, we are able to connect the magnetic field dependence of the electron spin revival amplitude in the mode-locked system to the emergence of different types of electron spin precession modes. Jäschke et al. [84] predicted two kinds of resonances at which the electron spin performs either an integer or half-integer number of revolutions between consecutive pump pulses. The semiclassical approach employed in Ref. [84] mostly indicated peaks in the Overhauser field distribution at both types of precession modes which are more or less pronounced depending on various physical parameters. A detailed analysis of the dependence on the external magnetic field however is absent in Ref. [84]. A quantum mechanical treatment based on perturbation theory for the number of spin flips during one repetition period [90, 91] was able to connect the mode type favored by the nuclei-induced frequency focusing to the nuclear Zeeman term. However, the perturbative quantum mechanical approach including 20 nuclear spins was limited to the simulation of 20000 repetition periods and therefore did not reach the quasistationary steady state. The full quantum mechanical treatment in this thesis finally allows for relating the resonance condition for the nuclear Larmor precession proposed in Ref. [91] and the according electron spin precession modes favored by the nuclei-induced frequency focusing to the electron spin revival amplitude. The numerical results resemble the nonmonotonic behavior of the revival amplitude as a function of the external magnetic field observed in pump-probe experiments [86]. Both, quantum mechanical calculation and experimental measurement, have a profound minimum of the revival amplitude at the external magnetic field of

4 T in common. A classical approach [85, 87] shows a nonmonotonic dependence of the revival amplitude on the magnetic field as well [86, 88, 89], but exhibits a relatively narrow minimum at 8 T which is not as pronounced in the experimental measurements and rather broad in the quantum mechanical results. We will return to this aspect in Sec. 7.4 when addressing a larger system in the box model limit of the hyperfine coupling constants.

The experimental data indicate an overall decrease in the revival amplitude for stronger external magnetic fields. Our quantum mechanical investigations allow for attributing this effect to a finite nonzero duration of the pump pulses. Due to the electron Larmor precession during the pulses, the generation of electron spin polarization through the pulse becomes inefficient. Furthermore, we attribute the additional modulations observed in the mode-locking experiments to the diverging resonance conditions for the spin precession of the various nuclear isotopes in the quantum dots. Including nuclear quadrupolar interactions in the quantum mechanical simulation of the pulse train, we found a significant weakening of the nuclei-induced frequency focusing effect. Therefore, we conclude that these effects induced by strain in the sample resulting from the growth process must not be too strong in the quantum dots in order to enable the mode-locking effect via nuclei-induced frequency focusing.

Chapter 7

Steady-state analysis of the periodically driven spin system

As an alternative to the iterative simulation of a periodic train of optical pulses acting on the singly charged quantum dots, the quantum mechanical spin dynamics can be obtained from the eigendecomposition of a linear mapping $\mathcal{M}$ for the density operator comprising the complete time evolution during one repetition period. Such a procedure was applied by Uhrig in Ref. [92] to extract the mode-locked steady state of a system with up to $N = 6$ nuclear spins. The mapping $\mathcal{M}$ contains the effect of the pump pulse and the subsequent spin dynamics governed by the Lindblad equation, Eq. (5.13). Accordingly, a matrix representation of the super operator $\mathcal{M}$ has the dimension $D' \times D'$ with $D' = d'^2$ corresponding to the square of the Hilbert space dimension d'. In this chapter, we analyze the full eigenspectrum of the mapping $\mathcal{M}$ in detail. Moreover, we develop a truncation scheme that reduces the matrix dimensions and thereby allows for the efficient computation of the quasistationary steady state in the box model limit of the hyperfine coupling constants. Subsequently, this scheme is employed for the evaluation of the magnetic field dependence of the electron spin revival amplitude in systems comprising several hundred nuclear spins. Based on recent pump-probe experiments [94, 95, 229] exploiting the mode-locking effect in the GHz regime of the pumping periodicity, we investigate the periodic optical excitation with a reduced repetition period of $T_R = 1\,\mathrm{ns}$. Furthermore, we implement an Arnoldi iteration for the efficient computation of the quasistationary steady state and apply this method to a variety of pulse trains.

7.1 Mapping for a repetition period

The complete spin dynamics during one repetition period of the periodic pulse train can be included in a linear mapping $\mathcal{M}$ for the density operator ρ as outlined in Ref. [92],

$$\mathcal{M} : \rho(N_P T_R^-) \to \rho((N_P + 1)T_R^-). \tag{7.1}$$

Here, $\rho(N_P T_R^-)$ denotes the density operator directly before a pump pulse, and $\rho((N_P+1)T_R^-)$ denotes the density operator directly before the subsequent pump pulse. The mapping $\mathcal{M}$ comprises the pulse action as well as the subsequent trion decay and the dynamics of the coupled electron-nuclear spin system in the external magnetic field. A matrix representation $\underline{\underline{M}}$ of the mapping $\mathcal{M}$ requires the dimensions $D' \times D'$ with

$$D' = {d'}^2 = 4(2I+1)^{2N}. \tag{7.2}$$

We exclude the trion state since the trion population decays to zero on the time scale of T_R after a pump pulse. Accordingly, the matrix elements $M_{a,b}^{a',b'}$ are assigned four indices. The indices a and b denote the matrix element of the initial density operator, and the index pair a' and b' labels the matrix elements of the density operator after the application of the mapping,

$$\rho_{a',b'}((N_P+1)T_R^-) = \sum_{a,b} M_{a,b}^{a',b'} \rho_{a,b}(N_P T_R^-). \tag{7.3}$$

We specify the matrix elements of $\underline{\underline{M}}$ for a general pump pulse captured by the unitary operator U_P according to Eq. (5.9) and the subsequent time evolution of duration T_L. For the latter part, we include the trion decay as well as the spin dynamics governed by the hyperfine interaction and the external magnetic field. Previously, we derived the dynamics of the density matrix based on the Lindblad equation, Eq. (5.13), with the Hamiltonian, Eq. (5.16), and obtained Eq. (5.34). Thus, it is convenient to employ the common eigenbasis, Eq. (5.36), of the Hamiltonian H_S, Eq. (5.33), and the total spin F^x as the basis for the matrix representation of $\mathcal{M}$. To establish the matrix elements $M_{a,b}^{a',b'}$, the matrix elements of the density operator after the pulse according to Eq. (5.9) are inserted into the time evolution, Eq. (5.34), as the starting condition at time t_0,

$$\begin{aligned} M_{a,b}^{a',b'} = e^{-i(\varepsilon_{S,a}-\varepsilon_{S,b})T_L} \Big\{ &(U_P)_{a',a} (U_P)_{b,b'} - G_{a',b'}^{(-1)} Q_{a',a}^{d} \left(Q_{b',b}^{u}\right)^* \\ &- G_{a',b'}^{(0)} \left[Q_{a',a}^{u} \left(Q_{b',b}^{u}\right)^* + Q_{a',a}^{d} \left(Q_{b',b}^{d}\right)^* \right] - G_{a',b'}^{(+1)} Q_{a',a}^{u} \left(Q_{b',b}^{d}\right)^* \Big\} \end{aligned} \tag{7.4}$$

with the abbreviations

$$Q^u = |\uparrow\rangle_x \langle T| U_P \qquad \text{and} \qquad Q^d = |\downarrow\rangle_x \langle T| U_P. \tag{7.5}$$

For the above format, we employed the unitary operator U_P of a general pump pulse. Moreover, we inserted the explicit form of the electron spin operators $S^{(\tau)}$ specified in Eq. (5.29) and use the coefficients $G_{a',b'}^{(\tau)}$ defined in Eq. (5.35).

A matrix representation $\underline{\underline{M}}$ of the mapping $\mathcal{M}$ is obtained by combining the indices a and b into a single index $i \in \{1, \ldots, D'\}$. The index pair a' and b' is analogously

condensed into $i' \in \{1, \ldots, D'\}$ such that Eq. (7.4) produces matrix elements of the type $M_{i',i}$. Accordingly, the matrix elements of the density operator are rearranged into a vector with D' components denoted as $\vec{\rho}(t)$. This allows for expressing the mapping as a matrix-vector multiplication,

$$\vec{\rho}((N_P+1)T_R^-) = \underline{\underline{M}}\vec{\rho}(N_P T_R^-). \tag{7.6}$$

The evolution of the spin system under a periodic pulse train in terms of the matrix $\underline{\underline{M}}$ is described by

$$\vec{\rho}(N_P T_R^-) = \underline{\underline{M}}^{N_P}\vec{\rho}_0 \tag{7.7}$$

with the vector representations of the initial density operator ρ_0 and the density operator $\rho(N_P T_R^-)$ after N_P repetition periods directly before the incidence of the (N_P+1)-th pump pulse. For access to the quasistationary steady state under the periodic optical excitation, the eigendecomposition of the nonhermitian mapping matrix is examined,

$$\underline{\underline{M}} = \sum_i \Lambda_i \vec{r}_i \vec{l}_i^{\dagger}, \tag{7.8}$$

with the complex eigenvalues Λ_i, the right eigenvectors $\vec{r}_i$ as well as the left eigenvectors $\vec{l}_i^{\dagger}$ that can be chosen pairwise biorthogonal, $\vec{l}_i^{\dagger}\vec{r}_j = \delta_{i,j}$. The left and right eigenvectors are transformed into their matrix versions in analogy to the density matrix. They represent the right and left eigenoperators l_i and r_i of the mapping $\mathcal{M}$ in the common eigenbasis of H_S and F^x.

In Ref. [92], Uhrig showed that the eigendecomposition of the mapping $\mathcal{M}$ has the following properties:

1. The identity operator $\mathbb{1}_{d'}$ is a left eigenoperator of $\mathcal{M}$ related to the eigenvalue 1. I.e., $\mathcal{M}$ has at least one eigenvalue 1.
2. The eigenoperators r_i related to an eigenvalue unequal to 1 are traceless.
3. At least one right eigenoperator r_i to the eigenvalue 1 has a finite nonzero trace.
4. No eigenvalue with an absolute value larger than 1 occurs.
5. If a nonreal eigenvalue Λ_i occurs, the complex conjugate value $\Lambda_j \equiv \Lambda_i^*$ is an eigenvalue as well. The related eigenoperators are hermitian conjugates, $r_j = r_i^{\dagger}$.

As a periodic pulse train corresponds to the iterative application of $\underline{\underline{M}}$ to the initial density vector $\vec{\rho}_0$ according to Eq. (7.7), the eigendecomposition of $\underline{\underline{M}}$ implies,

$$\vec{\rho}(N_P T_R^-) = \sum_i \Lambda_i^{N_P} c_i \vec{r}_i \tag{7.9}$$

with complex coefficients

$$c_i = \vec{l}_i^{\dagger} \vec{\rho}_0. \tag{7.10}$$

These coefficients are determined by the overlap of the vector representation of the initial density operator with the respective left eigenvector. The quasistationary steady state of the density matrix under periodic optical excitation results from the eigenvectors related to eigenvalues $|\Lambda_i| = 1$, since any other contributions in Eq. (7.9) vanish for $N_P \to \infty$. Aiming at the mode-locking effect, it is instructive to perform an eigendecomposition of the matrix $\underline{\underline{M}}$ and study the eigenvectors related to the eigenvalues $|\Lambda_i| = 1$.

7.2 Eigenspectrum of the mapping

As a first step for the investigation of the eigendecomposition of $\mathcal{M}$, we focus on the electron-nuclear spin system as addressed in Sec. 6.3. I.e., we study the average over $N_C = 100$ realizations of the system comprising $N = 6$ nuclear spins with the individual length $I = 1/2$. The hyperfine coupling constants in the respective realizations are drawn randomly from a uniform distribution and are subsequently scaled to the ensemble dephasing time $T^* = 1\,\mathrm{ns}$, cf. Eq. (5.37). Furthermore, the pump pulse is approximated to be instantaneous such that the unitary pulse operator U_P is given by Eq. (5.12). The eigendecomposition of the matrices $\underline{\underline{M}}$ in the individual realization is obtained numerically from an exact diagonalization. Finally, the results of the individual realizations are merged as outlined in Sec. 5.5.

In the system with random hyperfine coupling constants, we find a unique eigenvalue with $|\Lambda_0| = 1$, that is $\Lambda_0 = 1$. We label this eigenvalue by Λ_0 and the related left and right eigenvectors by $\vec{l}_0^{\dagger}$ and $\vec{r}_0$ respectively. The matrix version of $\vec{r}_0$ has a finite nonzero trace, and the matrix version of $\vec{l}_0^{\dagger}$ is proportional to the identity operator. Targeting the steady-state density matrix, we scale the trace to 1 and denote the resulting matrix by $\underline{\underline{R}}_0$. This matrix is hermitian and positive semidefinite by construction. The properly scaled matrix version $\underline{\underline{L}}_0$ of the left eigenvector $\vec{l}_0^{\dagger}$, $\vec{L}_0^{\dagger}\vec{R}_0 = 1$, corresponds to the identity matrix $\underline{\underline{L}}_0 = \underline{\underline{1}}_{d'}$. Figure 7.1 displays the relative Overhauser field distribution $p_r(B_N^x)$ calculated from $\underline{\underline{R}}_0$ (orange lines) for two exemplary external magnetic field strengths (a) $B = 1.95\,\mathrm{T}$ and (b) $B = 3.90\,\mathrm{T}$ respectively. In addition, the numerical results for $p_r(B_N^x)$ obtained from the iterative calculation of the pulse train with two million pump pulses are depicted (blue lines). The agreement between the two approaches indicates that the quasistationary steady state is reached after $N_P = 2 \times 10^6$ repetition periods at the given external magnetic field strengths. Hence, the matrix $\underline{\underline{R}}_0$ completely captures the mode-locked system.

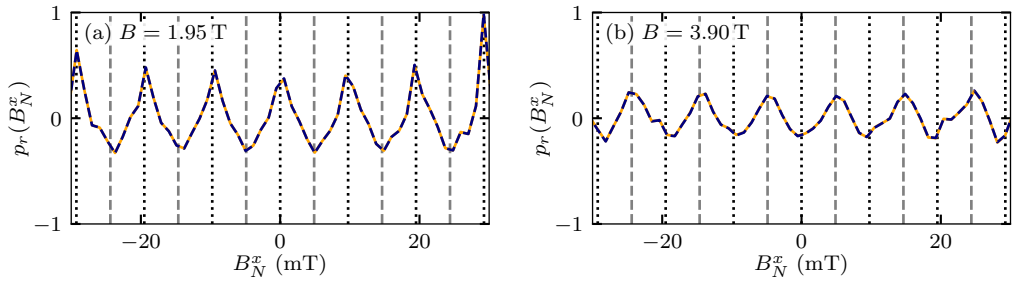

Figure 7.1: Results for the relative Overhauser field distribution $p_r(B_N^x)$ obtained by the iterative implementation of $N_P = 2 \times 10^6$ repetition periods (blue lines) and from the right eigenoperator with eigenvalue 1 of the mapping $\mathcal{M}$ (orange lines) respectively. The system comprises $N = 6$ nuclear spins with the individual length $I = 1/2$; the results are averaged over $N_C = 100$ realizations. Both approaches employ the same sets of hyperfine coupling constants. The external magnetic field is set to (a) $B = 1.95\,\mathrm{T}$ and (b) $B = 3.90\,\mathrm{T}$.

7.2.1 Absolute value of the eigenvalues

The evolution of the electron-nuclear spin system under the periodic pulse train before reaching the quasistationary steady state is determined by the eigenvalues with $|\Lambda_i| < 1$. For examination of the full eigenspectrum of $\mathcal{M}$, we start with the probability distribution $p(|\Lambda|)$ of the absolute value of the eigenvalues. The data of the eigenvalues for the $N_C = 100$ realizations is processed into a histogram with appropriate binning, typically 50 bins in the range $[0; 1]$. The resulting distribution $p(|\Lambda|)$ is treated as a continuous function due to the dense eigenspectra. Figure 7.2 displays $p(|\Lambda|)$ for the two magnetic field strengths presented in Fig. 7.1. Both probability distributions demonstrate similar behavior: They exhibit a sharp peak at $|\Lambda| = 0$ which contains half of the total weight of the distribution and is cut off in the figure to resolve the additional features of $p(|\Lambda|)$. Furthermore, the probability distributions exhibit two broader peaks at $|\Lambda| = 1/2$ and $|\Lambda| = 1$, respectively.

To understand the individual contributions in $p(|\Lambda|)$, we address the spin dynamics on the relatively short time scale of a couple of repetition periods. Here, we can neglect the feedback mechanism of the hyperfine interaction onto the nuclear spins such that the dynamics of the electron spin and the nuclear spins decouple. Accordingly, the mapping for the electron spin and the nuclear spins can be analyzed separately, and the related eigenvalues can be combined afterward. The nuclear spin dynamics are predominantly determined by the precession about the external magnetic field. Therefore, the temporal evolution of the nuclear subsystem corresponds to a unitary transformation of the density operator which is related to eigenvalues of the mapping with the absolute value 1. We will come back to the nuclear dynamics later when

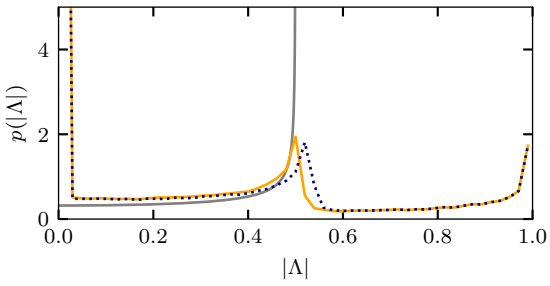

Figure 7.2: Distribution $p(|\Lambda|)$ of the absolute values of the eigenvalues of the mapping $\mathcal{M}$. The system comprises $N = 6$ nuclear spins with the individual length $I = 1/2$; $N_C = 100$. The external magnetic field amounts to $B = 1.95\,\mathrm{T}$ (blue dotted line) or $B = 3.90\,\mathrm{T}$ (orange line) respectively. The analytic prediction according to Eq. (7.18b) is added as a gray line.

addressing the complex phase of the eigenvalues Λ_i. First, we focus on the electron spin dynamics which govern the short time scales and thereby the distribution $p(|\Lambda|)$ for small values of $|\Lambda|$.

The electron spin dynamics on short time scales can be obtained in the frozen Overhauser field approximation. We omit the Overhauser field components perpendicular to the external magnetic field as they are suppressed by a strong external magnetic field. Hence, the electron spin dynamics can be addressed in the subspace of the density operator related to a fixed nuclear spin state producing the Overhauser field B_N^x. We denote this suboperator of the density operator by $\rho^e(t)$ and evaluate the dynamics of the matrix elements of $\rho^e(t)$ in the electron spin x basis. The effect of the instantaneous pump pulse is given by

$$\rho^e(t_0^+) = \frac{1}{4}\left(|\uparrow\rangle_x - |\downarrow\rangle_x\right)\left[\rho^e_{\uparrow\uparrow,x}(t_0^-) - \rho^e_{\uparrow\downarrow,x}(t_0^-) - \rho^e_{\downarrow\uparrow,x}(t_0^-) + \rho^e_{\downarrow\downarrow,x}(t_0^-)\right] \left(\langle\uparrow|_x - \langle\downarrow|_x\right), \tag{7.11}$$

$$\rho_{TT}(t_0^+) = \frac{1}{2}\left[\rho^e_{\uparrow\uparrow,x}(t_0^-) + \rho^e_{\uparrow\downarrow,x}(t_0^-) + \rho^e_{\downarrow\uparrow,x}(t_0^-) + \rho^e_{\downarrow\downarrow,x}(t_0^-)\right]. \tag{7.12}$$

The subsequent time evolution governed by the Lindblad equation, Eq. (5.13), in

the frozen Overhauser field approximation simplifies to

$$\begin{aligned}\rho^e(t_0+T_R^-) = {}& \rho^e_{\uparrow\uparrow,x}(t_0^+)\left|\uparrow\right\rangle_x\left\langle\uparrow\right|_x + e^{-i\omega T_R}\rho^e_{\uparrow\downarrow,x}(t_0^+)\left|\uparrow\right\rangle_x\left\langle\downarrow\right|_x \\ & + e^{i\omega T_R}\rho^e_{\downarrow\uparrow,x}(t_0^+)\left|\downarrow\right\rangle_x\left\langle\uparrow\right|_x + \rho^e_{\downarrow\downarrow,x}(t_0^+)\left|\downarrow\right\rangle_x\left\langle\downarrow\right|_x \\ & + \rho_{TT}(t_0^+)\left[\frac{1}{2}\left(\left|\uparrow\right\rangle_x\left\langle\uparrow\right|_x + \left|\downarrow\right\rangle_x\left\langle\downarrow\right|_x\right) + e^{-i\omega T_R}\frac{\gamma}{2\gamma - i\omega}\left|\uparrow\right\rangle_x\left\langle\downarrow\right|_x \right. \\ & \left. + e^{i\omega T_R}\frac{\gamma}{2\gamma + i\omega}\left|\downarrow\right\rangle_x\left\langle\uparrow\right|_x\right]. \end{aligned} \tag{7.13}$$

Here, the electron precession frequency $\omega = g_e\mu_B(-B + B_N^x)$ results from the combination of the external magnetic field and the respective Overhauser field B_N^x. Inserting the density operator after the pulse, Eqs. (7.11) and (7.12), as a starting condition into Eq. (7.13), we set up the (4×4)-dimensional matrix representation of the mapping for the electron spin in the basis, $\left|\uparrow\right\rangle_x\left\langle\uparrow\right|_x$, $\left|\downarrow\right\rangle_x\left\langle\uparrow\right|_x$, $\left|\uparrow\right\rangle_x\left\langle\downarrow\right|_x$, $\left|\downarrow\right\rangle_x\left\langle\downarrow\right|_x$,

$$\underline{\underline{M}}^e = \frac{1}{2}\begin{pmatrix} 1 & 0 & 0 & 1 \\ E^+\left(D^+ - \frac{1}{2}\right) & E^+\left(D^+ + \frac{1}{2}\right) & E^+\left(D^+ + \frac{1}{2}\right) & E^+\left(D^+ - \frac{1}{2}\right) \\ E^-\left(D^- - \frac{1}{2}\right) & E^-\left(D^- + \frac{1}{2}\right) & E^-\left(D^- + \frac{1}{2}\right) & E^-\left(D^- - \frac{1}{2}\right) \\ 1 & 0 & 0 & 1 \end{pmatrix} \tag{7.14}$$

with $E^\pm = e^{\pm i\omega T_R}$ and $D^\pm = \frac{\gamma}{2\gamma\pm i\omega}$ for brevity.

The eigenvalues of the above mapping for the electron spin read

$$\Lambda^e_{1,2} = 0, \quad \Lambda^e_3 = \frac{1}{2}\cos(\omega T_R) + \frac{\gamma(2\gamma\cos(\omega T_R) + \omega\sin(\omega T_R)}{4\gamma^2+\omega^2} \quad \text{and} \quad \Lambda^e_4 = 1. \tag{7.15}$$

Exploiting the rapid electron spin precession, $\gamma \ll \omega$, the third eigenvalue is approximated by

$$\Lambda_3 = \frac{1}{2}\cos(\omega T_R). \tag{7.16}$$

In the limit $\gamma \ll \omega$, the above matrix representation $\underline{\underline{M}}^e$ simplifies due to $D^\pm \approx 0$ such that the right eigenvectors are established conveniently. Their matrix counterparts read

$$\begin{aligned} &\underline{\underline{R}}^e_1 = \underline{\underline{\sigma}}^x, \quad \underline{\underline{R}}^e_2 = \underline{\underline{\sigma}}^y, \quad \underline{\underline{R}}^e_3 = \cos(\omega T_R)\underline{\underline{\sigma}}^z - \sin(\omega T_R)\underline{\underline{\sigma}}^y \\ &\text{and} \quad \underline{\underline{R}}^e_4 = \frac{1}{2}\underline{\underline{\sigma}}^0 - \frac{\cos(\omega T_R)}{2-\cos(\omega T_R)}\underline{\underline{\sigma}}^z + \frac{\sin(\omega T_R)}{2-\cos(\omega T_R)}\underline{\underline{\sigma}}^y \end{aligned} \tag{7.17}$$

making use of the Pauli matrices $\underline{\underline{\sigma}}^i$. For a physical interpretation of the eigenvalues $\Lambda^e_{1,2} = 0$, we focus on the effect of the resonant π pulse: The pump pulse completely

transfers the electron spin population in the $|\uparrow\rangle$ state into the trion state $|T\rangle$ which leaves only the contribution of the electron spin $|\downarrow\rangle$ state. Therefore, the electron spin components perpendicular to the optical axis vanish after the pulse. Accordingly, the matrix versions $\underline{\underline{R}}^e_1$ and $\underline{\underline{R}}^e_2$ of the right eigenvectors to the eigenvalues $\Lambda^e_{1,2} = 0$ are proportional to the Pauli matrices $\underline{\underline{\sigma}}^x$ and $\underline{\underline{\sigma}}^y$ and map any electron spin contribution perpendicular to the z axis to zero. This mechanism applies to the fully coupled electron-nuclear spin system as well, since the instantaneous pump pulse does not act on the nuclear spins. The distribution $p(|\Lambda|)$ in Fig. 7.2 reflects these eigenvalues by the well pronounced peak at $|\Lambda| = 0$, which holds half of the total weight. The eigenvalue $\Lambda^e_4 = 1$ captures the quasistationary steady state of the electron spin dynamics at a fixed magnetic field. The related matrix $\underline{\underline{R}}^e_4$ has a finite trace which we scaled to 1 in Eq. (7.17). Moreover, the steady state $\underline{\underline{R}}^e_4$ comprises electron spin contributions perpendicular to the external magnetic field whose share is determined by the combination of the precession frequency ω and the pulse separation T_R. For the integer modes of the electron spin precession, $\omega T_R = 2\pi a$ with an integer a, the electron spin directly before the pump pulse is aligned in negative z direction, i.e., the prefactor for the $\underline{\underline{\sigma}}^z$ matrix equals -1 and the prefactor for the $\underline{\underline{\sigma}}^y$ matrix is zero. For the half-integer modes, $\omega T_R = \pi(2a + 1)$ with an integer a, the electron spin is aligned in positive z direction before a pump pulse. The eigenvalue $\Lambda^e_3 \in [-1/2; 1/2]$ captures the electron spin dynamics complementing the steady state behavior on shorter time scales. This contribution vanishes during the pulse train due to $|\Lambda^e_3| < 1$. The related matrix $\underline{\underline{R}}^e_3$ is traceless and contains additional oscillatory components perpendicular to the external magnetic field.

To understand the distribution $p(|\Lambda|)$ in Fig. 7.2, we address the distribution of Λ_3 resulting from the randomly oriented Overhauser field which governs the precession frequency ω. Employing a Gaussian distribution $p(B^x_N)$, Eq. (2.13), the probability distribution of $\Lambda_3 \in [-1/2; 1/2]$ is given by

$$p(\Lambda_3) = \int_{-\infty}^{\infty} dB^x_N p(B^x_N) \delta\left(\Lambda_3 - f(B^x_N)\right) \tag{7.18a}$$

$$\approx \frac{4}{\pi\sqrt{1 - 4(\Lambda_3)^2}} \tag{7.18b}$$

with $f(B^x_N) = \cos(g_e \mu_B (B - B^x_N) T_R)/2$ introduced in compliance with Eq. (7.16). For the evaluation in the second line, we exploited that T^* introduced in Eq. (2.18) determines the inverse width of $p(B^x_N)$ and $T^* \ll T_R$. The analytic prediction $p(|\Lambda_3|) = 2p(\Lambda_3)$ is added in Fig. 7.2 as a gray line and roughly matches the numerically obtained distribution $p(|\Lambda|)$ for $|\Lambda| < 1/2$. In this range, additional effects of the hyperfine interaction beyond the frozen Overhauser field approximation are minor, and the precession of the nuclear spins about the external magnetic field only produces a complex phase negligible for the study of the absolute value $|\Lambda|$.

However, $p(|\Lambda|)$ obviously does not display a divergence at $|\Lambda| = 1/2$ as predicted by Eq. (7.18b) but rather a sharp peak due to the finite number of eigenvalues. On time scales related to $|\Lambda| \gtrsim 1/2$, the frozen Overhauser field approximation does not hold and the full hyperfine interaction comes into play. Accordingly, the eigenvalue $\Lambda = 1$ occurs only once for the full mapping matrix $\underline{\underline{M}}$ rather than being $(D'/4)$-fold degenerate. The remaining weight in the distribution $p(|\Lambda|)$ is transferred to absolute values $|\Lambda| < 1$ producing a broadening of the peak at $|\Lambda| = 1$.

7.2.2 Complex eigenvalues

The effect of the nuclear spin precession about the external magnetic field is included in the complex part of the eigenspectrum of $\mathcal{M}$. Figure 7.3 depicts the probability distribution $p(\Lambda)$ of the complex eigenvalues Λ at four different external magnetic field strengths corresponding to $n = 1, \ldots, 4$ in Eq. (6.13). The data of the $N_C = 100$ realizations is processed as a histogram on a grid spanned by typically 50×50 bins in the range $\mathrm{Re}(\Lambda) \in [-1; 1]$ and $\mathrm{Im}(\Lambda) \in [-1; 1]$. The main contribution of the nuclear spin dynamics results from the precession about the external magnetic field, whereas the Knight field is rather weak and, therefore, is neglected to obtain a basic understanding of $p(\Lambda)$. Accordingly, the nuclear spin dynamics becomes independent of the electron spin and is restricted to a density suboperator $\rho^n(t)$ acting in a reduced Hilbert space of the dimension $(2I+1)^N$. The dynamics of $\rho^n(t)$ are identical for all configurations of the electron spin. In the spin x basis, $|K\rangle \equiv |\{I_k^x\}\rangle$ with total spin $J^x = \sum_k I_k^x$, the temporal evolution of $\rho^n(t)$ during one repetition period of the pulse train is given by

$$\rho^n_{K,L}((N_P+1)T_R^-) = e^{-i\omega_n(J_K^x - J_L^x)T_R}\rho^n_{K,L}(N_P T_R^-). \tag{7.19}$$

The mapping matrix $\underline{\underline{M}}^n$ for the nuclear spin dynamics can be directly read off,

$$\rho^n_{K',L'}((N_P+1)T_R^-) = \sum_{K,L} M_{K,L}^{K',L'}\rho^n_{K,L}(N_P T_R^-) \tag{7.20}$$

with matrix elements

$$M_{K,L}^{K',L'} = \delta_{K,K'}\delta_{L,L'}e^{-i\omega_n(J_K^x - J_L^x)T_R}. \tag{7.21}$$

Thus, the matrix $\underline{\underline{M}}^n$ is diagonal. Its eigenvalues Λ_i^n result from $e^{-i\omega_n(J_K^x - J_L^x)T_R}$ with any combination of the nuclear spin states K and L. The eigenvalues Λ_i^n have the absolute value 1 and provide a complex phase. This phase is determined by $J_K^x - J_L^x$ which is an integer number in the range from $-N$ to N since J_K^x and $J_L^x \in \{-N/2, \ldots, N/2\}$.

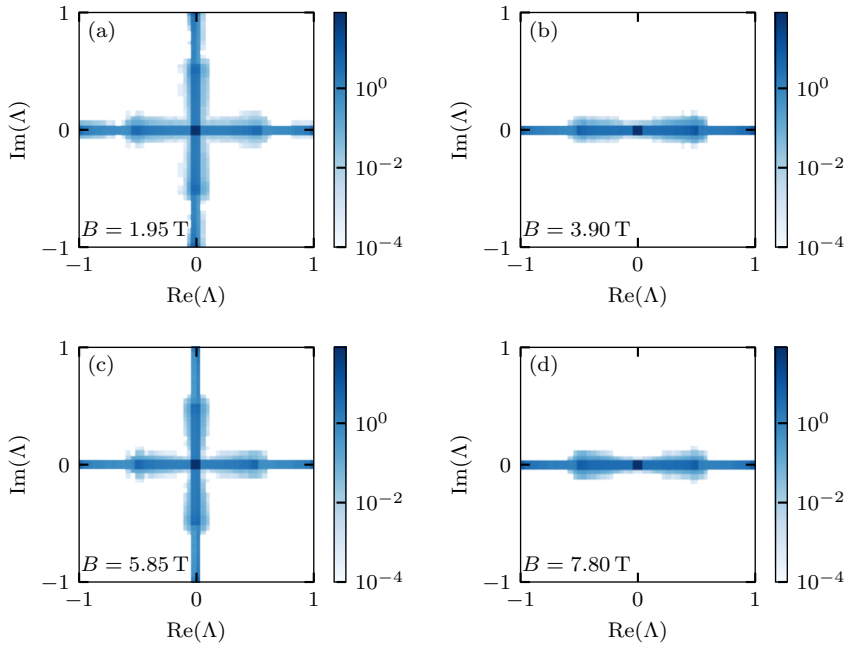

Figure 7.3: Distribution $p(\Lambda)$ of the complex eigenvalues Λ of the mapping $\mathcal{M}$. The system comprises $N = 6$ nuclear spins with the individual length $I = 1/2$; $N_C = 100$. Results for different external magnetic fields are presented that fulfill Eq. (6.13) with $n = 1, \ldots, 4$.

For the decoupled electron-nuclear spin system, the eigenvalues Λ_i of the total mapping matrix $\underline{\underline{M}}$ result from the product of any combination of the eigenvalues Λ_i^e and Λ_i^n. As a consequence, the real eigenvalues Λ_i^e of the electronic system provide the absolute value of Λ_i, whereas the eigenvalues Λ_i^n of the nuclear mapping determine the complex phase of Λ_i. The magnetic field strengths in Fig. 7.3 correspond to either a quarter, half, three half or full revolution of the nuclear spins during T_R, i.e., $n = 1, \ldots, 4$ in Eq. (6.13). The eigenspectra reflect this condition for the nuclear Larmor frequency: In Fig. 7.3(a), the nuclear spins perform a quarter revolution in between consecutive pump pulses such that $\omega_n T_R = \pi/2$ enters the exponent in the definition of Λ_i^n and produces the four branches of $p(\Lambda)$ in the complex plane. At $B = 3.90\,\mathrm{T}$, the nuclear spins make perform a revolution about the external magnetic field, $\omega_n T_R = \pi$, resulting in a distribution of Λ along the real axis, see Fig. 7.3(b). A three quarter revolution of the nuclear spins, $\omega_n T_R = 3\pi/2$, produces a similar image as for the quarter revolution, see Fig. 7.3(c). Finally, a full revolution of the nuclear spins during T_R, $\omega_n T_R = 2\pi$, leads to a distribution $p(\Lambda)$ whose weight is accumulated at the real axis, see Fig. 7.3(d). Here, the negative contributions of $\mathrm{Re}(\Lambda)$ stem from the negative values of Λ_3^e according to Eq. (7.16).

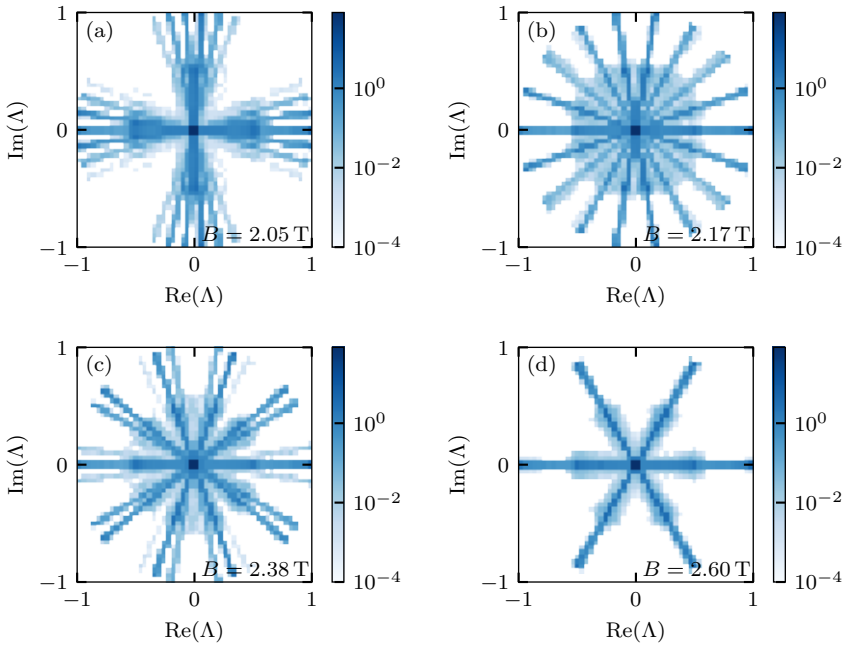

Figure 7.4: Distribution $p(\Lambda)$ of the complex eigenvalues Λ of the mapping $\mathcal{M}$. The system comprises $N = 6$ nuclear spins with the individual length $I = 1/2$; $N_C = 100$. Results for different external magnetic fields are presented, where (a) $n = 21/20$, (b) $n = 10/9$, (c) $n = 11/9$, and (d) $n = 4/3$ in Eq. (6.13) respectively.

The additional blurring of the distributions $p(\Lambda)$ can be attributed to the electron-nuclear spin feedback mechanism provided by the full hyperfine Hamiltonian which renders the eigenspectrum of the full mapping $\mathcal{M}$ more complex than the simplifying analytical prediction.

When the external magnetic field does not produce an integer number of quarter revolutions of the nuclear spins between consecutive pump pulses, the distribution $p(\Lambda)$ fans out and additional branches occur in the complex plane. Figure 7.4 presents the eigenspectrum of $\mathcal{M}$ at four further external magnetic field strengths, that do not fulfill the condition, Eq. (6.13), with an integer n. In Fig. 7.4(a), the magnetic field is adjusted to $n = 1+1/20$ such that the nuclear spins perform a little more than a quarter revolution during T_R. Accordingly, the four branches of $n = 1$ spread into several lines respectively. Moving further away from the resonance $n = 1$, the branches spread over the full complex plane, see Fig. 7.4(b) with $n = 1 + 1/9$. Here, the finite number of lines in the complex eigenspectrum is a result of the finite system size for which $J_K^x - J_L^x$ can only produce a limited number of integer values. For $B = 2.38\,\mathrm{T}$ in Fig. 7.4(c), the branches of $p(\Lambda)$ adjust to the number

$n = 1 + 2/9$ of quarter revolutions of the nuclear spin precession. At $n = 4/3$, the nuclear spins perform a third revolution between the pump pulses producing six equally spread lines in Fig. 7.4(d). We note that the number of lines in the complex eigenspectrum would still be finite for an irrational n as a result of the finite system size producing a limited number of integer values $J_K^x - J_L^x$.

7.2.3 Overlap with the initial density operator

Depending on the initial density operator ρ_0 before the periodic optical excitation, a subset of the eigenoperators of $\mathcal{M}$ contributes to the dynamics of $\rho(N_P T_R^-)$ during the pulse train. According to Eq. (7.9), only those right eigenvectors with finite nonzero overlap c_i to $\vec{\rho}_0$ as defined in Eq. (7.10) yield a contribution to the temporal evolution of the system. For the evaluation of the respective overlap, we scale the right eigenvectors $\vec{r}_i$ to the norm $\|\vec{r}_i\| = 1$ and adjust the left eigenvectors to fulfill $\vec{l}_i^\dagger \vec{r}_i = 1$. As the initial condition, we use the vector representation of $\rho_0 = \mathbb{1}_{d'}/d'$.

The distribution $p(|\Lambda|, |c|)$ as a function of the absolute values of the eigenvalue and the overlap, $|\Lambda|$ and $|c|$, is displayed in Fig. 7.5(a) for the exemplary external magnetic field of $B = 1.95\,\mathrm{T}$. A broad band with relatively small overlap spreads over the full range $0 \leq |\Lambda| \leq 1$. The peak at $|\Lambda| = 1/2$ observed for $p(|\Lambda|)$ in Fig. 7.2 is reflected by a vertical line in Fig. 7.5(a). Furthermore, an accumulation of weight arises at $|\Lambda| = 0$ connected to a notable overlap $|c| > 10^{-3}$. For $|\Lambda| < 1/2$ several eigenvalues with relevant overlap occur, whereas the eigenvalues in the range $1/2 < |\Lambda| < 1$ are related to eigenvectors with minor overlap to the initial vector $\vec{\rho}_0$. Only for $|\Lambda| \approx 1$, eigenvectors producing a relevant overlap with $\vec{\rho}_0$ exist.

The eigenspectrum $p(\Lambda)$ as a function of the complex eigenvalue Λ obtained from those eigenvalues Λ_i related to a relevant overlap $|c_i| > 10^{-3}$ is presented in Fig. 7.5(b). This selection of the eigenvalues Λ_i corresponds to those eigenvalues above the horizontal cut indicated by the black dotted line in Fig. 7.5(a). In contrast to the full eigenspectrum at the same magnetic field, presented in Fig. 7.3(a), the four lines are cut off at $|\Lambda| = 1/2$ respectively. Furthermore, the lines along the imaginary axis are significantly less pronounced than those along the real axis. At an absolute value $|\Lambda| > 1/2$, we only find contributions for $\Lambda \approx 1$ which are hard to detect in Fig. 7.5(b). These contributions are related to the quasistationary steady state and other long living eigenstates. We conclude that the temporal evolution starting from the initial density operator ρ_0 is mostly governed by the real eigenvalues with $|\Lambda| < 1/2$ which are related to the purely electronic steady state addressed in Sec. 6.1. Moreover, the long term dynamics associated with the emergence of the mode-locking effect via nuclei-induced frequency focusing are determined by the eigenvalues $\Lambda \approx 1$.

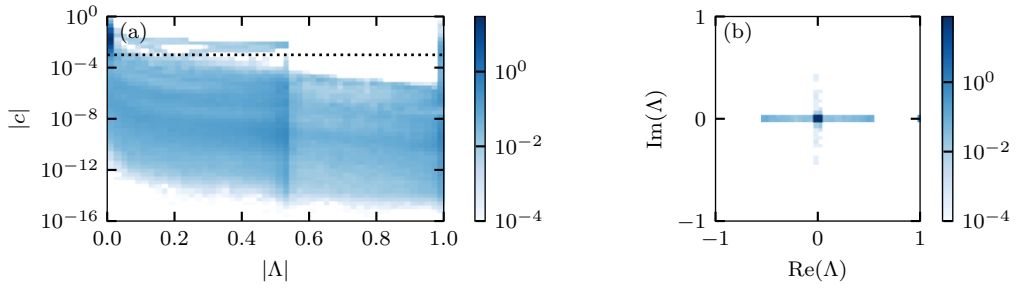

Figure 7.5: Relation between the eigenspectrum of the mapping matrix $\underline{\underline{M}}$ and the overlap c of the right eigenvectors with the initial density vector $\vec{\rho}_0$. A system with $N = 6$ nuclear spins ($I = 1/2$) is examined at the external magnetic field $B = 1.95\,\mathrm{T}$; $N_C = 100$. (a) Distribution $p(|\Lambda|, |c|)$ of the absolute values of the eigenvalue $|\Lambda|$ and the related overlap $|c|$. (b) Eigenspectrum $p(\Lambda)$ as a function of the complex eigenvalue Λ taking into account only those eigenvalues Λ_i related to an overlap $|c_i| > 10^{-3}$.

7.3 Truncation scheme

As the numerical eigendecomposition of the full mapping $\mathcal{M}$ with the $(D' \times D')$-dimensional matrix representation is computationally expensive, we strive for an approach reducing the computational effort. An efficient way to facilitate the eigendecomposition of larger systems is the reduction of the employed matrix dimensions. Therefore, we introduce a truncation scheme for the matrix elements of the density operator. The initial density operator of the electron-nuclear spin system before the pulse train is diagonal due to the applied high-temperature limit. Moreover, the density operator of the quasistationary steady state under periodic optical excitation proves to have nonzero entries mostly for the diagonal matrix elements in the eigenbasis of the Hamiltonian, Eq. (5.33), as well. Hence, it is convenient to focus on the relevant matrix elements of ρ and omit those parts that do not contribute to the dynamics. As a measure which elements of the density operator in the energy eigenbasis can be excluded from the calculations, we establish the difference between the total spin x component of the left hand and right hand spin state. Employing the common eigenbasis, Eq. (5.36), of H_S and F^x, we include those density matrix elements $\rho_{a,b}(t)$ for which $|F^x_a - F^x_b| \leq \Delta_F$ with a truncation parameter Δ_FS. Accordingly, the dimensions of the square mapping matrix $\underline{\underline{M}}$, which equal the number of included density matrix elements, reduce considerably. The truncation of the density matrix based on the difference $|F^x_a - F^x_b|$ is supported by the observation that the quantum number F^x is conserved by the unitary time evolution with H_S and can only be affected via the pump pulse or the trion decay. The latter two effects, however, are limited to a change of the electron

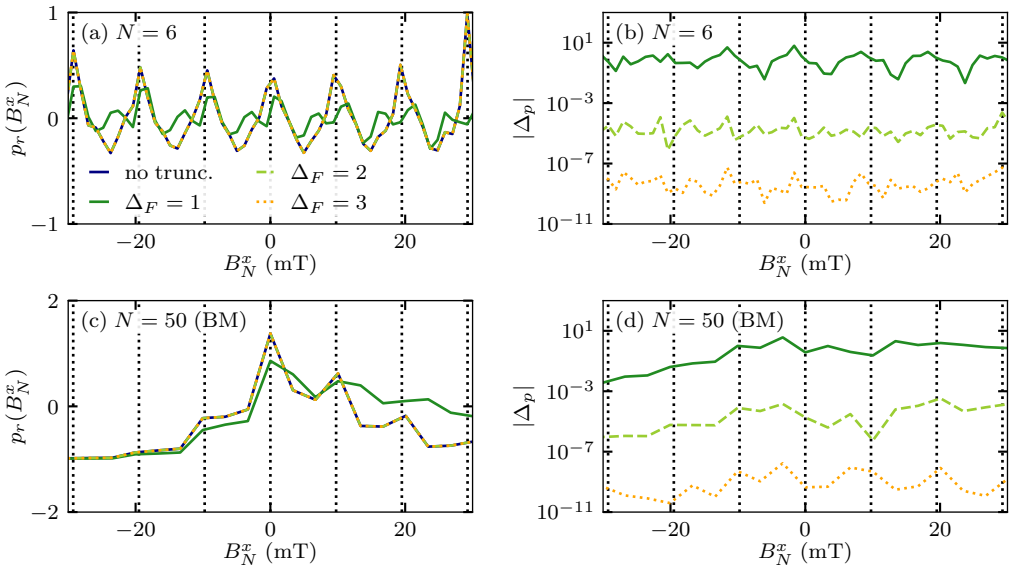

Figure 7.6: Comparison of different truncation parameters Δ_F for the density matrix entering the mapping $\underline{\underline{M}}$. We employ an instantaneous pump pulse and an external magnetic field of $B = 1.95\,\mathrm{T}$. (a) Relative Overhauser field distribution $p_r(B_N^x)$ of the system with $N = 6$ nuclear spins in the steady state ($I = 1/2$, $N_C = 100$). The legend indicating Δ_F applies to the entire figure. (b) Relative deviation of $p_r(B_N^x)$ for the truncated system from $p_r(B_N^x)$ in the full calculation based on the data in panel (a). (c) Steady-state distribution $p_r(B_N^x)$ of the system with $N = 50$ nuclear spins ($I = 1/2$) in the box model approximation. (d) Relative deviation of $p_r(B_N^x)$ for the truncated system from $p_r(B_N^x)$ in the full calculation referring to the data in panel (c).

spin contribution S^x by a maximum of ± 1 during one repetition period.

We compare the results of the relative Overhauser field distribution $p_r(B_N^x)$ of the quasistationary steady state related to the eigenvalue 1 of $\underline{\underline{M}}$ for different truncation parameter Δ_F in Fig. 7.6. For the external magnetic field, we choose $B = 1.95\,\mathrm{T}$ as an example. Thus, the integer modes of the electron spin precession indicated by the black dotted vertical lines are favored by the Overhauser field. In the system with $N = 6$ nuclear spins of the individual length $I = 1/2$, the distributions $p_r(B_N^x)$ obtained with truncation parameters $\Delta_F \geq 2$ fully match the result of the full calculation without truncation, see Fig. 7.6(a). The calculation with $\Delta_F = 1$, however, displays significant deviations from the steady-state solution of the full mapping. To resolve potential deviations for $\Delta_F \geq 2$, the relative deviation Δ_p of the steady-state distribution $p_r(B_N^x)$ for the truncated system from the data of the full calculation is presented in Fig. 7.6(b). The absolute value $|\Delta_p|$ of the

relative deviation decreases when increasing the number of density matrix elements included in the mapping, i.e., increasing Δ_F. For $\Delta_F = 2$, roughly 80% of the density matrix elements are included which produces a relative deviation $|\Delta_p|$ in the order of 10^{-5}.

The truncation scheme proves even more efficient in the case of large nuclear spin lengths. Aiming at the investigation of a system comprising many nuclear spins, we resort to the box model approximation. The hyperfine coupling constants are set to the same value A_0 for all nuclei guaranteeing the dephasing time $T^* = 1\,\mathrm{ns}$. Hence, the averaging over different realizations becomes redundant and therefore is omitted. In the box model approximation, the spin dynamics can be decomposed into subspaces with a fixed total nuclear spin J, $J \in \{0, \ldots, N/2\}$ (for even N) since the instantaneous pump pulse as well as the Lindblad master equation with the Hamiltonian H_S conserve the quantum number J. Accordingly, the mapping matrix for the repetition period is established separately for the individual subspaces reducing the involved matrix dimensions. After the diagonalization of the matrix representation of the mapping for the subspaces, the results are combined to the eigenspectrum of the full mapping $\mathcal{M}$. As a result of the conservation of J, the eigenvalue 1 is degenerate for the full mapping $\mathcal{M}$ in the box model approximation. For each value of J, a number of identical subspaces arise whereby the degree of degeneracy is given by Eq. (4.13). Each of these subspaces produces an eigenvalue 1 with the related right eigenoperator corresponding to the steady state in this subspace. Consequently, the degree of degeneracy of the eigenvalue 1 of the full mapping results from $\sum_J g_N(J) = \binom{N}{N/2}$. The quasistationary steady state $\vec{\rho}_{\mathrm{ss}}$ of the full system in dependence on the initial vector $\vec{\rho}_0$ is established by summing the steady-state contributions of the individual subspaces weighted by their overlap c_i with $\vec{\rho}_0$, Eq. (7.10),

$$\vec{\rho}_{\mathrm{ss}} = \sum_{\substack{i \\ \Lambda_i = 1}} c_i \vec{r}_i. \tag{7.22}$$

We compare the steady-state Overhauser field distribution $p_r(B_N^x)$ in the box model limit for various truncation parameters Δ_F with the full calculation in Fig. 7.6(c). The system size is set to $N = 50$ nuclear spins with the individual length $I = 1/2$ which corresponds to the largest system accessible by the full treatment in the box model approximation. Here, the truncation scheme with $\Delta_F = 2$ allows for reducing the dimension of the mapping matrix for the subspace $J = N/2 \equiv 25$ by a factor of 10^3. The results for $\Delta_F \geq 2$ coincide with the full calculation whereas significant deviations arise for $\Delta_F = 1$. The relative deviation of $p_r(B_N^x)$ in the truncated system from $p_r(B_N^x)$ resulting from the full analysis is shown in Fig. 7.6(d). At a fixed truncation parameter Δ_F, the relative error $|\Delta_p|$ is similar to the case of six nuclear spins with random hyperfine coupling constants. For $\Delta_F = 2$, $|\Delta_p|$

remains in the order of 10^{-5}. As a compromise between accuracy and numerical effort, we employ the truncation scheme with $\Delta_F = 2$ in the following unless stated otherwise.

7.4 Electron spin revival amplitude in the box model approximation

The truncation scheme for the density matrix elements included by the mapping enables the study of the quasistationary steady state in systems with up to $N = 500$ nuclear spins in the box model approximation. We exploit this accomplishment and address the magnetic field dependence of the mode-locking effect in such a large system. For simplicity, we employ instantaneous pump pulses. The electron spin revival amplitude $S^{\perp}$ directly before the pump pulse is extracted from the steady-state density operator. For evaluation of the electron spin expectation value $\langle S^{\alpha} \rangle = \mathrm{Tr}(\rho_{\mathrm{ss}} S^{\alpha})$ with $\alpha \in \{x, y, z\}$, the steady-state density operator ρ_{ss} in the energy eigenbasis is composed from the steady-state contributions of the subspaces related to a fixed total nuclear spin J according to Eq. (7.22). Figure 7.7 displays the revival amplitude $S^{\perp}$ as a function of the external magnetic field B for two different system sizes (a) $N = 200$ and (b) $N = 500$. The box model results of $S^{\perp}$ reflect the nonmonotonic magnetic field dependence induced by the condition for the nuclear Larmor precession, Eq. (6.13). Minima of the revival amplitude occur at roughly 4 T and 8 T respectively. However, the maxima in between are placed differently than for the system consisting of $N = 6$ nuclear spins with randomly

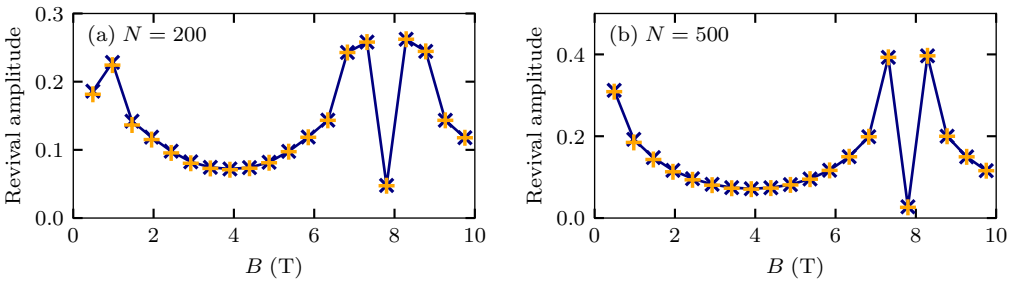

Figure 7.7: Electron spin revival amplitude $S^{\perp}$ in the quasistationary steady state as a function of the external magnetic field B (blue markers, the lines are a guide to the eye). Furthermore, the converged absolute value $|\langle S_c^z \rangle|$ of the electron spin polarization directly before a pump pulse is added (orange markers). The box model approximation is employed for systems of the size (a) $N = 200$ and (b) $N = 500$.

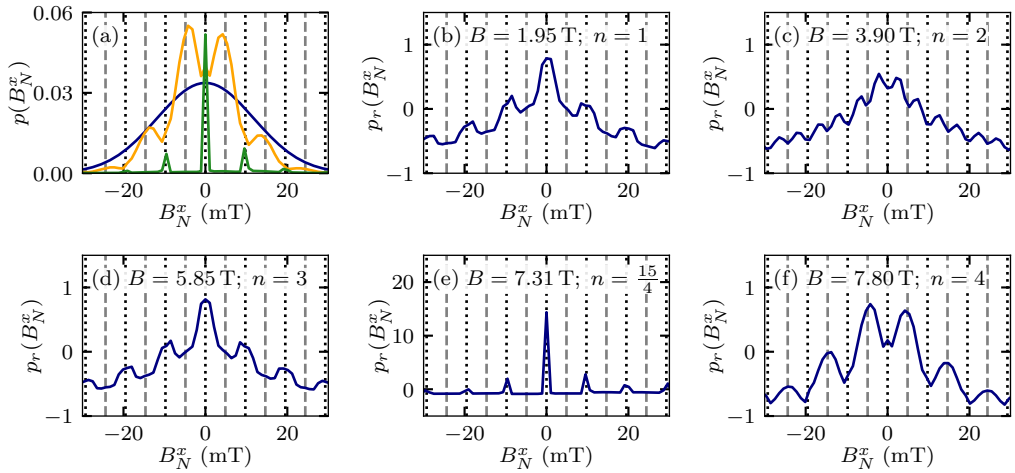

Figure 7.8: (a) Overhauser field distribution $p(B_N^x)$ in equilibrium (blue line) and in the quasistationary steady state under periodic optical excitation at $B = 7.31\,\mathrm{T}$ (green line, scaled by a factor of 1/10) and $B = 7.80\,\mathrm{T}$ (orange line) respectively. The system comprises $N = 500$ nuclear spins in the box model approximation. (b)-(f) Relative Overhauser field distributions $p_r(B_N^x)$ at various external magnetic field strengths that comply with the Eq. (6.13) with different numbers n. Electron spin precession modes with an integer (half-integer respectively) number of revolutions during T_R are indicated by black dotted (gray dashed) vertical lines.

distributed hyperfine coupling constants, cf. Fig. 6.3(b). In particular, the dip at 8 T becomes very narrow due to two maxima of $S^\perp$ located close to the minimum. The comparison of the data for $N = 200$ and $N = 500$ reveals that the dip at 8 T becomes sharper with growing system size N due to the increase in the maximum value of $S^\perp$. In comparison to the data in Fig. 6.3(b), the maximum value of $S^\perp$ increases by roughly a factor of two for the box model results with $N = 500$.

The Overhauser field distribution $p(B_N^x)$ for $N = 500$ nuclear spins in the box model approximation provides a relatively smooth distribution approximating the Gaussian, Eq. (2.13), in the high-temperature equilibrium situation, see Fig. 7.8(a) (blue line). In the quasistationary steady-state under periodic optical excitation, peaks emerge at the favored electron spin precession modes depending on the external magnetic field (orange and green line respectively). In comparison to the steady-state distribution of the spin system comprising $N = 6$ nuclear spins with randomly distributed hyperfine coupling constants, these peaks can become significantly more pronounced at some values of B. The distribution $p(B_N^x)$ at $B = 7.31\,\mathrm{T}$ (green line) for instance exhibits extremely sharp peaks at the integer modes of the electron spin precession; it is scaled by a factor of 1/10 to match the other distributions in the figure. For

a detailed analysis, we add the relative Overhauser field distributions $p_r(B_N^x)$ in the quasistationary steady state at selected values of the external magnetic field strength in Figs. 7.8(b)-7.8(f). At $B = 1.95\,\mathrm{T}$, $n = 1$ in Eq. (6.13), we observe peaks of $p_r(B_N^x)$ at the expected integer modes of electron spin precession, see Fig. 7.8(b). At $B = 3.90\,\mathrm{T}$ corresponding to $n = 2$, however, the distribution $p_r(B_N^x)$ in Fig. 7.8(c) displays peaks in between the integer and half-integer modes, whereas Eq. (6.13) predicts a favoring of the half-integer modes. The distribution at $B = 5.85\,\mathrm{T}$ ($n = 3$) exhibits the expected favoring of the integer modes again, see Fig. 7.8(d), and resembles the result at $B = 1.95\,\mathrm{T}$. The integer modes become even more pronounced at $B = 7.31\,\mathrm{T}$ ($n = 15/4$), see Fig. 7.8(e), which matches the maximum of the electron spin revival amplitude. A similar distribution $p_r(B_N^x)$ is obtained at $B = 8.29\,\mathrm{T}$ ($n = 17/4$, not displayed) producing the maximum of $S^\perp$ on the other side of the dip. For the external magnetic field related to the minimum of the electron spin revival amplitude, $B = 7.80\,\mathrm{T}$ ($n = 4$), the prediction of a favoring of the half-integer modes by Eq. (6.13) holds true again, see Fig. 7.8(f).

Overall, the electron spin precession modes produced by the nuclei-induced frequency focusing of a large system in the box model limit are slightly altered compared to a small system with randomly distributed hyperfine coupling constants. Interestingly, similar behavior of the electron spin revival amplitude as in the quantum mechanical calculations for the box model limit has been observed by a classical approach in Refs. [86, 88, 89, 224]. The classical data suggest a rather broad minimum of the revival amplitude as a function of the external magnetic field at $n = 2$ in Eq. (6.13) and a sharp dip at $n = 4$. Since this sharp dip does not match the experimental measurements, the question of its origin arises. It could either be an artifact of the theoretical modeling such as specific assumptions about the hyperfine coupling constants, or it could be superimposed by additional effects in experiments, e.g., nuclear quadrupolar interactions and dipole-dipole interactions broadening the peaks in the Overhauser field distribution as well as the spin precession during the noninstantaneous pump pulses.

7.5 Focusing of a single electron spin precession mode

Recent experiments [94, 95, 229] achieved the nuclei-induced frequency focusing of a single electron spin precession mode via optical excitation with a GHz repetition frequency, i.e., by a reduction of the repetition period to $T_R = 1\,\mathrm{ns}$. We address this regime by the diagonalization of the mapping $\mathcal{M}$ for the shortened repetition period. To this end, we adjust the trion decay rate to $\gamma = 20\,\mathrm{ns}^{-1}$ which ensures a full decay of the trion population within the numerical accuracy during one repetition

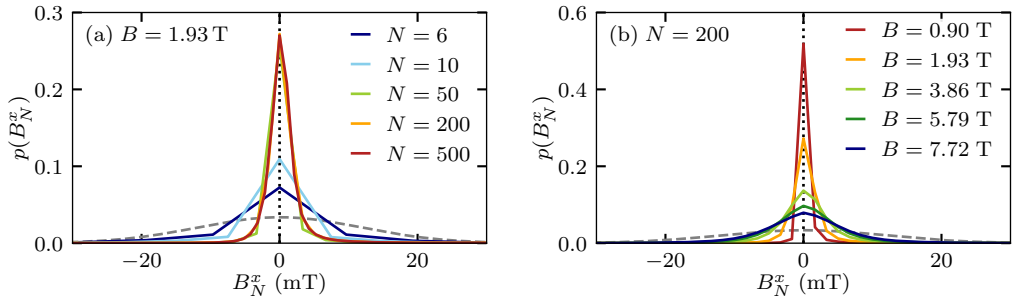

Figure 7.9: Overhauser field distribution $p(B_N^x)$ in the quasistationary steady state. The repetition time between the instantaneous pump pulses is reduced to $T_R = 1\,\mathrm{ns}$. The box model approximation of the hyperfine coupling constants enables the examination of a large nuclear spin bath. (a) $p(B_N^x)$ depending on the system size N at the fixed external magnetic field of $B = 1.93\,\mathrm{T}$. (b) $p(B_N^x)$ depending on the external magnetic field at a fixed system size of $N = 200$.

period. The pump pulse is modeled as instantaneous. For access to a large system, we employ the box model limit of the hyperfine coupling constants.

Figure 7.9(a) presents the Overhauser field distribution $p(B_N^x)$ in the mode-locked state at a fixed external magnetic field $B = 1.93\,\mathrm{T}$ with $m' = 15$ electron spin revolutions during $T_R = 1\,\mathrm{ns}$, cf. Eq. (6.11). Steady-state results for various system sizes $6 \leq N \leq 500$ are compared. The common initial Gaussian distribution governed by $T^* = 1\,\mathrm{ns}$ is indicated as a gray dashed line. We find that the nuclear spins under periodic optical excitation with a GHz repetition rate produce a single electron spin precession mode corresponding to an integer number $m' = 15$ of revolutions between consecutive pump pulses. The related peak in the Overhauser field distribution sharpens when increasing the number of nuclear spins in the system. We do not observe any further peaks in $p(B_N^x)$ in this regime as the next closest integer modes of electron precession would require an Overhauser field $B_N^x \approx \pm 130\,\mathrm{mT}$. This significantly exceeds the standard deviation of the initial Gaussian envelope function.

The magnetic field dependence of the Overhauser field distribution $p(B_N^x)$ at a fixed system size, $N = 200$, is shown in Fig. 7.9(b). In the presented range $0.90\,\mathrm{T} \leq B \leq 7.72\,\mathrm{T}$, the distributions exhibit a single peak at $B_N^x = 0\,\mathrm{mT}$ which broadens when increasing the magnetic field strength. Here, the number m' of electron spin revolutions between consecutive pump pulses with separation $T_R = 1\,\mathrm{ns}$ amounts to $7 \leq m' \leq 60$ according to Eq. (6.11). The presented distributions $p(B_N^x)$ all favor the integer precession mode of the electron spin, and the condition in Eq. (6.13) does not apply due to $n \ll 1$ for the presented magnetic field strengths.

The broadening of the single peak in $p(B_N^x)$ with strengthening B is attributed to the suppression of the spin flips terms in the hyperfine Hamiltonian by strong external magnetic fields [90]. In the experiments, an additional broadening due to ensemble inhomogeneities, such as the variation of the electron g factor in the quantum dot ensemble, has to be overcome for a single mode operation of the system [94]. These effects are omitted in the theoretical investigation for simplicity.

7.6 Sweeping of the external magnetic field

Evers et al. [95] demonstrated the repopulation of the electron spin precession modes in an (In,Ga)As quantum dot ensemble by sweeping the external magnetic field during the periodic optical excitation with a repetition time $T_R = 1\,\mathrm{ns}$. Starting from an initial value, the magnetic field strength is continuously increased while the periodic optical pump pulses are switched on. The experimental data demonstrates a dragging of the electron spin precession modes and the emergence of a strong polarization of the Overhauser field which adjusts to the external magnetic field and reaches up to 1.5 T in Ref. [95].

We investigate the effect of the magnetic field sweep by means of the quantum mechanical superoperator $\mathcal{M}$ for the repetition period. Employing the box model limit of the hyperfine coupling constants for a system with $N = 200$ nuclear spins, we start from the disordered spin system ρ_0. The initial external magnetic field is adjusted to $B_1 = 1.93\,\mathrm{T}$ producing $m' = 15$ electron spin revolutions during $T_R = 1\,\mathrm{ns}$ according to Eq. (6.11). We apply a select number N_P of instantaneous pump pulses and subsequently increase the external magnetic field strength by a small amount. For the new field strength B_2, we apply again N_P pump pulses with separation $T_R = 1\,\mathrm{ns}$. This procedure is iterated until we reach the magnetic field value $B_{N_B} = 2.06\,\mathrm{T}$ corresponding to $m' = 16$. The number of magnetic field steps for sweeping from $m' = 15$ to $m' = 16$ is set to $N_B = 100$. This resolution is deemed adequate since a further increase in N_B does not change the physical results (with properly adjusted N_P per magnetic field step) but only generates additional computational effort. For the implementation of the magnetic field sweep, we employ the eigendecomposition of the mapping matrices $\underline{\underline{M}}^{(j)}$ at the respective magnetic field values B_j. The vector $\vec{\rho}_j$ for the magnetic field step j is obtained iteratively from $\vec{\rho}_{j-1}$ at the previous magnetic field,

$$\vec{\rho}_j = \sum_i \left(\Lambda_i^{(j)}\right)^{N_P} c_i^{(j)} \vec{r}_i^{(j)} \tag{7.23}$$

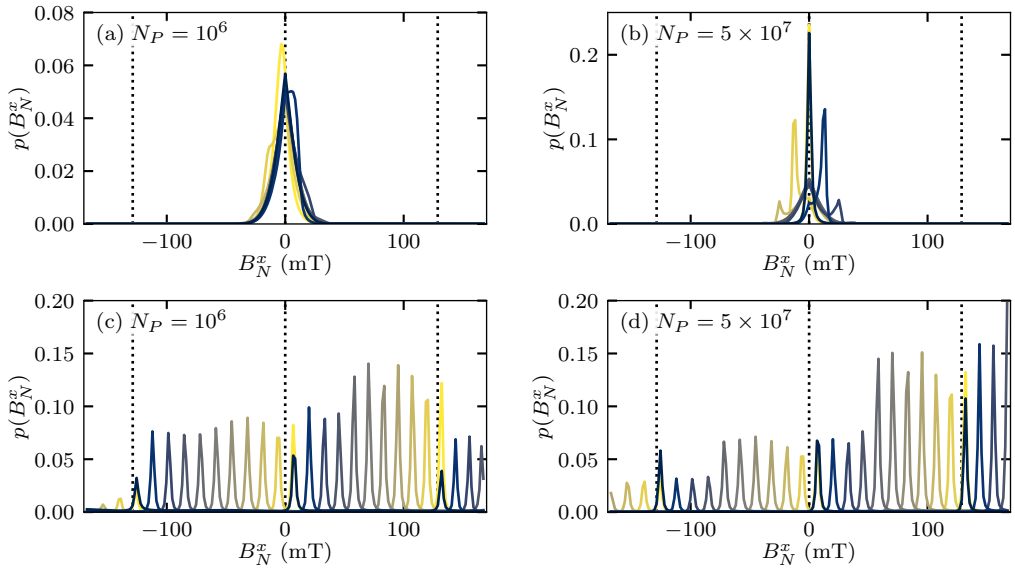

Figure 7.10: Overhauser field distribution $p(B_N^x)$ when sweeping the external magnetic field from $B_1 = 1.94\,\mathrm{T}$ ($m' = 15$, blue lines) to $B_{100} = 2.06\,\mathrm{T}$ ($m' = 16$, yellow lines) under periodic optical excitation with repetition time $T_R = 1\,\mathrm{ns}$. The system comprises $N = 200$ nuclear spins in the box model approximation. The external magnetic field is swept in 100 steps with (a) $N_P = 10^6$ or (b) $N_P = 5 \times 10^7$ pump pulses per magnetic field step respectively. Panels (c) and (d) display $p(B_N^x)$ in the subspace of fixed total nuclear spin $J = 100$ and refer to panel (a) and (b) respectively. The integer modes of the electron spin precession for external magnetic fields with an integer number m' in Eq. (6.11) are indicated by black dotted vertical lines at $B_N^x = 0\,\mathrm{mT}$ and $B_N^x \approx \pm 130\,\mathrm{mT}$ respectively.

with coefficients

$$c_i^{(j)} = \left(\vec{l}_i^{(j)}\right)^\dagger \vec{\rho}_{j-1}. \tag{7.24}$$

Here, $\vec{r}_i^{(j)}$, $\left(\vec{l}_i^{(j)}\right)^\dagger$ and $\Lambda_i^{(j)}$ denote the right eigenvectors, the left eigenvectors and the eigenvalues of $\underline{\underline{M}}^{(j)}$ respectively.

Figure 7.10 displays the evolution of the Overhauser field distribution $p(B_N^x)$ during the sweep. The distribution for every tenth magnetic field step is depicted with color coding ranging from blue (B_1) to yellow (B_{100}). For Fig. 7.10(a), the number of pump pulses per magnetic field step amounts to $N_P = 10^6$, whereas $N_P = 5 \times 10^7$ in Fig. 7.10(b). Thus, the total duration covered by the numerical simulation corresponds to 0.1 s and 5.0 s, respectively. In the beginning, the Overhauser field distribution is centered symmetrically around $B_N^x = 0\,\mathrm{mT}$. The integer modes of

the electron spin precession for $B_1 = 1.93\,\mathrm{T}$ ($m' = 15$) are indicated by black dotted vertical lines in Fig. 7.10. When sweeping the magnetic field, the weight of $p(B_N^x)$ moves to positive values of B_N^x as the Overhauser field compensates for the mismatch of the external magnetic field from an integer number of electron spin revolutions during T_R. However, when the integer mode of the electron spin precession moves out of the range in which the initial Gaussian distribution has substantial weight, the distribution $p(B_N^x)$ cannot follow the magnetic field sweep. Thus, $p(B_N^x)$ becomes symmetrically centered around $B_N^x = 0\,\mathrm{mT}$ again. Finally, the integer mode moves into the Overhauser field range at negative values of B_N^x and the weight of the distribution $p(B_N^x)$ is shifted to negative Overhauser field components. When the external magnetic field reaches $B_{100} = 2.06\,\mathrm{T}$ ($m' = 16$), the integer modes of the electron spin precession correspond again to the black dotted vertical lines in Fig. 7.10. The comparison of the results with $N_P = 10^6$ and $N_P = 5 \times 10^7$ pump pulses per magnetic field step respectively reveals significant differences. The distributions $p(B_N^x)$ in Fig. 7.10(b) correspond to the steady-state distributions under a long pulse train at a fixed magnetic field of the respective field strength due to the slow sweeping rate. For the faster sweeping in Fig. 7.10(a), the system does not reach the quasistationary steady-state at the individual magnetic field steps. Hence, the distributions $p(B_N^x)$ exhibit only minor deviations from the initial Gaussian distribution. Obviously, the mode dragging achieved in the experiments [95] is absent in the numerical results. We attribute this observation to the special symmetries of the box model approximation. The total nuclear spin J is conserved during the complete pulse train. Small values of J carry much weight for the initial density operator ρ_0 due to the high level of degeneracy of the associated subspaces, cf. Eq. (4.13). Therefore, the Overhauser field distribution will retain most of its weight at small values of B_N^x rather than following the dragging of the electron spin precession modes.

In the subspace with maximum value $J = N/2 = 100$, however, the Overhauser field can reach up to roughly $\pm 170\,\mathrm{mT}$. To extract a potential reorganization of the nuclear spins in this subspace, we present the Overhauser field distribution obtained for fixing $J = 100$ in Figs. 7.10(c) and 7.10(d). In compliance with the previous data, the number of pump pulses per magnetic field step amounts to $N_P = 10^6$ and $N_P = 5 \times 10^7$ respectively. Accordingly, the results in Fig. 7.10(d) correspond to the steady-state distributions at the respective external magnetic field, and the distribution before the sweep at $B_1 = 1.93\,\mathrm{T}$ fully coincides with $p(B_N^x)$ at the end of the sweep with $B_{100} = 2.06\,\mathrm{T}$. For the faster sweep of the magnetic field in Fig. 7.10(c), the distributions at B_1 and B_{100} do not match. The comparison of the distribution at the end of the sweep with $N_P = 10^6$ pulses per magnetic field step (yellow line in Fig. 7.10(c)) to the steady-state distribution at $B_{100} = 2.06\,\mathrm{T}$ (blue line in Fig. 7.10(d)) indicates a minor redistribution of the weight between

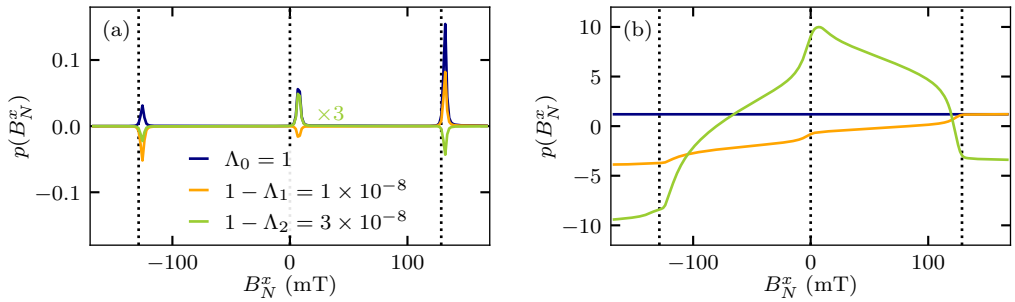

Figure 7.11: Eigenvectors related to the three largest eigenvalues of $\underline{\underline{M}}$ at $B = 1.93\,\mathrm{T}$. The box model approximation is applied for the system with $N = 200$ nuclear spins. The results focus on the subspace of the largest total nuclear spin $J = 100$. (a) Overhauser field distribution $p_r(B_N^x)$ extracted from the right eigenvectors. The distribution related to the eigenvalue Λ_2 is scaled by a factor of three. (b) Distribution of B_N^x obtained from the left eigenvectors related to the right eigenvectors in panel (a). The integer modes of the electron spin precession are indicated by black dotted vertical lines at $B_N^x = 0\,\mathrm{mT}$ and $B_N^x \approx \pm 130\,\mathrm{mT}$ respectively.

the three relevant integer modes of the electron spin precession. As a result of the magnetic field sweep with $N_P = 10^6$ pump pulses per magnetic field step, the peak at $B_N^x \approx -130\,\mathrm{mT}$ has a weaker amplitude than in the steady-state whereas the amplitude of the peak at $B_N^x \approx 0\,\mathrm{mT}$ slightly increases. The peak of $p(B_N^x)$ at $B_N^x \approx 130\,\mathrm{mT}$ has roughly equal amplitude in the two scenarios.

The relatively weak redistribution of the weight between the peaks of $p(B_N^x)$ in the subspace with a fixed value $J = 100$ through the magnetic field sweep can be connected to the eigendecomposition of $\underline{\underline{M}}$. Figure 7.11(a) presents the Overhauser field distributions related to the three largest eigenvalues of the mapping in the subspace with $J = 100$ at an external magnetic field of $B = 1.93\,\mathrm{T}$. The distribution $p(B_N^x)$ in the quasistationary steady state (blue line) belongs to the eigenvalue $\Lambda_0 = 1$, which equals 1 within the range of numerical accuracy, i.e., 10^{-15}. The two second largest eigenvalues $\Lambda_1 = 1 - 10^{-8}$ and $\Lambda_2 = 1 - 3 \times 10^{-8}$ are real and slightly smaller than 1. The Overhauser field distributions extracted from the related right eigenvectors scaled by the overlap with $\vec{\rho}_0$ (orange and green line respectively) reflect the integer modes of the electron spin precession similar to the steady-state distribution. However, the sign of the peaks corresponding to the individual modes may be negative. Generally, the combination of the three Overhauser field distributions allows for the formation of a distribution $p(B_N^x)$ with an arbitrary distribution of the weight between the three integer modes in the Overhauser field range. The Overhauser field distributions $p(B_N^x)$ obtained from

the related left eigenvectors, see Fig. 7.11(b), indicate the overlap with the initial distribution of B_N^x in $\vec{\rho}_0$. While the quasistationary steady state has equal overlap with any value of B_N^x, the eigenvector to Λ_1 produces a relevant contribution when the initial Overhauser field distribution has an asymmetric distribution of the weight for $B_N^x > 0\,\mathrm{mT}$ and $B_N^x < 0\,\mathrm{mT}$. The eigenvector to Λ_2 acquires relevant overlap when small values of $|B_N^x|$ have a substantially larger weight than large values of $|B_N^x|$ or vice versa.

The eigenvalues Λ_1 and Λ_2 produce a lower bound of the sweeping rate below which the weight of $p(B_N^x)$ redistributes between the modes according to the steady-state rather than following the mode shift resulting from the magnetic field sweep. Contributions in the density operator related to the eigenoperators belonging to Λ_1 or Λ_2 decay to the fraction $1/e$ on the time scale of $N_P = -1/\ln(\Lambda_i)$ repetition periods which equals $N_P \approx 8 \times 10^7$ for Λ_1 and $N_P \approx 3 \times 10^7$ for Λ_2 respectively. The sweep with $N_P = 5 \times 10^7$ pump pulses per magnetic field step, which produces $N_P = 5 \times 10^9$ repetition periods in total, clearly exceeds this limit. Therefore, any potential redistribution of the peak weights through the sweep is lost immediately. For $N_P = 10^6$ pump pulses per magnetic field step, the total number of $N_P = 10^8$ repetition periods during the full sweep corresponds to the order of magnitude of the decay time scale produced by Λ_1 and Λ_2. Thereby, it allows for a slight redistribution of $p(B_N^x)$. As the sweep rate is relatively fast here, the Overhauser field cannot follow the mode shift, however. For the given setting, we find no window of the sweeping rate for which a dragging of substantial weight in $p(B_N^x)$ to a specific mode can be achieved.

Overall, the minor redistribution of the weight between the electron spin precession modes does not meet the extent of mode dragging observed in the experiments by Evers et al. [95]. We attribute this discrepancy to the simplified theoretical modeling which lacks the distribution of the hyperfine coupling constants and the dimension of the real system with $N = 10^5$ in (In,Ga)As quantum dots.

7.7 Variation of the pulse train

Tailoring of the pulse train applied to the quantum dot sample allows for coherent control of the spin dynamics. Pump-probe experiments [68, 74, 76] employed two pump pulses with different incidence times during the repetition period of $T_R = 13.2\,\mathrm{ns}$, and achieved efficient manipulation of the electron spin precession modes in the quantum dot ensemble. In particular, the revival of the electron spin polarization could be controlled coherently. For the quantum mechanical calculations, the computational effort scales with the number of applied pump pulses

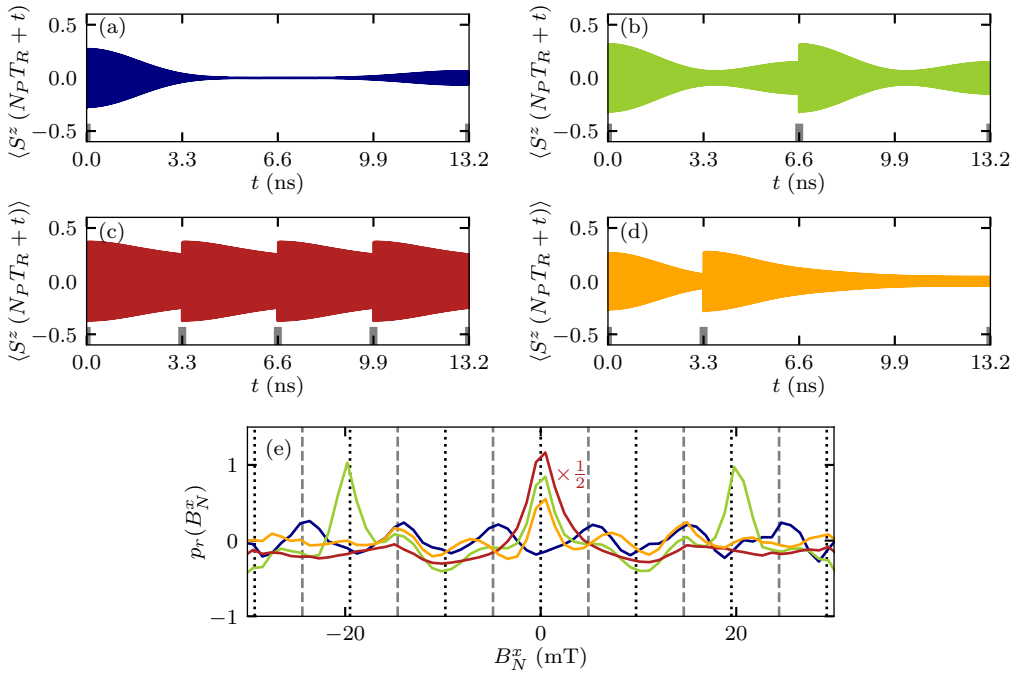

Figure 7.12: Variations of the pulse train at a fixed external magnetic field of $B = 3.90\,\mathrm{T}$. The system comprises $N = 6$ nuclear spins ($I = 1/2$) with randomly distributed hyperfine coupling constants; $N_C = 100$. The incidence time of the pump pulses is indicated by gray bars at the bottom of panels (a)-(d) respectively. (a) Single pulse per repetition period $T_R = 13.2\,\mathrm{ns}$. (b) Two equidistant pump pulses in the repetition period $T_R = 13.2\,\mathrm{ns}$, equivalent to a shortened repetition period $T_R = 6.6\,\mathrm{ns}$. (c) Four equidistant pump pulses in the repetition period $T_R = 13.2\,\mathrm{ns}$, equivalent to a shortened repetition period $T_R = 3.3\,\mathrm{ns}$. (d) Two pump pulses per repetition period $T_R = 13.2\,\mathrm{ns}$ at $t = 0\,\mathrm{ns}$ and $t = 3.3\,\mathrm{ns}$ respectively. (e) Relative Overhauser field distributions $p_r(B_N^x)$ associated to the electron spin dynamics in panels (a)-(d). The color coding indicates the respective scenario. The red curve was scaled by a factor of 1/2. The integer/half-integer modes of the electron spin precession for $T_R = 13.2\,\mathrm{ns}$ are indicated by black dotted/gray dashed vertical lines.

rather than with the time scale covered by the simulations. For efficient access to the quasistationary steady-state under a pulse train with several pump pulses per repetition period, we implement an Arnoldi method [208, 209]. Applied to the mapping $\mathcal{M}$ for one repetition period, the Arnoldi iteration provides the eigenvector related to the largest eigenvalue, i.e., $\Lambda_0 = 1$.

We focus on the system with $N = 6$ nuclear spins with the individual length $I = 1/2$ and employ randomly distributed hyperfine coupling constants as outlined in Sec. 5.5.

For this scenario, we require roughly ten restarts of the Arnoldi method with 10^3 iterations each. Rather than implementing the matrix representation of the mapping for the respective repetition period, we employ the procedure introduced in Sec. 5.4. This prevents us from handling huge matrices in the superoperator space with the dimensions $D' \times D'$ and restricts the matrix dimensions to the Hilbert space dimension d'. In comparison to the complete iterative calculation of the pulse train with $N_P = 10^6$ repetition periods, the Arnoldi method in total requires a factor of 100 fewer iterations, and thereby significantly reduces the computational effort.

The results for the quasistationary steady state under various trains of instantaneous pump pulses at a fixed external magnetic field $B = 3.90\,\mathrm{T}$ are presented in Fig. 7.12. For a single pump pulse in the repetition period $T_R = 13.2\,\mathrm{ns}$, the electron spin evolution in Fig. 7.12(a) displays the expected revival directly before the incidence of the next pump pulse. The magnitude of the revival amplitude is relatively small due to the nuclei-induced frequency focusing of the half-inter modes of the electron spin precession according to Eq. (6.13), see the related relative Overhauser field distribution in Fig. 7.12(e) (blue line). The addition of a second pump pulse in the middle of the repetition period effectively reduces the repetition time to $T_R = 6.6\,\mathrm{ns}$, see Fig. 7.12(b). Hence, the nuclear spins perform a quarter revolution between consecutive pump pulses, and $n = 1$ in the Eq. (6.13) predicts the favoring of the integer precession modes. As a result, the electron spin revival amplitude increases for $T_R = 6.6\,\mathrm{ns}$ in comparison to $T_R = 13.2\,\mathrm{ns}$. Due to the reduced repetition time, the peaks of the Overhauser field distribution $p_r(B_N^x)$ in Fig. 7.12(e) (green line) have the double distance as for $T_R = 13.2\,\mathrm{ns}$ and are located at every second black dotted vertical line. Reducing the repetition time further to $T_R = 3.3\,\mathrm{ns}$, see Fig. 7.12(c), the electron spin polarization only partially dephases between the pulses such that we do not observe a separate revival. The related Overhauser field distribution in Fig. 7.12(e) (red line) exhibits a single strongly pronounced peak at $B_N^x = 0\,\mathrm{mT}$. In this regime, the prediction according to Eq. (6.13) does not hold anymore ($n < 1$) and further integer precession modes are out of the relevant Overhauser field range in such a small system. For a pulse train with the repetition period $T_R = 13.2\,\mathrm{ns}$ comprising two pump pulses with a delay of 3.3 ns, see Fig. 7.12(d), the behavior is less clear. The electron spin polarization generated by the pump pulses dephases with a prolonged envelope function. However, no revival occurs. The pulse separation of 3.3 ns and 9.9 ns respectively produces several peaks in the Overhauser field distribuiton in Fig. 7.12(e) (orange line).

The complex interplay of the condition, Eq. (6.13), and the electron spin precession leads to differing quasistationary steady states of the pulse trains. The variation of the repetition period not only produces a variation of the distance between the equidistant electron spin precession frequencies but also a redistribution of weight

between the two types of modes. Hence, the customization of the pulse train allows for the adjustment of specific electron spin precession modes.

7.8 Chapter conclusion

The effect of one repetition period of a periodic pulse train can be captured by a linear mapping $\mathcal{M}$ for the density operator similar as outlined in Ref. [92]. The eigendecomposition of this mapping encodes the dynamics of the electron-nuclear spin system during a pulse train. In particular, the eigenvectors of $\underline{\underline{M}}$ related to the eigenvalue 1 correspond to the quasistationary steady state and match the results of the iterative approach after several million pump pulses. Additional eigenvalues are complex as a result of the nonhermitian mapping matrix and govern the evolution of the spin system under the periodic excitation before the quasistationary steady state is reached. The square mapping matrix however has the dimension $D' \times D'$ of the squared Hilbert space dimension d', $D' = d'^2$. Hence, the diagonalization of this matrix is computationally expensive. To overcome this obstacle, we developed a truncation scheme for the density matrix elements that allows for efficiently setting up the eigendecomposition in the box model approximation of the hyperfine coupling constants. The truncation scheme enables the investigation of systems consisting of several hundred nuclear spins. For a pumping periodicity of $T_R = 13.2\,\mathrm{ns}$, the electron spin revival amplitude in such a large system reflects the nonmonotonic magnetic field dependence governed by the nuclear Zeeman term, Eq. (6.13). The revival amplitude exhibits a relatively sharp dip at roughly 8 T similar to classical predictions [86, 88, 89, 224], whereas the quantum mechanical results for a small system with random hyperfine coupling constants and the pump-probe experiments indicate rather broad minima. The origin of this mismatch remains to be resolved by future analysis.

A reduced repetition period of $T_R = 1\,\mathrm{ns}$ produces the nuclei-induced frequency focusing of a single electron spin precession mode. The sweeping of the external magnetic field in the GHz pumping regime is expected to lead to a substantial polarization of the Overhauser field by mode dragging based on experimental observations [95, 229]. As the quantum mechanical calculations in this thesis are limited to $N = 200$ nuclear spins in the box model approximation, our results do not reproduce the extent of the Overhauser field redistribution of experimental findings. Here, including a realistic distribution of the hyperfine coupling constants in the large system would be crucial. We concluded by supplying an Arnoldi method that reduces the number of simulated repetition periods by a factor of roughly 100 in comparison to the iterative calculations. The Arnoldi iteration is exemplarily applied to a variety of pulse trains comprising several pump pulses during the repetition

time $T_R = 13.2\,\mathrm{ns}$ and opens the door to future investigations of more intricate situations.

Chapter 8

Conclusion

In this thesis, we achieved a fully quantum mechanical description of two nonequilibrium phenomena arising for localized charge carriers in semiconductor nanostructures. We focused on the nuclear-spin polaron state predicted to form in the cooled spin system as well as on the mode-locking effect via nuclei-induced frequency focusing of the electron spin precession emerging in periodically excited quantum dots. Both nonequilibrium situations are characterized by a profound reorientation of the nuclear spin system compared to the high-temperature equilibrium state. In the case of nuclear-spin polaron formation, the nuclear spins align oppositely to the charge carrier spin to minimize the hyperfine energy. The specific orientation of the polaronic state depends on the hyperfine anisotropy, i.e., the polaron state will be aligned along the axes of the strongest hyperfine coupling. In the mode-locked electron-nuclear spin system, the nuclear spins align in such a way that the electron spin performs a well defined number of revolutions for the Larmor precession between consecutive pump pulses. The nuclear Overhauser field acting on the electron spin in addition to the external magnetic field adjusts to specific modes corresponding to either an integer or half-integer number of electron spin revolutions during the repetition time T_R. As a result of the ordering in the nuclear spin bath, the nuclear-spin polaron state as well as the mode-locked spin system exhibit significantly prolonged spin coherence times.

Our description by kinetic rate equations and a generalized Lindblad formalism allowed for accurately capturing the nuclear-spin polaron formation over the full range of the effective electron and nuclear spin temperatures. Establishing the two differing spin temperatures via coupling to two separate external reservoirs inducing spin flips with temperature-dependent rates ensured the correct thermodynamic equilibrium for equal temperatures and enabled the investigation of a cooled nuclear spin system at temperatures lower than the lattice temperature. In contrast to previous theoretical approaches [66, 70], we included the quantum fluctuations of the charge carrier spin as well as of the nuclear spins. Our calculations provide a temperature criterion for the formation of the polaronic state that matches the mean-field critical temperature in an intermediate temperature range but yields a corrected crossover temperature when the spin fluctuations become relevant. A

Monte Carlo simulation of the cooled spin system with a realistic distribution of the hyperfine coupling constants allowed to map the observed crossover temperature to the analytic temperature criterion obtained in the box model limit of the hyperfine couplings by introducing an effective number of nuclear spins that determine the dynamics. The dependence of the polaron orientation on the hyperfine anisotropy parameter λ is connected to a change of the ground state of the hyperfine Hamiltonian. Therefore, the nature of the nuclear-spin polaron state depends on the value of λ: At the quantum phase transition, $\lambda_c = 1$, the nuclear-spin polaron state changes its character. These differences transfer to the spin autocorrelation functions. In the Ising limit of the hyperfine coupling, we observe extremely long living spin correlations at low temperatures due to two disconnected ground states. For the isotropic system, the correlation time is significantly prolonged in the polaronic regime compared to the disordered high-temperature state but is ultimately limited by the rotation of the polaron state enabled by a lack of spatial preference. A strong in-plane hyperfine interaction relevant for localized light holes, however, does not protect the system from a loss of spin correlation at low temperatures. Our results provide a basis for future experimental attempts of detecting the polaronic state. The autocorrelation spectrum of the charge carrier is experimentally accessible by spin noise measurements. Our calculations hint at a clear signature of the polaron formation in the low frequency range of the spectrum. For future theoretical approaches, a microscopic theory of the spin interactions beyond the hyperfine interaction, e.g., the nuclear quadrupolar interactions, could be helpful since these interactions are expected to affect the crossover temperature to polaron formation. Moreover, an explicit treatment of the optical cooling could reveal how a nuclear-spin polaron state is eventually realized and detected in experiments.

The quantum mechanical approach to the mode-locking effect in the periodically driven electron-nuclear spin system reproduces the revival of the electron spin polarization directly before the pump pulses observed in experiments [68, 86]. Moreover, the theoretical description enables a detailed study of the reorientation of the nuclear spins by means of the Overhauser field distribution. The system favors integer or half-integer modes of the electron spin precession between consecutive pump pulses according to a resonance condition for the nuclear Larmor precession established in Ref. [91]. Our findings reveal that the interplay of these two mode types determines the revival amplitude. Thereby, we could attribute the nonmonotonic magnetic field dependence of the revival amplitude to the nuclear Zeeman term. As the experimental results for the electron spin revival amplitude as a function of the external magnetic field show additional features, we performed an in-depth investigation of additional influences. A finite nonzero pulse duration produces an overall decrease in the revival amplitude for strong external magnetic fields since the generation of electron spin polarization by the pump pulses becomes

inefficient. Furthermore, a detuning of the trion energy with respect to the laser frequency can induce a polarization of the Overhauser field but does not affect the favored mode type and the revival amplitude. Nuclear quadrupolar interactions significantly weaken the mode-locking effect and, therefore, constitute an obstacle to the experimental realization of the mode-locking effect. Additional modulations in the experimental data of the electron spin revival amplitude depending on the external magnetic field are ascribed to the differing g factors of the various nuclear isotopes in the quantum dots.

While the first part of the quantum mechanical exploration of the mode-locking effect in this thesis is based on a relatively small system comprising $N = 6$ nuclear spins with randomly distributed hyperfine coupling constants, we employ an extended version of the mapping approach outlined in Ref. [92] for the second part. A newly developed truncation scheme allows for the examination of larger systems with up to $N = 500$ nuclear spins in the box model limit of the hyperfine couplings. For such large spin baths, the Overhauser field distribution exhibits extremely sharp peaks depending on the applied magnetic field. The resulting electron revival amplitude as a function of the external magnetic field agrees with the periodicity predicted by the nuclear Zeeman term. The specific shape with a sharp dip at roughly 8 T, however, resembles classical calculations [86, 88, 89, 224] rather than the quantum mechanical results for the smaller system and the experimental data. For future theoretical approaches, the quantitative agreement with the experimental data constitutes a major challenge. Reaching realistic system sizes of $N = 10^5$ nuclear spins with a realistic distribution of the hyperfine coupling constants [160] would be especially desirable for reproducing the mode dragging achieved in pump-probe experiments via sweeping the magnetic field during the periodic optical excitation [95].

Bibliography

[1] A. Steane, *Quantum computing*, Reports on Progress in Physics **61**, 117 (1998).

[2] C. H. Bennett and D. P. DiVincenzo, *Quantum information and computation*, Nature **404**, 247 (2000).

[3] S. Barnett, *Quantum Information*, Oxford Master Series in Physics (OUP Oxford, 2009).

[4] J. L. O'Brien, A. Furusawa, and J. Vučković, *Photonic quantum technologies*, Nature Photonics **3**, 687 (2009).

[5] G. Kurizki, P. Bertet, Y. Kubo, K. Mølmer, D. Petrosyan, P. Rabl, and J. Schmiedmayer, *Quantum technologies with hybrid systems*, Proceedings of the National Academy of Sciences **112**, 3866 (2015).

[6] A. Montanaro, *Quantum algorithms: an overview*, npj Quantum Information **2**, 15023 (2016).

[7] Y. S. Weinstein, M. A. Pravia, E. M. Fortunato, S. Lloyd, and D. G. Cory, *Implementation of the Quantum Fourier Transform*, Phys. Rev. Lett. **86**, 1889 (2001).

[8] T. Monz, D. Nigg, E. A. Martinez, M. F. Brandl, P. Schindler, R. Rines, S. X. Wang, I. L. Chuang, and R. Blatt, *Realization of a scalable Shor algorithm*, Science **351**, 1068 (2016).

[9] E. R. MacQuarrie, C. Simon, S. Simmons, and E. Maine, *The emerging commercial landscape of quantum computing*, Nature Reviews Physics **2**, 596 (2020).

[10] J. Preskill, in Proceedings of the 25th Solvay Conference on Physics: The Theory of the Quantum World (2011), pp. 63–80.

[11] S. Boixo, S. V. Isakov, V. N. Smelyanskiy, R. Babbush, N. Ding, Z. Jiang, M. J. Bremner, J. M. Martinis, and H. Neven, *Characterizing quantum supremacy in near-term devices*, Nature Physics **14**, 595 (2018).

[12] C. Neill, P. Roushan, K. Kechedzhi, S. Boixo, S. V. Isakov, V. Smelyanskiy, A. Megrant, B. Chiaro, A. Dunsworth, K. Arya, et al., *A blueprint for demonstrating quantum supremacy with superconducting qubits*, Science **360**, 195 (2018).

[13] F. Arute, K. Arya, R. Babbush, D. Bacon, J. C. Bardin, R. Barends, R. Biswas, S. Boixo, F. G. S. L. Brandao, D. A. Buell, et al., *Quantum supremacy using a programmable superconducting processor*, Nature **574**, 505 (2019).

[14] E. Pednault, J. A. Gunnels, G. Nannicini, L. Horesh, and R. Wisnieff, *Leveraging Secondary Storage to Simulate Deep 54-qubit Sycamore Circuits*, 2019.

[15] T. D. Ladd, F. Jelezko, R. Laflamme, Y. Nakamura, C. Monroe, and J. L. O'Brien, *Quantum computers*, Nature **464**, 45 (2010).

[16] D. P. DiVincenzo, *Quantum Computation*, Science **270**, 255 (1995).

[17] J. Stolze and D. Suter, *Quantum computing: A Short Course from Theory to Experiment* (Wiley-VCH, 2004).

[18] Y. I. Manin, *Mathematics as Metaphor: Selected Essays of Yuri I. Manin* (American Mathematical Society, 2007).

[19] R. P. Feynman, *Simulating physics with computers*, International Journal of Theoretical Physics **21**, 467 (1982).

[20] D. Deutsch and R. Penrose, *Quantum theory, the Church-Turing principle and the universal quantum computer*, Proceedings of the Royal Society of London. A. Mathematical and Physical Sciences **400**, 97 (1985).

[21] R. P. Feynman, *Quantum mechanical computers*, Foundations of Physics **16**, 507 (1986).

[22] D. Deutsch and R. Jozsa, *Rapid solution of problems by quantum computation*, Proceedings of the Royal Society of London. Series A: Mathematical and Physical Sciences **439**, 553 (1992).

[23] D. Coppersmith, *An approximate Fourier transform useful in quantum factoring*, in IBM Research Report No. RC19642 (1994).

[24] P. Shor, *Algorithms for quantum computation: discrete logarithms and factoring*, in Proceedings, 35th Annual Symposium on Foundations of Computer Science (1994), pp. 124–134.

[25] P. W. Shor, *Polynomial-Time Algorithms for Prime Factorization and Discrete Logarithms on a Quantum Computer*, SIAM Journal on Computing **26**, 1484 (1997).

[26] L. K. Grover, *A fast quantum mechanical algorithm for database search*, in Proc. 28th Annual ACM Symposium on the Theory of Computation (1996), pp. 212–219.

[27] L. K. Grover, *A fast quantum mechanical algorithm for database search*, 1996.

[28] D. P. DiVincenzo, *The Physical Implementation of Quantum Computation*, Fortschritte der Physik **48**, 771 (2000).

[29] W. G. Unruh, *Maintaining coherence in quantum computers*, Phys. Rev. A **51**, 992 (1995).

[30] G. S. Uhrig, *Keeping a Quantum Bit Alive by Optimized π-Pulse Sequences*, Phys. Rev. Lett. **98**, 100504 (2007).

[31] A. M. Souza, G. A. Álvarez, and D. Suter, *Robust dynamical decoupling*, Philosophical Transactions of the Royal Society A: Mathematical, Physical and Engineering Sciences **370**, 4748 (2012).

[32] V. Cerletti, W. A. Coish, O. Gywat, and D. Loss, *Recipes for spin-based quantum computing*, Nanotechnology **16**, R27 (2005).

[33] D. G. Cory, A. F. Fahmy, and T. F. Havel, *Ensemble quantum computing by NMR spectroscopy*, Proceedings of the National Academy of Sciences **94**, 1634 (1997).

[34] L. M. K. Vandersypen, M. Steffen, G. Breyta, C. S. Yannoni, M. H. Sherwood, and I. L. Chuang, *Experimental realization of Shor's quantum factoring algorithm using nuclear magnetic resonance*, Nature **414**, 883 (2001).

[35] J. I. Cirac and P. Zoller, *Quantum Computations with Cold Trapped Ions*, Phys. Rev. Lett. **74**, 4091 (1995).

[36] J. I. Cirac and P. Zoller, *A scalable quantum computer with ions in an array of microtraps*, Nature **404**, 579 (2000).

[37] D. Jaksch, H.-J. Briegel, J. I. Cirac, C. W. Gardiner, and P. Zoller, *Entanglement of Atoms via Cold Controlled Collisions*, Phys. Rev. Lett. **82**, 1975 (1999).

[38] G. K. Brennen, C. M. Caves, P. S. Jessen, and I. H. Deutsch, *Quantum Logic Gates in Optical Lattices*, Phys. Rev. Lett. **82**, 1060 (1999).

[39] Y. Makhlin, G. Scöhn, and A. Shnirman, *Josephson-junction qubits with controlled couplings*, Nature **398**, 305 (1999).

[40] J. Clarke and F. K. Wilhelm, *Superconducting quantum bits*, Nature **453**, 1031 (2008).

[41] M. H. Devoret and R. J. Schoelkopf, *Superconducting Circuits for Quantum Information: An Outlook*, Science **339**, 1169 (2013).

[42] M. V. G. Dutt, L. Childress, L. Jiang, E. Togan, J. Maze, F. Jelezko, A. S. Zibrov, P. R. Hemmer, and M. D. Lukin, *Quantum Register Based on Individual Electronic and Nuclear Spin Qubits in Diamond*, Science **316**, 1312 (2007).

[43] M. W. Doherty, N. B. Manson, P. Delaney, F. Jelezko, J. Wrachtrup, and L. C. Hollenberg, *The nitrogen-vacancy colour centre in diamond*, Physics Reports **528**, The nitrogen-vacancy colour centre in diamond, 1 (2013).

[44] D. Loss and D. P. DiVincenzo, *Quantum computation with quantum dots*, Phys. Rev. A **57**, 120 (1998).

[45] A. Imamoglu, D. D. Awschalom, G. Burkard, D. P. DiVincenzo, D. Loss, M. Sherwin, and A. Small, *Quantum Information Processing Using Quantum Dot Spins and Cavity QED*, Phys. Rev. Lett. **83**, 4204 (1999).

[46] J. Gorman, D. G. Hasko, and D. A. Williams, *Charge-Qubit Operation of an Isolated Double Quantum Dot*, Phys. Rev. Lett. **95**, 090502 (2005).

[47] A. Imamoglu, *Are quantum dots useful for quantum computation?* Physica E: Low-dimensional Systems and Nanostructures **16**, Proceedings of the Twelfth International Winterschool on New Developments in Solids State Physics, "Low- Dimensional Systems: From 2D to Molecules", 47 (2003).

[48] R. Hanson, L. P. Kouwenhoven, J. R. Petta, S. Tarucha, and L. M. K. Vandersypen, *Spins in few-electron quantum dots*, Rev. Mod. Phys. **79**, 1217 (2007).

[49] F. P. G. de Arquer, D. V. Talapin, V. I. Klimov, Y. Arakawa, M. Bayer, and E. H. Sargent, *Semiconductor quantum dots: Technological progress and future challenges*, Science **373**, eaaz8541 (2021).

[50] W. A. Coish and D. Loss, *Hyperfine interaction in a quantum dot: Non-Markovian electron spin dynamics*, Phys. Rev. B **70**, 195340 (2004).

[51] F. H. L. Koppens, C. Buizert, K. J. Tielrooij, I. T. Vink, K. C. Nowack, T. Meunier, L. P. Kouwenhoven, and L. M. K. Vandersypen, *Driven coherent oscillations of a single electron spin in a quantum dot*, Nature **442**, 766 (2006).

[52] W. A. Coish, V. N. Golovach, J. C. Egues, and D. Loss, *Measurement, control, and decay of quantum-dot spins*, physica status solidi (b) **243**, 3658 (2006).

[53] B. Urbaszek, X. Marie, T. Amand, O. Krebs, P. Voisin, P. Maletinsky, A. Högele, and A. Imamoglu, *Nuclear spin physics in quantum dots: An optical investigation*, Rev. Mod. Phys. **85**, 79 (2013).

[54] A. V. Khaetskii, D. Loss, and L. Glazman, *Electron Spin Decoherence in Quantum Dots due to Interaction with Nuclei*, Phys. Rev. Lett. **88**, 186802 (2002).

[55] I. A. Merkulov, A. L. Efros, and M. Rosen, *Electron spin relaxation by nuclei in semiconductor quantum dots*, Phys. Rev. B **65**, 205309 (2002).

[56] R. de Sousa and S. Das Sarma, *Electron spin coherence in semiconductors: Considerations for a spin-based solid-state quantum computer architecture*, Phys. Rev. B **67**, 033301 (2003).

[57] J. Schliemann, A. Khaetskii, and D. Loss, *Electron spin dynamics in quantum dots and related nanostructures due to hyperfine interaction with nuclei*, Journal of Physics: Condensed Matter **15**, R1809 (2003).

[58] J. R. Petta, A. C. Johnson, J. M. Taylor, E. A. Laird, A. Yacoby, M. D. Lukin, C. M. Marcus, M. P. Hanson, and A. C. Gossard, *Coherent Manipulation of Coupled Electron Spins in Semiconductor Quantum Dots*, Science **309**, 2180 (2005).

[59] W. Yao, R.-B. Liu, and L. J. Sham, *Theory of electron spin decoherence by interacting nuclear spins in a quantum dot*, Phys. Rev. B **74**, 195301 (2006).

[60] J. Fischer, M. Trif, W. Coish, and D. Loss, *Spin interactions, relaxation and decoherence in quantum dots*, Solid State Communications **149**, Fundamental Phenomena and Applications of Quantum Dots, 1443 (2009).

[61] M. Bayer, *All for one and one for all*, Science **364**, 30 (2019).

[62] D. Stepanenko, G. Burkard, G. Giedke, and A. Imamoglu, *Enhancement of Electron Spin Coherence by Optical Preparation of Nuclear Spins*, Phys. Rev. Lett. **96**, 136401 (2006).

[63] H. Bluhm, S. Foletti, D. Mahalu, V. Umansky, and A. Yacoby, *Enhancing the Coherence of a Spin Qubit by Operating it as a Feedback Loop That Controls its Nuclear Spin Bath*, Phys. Rev. Lett. **105**, 216803 (2010).

[64] L. B. Gravert, P. Lorenz, C. Nase, J. Stolze, and G. S. Uhrig, *Increased coherence time in narrowed bath states in quantum dots*, Phys. Rev. B **94**, 094416 (2016).

[65] W. Zhang, V. V. Dobrovitski, L. F. Santos, L. Viola, and B. N. Harmon, *Dynamical control of electron spin coherence in a quantum dot: A theoretical study*, Phys. Rev. B **75**, 201302 (2007).

[66] I. A. Merkulov, *Formation of a nuclear spin polaron under optical orientation in GaAs-type semiconductors*, Physics of the Solid State **40**, 930 (1998).

[67] A. Greilich, D. R. Yakovlev, A. Shabaev, A. L. Efros, I. A. Yugova, R. Oulton, V. Stavarache, D. Reuter, A. Wieck, and M. Bayer, *Mode Locking of Electron Spin Coherences in Singly Charged Quantum Dots*, Science **313**, 341 (2006).

[68] A. Greilich, A. Shabaev, D. R. Yakovlev, A. L. Efros, I. A. Yugova, D. Reuter, A. D. Wieck, and M. Bayer, *Nuclei-Induced Frequency Focusing of Electron Spin Coherence*, Science **317**, 1896 (2007).

[69] M. Gaudin, *Diagonalisation d'une classe d'hamiltoniens de spin*, Journal De Physique **37**, 1087 (1976).

[70] D. Scalbert, *Nuclear polaron beyond the mean-field approximation*, Phys. Rev. B **95**, 245209 (2017).

[71] M. Vladimirova, D. Scalbert, M. S. Kuznetsova, and K. V. Kavokin, *Electron-induced nuclear magnetic ordering in n-type semiconductors*, Phys. Rev. B **103**, 205207 (2021).

[72] R. Oulton, A. Greilich, S. Y. Verbin, R. V. Cherbunin, T. Auer, D. R. Yakovlev, M. Bayer, I. A. Merkulov, V. Stavarache, D. Reuter, et al., *Subsecond Spin Relaxation Times in Quantum Dots at Zero Applied Magnetic Field Due to a Strong Electron-Nuclear Interaction*, Phys. Rev. Lett. **98**, 107401 (2007).

[73] M. Vladimirova, S. Cronenberger, D. Scalbert, I. I. Ryzhov, V. S. Zapasskii, G. G. Kozlov, A. Lemaître, and K. V. Kavokin, *Spin temperature concept verified by optical magnetometry of nuclear spins*, Phys. Rev. B **97**, 041301 (2018).

[74] A. Greilich, M. Wiemann, F. G. G. Hernandez, D. R. Yakovlev, I. A. Yugova, M. Bayer, A. Shabaev, A. L. Efros, D. Reuter, and A. D. Wieck, *Robust manipulation of electron spin coherence in an ensemble of singly charged quantum dots*, Phys. Rev. B **75**, 233301 (2007).

[75] A. Greilich, S. E. Economou, S. Spatzek, D. R. Yakovlev, D. Reuter, A. D. Wieck, T. L. Reinecke, and M. Bayer, *Ultrafast optical rotations of electron spins in quantum dots*, Nature Physics **5**, 262 (2009).

[76] A. Greilich, S. Spatzek, I. A. Yugova, I. A. Akimov, D. R. Yakovlev, A. L. Efros, D. Reuter, A. D. Wieck, and M. Bayer, *Collective single-mode precession of electron spins in an ensemble of singly charged (In,Ga)As/GaAs quantum dots*, Phys. Rev. B **79**, 201305 (2009).

[77] A. Greilich, D. R. Yakovlev, and M. Bayer, *Optical tailoring of electron spin coherence in quantum dots*, Solid State Communications **149**, Fundamental Phenomena and Applications of Quantum Dots, 1466 (2009).

[78] S. Spatzek, S. Varwig, M. M. Glazov, I. A. Yugova, A. Schwan, D. R. Yakovlev, D. Reuter, A. D. Wieck, and M. Bayer, *Generation and detection of mode-locked spin coherence in (In,Ga)As/GaAs quantum dots by laser pulses of long duration*, Phys. Rev. B **84**, 115309 (2011).

[79] S. Varwig, A. Greilich, D. R. Yakovlev, and M. Bayer, *Spin mode locking in quantum dots revisited*, physica status solidi (b) **251**, 1892 (2014).

[80] M. M. Glazov, I. A. Yugova, and A. L. Efros, *Electron spin synchronization induced by optical nuclear magnetic resonance feedback*, Phys. Rev. B **85**, 041303 (2012).

[81] I. A. Yugova, M. M. Glazov, D. R. Yakovlev, A. A. Sokolova, and M. Bayer, *Coherent spin dynamics of electrons and holes in semiconductor quantum wells and quantum dots under periodical optical excitation: Resonant spin amplification versus spin mode locking*, Phys. Rev. B **85**, 125304 (2012).

[82] N. Jäschke, F. B. Anders, and M. M. Glazov, *Electron spin noise under the conditions of nuclei-induced frequency focusing*, Phys. Rev. B **98**, 045307 (2018).

[83] M. Y. Petrov and S. V. Yakovlev, *Comparison of quantum-mechanical and semiclassical approaches for an analysis of spin dynamics in quantum dots*, Journal of Experimental and Theoretical Physics **115**, 326 (2012).

[84] N. Jäschke, A. Fischer, E. Evers, V. V. Belykh, A. Greilich, M. Bayer, and F. B. Anders, *Nonequilibrium nuclear spin distribution function in quantum dots subject to periodic pulses*, Phys. Rev. B **96**, 205419 (2017).

[85] B. Fauseweh, P. Schering, J. Hüdepohl, and G. S. Uhrig, *Efficient algorithms for the dynamics of large and infinite classical central spin models*, Phys. Rev. B **96**, 054415 (2017).

[86] I. Kleinjohann, E. Evers, P. Schering, A. Greilich, G. S. Uhrig, M. Bayer, and F. B. Anders, *Magnetic field dependence of the electron spin revival amplitude in periodically pulsed quantum dots*, Phys. Rev. B **98**, 155318 (2018).

[87] P. Schering, J. Hüdepohl, G. S. Uhrig, and B. Fauseweh, *Nuclear frequency focusing in periodically pulsed semiconductor quantum dots described by infinite classical central spin models*, Phys. Rev. B **98**, 024305 (2018).

[88] P. Schering, P. W. Scherer, and G. S. Uhrig, *Interplay of spin mode locking and nuclei-induced frequency focusing in quantum dots*, Phys. Rev. B **102**, 115301 (2020).

[89] P. Schering and G. S. Uhrig, *Nuclear magnetic resonance spectroscopy of nonequilibrium steady states in quantum dots*, EPL (Europhysics Letters) **133**, 57003 (2021).

[90] W. Beugeling, G. S. Uhrig, and F. B. Anders, *Quantum model for mode locking in pulsed semiconductor quantum dots*, Phys. Rev. B **94**, 245308 (2016).

[91] W. Beugeling, G. S. Uhrig, and F. B. Anders, *Influence of the nuclear Zeeman effect on mode locking in pulsed semiconductor quantum dots*, Phys. Rev. B **96**, 115303 (2017).

[92] G. S. Uhrig, *Quantum Coherence from Commensurate Driving with Laser Pulses and Decay*, SciPost Phys. **8**, 40 (2020).

[93] M. Y. Petrov, G. G. Kozlov, I. V. Ignatiev, R. V. Cherbunin, D. R. Yakovlev, and M. Bayer, *Coupled electron-nuclear spin dynamics in quantum dots: A graded box model approach*, Phys. Rev. B **80**, 125318 (2009).

[94] E. Evers, N. E. Kopteva, I. A. Yugova, D. R. Yakovlev, D. Reuter, A. D. Wieck, M. Bayer, and A. Greilich, *Suppression of nuclear spin fluctuations in an InGaAs quantum dot ensemble by GHz-pulsed optical excitation*, npj Quantum Information **7**, 60 (2021).

[95] E. Evers, N. E. Kopteva, I. A. Yugova, D. R. Yakovlev, M. Bayer, and A. Greilich, *Shielding of external magnetic field by dynamic nuclear polarization in (In,Ga)As quantum dots*, Phys. Rev. B **104**, 075302 (2021).

[96] A. Abragam, *Principles of Nuclear Magnetism* (Oxford Science Publications, 2002).

[97] M. I. Dyakonov, ed., *Spin physics in semiconductors*, 2nd ed., Springer Series in Solid-State Sciences 157 (Springer International Publishing, 2017).

[98] T. Auer, R. Oulton, A. Bauschulte, D. R. Yakovlev, M. Bayer, S. Y. Verbin, R. V. Cherbunin, D. Reuter, and A. D. Wieck, *Measurement of the Knight field and local nuclear dipole-dipole field in an InGaAs/GaAs quantum dot ensemble*, Phys. Rev. B **80**, 205303 (2009).

[99] S. Spatzek, A. Greilich, S. E. Economou, S. Varwig, A. Schwan, D. R. Yakovlev, D. Reuter, A. D. Wieck, T. L. Reinecke, and M. Bayer, *Optical Control of Coherent Interactions between Electron Spins in InGaAs Quantum Dots*, Phys. Rev. Lett. **107**, 137402 (2011).

[100] S. Varwig, A. René, S. E. Economou, A. Greilich, D. R. Yakovlev, D. Reuter, A. D. Wieck, T. L. Reinecke, and M. Bayer, *All-optical tomography of electron spins in (In,Ga)As quantum dots*, Phys. Rev. B **89**, 081310 (2014).

[101] A. Fischer, E. Evers, S. Varwig, A. Greilich, M. Bayer, and F. B. Anders, *Signatures of long-range spin-spin interactions in an (In,Ga)As quantum dot ensemble*, Phys. Rev. B **98**, 205308 (2018).

[102] A. Fischer, I. Kleinjohann, N. A. Sinitsyn, and F. B. Anders, *Cross-correlation spectra in interacting quantum dot systems*, Phys. Rev. B **105**, 035303 (2022).

[103] F. Vonhoff, A. Fischer, K. Deltenre, and F. B. Anders, *Microscopic origin of the effective spin-spin interaction in a semiconductor quantum dot ensemble*, `10.48550/ARXIV.2207.02707` (2022).

[104] P. YU and M. Cardona, *Fundamentals of Semiconductors*, 3rd ed. (Springer, Berlin, Heidelberg, 1996).

[105] R. C. Ashoori, *Electrons in artificial atoms*, Nature **379**, 413 (1996).

[106] J. Y. Kim, O. Voznyy, D. Zhitomirsky, and E. H. Sargent, *25th Anniversary Article: Colloidal Quantum Dot Materials and Devices: A Quarter-Century of Advances*, Advanced Materials **25**, 4986 (2013).

[107] V. I. Klimov, A. A. Mikhailovsky, S. Xu, A. Malko, J. A. Hollingsworth, C. A. Leatherdale, H.-J. Eisler, and M. G. Bawendi, *Optical Gain and Stimulated Emission in Nanocrystal Quantum Dots*, Science **290**, 314 (2000).

[108] M. Liu, N. Yazdani, M. Yarema, M. Jansen, V. Wood, and E. H. Sargent, *Colloidal quantum dot electronics*, Nature Electronics **4**, 548 (2021).

[109] S. Franchi, G. Trevisi, L. Seravalli, and P. Frigeri, *Quantum dot nanostructures and molecular beam epitaxy*, Progress in Crystal Growth and Characterization of Materials **47**, Vapour Growth of Bulk Crystals and Epitaxy: Part I, 166 (2003).

[110] K. E. Sautter, K. D. Vallejo, and P. J. Simmonds, *Strain-driven quantum dot self-assembly by molecular beam epitaxy*, Journal of Applied Physics **128**, 031101 (2020).

[111] C. E. Reilly, S. Keller, S. Nakamura, and S. P. DenBaars, *Metalorganic chemical vapor deposition of InN quantum dots and nanostructures*, Light: Science & Applications **10**, 150 (2021).

[112] T. Fukui, S. Ando, Y. Tokura, and T. Toriyama, *GaAs tetrahedral quantum dot structures fabricated using selective area metalorganic chemical vapor deposition*, Applied Physics Letters **58**, 2018 (1991).

[113] I. N. Stranski and L. Krastanow, *Zur Theorie der orientierten Ausscheidung von Ionenkristallen aufeinander*, Monatshefte für Chemie und verwandte Teile anderer Wissenschaften **71**, 351 (1937).

[114] A. O. Kosogov, P. Werner, U. Gösele, N. N. Ledentsov, D. Bimberg, V. M. Ustinov, A. Y. Egorov, A. E. Zhukov, P. S. Kop'ev, N. A. Bert, et al., *Structural and optical properties of InAs–GaAs quantum dots subjected to high temperature annealing*, Applied Physics Letters **69**, 3072 (1996).

[115] M. Y. Petrov, I. V. Ignatiev, S. V. Poltavtsev, A. Greilich, A. Bauschulte, D. R. Yakovlev, and M. Bayer, *Effect of thermal annealing on the hyperfine interaction in InAs/GaAs quantum dots*, Phys. Rev. B **78**, 045315 (2008).

[116] N. H. Bonadeo, J. Erland, D. Gammon, D. Park, D. S. Katzer, and D. G. Steel, *Coherent Optical Control of the Quantum State of a Single Quantum Dot*, Science **282**, 1473 (1998).

[117] P. Chen, C. Piermarocchi, L. J. Sham, D. Gammon, and D. G. Steel, *Theory of quantum optical control of a single spin in a quantum dot*, Phys. Rev. B **69**, 075320 (2004).

[118] M. H. Kolodrubetz and J. R. Petta, *Coherent Holes in a Semiconductor Quantum Dot*, Science **325**, 42 (2009).

[119] A. J. Ramsay, *A review of the coherent optical control of the exciton and spin states of semiconductor quantum dots*, Semiconductor Science and Technology **25**, 103001 (2010).

[120] U. Woggon, *Optical Properties of Semiconductor Quantum Dots* (Springer, Berlin, Heidelberg, 1997).

[121] M. M. Glazov and E. L. Ivchenko, *Spin noise in quantum dot ensembles*, Phys. Rev. B **86**, 115308 (2012).

[122] J. Hackmann, P. Glasenapp, A. Greilich, M. Bayer, and F. B. Anders, *Influence of the Nuclear Electric Quadrupolar Interaction on the Coherence Time of Hole and Electron Spins Confined in Semiconductor Quantum Dots*, Phys. Rev. Lett. **115**, 207401 (2015).

[123] P. Glasenapp, D. S. Smirnov, A. Greilich, J. Hackmann, M. M. Glazov, F. B. Anders, and M. Bayer, *Spin noise of electrons and holes in (In,Ga)As quantum dots: Experiment and theory*, Phys. Rev. B **93**, 205429 (2016).

[124] N. A. Sinitsyn and Y. V. Pershin, *The theory of spin noise spectroscopy: a review*, Reports on Progress in Physics **79**, 106501 (2016).

[125] D. S. Smirnov, V. N. Mantsevich, and M. M. Glazov, *Theory of optically detected spin noise in nanosystems*, Physics-Uspekhi **64**, 923 (2021).

[126] B. Eble, P. Desfonds, F. Fras, F. Bernardot, C. Testelin, M. Chamarro, A. Miard, and A. Lemaître, *Hole and trion spin dynamics in quantum dots under excitation by a train of circularly polarized pulses*, Phys. Rev. B **81**, 045322 (2010).

[127] A. Greilich, R. Oulton, E. A. Zhukov, I. A. Yugova, D. R. Yakovlev, M. Bayer, A. Shabaev, A. L. Efros, I. A. Merkulov, V. Stavarache, et al., *Optical Control of Spin Coherence in Singly Charged* (In, Ga)As/GaAs *Quantum Dots*, Phys. Rev. Lett. **96**, 227401 (2006).

[128] I. A. Yugova, M. M. Glazov, E. L. Ivchenko, and A. L. Efros, *Pump-probe Faraday rotation and ellipticity in an ensemble of singly charged quantum dots*, Phys. Rev. B **80**, 104436 (2009).

[129] M. M. Glazov, I. A. Yugova, S. Spatzek, A. Schwan, S. Varwig, D. R. Yakovlev, D. Reuter, A. D. Wieck, and M. Bayer, *Effect of pump-probe detuning on the Faraday rotation and ellipticity signals of mode-locked spins in (In,Ga)As/GaAs quantum dots*, Phys. Rev. B **82**, 155325 (2010).

[130] L. M. Roth, B. Lax, and S. Zwerdling, *Theory of Optical Magneto-Absorption Effects in Semiconductors*, Phys. Rev. **114**, 90 (1959).

[131] A. A. Kiselev, E. L. Ivchenko, and U. Rössler, *Electron g factor in one- and zero-dimensional semiconductor nanostructures*, Phys. Rev. B **58**, 16353 (1998).

[132] K. Gawarecki and M. Zieliński, *Electron g-factor in nanostructures: continuum media and atomistic approach*, Scientific Reports **10**, 22001 (2020).

[133] A. Schwan, B.-M. Meiners, A. Greilich, D. R. Yakovlev, M. Bayer, A. D. B. Maia, A. A. Quivy, and A. B. Henriques, *Anisotropy of electron and hole g-factors in (In,Ga)As quantum dots*, Applied Physics Letters **99**, 221914 (2011).

[134] A. V. Trifonov, I. A. Akimov, L. E. Golub, E. L. Ivchenko, I. A. Yugova, A. N. Kosarev, S. E. Scholz, C. Sgroi, A. Ludwig, A. D. Wieck, et al., *Homogeneous optical anisotropy in an ensemble of InGaAs quantum dots induced by strong enhancement of the heavy-hole band Landé parameter q*, Phys. Rev. B **104**, L161405 (2021).

[135] N. J. Stone, *Table of nuclear magnetic dipole and electric quadrupole moments*, Atomic Data and Nuclear Data Tables **90**, 75 (2005).

[136] M. Gaudin, *La fonction d'onde de Bethe*, Collection CEA : Série scientifique (Masson, 1983).

[137] R. Hanson, V. V. Dobrovitski, A. E. Feiguin, O. Gywat, and D. D. Awschalom, *Coherent Dynamics of a Single Spin Interacting with an Adjustable Spin Bath*, Science **320**, 352 (2008).

[138] M. Niknam, L. F. Santos, and D. G. Cory, *Experimental Detection of the Correlation Rényi Entropy in the Central Spin Model*, Phys. Rev. Lett. **127**, 080401 (2021).

[139] L. Amico, A. Di Lorenzo, and A. Osterloh, *Integrable Model for Interacting Electrons in Metallic Grains*, Phys. Rev. Lett. **86**, 5759 (2001).

[140] I. D. Avdeev and D. S. Smirnov, *Hyperfine interaction in atomically thin transition metal dichalcogenides*, Nanoscale Adv. **1**, 2624 (2019).

[141] G. A. Álvarez, A. Ajoy, X. Peng, and D. Suter, *Performance comparison of dynamical decoupling sequences for a qubit in a rapidly fluctuating spin bath*, Phys. Rev. A **82**, 042306 (2010).

[142] M. Bortz and J. Stolze, *Exact dynamics in the inhomogeneous central-spin model*, Phys. Rev. B **76**, 014304 (2007).

[143] M. Bortz, S. Eggert, and J. Stolze, *Spectrum and screening cloud in the central spin model*, Phys. Rev. B **81**, 035315 (2010).

[144] M. Bortz, S. Eggert, C. Schneider, R. Stübner, and J. Stolze, *Dynamics and decoherence in the central spin model using exact methods*, Phys. Rev. B **82**, 161308 (2010).

[145] M. A. Jivulescu, E. Ferraro, A. Napoli, and A. Messina, *Dynamical behaviour of an XX central spin model through Bethe ansatz techniques*, Reports on Mathematical Physics **64**, 315 (2009).

[146] A. Faribault, O. El Araby, C. Sträter, and V. Gritsev, *Gaudin models solver based on the correspondence between Bethe ansatz and ordinary differential equations*, Phys. Rev. B **83**, 235124 (2011).

[147] A. Faribault and D. Schuricht, *Integrability-Based Analysis of the Hyperfine-Interaction-Induced Decoherence in Quantum Dots*, Phys. Rev. Lett. **110**, 040405 (2013).

[148] A. Faribault and D. Schuricht, *Spin decoherence due to a randomly fluctuating spin bath*, Phys. Rev. B **88**, 085323 (2013).

[149] A. Khaetskii, D. Loss, and L. Glazman, *Electron spin evolution induced by interaction with nuclei in a quantum dot*, Phys. Rev. B **67**, 195329 (2003).

[150] W. A. Coish, J. Fischer, and D. Loss, *Free-induction decay and envelope modulations in a narrowed nuclear spin bath*, Phys. Rev. B **81**, 165315 (2010).

[151] H.-P. Breuer, D. Burgarth, and F. Petruccione, *Non-Markovian dynamics in a spin star system: Exact solution and approximation techniques*, Phys. Rev. B **70**, 045323 (2004).

[152] J. Fischer and H.-P. Breuer, *Correlated projection operator approach to non-Markovian dynamics in spin baths*, Phys. Rev. A **76**, 052119 (2007).

[153] E. Ferraro, H.-P. Breuer, A. Napoli, M. A. Jivulescu, and A. Messina, *Non-Markovian dynamics of a single electron spin coupled to a nuclear spin bath*, Phys. Rev. B **78**, 064309 (2008).

[154] E. Barnes, Ł. Cywi ński, and S. Das Sarma, *Master equation approach to the central spin decoherence problem: Uniform coupling model and role of projection operators*, Phys. Rev. B **84**, 155315 (2011).

[155] E. Barnes, Ł. Cywi ński, and S. Das Sarma, *Nonperturbative Master Equation Solution of Central Spin Dephasing Dynamics*, Phys. Rev. Lett. **109**, 140403 (2012).

[156] S. Bhattacharya, A. Misra, C. Mukhopadhyay, and A. K. Pati, *Exact master equation for a spin interacting with a spin bath: Non-Markovianity and negative entropy production rate*, Phys. Rev. A **95**, 012122 (2017).

[157] E. M. Kessler, G. Giedke, A. Imamoglu, S. F. Yelin, M. D. Lukin, and J. I. Cirac, *Dissipative phase transition in a central spin system*, Phys. Rev. A **86**, 012116 (2012).

[158] J. Jing and L.-A. Wu, *Decoherence and control of a qubit in spin baths: an exact master equation study*, Scientific Reports **8**, 1471 (2018).

[159] V. V. Dobrovitski and H. A. De Raedt, *Efficient scheme for numerical simulations of the spin-bath decoherence*, Phys. Rev. E **67**, 056702 (2003).

[160] J. Hackmann and F. B. Anders, *Spin noise in the anisotropic central spin model*, Phys. Rev. B **89**, 045317 (2014).

[161] N. Wu, N. Fröhling, X. Xing, J. Hackmann, A. Nanduri, F. B. Anders, and H. Rabitz, *Decoherence of a single spin coupled to an interacting spin bath*, Phys. Rev. B **93**, 035430 (2016).

[162] D. Stanek, C. Raas, and G. S. Uhrig, *Dynamics and decoherence in the central spin model in the low-field limit*, Phys. Rev. B **88**, 155305 (2013).

[163] D. Stanek, C. Raas, and G. S. Uhrig, *From quantum-mechanical to classical dynamics in the central-spin model*, Phys. Rev. B **90**, 064301 (2014).

[164] W. M. Witzel, R. de Sousa, and S. Das Sarma, *Quantum theory of spectral-diffusion-induced electron spin decoherence*, Phys. Rev. B **72**, 161306 (2005).

[165] W. M. Witzel and S. Das Sarma, *Quantum theory for electron spin decoherence induced by nuclear spin dynamics in semiconductor quantum computer architectures: Spectral diffusion of localized electron spins in the nuclear solid-state environment*, Phys. Rev. B **74**, 035322 (2006).

[166] S. K. Saikin, W. Yao, and L. J. Sham, *Single-electron spin decoherence by nuclear spin bath: Linked-cluster expansion approach*, Phys. Rev. B **75**, 125314 (2007).

[167] J. R. Maze, J. M. Taylor, and M. D. Lukin, *Electron spin decoherence of single nitrogen-vacancy defects in diamond*, Phys. Rev. B **78**, 094303 (2008).

[168] W. Yang and R.-B. Liu, *Quantum many-body theory of qubit decoherence in a finite-size spin bath*, Phys. Rev. B **78**, 085315 (2008).

[169] W. Yang and R.-B. Liu, *Quantum many-body theory of qubit decoherence in a finite-size spin bath. II. Ensemble dynamics*, Phys. Rev. B **79**, 115320 (2009).

[170] W. M. Witzel, M. S. Carroll, Ł. Cywi ński, and S. Das Sarma, *Quantum decoherence of the central spin in a sparse system of dipolar coupled spins*, Phys. Rev. B **86**, 035452 (2012).

[171] G. S. Uhrig, J. Hackmann, D. Stanek, J. Stolze, and F. B. Anders, *Conservation laws protect dynamic spin correlations from decay: Limited role of integrability in the central spin model*, Phys. Rev. B **90**, 060301 (2014).

[172] U. Seifert, P. Bleicker, P. Schering, A. Faribault, and G. S. Uhrig, *Persisting correlations of a central spin coupled to large spin baths*, Phys. Rev. B **94**, 094308 (2016).

[173] J. Schliemann, A. V. Khaetskii, and D. Loss, *Spin decay and quantum parallelism*, Phys. Rev. B **66**, 245303 (2002).

[174] Ł. Cywi ński, V. V. Dobrovitski, and S. Das Sarma, *Spin echo decay at low magnetic fields in a nuclear spin bath*, Phys. Rev. B **82**, 035315 (2010).

[175] R. Röhrig, P. Schering, L. B. Gravert, B. Fauseweh, and G. S. Uhrig, *Quantum mechanical treatment of large spin baths*, Phys. Rev. B **97**, 165431 (2018).

[176] L. P. Lindoy and D. E. Manolopoulos, *Simple and Accurate Method for Central Spin Problems*, Phys. Rev. Lett. **120**, 220604 (2018).

[177] W.-B. He, S. Chesi, H.-Q. Lin, and X.-W. Guan, *Exact quantum dynamics of XXZ central spin problems*, Phys. Rev. B **99**, 174308 (2019).

[178] S. I. Erlingsson and Y. V. Nazarov, *Evolution of localized electron spin in a nuclear spin environment*, Phys. Rev. B **70**, 205327 (2004).

[179] K. A. Al-Hassanieh, V. V. Dobrovitski, E. Dagotto, and B. N. Harmon, *Numerical Modeling of the Central Spin Problem Using the Spin-Coherent-State P Representation*, Phys. Rev. Lett. **97**, 037204 (2006).

[180] G. Chen, D. L. Bergman, and L. Balents, *Semiclassical dynamics and long-time asymptotics of the central-spin problem in a quantum dot*, Phys. Rev. B **76**, 045312 (2007).

[181] J. Hackmann, D. S. Smirnov, M. M. Glazov, and F. B. Anders, *Spin noise in a quantum dot ensemble: From a quantum mechanical to a semi-classical description*, physica status solidi (b) **251**, 1270 (2014).

[182] E. Fermi, *Über die magnetischen Momente der Atomkerne*, Zeitschrift für Physik **60**, 320 (1930).

[183] M. M. Glazov, *Electron & Nuclear Spin Dynamics in Semiconductor Nanostructures*, Series on Semiconductor Science and Technology (OUP Oxford, 2018).

[184] C. Testelin, F. Bernardot, B. Eble, and M. Chamarro, *Hole–spin dephasing time associated with hyperfine interaction in quantum dots*, Phys. Rev. B **79**, 195440 (2009).

[185] J. Fischer, W. A. Coish, D. V. Bulaev, and D. Loss, *Spin decoherence of a heavy hole coupled to nuclear spins in a quantum dot*, Phys. Rev. B **78**, 155329 (2008).

[186] B. Eble, C. Testelin, P. Desfonds, F. Bernardot, A. Balocchi, T. Amand, A. Miard, A. Lemaître, X. Marie, and M. Chamarro, *Hole–Nuclear Spin Interaction in Quantum Dots*, Phys. Rev. Lett. **102**, 146601 (2009).

[187] D. Paget, G. Lampel, B. Sapoval, and V. I. Safarov, *Low field electron-nuclear spin coupling in gallium arsenide under optical pumping conditions*, Phys. Rev. B **15**, 5780 (1977).

[188] A. W. Overhauser, *Polarization of Nuclei in Metals*, Phys. Rev. **92**, 411 (1953).

[189] K. Flisinski, I. Y. Gerlovin, I. V. Ignatiev, M. Y. Petrov, S. Y. Verbin, D. R. Yakovlev, D. Reuter, A. D. Wieck, and M. Bayer, *Optically detected magnetic resonance at the quadrupole-split nuclear states in (In,Ga)As/GaAs quantum dots*, Phys. Rev. B **82**, 081308 (2010).

[190] R. V. Cherbunin, K. Flisinski, I. Y. Gerlovin, I. V. Ignatiev, M. S. Kuznetsova, M. Y. Petrov, D. R. Yakovlev, D. Reuter, A. D. Wieck, and M. Bayer, *Resonant nuclear spin pumping in (In,Ga)As quantum dots*, Phys. Rev. B **84**, 041304 (2011).

[191] P. S. Sokolov, M. Y. Petrov, T. Mehrtens, K. Müller-Caspary, A. Rosenauer, D. Reuter, and A. D. Wieck, *Reconstruction of nuclear quadrupole interaction in (In,Ga)As/GaAs quantum dots observed by transmission electron microscopy*, Phys. Rev. B **93**, 045301 (2016).

[192] M. S. Kuznetsova, R. V. Cherbunin, I. Y. Gerlovin, I. V. Ignatiev, S. Y. Verbin, D. R. Yakovlev, D. Reuter, A. D. Wieck, and M. Bayer, *Spin dynamics of quadrupole nuclei in InGaAs quantum dots*, Phys. Rev. B **95**, 155312 (2017).

[193] C. P. Slichter, *Principles of Magnetic Resonance*, 3rd ed., Springer Series in Solid-State Sciences (Springer Berlin, Heidelberg, 1990).

[194] C. Bulutay, *Quadrupolar spectra of nuclear spins in strained $In_xGa_{1-x}As$ quantum dots*, Phys. Rev. B **85**, 115313 (2012).

[195] C. Bulutay, E. A. Chekhovich, and A. I. Tartakovskii, *Nuclear magnetic resonance inverse spectra of InGaAs quantum dots: Atomistic level structural information*, Phys. Rev. B **90**, 205425 (2014).

[196] N. A. Sinitsyn, Y. Li, S. A. Crooker, A. Saxena, and D. L. Smith, *Role of Nuclear Quadrupole Coupling on Decoherence and Relaxation of Central Spins in Quantum Dots*, Phys. Rev. Lett. **109**, 166605 (2012).

[197] A. Bechtold, D. Rauch, F. Li, T. Simmet, P.-L. Ardelt, A. Regler, K. Müller, N. A. Sinitsyn, and J. J. Finley, *Three-stage decoherence dynamics of an electron spin qubit in an optically active quantum dot*, Nature Physics **11**, 1005 (2015).

[198] A. Fischer, I. Kleinjohann, F. B. Anders, and M. M. Glazov, *Kinetic approach to nuclear-spin polaron formation*, Phys. Rev. B **102**, 165309 (2020).

[199] I. Kleinjohann, A. Fischer, M. M. Glazov, and F. B. Anders, *Nuclear-spin polaron formation: Anisotropy effects and quantum phase transition*, Phys. Rev. B **105**, 195309 (2022).

[200] E. A. Chekhovich, A. Ulhaq, E. Zallo, F. Ding, O. G. Schmidt, and M. S. Skolnick, *Measurement of the spin temperature of optically cooled nuclei and GaAs hyperfine constants in GaAs/AlGaAs quantum dots*, Nature Materials **16**, 982 (2017).

[201] M. Kotur, D. O. Tolmachev, V. M. Litvyak, K. V. Kavokin, D. Suter, D. R. Yakovlev, and M. Bayer, *Ultra-deep optical cooling of coupled nuclear spin-spin and quadrupole reservoirs in a GaAs/(Al,Ga)As quantum well*, Communications Physics **4**, 193 (2021).

[202] K. Binder, *Finite size scaling analysis of ising model block distribution functions*, Zeitschrift für Physik B Condensed Matter **43**, 119 (1981).

[203] D. P. Landau and K. Binder, *A Guide to Monte Carlo Simulations in Statistical Physics*, 4th ed. (Cambridge University Press, 2014).

[204] L. D. Landau and E. M. Lifshitz, *Statistical Physics, Part 1* (Butterworth-Heinemann, Oxford, 2000).

[205] H. J. Carmichael, *Statistical Methods in Quantum Optics 1* (Springer Verlag, Berlin Heidelberg, 1999).

[206] D. Manzano, *A short introduction to the Lindblad master equation*, AIP Advances **10**, 025106 (2020).

[207] G. G. Kozlov, *Exactly solvable spin dynamics of an electron coupled to a large number of nuclei; the electron-nuclear spin echo in a quantum dot*, Journal of Experimental and Theoretical Physics **105**, 803 (2007).

[208] W. E. Arnoldi, *The principle of minimized iterations in the solution of the matrix eigenvalue problem*, Quarterly of Applied Mathematics **9**, 17 (1951).

[209] Y. Saad, *Iterative Methods for Sparse Linear Systems* (Society for Industrial and Applied Mathematics, Philadelphia, USA, 2003).

[210] H. Spohn, *Approach to equilibrium for completely positive dynamical semigroups of N-level systems*, Reports on Mathematical Physics **10**, 189 (1976).

[211] D. Nigro, *On the uniqueness of the steady-state solution of the Lindblad–Gorini–Kossakowski–Sudarshan equation*, Journal of Statistical Mechanics: Theory and Experiment **2019**, 043202 (2019).

[212] O. Perron, *Zur Theorie der Matrices*, Mathematische Annalen **64**, 248 (1907).

[213] G. Frobenius, *Über Matrizen aus nicht negativen Elementen*, Preussische Akademie der Wissenschaften Berlin: Sitzungsberichte der Preußischen Akademie der Wissenschaften zu Berlin (Reichsdr., 1912).

[214] F. G. G. Hernandez, A. Greilich, F. Brito, M. Wiemann, D. R. Yakovlev, D. Reuter, A. D. Wieck, and M. Bayer, *Temperature-induced spin-coherence dissipation in quantum dots*, Phys. Rev. B **78**, 041303 (2008).

[215] S. A. Crooker, J. Brandt, C. Sandfort, A. Greilich, D. R. Yakovlev, D. Reuter, A. D. Wieck, and M. Bayer, *Spin Noise of Electrons and Holes in Self-Assembled Quantum Dots*, Phys. Rev. Lett. **104**, 036601 (2010).

[216] R. Dahbashi, J. Hübner, F. Berski, K. Pierz, and M. Oestreich, *Optical Spin Noise of a Single Hole Spin Localized in an (InGa)As Quantum Dot*, Phys. Rev. Lett. **112**, 156601 (2014).

[217] J. Hübner, F. Berski, R. Dahbashi, and M. Oestreich, *The rise of spin noise spectroscopy in semiconductors: From acoustic to GHz frequencies*, physica status solidi (b) **251**, 1824 (2014).

[218] G. M. Müller, M. Oestreich, M. Römer, and J. Hübner, *Semiconductor spin noise spectroscopy: Fundamentals, accomplishments, and challenges*, Physica E: Low-dimensional Systems and Nanostructures **43**, 569 (2010).

[219] M. Lax, *Formal Theory of Quantum Fluctuations from a Driven State*, Phys. Rev. **129**, 2342 (1963).

[220] F. Berski, J. Hübner, M. Oestreich, A. Ludwig, A. D. Wieck, and M. Glazov, *Interplay of Electron and Nuclear Spin Noise in n-Type GaAs*, Phys. Rev. Lett. **115**, 176601 (2015).

[221] N. Fröhling, F. B. Anders, and M. Glazov, *Nuclear spin noise in the central spin model*, Phys. Rev. B **97**, 195311 (2018).

[222] A. Schwan, B.-M. Meiners, A. B. Henriques, A. D. B. Maia, A. A. Quivy, S. Spatzek, S. Varwig, D. R. Yakovlev, and M. Bayer, *Dispersion of electron g-factor with optical transition energy in (In,Ga)As/GaAs self-assembled quantum dots*, Applied Physics Letters **98**, 233102 (2011).

[223] N. Jäschke, *A semiclassical approach to the spin dynamics in a singly charged semiconductor quantum dot*, PhD thesis (TU Dortmund University, 2019).

[224] P. Schering, *Nonequilibrium spin phenomena in quantum dots induced by periodic optical excitation*, PhD thesis (TU Dortmund University, 2021).

[225] A. Vezvaee, G. Sharma, S. E. Economou, and E. Barnes, *Driven dynamics of a quantum dot electron spin coupled to a bath of higher-spin nuclei*, Phys. Rev. B **103**, 235301 (2021).

[226] S. Lee, P. von Allmen, F. Oyafuso, G. Klimeck, and K. B. Whaley, *Effect of electron-nuclear spin interactions for electron-spin qubits localized in InGaAs self-assembled quantum dots*, Journal of Applied Physics **97**, 043706 (2005).

[227] E. Evers, V. V. Belykh, N. E. Kopteva, I. A. Yugova, A. Greilich, D. R. Yakovlev, D. Reuter, A. D. Wieck, and M. Bayer, *Decay and revival of electron spin polarization in an ensemble of (In,Ga)As quantum dots*, Phys. Rev. B **98**, 075309 (2018).

[228] N. Fröhling and F. B. Anders, *Long-time coherence in fourth-order spin correlation functions*, Phys. Rev. B **96**, 045441 (2017).

[229] E. Evers, *Nuclear-electron spin interaction in low-dimensional semiconductors*, PhD thesis (TU Dortmund University, 2021).

Acknowledgments

First of all, I would like to thank my supervisor Prof. Dr. Frithjof B. Anders for his invaluable advice and continuous support over the past years. My gratitude extends to Prof. Dr. Götz S. Uhrig who takes on the role of the second assessor. Furthermore, I would like to thank Prof. Dr. Mikhail M. Glazov for his warm welcome during my visits to St. Petersburg and his scientific input regarding the first part of this thesis. I would also like to thank Dr. Eiko Evers, PD Dr. Alex Greilich, and Prof. Dr. Manfred Bayer for the experimental insights and the fruitful collaboration. I am grateful to all my colleagues of the former chair "T2" who made sure lunch and tea/coffee breaks never got boring and helped me through my PhD time. Special thanks go to Andreas Fischer for many fruitful discussions about physics and the proofreading of this thesis. Finally, I thank my family, especially my parents, for their encouragement and support all through my studies.